

TO MY MOTHER
AND
IN THE MEMORY OF MY
DEAR FATHER

TOUGHNESS MEASUREMENT OF
HOT WORK DIE STEEL

Wafia Mahmood Hussain

Submitted for the Degree of
Master of Philosophy

The University of Aston in Birmingham

November 1982

TITLE: TOUGHNESS MEASUREMENTS OF HOT WORK
DIE STEEL

NAME: WAFIA MAHMOOD HUSSAIN

DEGREE: M.Phil.

YEAR: 1982

SYNOPSIS

In this present work attempts are made to relate microstructure and fracture toughness (K_{ICSB} and COD) for Electem, Thermodie, Hydrie and Somdie hot work die steels. Structural features studied were the fracture surfaces and general microstructures, using a scanning electron microscope and optical microscope.

The test samples were taken from three different sections representing the top, mid-radius and centre of the die block. Notched three point bend tests were carried out also on Thermodie, Hydrie and Somdie steels. The notches were pre-fatigue cracked using an Amsler Vibrophor 2 tonne capacity machine.

Microstructures and fracture surfaces were investigated using optical electron microscope and scanning electron microscope techniques to establish possible failure mechanisms. A dominant feature of the work is the effect of grain size variation arising from the position in the die block.

Special attention was paid to the effects of inclusions on the mechanical properties and fracture toughness of these die steels. This latter effect is related to the inclusion distribution and machinability of the die block.

The results are presented in terms of the K_{ICSB} , derived from short bar toughness test and K_{IC} derived from a three point bend test to BS.5447. For different specimens, namely short bar, short rod and three point bend, the variation of fracture toughness with position in the block is considerable. The fracture mechanism was void growth and coalescence, which resulted in a ductile dimple, and some areas of cleavage. The fracture surfaces showed formation of elongated dimples in some specimens, these were related to certain features of the microstructure.

KEY WORDS: Electem, Thermodie, Hydrie, Somdie steel,
Fracture toughness.

CONTENTS

	<u>PAGE</u>
Synopsis	(i)
List of Tables	(ii)
List of Figures	(iii)
List of Plates	(iv)
Acknowledgements	(v)
1 INTRODUCTION	1
2 DEVELOPMENT IN FRACTURE MECHANICS	7
2.1 Stress Intensity Factor	8
2.2 Energy Balance Approach	9
2.3 Linear Elastic Fracture Mechanics	10
2.3.1 Thickness Effect	14
2.3.2 Plastic Zone	15
2.3.3 Plane Stress	16
2.3.4 Plane Strain	16
2.4 Microstructure	24
2.4.1 Influence of Microstructure on Crack Propagation Mechanism and Fracture Toughness	24
2.4.2 Residual Stress Effect	30
3. MICROMECHANISM OF FRACTURE MECHANICS	36
3.1 Cracking Process	36
3.2 Rupture Process	36
4. METHOD FOR EVALUATION OF FRACTURE TOUGHNESS	38

		<u>PAGE</u>
4.1	Previous and Recent Work for Measuring Fracture Toughness	38
4.1.1	Short Rod/Bar Techniques	45
4.1.2	Crack Opening Displacement (COD) Technique	46
4.1.3	The 5% Secant LEFM	46
4.2	General Yield of Fracture Mechanics	51
4.2.1	The Crack Opening Displacement (COD)	51
4.2.2	J-Integral	56
4.2.2.1	Limitation of J-Integral as a Fracture Criterion	57
5.	INFLUENCE OF ALLOY CONSTITUENT ON THE PROPERTIES OF STEEL	59
5.1	Heat Treatment and Isothermal Transformation	59
5.1.1	Bainitic Transformation	62
5.1.2	Martensitic Transformation	63
5.1.2.1	Deformation Induced Martensitic Transformation and Transformation Induced Plasticity in Steel	76
5.1.2.1.1	Deformation Induced Martensitic Transformation	76
6.	EXPERIMENTAL WORK	82
6.1	Material Used	82
6.2	Specimen Preparation and Dimensions	82
6.2.1	Short Rod/bar	82
6.2.2	Three Point Bend Specimens	87

	<u>PAGE</u>	
6.3	Short Rod/bar Fracture Toughness	89
	Testing K_{ICSB}	
6.4	Three Point Bend Test (K_{IC})	90
6.5	Mechanical Testing	140
6.5.1	Tensile Test	140
6.5.2	Hardness Test	169
6.5.3	Metallography and Fractography	169
6.6	Heat Tinting Process	170
7.	DATA ANALYSIS	171
7.1	K_{ICSB}	171
7.2	K_{IC} Three Point Bend	173
8.	RESULTS	175
9.	DISCUSSION	189
9.1	Metallography and Fractography	189
9.2	Relation between Fracture Toughness and Microstructure	194
9.2.1	Toughness and Microstructure	194
9.2.2	Toughness and Fractography	200
9.3	Load/Crack Mouth Opening Displacement Record for Measuring K_{ICSB}	203
9.4	Variation of Fracture Toughness along the Block of Die Steels	205
9.5	Notch Bending Test	206
9.6	Stress Assisted Martensite Formation	208
10	CONCLUSIONS	307
	REFERENCES	310

LIST OF TABLES

<u>TABLE</u>		<u>PAGE</u>
1	Condition used for treatment of Electem, Somdie, Thermodie (short rod), Hydie and Somdie (short bar) die blocks	176
2	Chemical analysis of short rod/bar test specimens	177
3	Mechanical properties of an investigated alloy at room temperature under conditions set in table 2 (short rod)	178
4	Mechanical properties of an investigated alloy at room temperature under conditions set in table 2 (short bar)	179
5	Specimen dimensions of H.W. die steels Electem, Somdie and Thermodie (short rod)	180
6	H.W. die steel fracture toughness K_{ICSB} results, Electem, Somdie and Thermodie (short rod)	181
7	Specimen dimension of Hydie steel (short bar)	182
8	Fracture toughness K_{ICSB} results of Hydie steel (short bar)	183
9	Hydie crack length measurement for (short bar)	184
10	Specimen dimension of Somdie steel (short bar)	185

<u>TABLE</u>		<u>PAGE</u>
11	Fracture toughness (K_{ICSB}) Results of Somdie steel (short bar)	186
12	Fracture toughness (K_{IC}) results for three point bend specimens, Hydie and Somdie steel	187
13	Test results of short rod/bar with standard deviation	188

LIST OF FIGURES

<u>FIGURE</u>		<u>PAGE</u>
1	Energy balance of crack	17
2a	Plane strain condition	18
2b	Plane stress condition	18
3	Typical form of the relationship between fracture toughness and component thickness	19
4	The basic modes of crack surface displacement	20
5	Elastic stress singularities of the different crack deformation modes ⁽⁶⁾	21
6	Variation of stress intensity factor and fracture profile with thickness of test piece	22
7	Displacement (2V) associated with crack opening, with elongated shape of plastic zone	23
8	Yield zones on the surface and cross-section of cracked sheet under uniaxial tensile loading in plane strain (hinge type plastic zone)	23
9	Schematic representation of the influence of grain size, loading rate and inclusion content on crack propagation mechanism and fracture toughness.	26

<u>FIGURE</u>		<u>PAGE</u>
10	Influence of sulphur level on fracture toughness of 0.45 Ni-Cr-Mo steels (Birkle et al)	27
11	Fracture toughness of steel AISI 4340 as a function of tempering temperature (Zackagl)	28
12	Fracture toughness of steel AISI 4130 as a function of tempering temperatures	29
13	Effect of thickness on K_C of averaged 7000 series alloys with various grain sizes (Thompson and Zinkham)	31
14	Schematic of the short rod (Barker)	34
15	Schematic of elastic plastic specimen behaviour	35
16	Relation between the geometry and ratio of crack length	42
17	Grip method of loading to short rod/bar specimen	43
18	Fractometer method of loading short rod specimens	44
19	Principle type of force/displacement record	49
20	Force/displacement record for calculation	50
20	COD Principle type of force/displacement record	50

FIGUREPAGE

21	Schematic representation of local plasticity and crack tip for theoretical analysis (3)	55
22-1	TTT diagram for commercial low alloy steel a - 0.4% C, 1% Mn, b - 0.4% C, 1% Mn, 0.9% Cr	65
22-2	TTT diagram for commercial low alloy steel, a - 0.4% C, 1% Mn, 1% Cr, 0.2% Mo b - 0.4% C, 1% Mn, 0.8% Cr, 0.3% Mo and 1.8% Ni	66
23	The effect of carbon content in steel on the M_s and M_f point	67
23-1	TTT diagram of a molybdenum steel 0.3% C, 2.0% Mo	68
23-2	TTT diagram of a molybdenum steel 0.4% C, 0.2% Mo	68
24-1	Relation between cooling curves for the surface and core of an oil quenched 95 mm diameter bar and the microstructure. The surface fully martensitic	69
24-2	Typical cooling curves of 386 mm ² water and oil quench of Electem die block, quenching time 50 minutes	70
24-3	Typical cooling curves of 380 mm ² Somdie block, water quench, quenching time 35 minutes	71

<u>FIGURE</u>		<u>PAGE</u>
25-1	Continuous cooling transformation diagram and isothermal transformation diagram for Electem die steel	72
25-2	Continuous cooling transformation diagram for Thermodie steel	73
25-3	Continuous cooling transformation diagram for Somdie steel	74
26	Diagram of isothermal decomposition of austenite in alloy steels with separate C-curve for pearlite and bainite transformation	75
27	Chemical free energy of austenite and martensite as a function of temperature	79
28	Relation between applied stress axis, A, θ and α , N - normal direction to plan p S is shear direction of martensitic transformation and S_m is maximum shear direction on p	80
29	Critical stress for martensite formation as a function of temperature	81
30	Short rod/bar specimen (general view)	83
31	a. Short rod dimension b. Short bar dimension (Test configuration for Instron)	84

<u>FIGURE</u>		<u>PAGE</u>
32	Schematic plan of work for Hydrie, Somdie steel (short bar)	85
33	Schematic plan of work for Electem, Somdie and Thermodie steel (short rod)	86
34	3-point bend specimen	88
35	Schematic plan of work for 3-point bend test specimens	88
36-1	Force/clip gauge opening displacement record for A0	93
36-2	Force/clip gauge opening displacement record for B0	94 -
36-3	Force/clip gauge opening displacement record for C0	95
36-4	Force/clip gauge opening displacement record for D0	96
36-5	Force/clip gauge opening displacement record for BM	97
36-6	Force/clip gauge opening displacement record for CM	98
36-7	Force/clip gauge opening displacement record for DM	99

<u>FIGURE</u>		<u>PAGE</u>
36-8	Force/clip gauge opening displacement record for AC	100
36-9	Force/clip gauge opening displacement record for BC	101
36-10	Force/clip gauge opening displacement record for CC	102
36-11	Force/clip gauge opening displacement record for DC	103
36-12	Force/clip gauge opening displacement record for EC	104
37-1	Force/clip gauge opening displacement record for H10	105
37-2	Force/clip gauge opening displacement record for H1M	106
37-3	Force/clip gauge opening displacement record for H1C	107
37-4	Force/clip gauge opening displacement record for H1A	108
37-5	Force/clip gauge opening displacement record for H1B	109
37-6	Force/clip gauge opening displacement record for H20	110

<u>FIGURE</u>		<u>PAGE</u>
37-7	Force/clip gauge opening displacement record for H2M	111
37-8	Force/clip gauge opening displacement record for H2C	112
37-9	Force/clip gauge opening displacement record for H2A	113
37-10	Force/clip gauge opening displacement record for H2B	114
37-11	Force/clip gauge opening displacement record for H3O	115
37-12	Force/clip gauge opening displacement record for H3M	116
37-13	Force/clip gauge opening displacement record for H3C	117
37-14	Force/clip gauge opening displacement record for H3A	118
37-15	Force/clip gauge opening displacement record for H3B	119
38-1	Force/clip gauge opening displacement record for S10	120

<u>FIGURE</u>		<u>PAGE</u>
38-2	Force/clip gauge opening displacement record for S1M	121
38-3	Force/clip gauge opening displacement record for S1C	122
38-4	Force/clip gauge opening displacement record for S1A	123
38-5	Force/clip gauge opening displacement record for S1B	124
38-6	Force/clip gauge opening displacement record for S2O	125
38-7	Force/clip gauge opening displacement record for S2M	126
38-8	Force/clip gauge opening displacement record for S2C	127
38-9	Force/clip gauge opening displacement record for S2A	128
38-10	Force/clip gauge opening displacement record for S2B	129
38-11	Force/clip gauge opening displacement record for S3O	130

<u>FIGURE</u>		<u>PAGE</u>
38-12	Force/clip gauge opening displacement record for S3M	131
38-13	Force/clip gauge opening displacement for S3C	132
38-14	Force/clip gauge opening displacement record for S3B	133
39	Typical load vs clip gauge opening dis- placement record obtained from notch bending test	
	Hydie (39-1, 39-2, 39-3)	134-136
	Somdie (39-4, 39-5, 39-6)	137-139
40	Tensile test specimen No. 12 showing the dimension and cross-sectional area A	141
41-1	Load/Extension curve for H.W. die steel AO	142
41-2	Load/extension curve for H.W. die steel CO	143
41-3	Load/extension curve for H.W. die steel DO	144
41-4	Load/extension curve for H.W. die steel AM	145
41-5	Load/extension curve for H.W. die steel BM	146
41-6	Load/extension curve for H.W. die steel DM	147
41-7	Load/extension curve for H.W. die steel BC	148
41-8	Load/extension curve for H.W. die steel DC	149
41-9	Load/extension curve for H.W. die steel EC	150

<u>FIGURE</u>		<u>PAGE</u>
42-1	Load/extension curve of Hydie steel H10	151
42-2	Load/extension curve of Hydie steel H1C	152
42-3	Load/extension curve of Hydie steel H1B	153
42-4	Load/extension curve of Hydie steel H20	154
42-5	Load/extension curve of Hydie steel H2C	155
42-6	Load/extension curve of Hydie steel H2B	156
42-7	Load/extension curve of Hydie steel H30	157
42-8	Load/extension curve of Hydie steel H3C	158
42-9	Load/extension curve of Hydie steel H3B	159
43-1	Load/extension curve of Somdie steel S10	160
43-2	Load/extension curve of Somdie steel S1C	161
43-3	Load/extension curve of Somdie steel S1B	162
43-4	Load/extension curve of Somdie steel S20	163
43-5	Load/extension curve of Somdie steel S2C	164
43-6	Load/extension curve of Somdie steel S2B	165
43-7	Load/extension curve of Somdie steel S30	166
43-8	Load/extension curve of Somdie steel S3C	167
43-9	Load/extension curve of Somdie steel S3B	168

LIST OF PLATES

<u>PLATE</u>		<u>PAGE</u>
1	View of the specimen on machine (three point bend)	92
2	Fracture surface of H.W. die steel (short rod) AO	212
3	Fracture surface of H.W. die steel (short rod) AM	214
4	Fracture surface of H.W. die steel (short rod) AC	216
5	Fracture surface of H.W. die steel (short rod) BO	218
6	Fracture surface of H.W. die steel (short rod) BM	220
7	Fracture surface of H.W. die steel (short rod) BC	222
8	Fracture surface of H.W. die steel (short rod) CO	224
9	Fracture surface of H.W. die steel (short rod) CM	226
10	Fracture surface of H.W. die steel (short rod) CC	228
11	Fracture surface of H.W. die steel (short rod) DO	230

<u>PLATE</u>		<u>PAGE</u>
12	Fracture surface of H.W. die steel (short rod) DM	232
13	Fracture surface of H.W. die steel (short rod) DC	234
14	Fracture surface of H.W. die steel (short rod) EO	236
15	Fracture surface of H.W. die steel (short rod) EC	238
16	Fracture surface of H.W. die steel (Hydie) H2O	240
17	Fracture surface of H.W. die steel (Hydie) H2M	242
18	Fracture surface of H.W. die steel (Hydie) H2C	244
19	Fracture surface of H.W. die steel (Hydie) H2A	246
20	Fracture surface of H.W. die steel (Hydie) H2B	248
21	Fracture surface of H.W. die steel (Hydie) H3O	250
22	Fracture surface of H.W. die steel (Hydie) H3M	252

<u>PLATE</u>		<u>PAGE</u>
23	Fracture surface of H.W. die steel (Hydie) H3C	254
24	Fracture surface of H.W. die steel (Hydie) H3A	256
25	Fracture surface of H.W. die steel (Hydie) H3B	258
26	Fracture surface of H.W. die steel (Somdie) S10	260
27	Fracture surface of H.W. die steel (Somdie) S1M	262
28	Fracture surface of H.W. die steel (Somdie) S1C	264
29	Fracture surface of H.W. die steel (Somdie) S1A	266
30	Fracture surface of H.W. die steel (Somdie) S1B	268
31	Fracture surface of H.W. die steel (Somdie) S20	270
32	Fracture surface of H.W. die steel (Somdie) S2M	272
33	Fracture surface of H.W. die steel (Somdie) S2C	275
34	Fracture surface of H.W. die steel (Somdie) S2A	277
34a	Crack path of short bar specimen S2A Somdie steel	278

<u>PLATE</u>		<u>PAGE</u>
35	Fracture surface of H.W. die steel (Somdie) S2B	280
36	Fracture surface of H.W. die steel (Somdie) S30	282
36a	Crack path start at chevron point down to the centre of the fracture surface. Notice the coalescence of cavities formed at inclusion	283
37	Fracture surface of H.W. die steel (Somdie) S3M	285
38	Fracture surface of H.W. die steel (Somdie) S3C	287
39	Fracture surface of H.W. die steel (Somdie) S3B	289
40	Microstructure of H.W. die steel (short rod) A0	211
41	Microstructure of H.W. die steel (short rod) AM	213
42	Microstructure of H.W. die steel (Short rod) AC	215
43	Microstructure of H.W. die steel (short rod) B0	217
44	Microstructure of H.W. die steel (short rod) BM	219
45	Microstructure of H.W. die steel (short rod) BC	221
46	Microstructure of H.W. die steel (short rod) C0	223

<u>PLATE</u>		<u>PAGE</u>
47	Microstructure of H.W. die steel (short rod) CM	225
48	Microstructure of H.W. die steel (short rod) CC	227
49	Microstructure of H.W. die steel (short rod) DO	229
50	Microstructure of H.W. die steel (short rod) DM	231
51	Microstructure of H.W. die steel (short rod) DC	233
52	Microstructure of H.W. die steel (short rod) EO	235 -
53	Microstructure of H.W. die steel (short rod) EC	237
54	Microstructure of H.W. die steel (Hydie) H2O	239
55	Microstructure of H.W. die steel (Hydie) H2M	241
56	Microstructure of H.W. die steel (Hydie) H2C	243
57	Microstructure of H.W. die steel (Hydie) H2A	245
58	Microstructure of H.W. die steel (Hydie) H2B	247

<u>PLATE</u>		<u>PAGE</u>
59	Microstructure of H.W. die steel (Hydie) H30	249
60	Microstructure of H.W. die steel (Hydie) H3M	251
61	Microstructure of H.W. die steel (Hydie) H3C	253
62	Microstructure of H.W. die steel (Hydie) H3A	255
63	Microstructure of H.W. die steel (Hydie) H3B	257
64	Microstructure of H.W. die steel (Somdie) S10	259 -
65	Microstructure of H.W. die steel (Somdie) S1M	261
66	Microstructure of H.W. die steel (Somdie) S1C	263
67	Microstructure of H.W. die steel (Somdie) S1A	265
68	Microstructure of H.W. die steel (Somdie) S1B	267
69	Microstructure of H.W. die steel (Somdie) S20	269
70	Microstructure of H.W. die steel (Somdie) S2M	271

<u>PLATE</u>		<u>PAGE</u>
70a	Crack path of short bar specimen S2M Somdie steel	273
71	Microstructure of H.W. die steel (Somdie) S2C	274
72	Microstructure of H.W. die steel (Somdie) S2A	276
73	Microstructure of H.W. die steel (Somdie) S2B	279
74	Microstructure of H.W. die steel (Somdie) S3O	281
75	Microstructure of H.W. die steel (Somdie) S3M	284
76	Microstructure of H.W. die steel (Somdie) S3C	286
77	Microstructure of H.W. die steel (Somdie) S3B	288
78	Fracture surface for three point bend (area under fatigue crack) Hydie HO	290
79	Fracture surface for three point bend (area under fatigue crack) Hydie HM	290
80	Fracture surface for three point bend (area under fatigue crack) Hydie HC	290
81	Fracture surface for three point bend (area under fatigue crack) Somdie S1	291

<u>PLATE</u>		<u>PAGE</u>
82	Fracture surface for three point bend (area under fatigue crack) Somdie S2	291
83	Fracture surface for three point bend (area under fatigue crack) Somdie S3	291
84	General appearance of short rod fracture toughness test specimen halves with imperfect crack guidance by the slot	292
85	General appearance of short bar fracture toughness test specimen Hydie	293
86	General appearance of short bar fracture toughness test specimen after heat tinting process	294
87	General appearance of short bar fracture toughness test specimen Somdie	295
88-1	Variation of fracture toughness of H.W. die steel with distance from top block, Electem	297
88-2	Variation of fracture toughness of H.W. die steel with distance from top block, Somdie short rod	299
88-3	Variation of fracture toughness of H.W. die steel with distance from top block, Thermodie short rod	300

<u>PLATE</u>		<u>PAGE</u>
88-4	Variation of fracture toughness of H.W. die steel with distance from top block, Hydrie short bar	303
88-5	Variation of fracture toughness of H.W. die steel with distance from top block, Somdie short bar	305
89	General appearance of three-point bend specimens	306

ACKNOWLEDGEMENTS

I wish to express deepest gratitude to my supervisor, Professor J. T. Barnby for his encouragement and assistance throughout this work.

I am also grateful to the staff of Walter Somers Limited for the preparation of die steel specimens used in this work.

I should also like to thank the technicians in the Department of Metallurgy and Materials Engineering for their help where appropriate.

In addition, I would like to record my appreciation to the University of Mosul for granting me a study leave.

A special thanks is deserved by Mrs. H. Howell for typing this thesis.

Most of all, I am indebted to my family for their support and encouragement throughout this work.

1. INTRODUCTION

Fracture ⁽¹⁾ is the separation or fragmentation of a solid body into two or more parts under the action of stress. The process of fracture can be considered as being made up of two components:-

- (a) crack initiation
- (b) crack propagation

Fracture can also be viewed as a non-homogeneous process of deformation that causes regions of material to separate, which in turn reduces the carrying capacity to zero.

Fracture occurs when the local stresses build up either to the theoretical cohesive strength ($\sigma_c \approx E/10$) or to the theoretical shear strength ($T_c = G/10$) where E and G are the respective elastic and shear modulae.

Fracture can be classified into:

- (a) Ductile Fracture
- (b) Brittle Fracture

Ductile Fracture is characterised by appreciable plastic deformation prior to and during the propagation of the crack. An amount of gross deformation is usually present at the fracture surfaces.

Brittle Fracture in metal is characterised by a rapid rate of crack propagation, with no gross deformation

and very little microdeformation. The tendency to brittle fracture increases with:

- (a) strain rate
- (b) triaxial stress conditions
- (c) decrease in temperature.

Furthermore, brittle fracture is often characterised by separation normal to the tensile stress.

The way in which a fracture occurs depends on the following:

- (a) stress state
- (b) stress rate application
- (c) temperature.

Additionally, metals can exhibit many different types of fracture, depending on:

- (a) materials
- (b) temperatures
- (c) stress state
- (d) loading rate

Fracture can be further classified in terms of such characteristics as strain to fracture, crystallographic mode of fracture and the appearance of the fracture.

In the case of fracture toughness of a material, which is a material property relating the defect size to the

applied stress to cause fracture, in practice, fracture toughness is generally expressed by the critical intensity factor K_{IC} . This is a material property which is independent of crack length, specimen geometry or applied stress.

L.M. Barker ⁽²⁾ pointed out that the fracture toughness must somehow specify the configuration of the crack tip.

The present view of fracture started with the Griffith's concept of crack propagation which was presented in 1920. The now well known concept essentially states that an existing crack will propagate if the total energy of the system is ^{there by} lowered. The stress analysis used to calculate the stored elastic energy was taken from Inglis's work published in 1913. The Griffith's theory provides a means of estimating the theoretical strength of solids. It is also given for brittle materials, the correct relationship between fracture strength and defect size. In 1948 Irwin confirmed Orowan's view that the Griffith's type energy balance must be between the strain energy stored in the specimen and the surface energy plus the work done in plastic deformation. Irwin also recognised that the work done against surface tension for relatively ductile materials is generally not significant in comparison with the work done against plastic deformation. Recent work at the Lewis Research Centre indicates the need to study plane-strain crack extension.

Plasticity treatment of the stress and strain fields of notches were given by Hill, Hult and McClintock, in 1956 presented a plasticity analysis of the stress and strain fields of sharp cracks in shear; McClintock applied this analysis to ductile fracture.

The Inglis ⁽³⁾ analysis provided a solution for the stress distribution around an internal crack, with the maximum stress being given by

$$\sigma_{\max} = 2\sigma_0 \sqrt{\frac{c}{p}} \dots\dots\dots(1)$$

σ_0 is the applied stress remote from the crack

$2c$ is the crack length

p is the radius of the curvature at the end of the major axis of the elliptical crack.

Griffith developed an analysis based upon energy consideration. Griffith calculated elastic energy per unit of volume stored in the material from the stress distribution around an elliptical crack. He obtained the following for a plate of unit thickness

$$U_e = \pi C^2 \sigma_0^2 / E \dots\dots\dots(2)$$

U is the elastic energy stored in the plate

E Young's modulus.

Irwin used a method of analysis developed by Westergaard for determining the modification needed for a specimen of finite width W . He obtained the following relationship for the energy release rate

$$G = \frac{\sigma_o^2 W}{E} \tan \frac{\pi c}{W} \dots\dots\dots(3)$$

The Westergaard analysis leads to the following equations for stress analysis in the vicinity of a crack apex

$$\sigma_y = \frac{\sigma_o}{\sqrt{2r/c}} \cos \frac{\theta}{2} \left[1 + \sin \frac{\theta}{2} \sin \frac{3\theta}{2} \right] \dots\dots\dots(4)$$

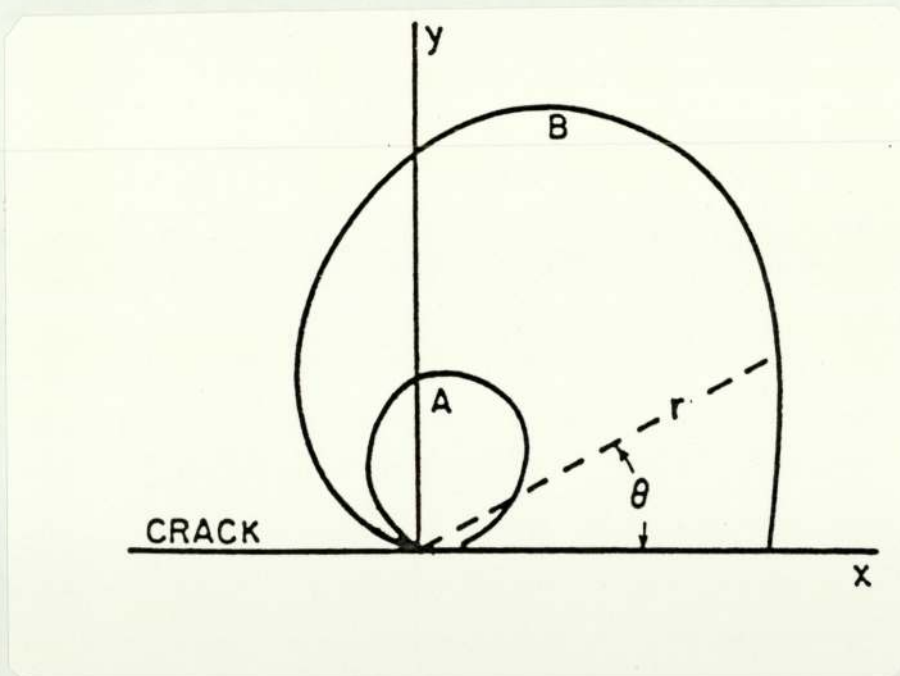
$$\sigma_x = \frac{\sigma_o}{\sqrt{2r/c}} \cos \frac{\theta}{2} \left[1 - \sin \frac{\theta}{2} \sin \frac{3\theta}{2} \right] \dots\dots\dots(5)$$

$$T_{xy} = \frac{\sigma_o}{\sqrt{2r/c}} \sin \frac{\theta}{2} \cos \frac{\theta}{2} \cos \frac{3\theta}{2} \dots\dots\dots(6)$$

where $\sigma_z = 0$ for plane stress or
 $\sigma_z = \nu(\sigma_x + \sigma_y) = \frac{2\nu\sigma_o}{2r/c} \cos \frac{\theta}{2}$ for plane strain

where σ_y is the stress due to the load acting perpendicular to the notch
 σ_x is the stress due to the load parallel to the notch
 σ_z is the induced thickness direction stress.
 r and θ are polar co-ordinates (depend on the apex of the notch as the origin)
 r being the distance to any point in the plates and θ being the angle between r and the line of the notch.

Irwin was able to use the Westergaard analysis to calculate the relative sizes of the plastic zones for plane stresses and strain states. These results are shown below.



2. DEVELOPMENT IN FRACTURE MECHANICS

The fracture ⁽⁴⁾ of any structure demands the creation of a new surface. The energy required to create this surface is the fracture energy; it is made up of two components.

- (a) the energy required to create the surface
- (b) the energy dissipated in the material as deformation.

Griffith originated the above concept and applied it only to brittle material in which the plastic flow was negligible and the fracture energy was the surface energy of the substances (Irwin modified this concept by accounting for the energy dissipated at the crack tip). In many engineering materials this energy is greater than the surface energy, but the volume of material deformed plastically is essentially small and uniform as the crack tip deepens. Furthermore, the concept of fracture energy is a measure of a material's resistance to fracture.

Irwin determined the stress state in an isotropic elastic medium near the crack tip and showed it to be related to a function of position and a quantity that depended on the nature of the crack and the load on the body. He referred to this quantity as the stress intensity factor, K , and K_{IC} is the critical intensity factor, so that when a load on a body containing a crack reaches a critical value the crack will propagate. Hence the structure's ability to resist crack propagation is measured either by

the critical stress intensity factor K_{IC} or by its fracture energy G_{IC} .

Both Griffith's and Irwin's ⁽⁴⁾ theories determine the necessary energetic conditions for fracture accordingly, a flaw or crack must be present in the materials before fracture. But in the case of fracture toughness, which is a correlation of the effects of load and crack length, the fracture toughness test would involve a measurement of the load and the length (depth) of the crack during the test.

2.1 Stress Intensity Factor

The essential concepts of K_{IC} was first described by Irwin 1958 ⁽⁵⁾. The concept depends on the stress analysis of cracks in linear elastic bodies and is measured in terms of the opening mode stress intensity factor K_I . The important distinction between mathematical K_I and material property K_{IC} is similar to distinction between stress and strength ⁽⁶⁾.

K_{IC} toughness of material can be used to estimate the load that a structural member containing a crack of known dimensions could sustain without fracture.

Strength estimates based also on K_{IC} assume a high degree of elastic constraint to plastic flow of material at the crack tip. This degree of constraint exists when a sufficiently large crack occurs in a sufficiently heavy

section in relation to plastic zone size factor $(K_{IC}/\sigma_{ys})^2$. There is a general tendency for K_{IC} to decrease as the yield strength increases and the size factor for very high strength steel can be as small as 0.254 mm or less. With less constraint such as in a thin plate, the effective toughness of material may be substantially greater than K_{IC} . Therefore, it is appropriate to regard K_{IC} as a basic material property since it is the lower limit of effective toughness with increase in the degree of constraint to plastic deformation.

2.2 Energy Balance Approach

Griffith (7) originally proposed the energy balance approach to the study of the fracture phenomenon in a cracked body. His theory was that unstable crack growth ^{results} in more stored energy being released than is absorbed by the creation of the new crack surface.

Griffith argued that there were two energy terms to consider when a crack was extended. First, there would be a release of elastic energy and, secondly, there would be an increase in surface energy. In plane strain for unit thickness, his calculations gave for the energy release

$$W = \frac{-\sigma_{app}^2 \pi a^2}{2E} (1 - \nu^2) \dots\dots\dots(7)$$

and for the surface energy increase

$$S = 2\gamma a$$

where γ is the surface energy per unit area.

These expressions are plotted as functions of crack length as shown in Fig. 1.

$U = W + S$ is the total energy of the system.

It can be seen that the total energy is a maximum when

$$\frac{du}{da} = \frac{dw}{da} + \frac{ds}{da} = 0$$

i.e. when

$$\frac{-\sigma_{app}^2 \pi a^2}{E} (1-\nu^2) + 2\gamma = 0$$

$$\sigma_{app}^2 = \frac{2E\gamma}{\pi(1-\nu^2)a^2} \dots\dots\dots(8)$$

$$2\gamma = \frac{\sigma_{app}^2 \pi a^2}{E} (1-\nu^2) ..$$

where σ_{app} is the applied stress
 E is the Young's Modulus
 ν is the Poisson's ratio
 γ is the surface energy

2.3 Linear Elastic Fracture Mechanics

The result of high elastic stress near the crack tip is the formation of the plastic zone. The size of the plastic zone depends on the stresses whether developed in plane stress ($\sigma_3 = 0$) or in plane strain. A plastic region near the surface of a thick section is typically under the plane stress condition, while the plane strain in the centre region, as can be seen in Fig. 2 a, b.

The radius^{is} given by:

$$r_y = \frac{1}{2\pi} \left(\frac{K_{IC}}{\sigma_{ys}} \right)^2 \text{ plane stress}$$

$$r_y = \frac{1}{5.6\pi} \left(\frac{K_{IC}}{\sigma_{ys}} \right)^2 \text{ plane strain}$$

In the earlier draft (8) recommends that the thickness should be

$$B > 2.5 \left(\frac{K_{IC}}{\sigma_{ys}} \right)^2$$

In applying linear elastic fracture mechanics the thickness of a body should be of sufficient size in order to completely contain the plastic zone (plane strain). Fig. 3 shows that the specimen thickness, B, increases as the stress intensity decreases. However, after a certain minimum thickness (B_{min}) is reached, the stress intensity level can be seen to be beyond the plane stress zone. In practice (9,10) to ensure that the stress intensity factor is obtained in plane strain condition the value B should be

$$B > 4 \left(\frac{K_{IC}}{\sigma_y} \right)^2$$

A modified criterion (11) is developed on an empirical basis for the minimum thickness B_{min} of a plane strain fracture toughness test specimen.

$$B_{min} = 400 \frac{K_{IC}^2}{E\sigma_y}$$

K_{IC} = plane strain fracture toughness

E = Young's Modulus

σ_y = Yield stress of the material

In the Irwin development of Griffith's theory the surface energy is replaced by the strain energy release rate or crack extension force 'G'; crack extension required a fixed rate of dissipation of energy. By definition 'G' is the quantity of stored elastic strain energy released from a cracking specimen as a result of extension of crack by unit length, G being measured in a unit in lb/in^2 . In the above case the propagation of an unstable crack is associated with the critical value of G, such that the release in strain energy as the crack extends just exceeds the rate of energy dissipation needed for creation of a new crack surface. The critical value is designated G_{IC} or G_C , which is known as the fracture toughness. The subscripts I, refer to the opening mode of crack behaviour. Furthermore, there are three kinematic movements of crack surface, relative to one another. All these three modes describe all possible modes of crack behaviour (the displacement mode is illustrated in Fig. 4). Any particular problem may be treated as one mode or as a combination of these modes.

The opening mode corresponds to the usual case of tensile loading, plane strain conditions applying to opening mode or cleavage type fractures in which the fracture surface is flat and normal to the applied stress while the plane stress condition is associated with the shear mode of fracture occurring in thin sheets. All these conditions are shown in Figs. 2 and 5.

The fracture toughness represents the work which is irreversibly consumed in local plastic flow and cleavage in the creation of a unit area "fracture surface". The relation between fracture stress σ_F and fracture toughness G_c is given by:

$$\sigma_F = \sqrt{\frac{E G_c}{\pi a}} \quad 2a = \text{crack length}$$

Linear Engineering Fracture Mechanics "LEFM" is based on the concept that the local stress field near the crack can be expressed in terms of a unique stress field, ^{which in} linear elastic situations is related to the strain energy release rate G . The relationship being:

$$\text{Plane stress} \quad K^2 = EG$$

$$\text{Plane strain} \quad K^2 = EG/(1-\nu)^2$$

The critical stress intensity factor is a necessary and sufficient condition for cracking and has the considerable advantage that if the failure occurs under a critical stress, a Griffith's type relationship results without consideration of any dissipation ^{of} energy.

The limitation of LEFM as a method for evaluating the fracture properties of materials has brought about the development of yielding fracture mechanics. The concept of yielding fracture mechanics enables the fracture toughness of material to be assessed after gross plastic deformation has taken place.

2.3.1 Thickness Effect

The fracture toughness increases if the thickness of steel increases (12) until a certain thickness is reached, at which point the fracture toughness will begin to fall with further increases in thickness. Eventually, the value of fracture toughness will become constant with regard to section thickness. This constant value of fracture toughness is defined as the plane strain fracture toughness whereas the fracture toughness on the rising portion of the curve is a combination of the two. Therefore, as the thickness increases, stresses are developed in the thickness direction as well as in the width and tension direction. These stresses arise because the region very close to the crack tip undergoes a large elastic or plastic stretch whereas outside this region the stretch is small. Furthermore, in thick plates there is no constraint stress at the side free surfaces, so that near these surfaces the condition is similar to the plane stress zone for thin sheet.

Since the plane strain zone consumes much less energy than its plane stress, therefore a decrease in G_{IC} and K_{IC} with increasing thickness are shown in Fig. 6.

In practice, to ensure that the stress intensity factor is obtained in plane strain conditions, Standards^(9,10), specify that the value of thickness, B , of the test specimen should be greater than or equal to:

$$B > 2.5 (K_{IC}/\sigma_{ys})^2$$

Nelson, Schillin and Kaufman ⁽¹³⁾ also obtained a constant value of K_{IC} from their work on aluminium alloys by using thickness and crack lengths greater than

$$B > 2.5 (K_{IC}/\sigma_{ys})^2$$

J.T. Knott and D. Elliott ⁽¹⁴⁾ have shown that linear elastic stress analysis can be applied only if the extent of in-plane plasticity is small compared with test piece dimensions. Additionally, they mention that the test ^{piece} must be sufficiently thick in order that most of the deformation occurs under plane strain conditions.

2.3.2 Plastic Zone

Localised plastic deformation ⁽¹⁵⁾ occurs when the appropriate yield criterion is satisfied in the vicinity of the crack, and a plastic zone is created near the crack tip. The size and shape of the plastic zone depends on the mode of deformation that acts on the crack and on the criterion for yielding.

The plastic zone has either an elongated shape (Fig. 7) or forms hinges (Fig. 8).

The plastic zone size is smaller at a constant value of stress intensification in plane strain deformation than in plane stress deformation.

2.3.3 Plane Stress

If the plastic zone is large compared with the component thickness the triaxiality may be relaxed and through thickness stresses normal to the plane of the component will be negligible. In this condition the size of plastic zone is substantially constant through the component thickness and the stress state is biaxial (Fig. 2a).

The stress conditions will influence the fracture toughness of materials. The relaxation of triaxial stresses in thin sheet components allows a condition of plane stress to be reached. Therefore, there is an increase in the value of material fracture toughness, until it reaches a maximum. Further reduction of the thickness is found to give a decrease in the fracture toughness. In this case the fracture toughness must be of the K_{IC} type and not of the K_C type.

2.3.4 Plane Strain

Tensile stresses are set up in the thickness direction of the plastic zone so that the stress state is triaxial. If the plastic zone is small in relation to the component thickness then contraction through the thickness is suppressed by the surrounding elastic material (Fig. 2b).

A state of plane strain may exist at the centre of the test specimen which is less thick than the recommended value.

$$B > 2.5 \left[\frac{K_{IC}}{\sigma_{ys}} \right]^2$$

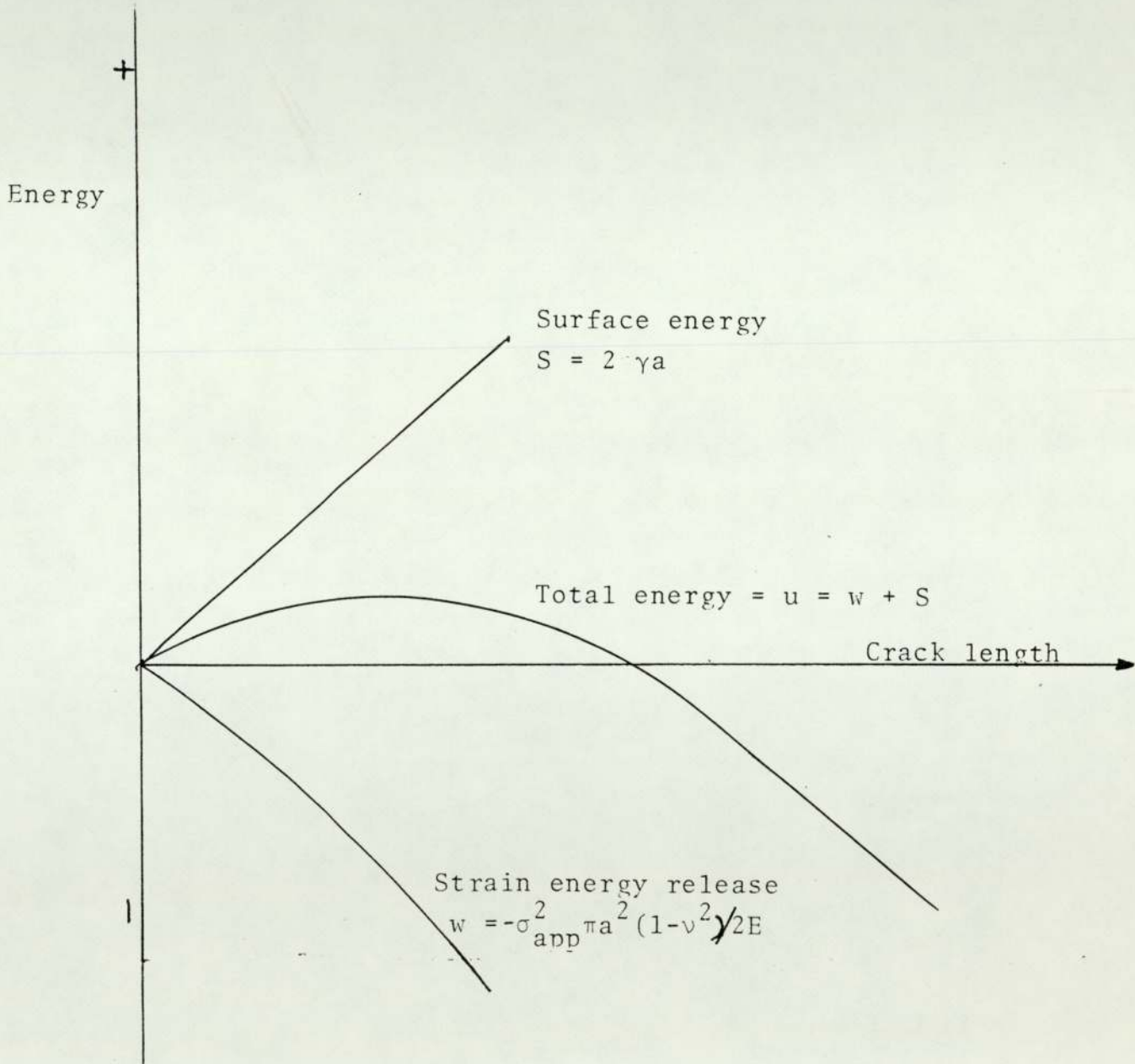
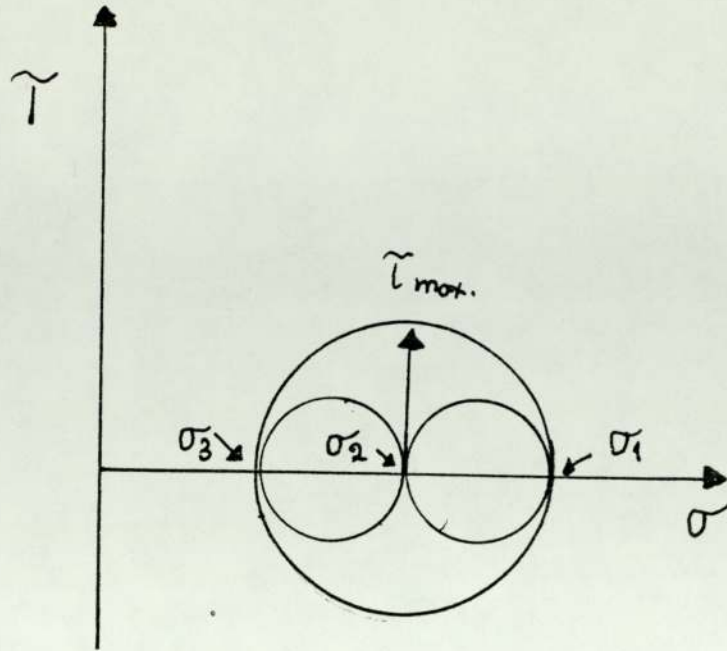
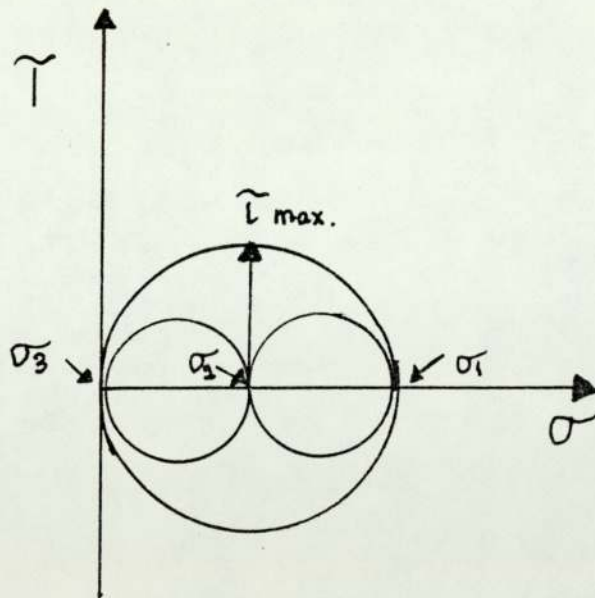


FIGURE 1 Energy balance of crack



-a-



-b-

FIGURE 2 a. Plane strain condition
b. Plane stress condition

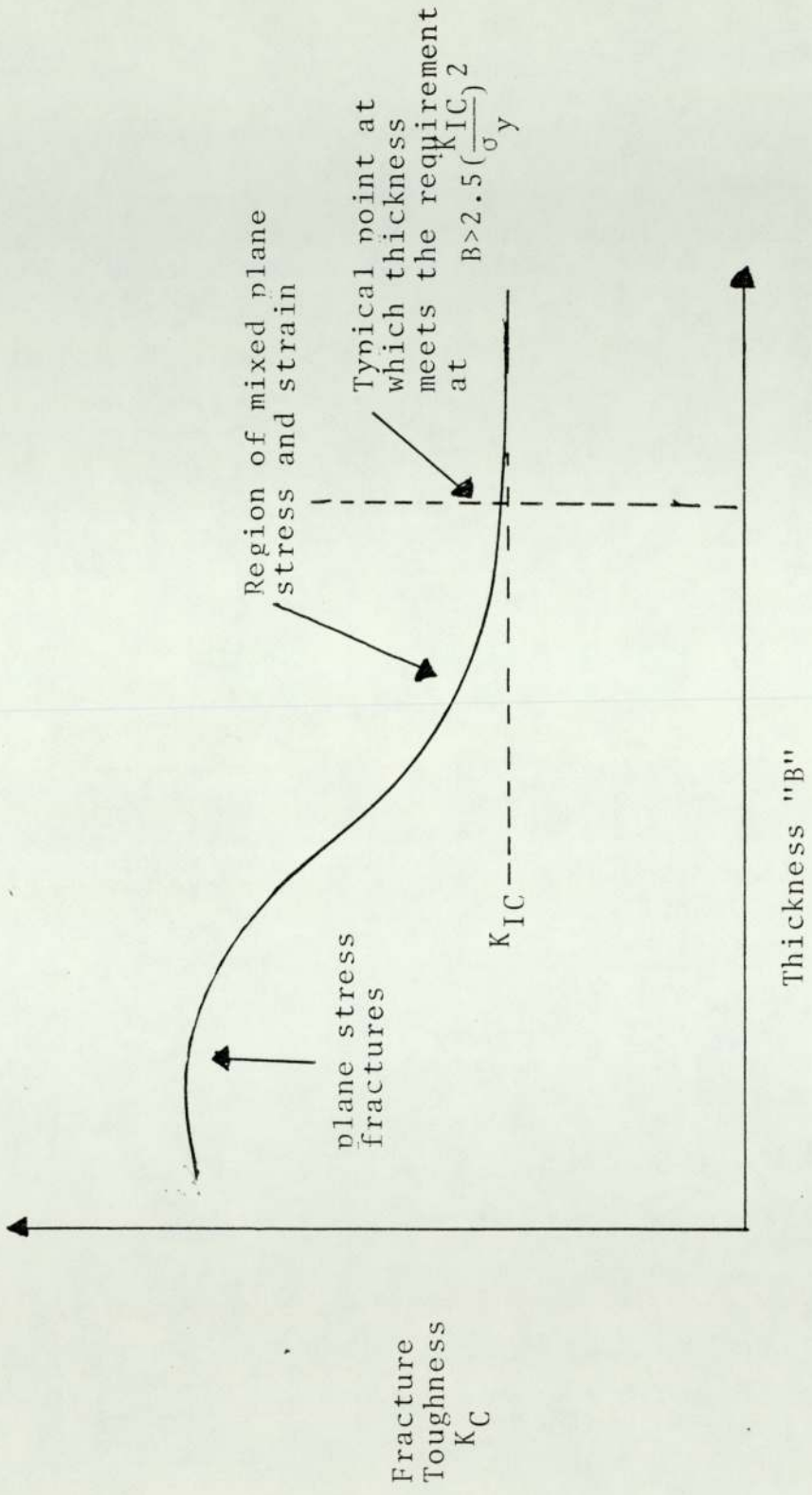


FIGURE 3 Typical form of the relationship between fracture toughness and component thickness

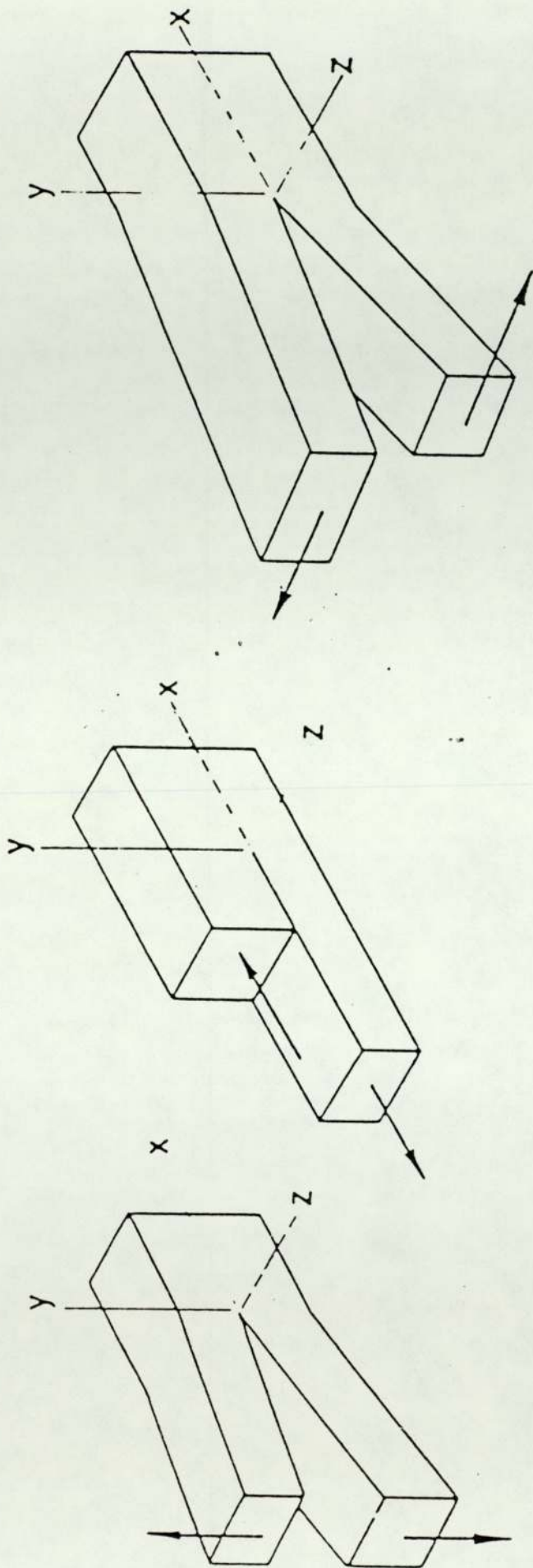


FIGURE 4 The basic modes of crack surface displacement

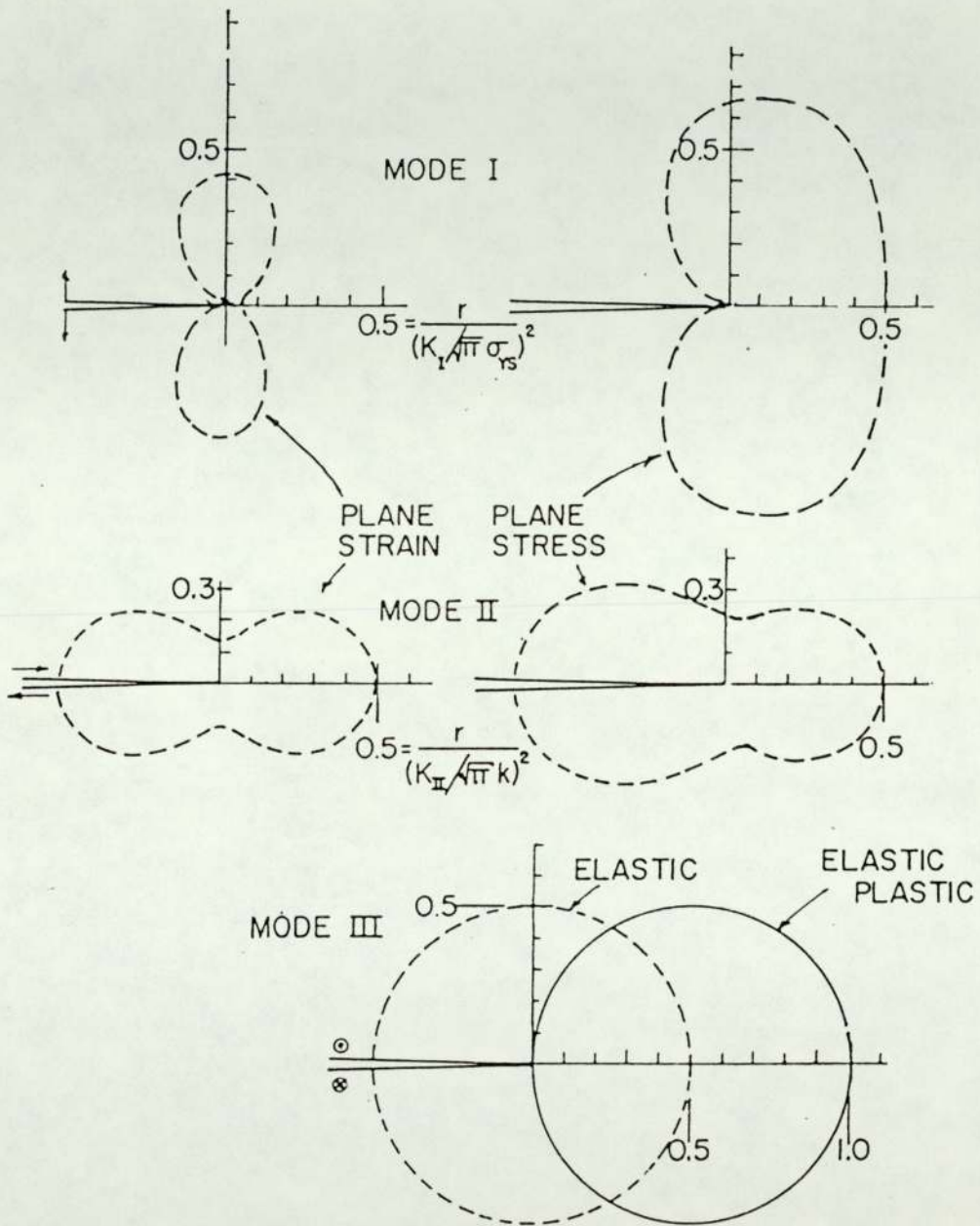


FIGURE 5 Elastic stress singularities of the different crack deformation modes (15)

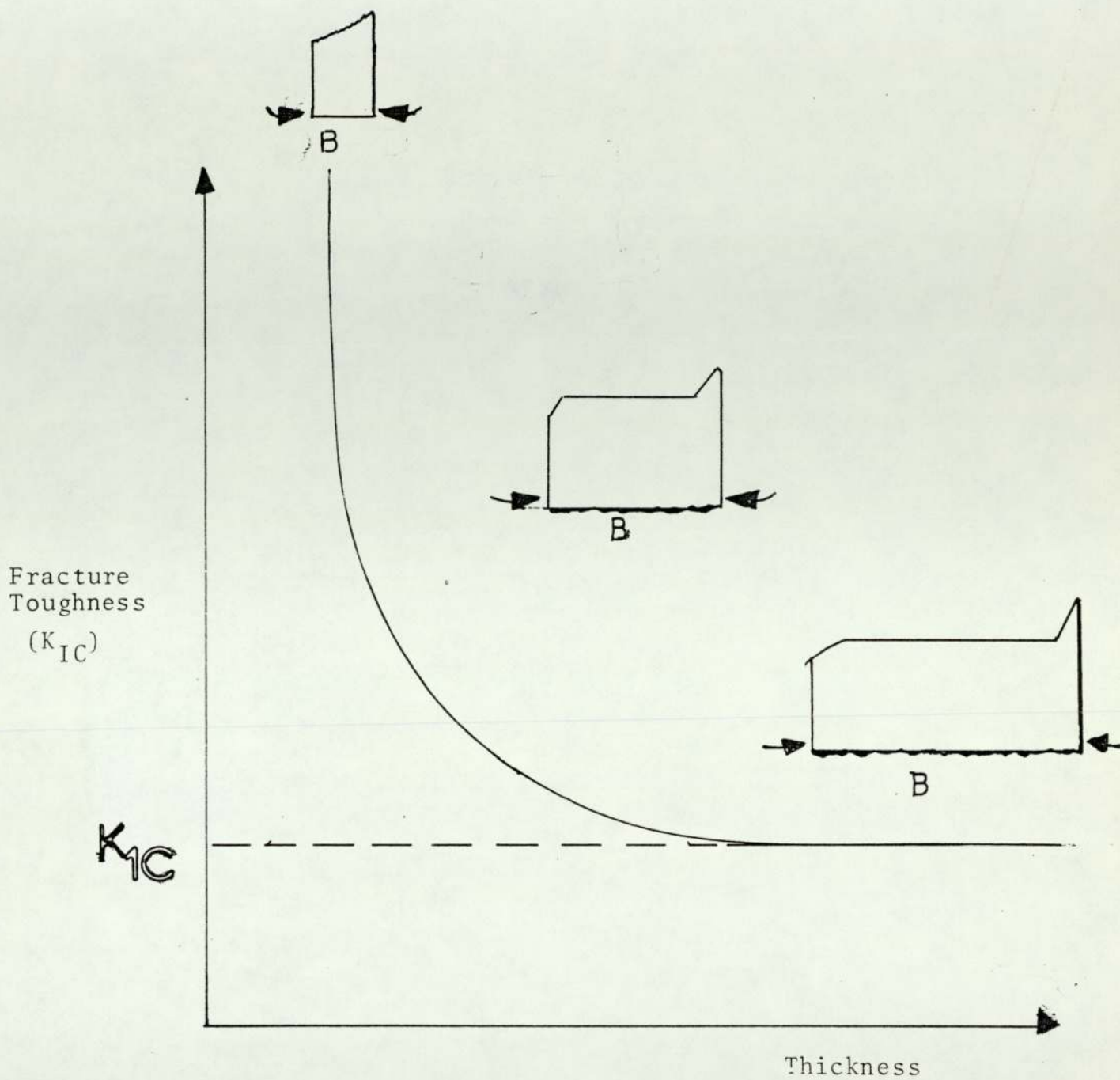


FIGURE 6 Variation of stress intensity factor and fracture profile with thickness of test piece

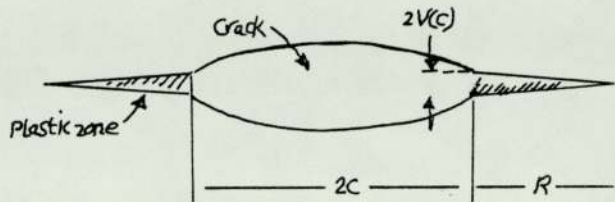


FIGURE 7 Displacement $2V$ associated with crack opening, with elongated shape of plastic zone

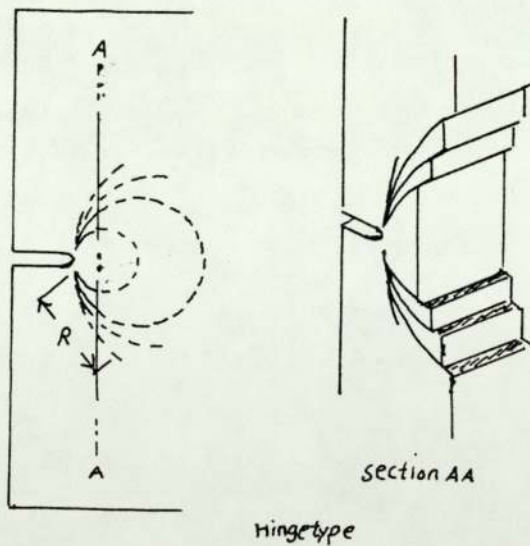


FIGURE 8 Yield zones on the surface and cross section of cracked sheet under uniaxial tensile loading in plane strain (hinge type plastic zone)

2.4 Microstructure

2.4.1 The Influence of Microstructure on Crack Propagation Mechanism and Fracture Toughness

Karl-Heinz (17) found that the mechanical properties of a material, especially plastic deformation and fracture, are defined by its microstructure, i.e. the microstructure mechanics are necessary for understanding the mechanical behaviour of material.

A knowledge of

↑ The influence of microstructure on crack propagation supports the solution of some problems.

- (a) systematic development of tougher material
- (b) inverse relationship between strength and toughness of specific material
- (c) material heat treated by different procedures resulting in identical strength levels can exhibit quite different toughness
- (d) different materials with different strengths can be equally tough and vice versa
- (e) physical models designed for calculation of crack propagation require detailed information about the mechanical behaviour of the elements of the material's microstructure in the stress and strain field.

Karl-Heinz (17) mentions that the mean particle distance "d" can be calculated by a given volume fraction "v" of the second phase as follows:

$$d = D \sqrt{\frac{2}{3\nu}} (1-\nu)$$

D = particle diameter

According to a compilation of Rosenfield, Hahn and Embury the cleavage fracture stress of steels is mainly dependent on the ferrite grain size and can be approximated by:

$$\sigma_{\text{cleavage}} = 343 + 103 D^{-\frac{1}{2}} \text{ (MN/m}^2\text{)}$$

D in mm.

Systematic investigation has shown that the grain size effect on K_{IC} is comparable to that of loading rate, \dot{K} . Increasing inclusion concentration, $\dot{\nu}$, has probably the same effect as increasing D and \dot{K} .

Mulkerin (18) also investigated the influence of inclusion content on the toughness.

Increased plastic crack tip deformation can be obtained by increasing the temperature, and hence increasing the crack tip blunting (Fig. 9).

Furthermore, the fracture toughness increases with increasing material purity, i.e. increasing inclusion distance.

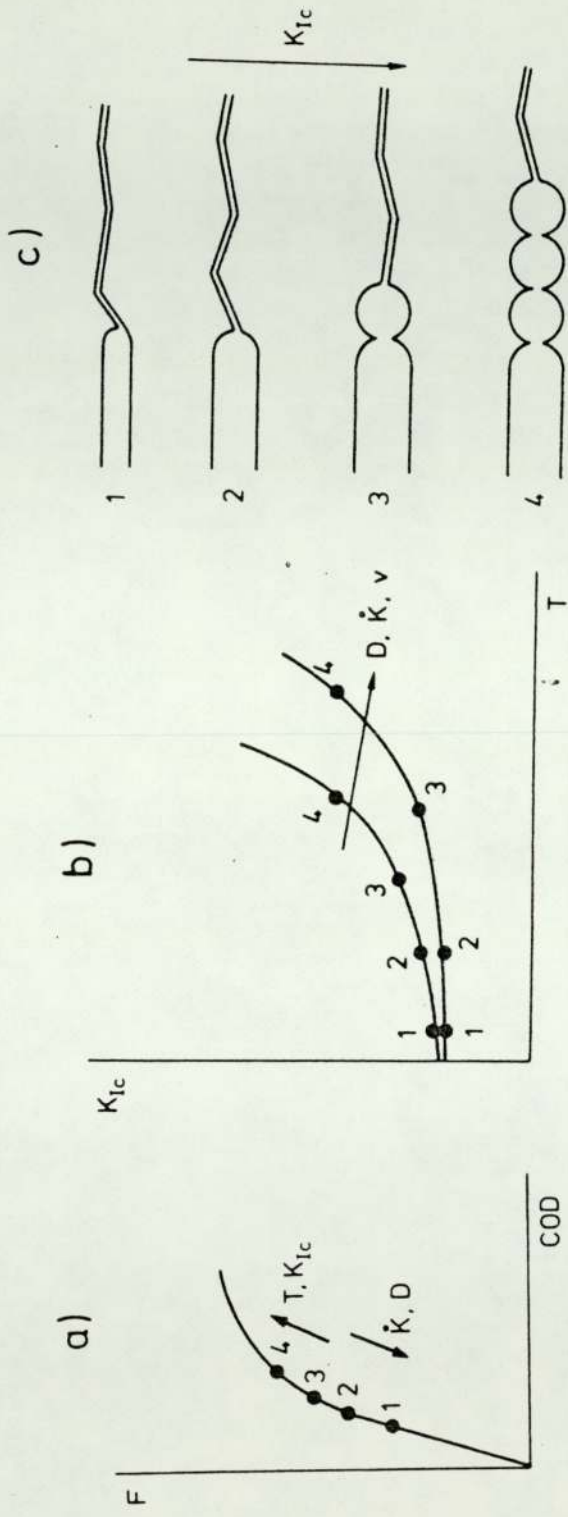


Fig. 9 Schematic representation of the influence of grain size, loading rate and inclusion content on crack propagation mechanism and fracture toughness. (18)

Fig. 10 shows the inverse relationship between toughness and strength of 0.45 C-Ni-Cr-Mo steels and also shows the influence of sulphur level on fracture toughness of the same steels.

Improving toughness by microstructure refinement has been demonstrated by Zackay. Austenitising and quenching treatments of steel AISI 4130 produces blocky martensite and ferrite. Retained austenite is a microstructural element which is advantageous to the fracture toughness of quenched and tempered steels. Figs. 11 and 12 show the relation between fracture toughness and tempering temperature. (17)

The plane stress fracture toughness data of Thompson and Zinkham are indeed in accordance that K_{IC} should increase with decreased grain size, Fig. 13. (19)

K_{IC} increases with increasing specimen size. Hence, K_{IC} values can only be compared when they are obtained from equally-sized specimens. In addition it is to be expected that there are different properties near the specimen surface and in the interior of the specimen.

2.4.2 Residual Stress Effects on Fracture Toughness Measurements

Two types of residual stresses occur in a material; that is macroscopic and microscopic residual stresses (20).

Microscopic residual stresses fluctuate from maximum compression to maximum tension over distances which are of the same order as the microstructure of the material. Thus, although microscopic residual stresses may well affect the fracture toughness, macroscopic residual stresses can affect the measurement of fracture toughness by causing an entire crack front of macroscopic dimension to be in a state of tension or compression before the application of any external load.

Irwin and Kies ⁽⁸⁾ have assumed that there are no macroscopic residual stresses in the test specimen.

The short rod test by Barker ⁽²⁰⁾ has been done by increasing the load, F, on the specimen until crack initiates at the point of the "V". The equation for the plane strain critical stress intensity factor, $K_{ICSR} = \frac{P_{max} A}{3}$. He assumed that the plasticity effects in the specimen were negligible. He also assumed that the energy required to advance a steady-state crack, a small distance, Δ_a , (Fig. 14 a, b, c).

$$\Delta w = G_{IC} \bar{b} \Delta_a$$

\bar{b} is the average width of the crack front
 a and Δ_a , G_{IC} = material property, energy/unit area

Barker assumed that there is no plasticity in presence of residual stress, p.

The degree of LEFM might be measured by P in some particular test, but in Barker's work (20), he regards P as a measure of residual stress effect in the fracture toughness measurement.

Calibration of the specimen mouth opening displacement is not required, because the calibration constant cancels out on taking the ratio

$$\frac{\Delta X_0}{\Delta X} \quad \text{Fig. 15}$$

The measured residual stress effect was taken into account by calculating

$$K_{ICSR} = (1+P)K_{QSR} \quad \dots\dots\dots(9)$$

Finally, macroscopic residual stresses (21) which are frozen into material can affect the measurement of fracture toughness by causing the test crack to be in a state of tension or compression before the application of external load.

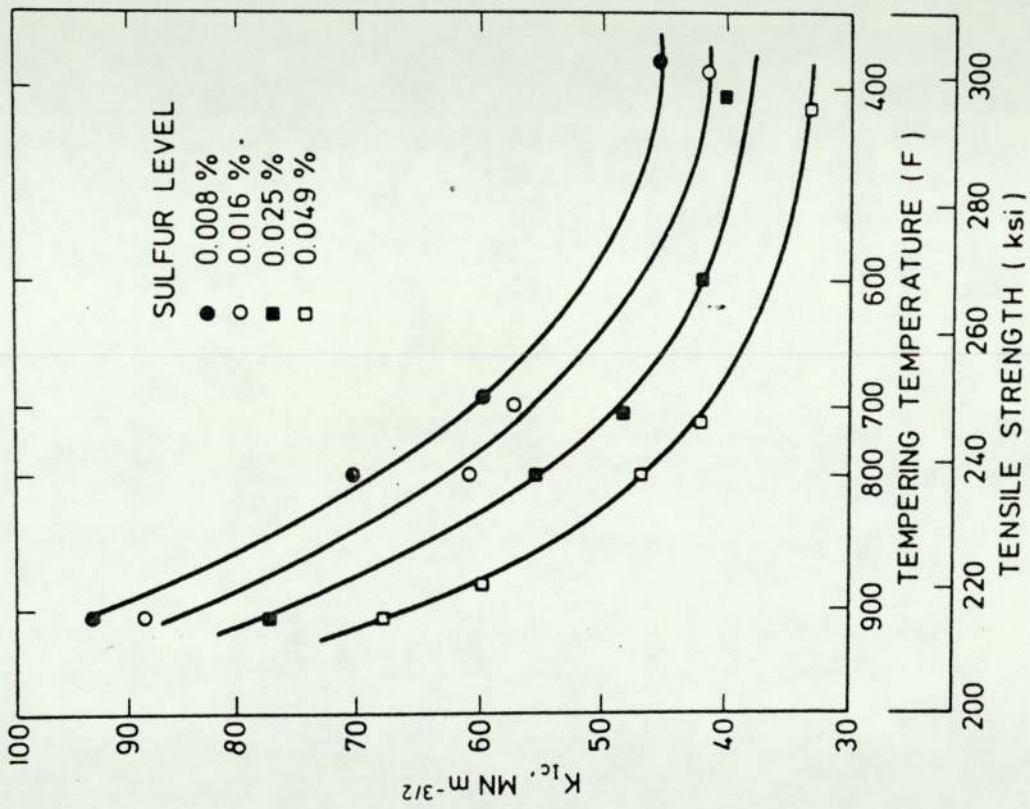


Fig. 10 Influence of sulfur level on fracture toughness of 0.45 C-Ni-Cr-Mo steels, Birkle *et al.* [18].

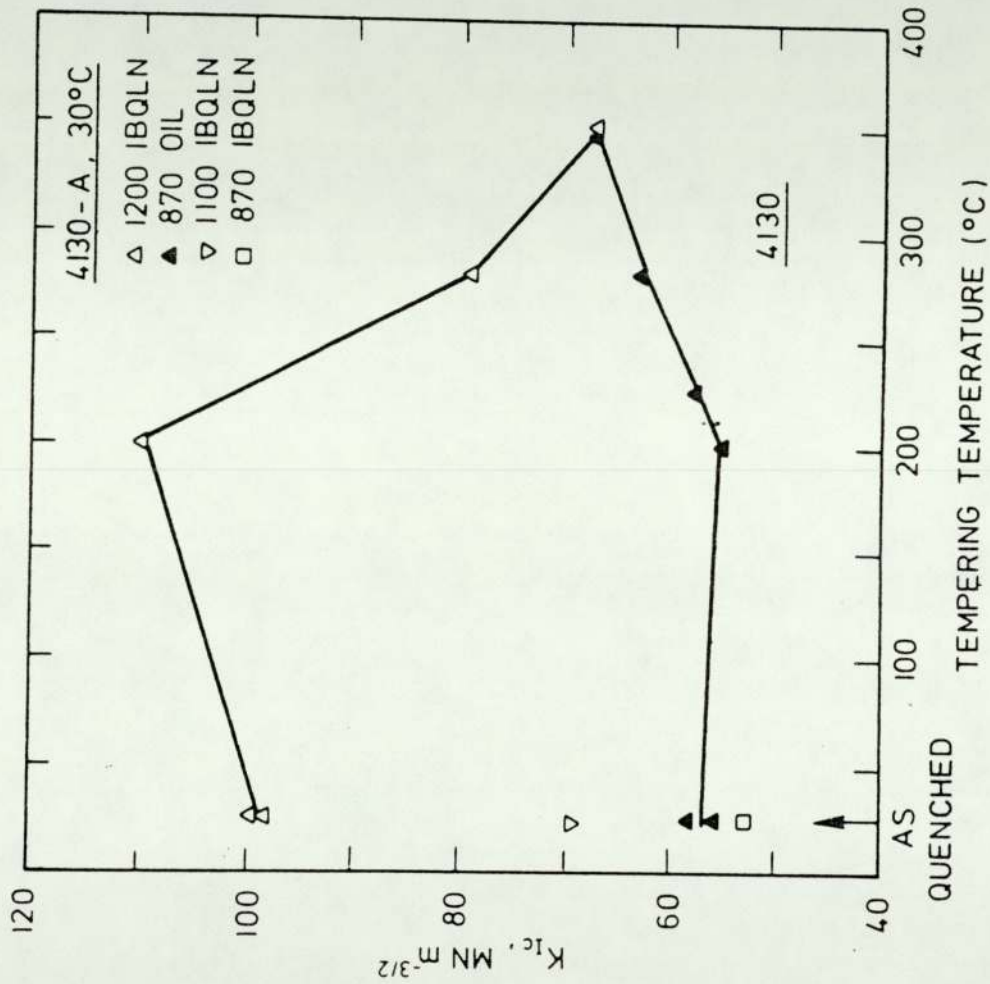


Fig. 11. Fracture toughness of steel AISI 4130 as a function of tempering temperature; Zackay [7].

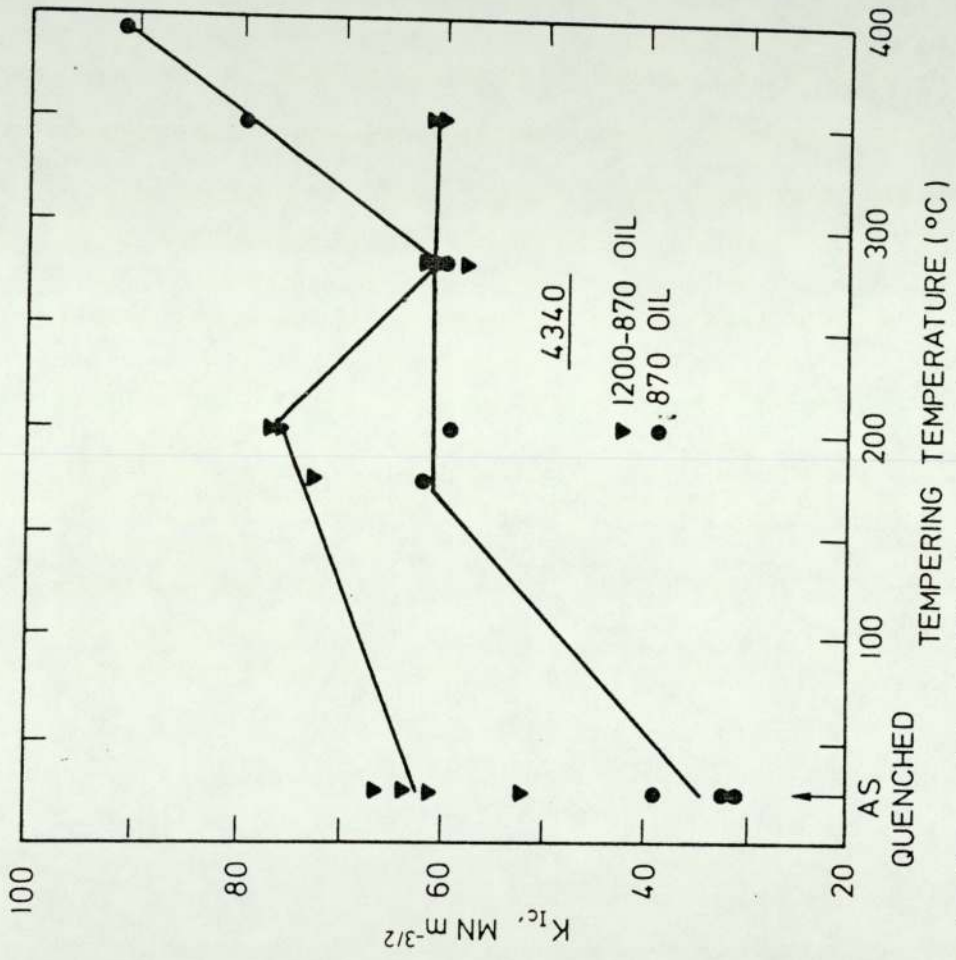


Fig. 12. Fracture toughness of steel AISI 4340 as a function of tempering temperature; Zackay [7].

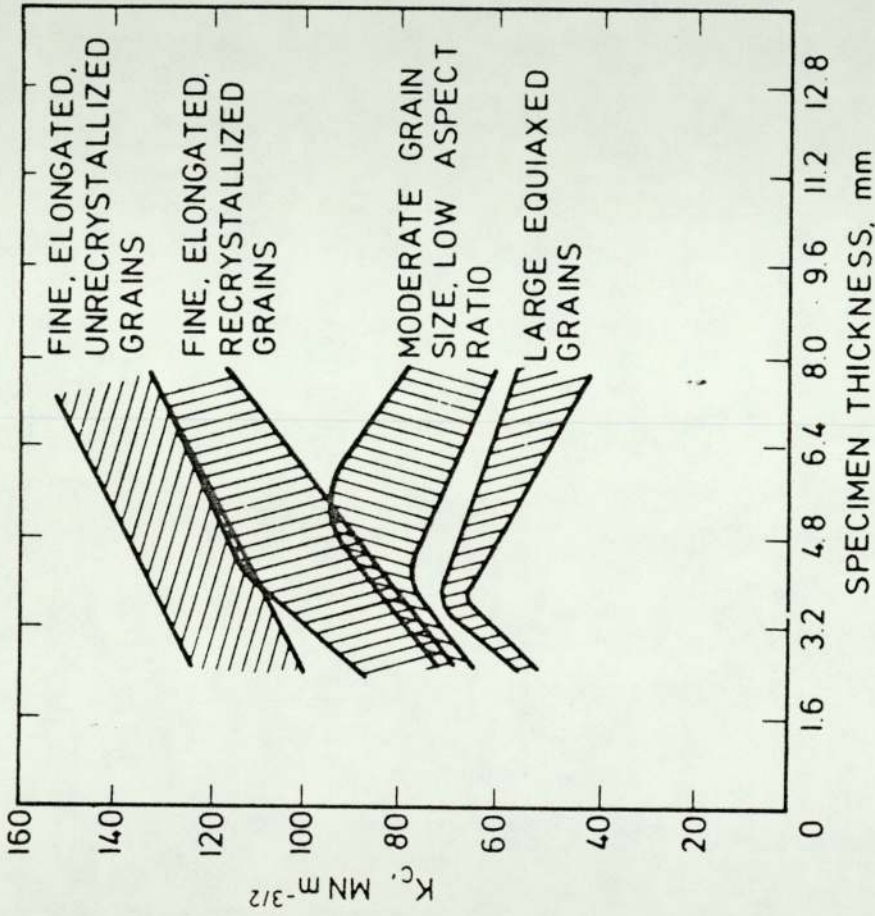
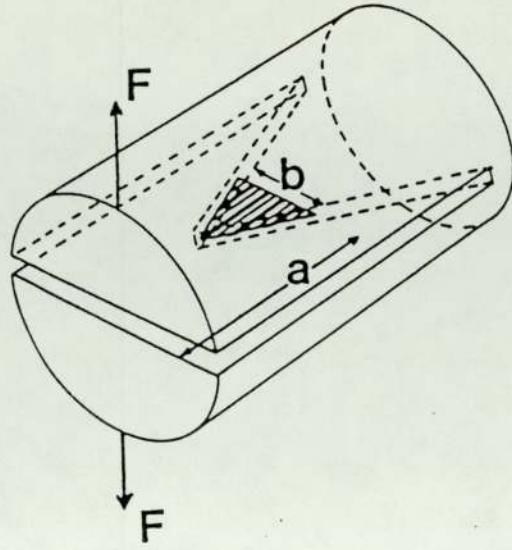
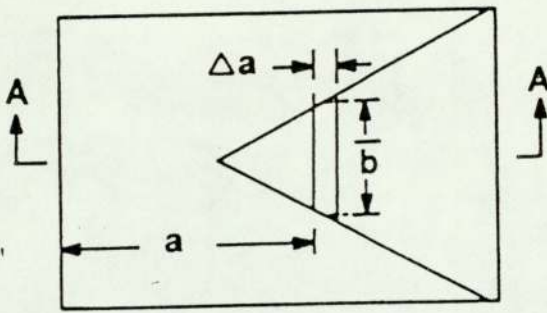


Fig. 13 Effect of thickness on K_c of overaged 7000 series alloys with various grain sizes; Thompson and Zinkham [19].

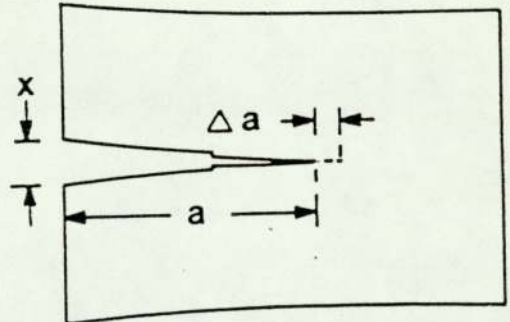


a



PLAN VIEW

b



SECTION A-A

c

FIGURE 14 Schematics of the short rod specimen

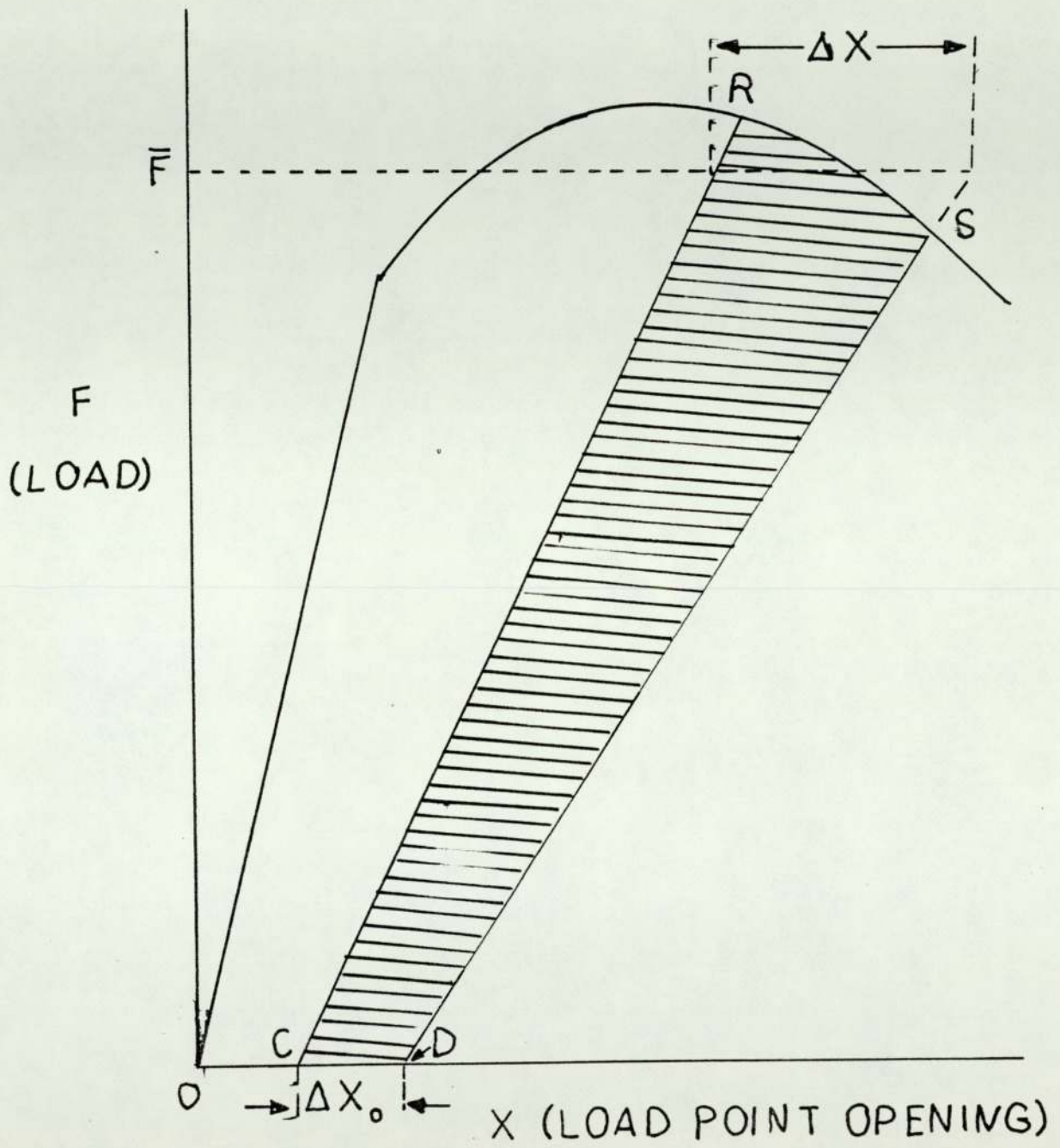


FIGURE 15 Schematic of elastic-plastic specimen behaviour

3. MICRO-MECHANISMS OF FRACTURE

Micro-mechanisms of fracture can be divided into

1. cracking processes recognised by
 - (a) cleavage,
 - (b) low temperature intergranular fracture,
2. rupture processes, typified by
 - (a) void coalescence internal necking,
 - (b) shear linkage.

3.1 Cracking Process

Cleavage can be defined as the separation of a crystal and this can occur by breaking bonds perpendicular to the fracture plane ⁽²²⁾. This fracture is produced, usually at low temperature, under a condition of high triaxial stress, or at high deformation rate.

Griffith ⁽²²⁾ pointed out that cracks at finite length must be present for crack propagation. Whilst it is known that cracks, as such, at this magnitude are not present before yielding, this leads to the conclusion that even in very brittle notched bars, cleavage fracture is preceded by a small amount of local yielding around the notch root.

3.2 Rupture Processes

In most ductile and tough materials the fracture mechanism is caused by microvoid initiated growth and coalescence.

Beacham et al (23) showed that microvoids usually initiate during plastic flow at inclusions, undissolved second phase particles (such as carbides), grain boundaries, cleavage planes, or at any site where a discontinuity concentrates the plastic flow.

Separation at the site of microvoid initiation can occur across a second phase particle or at a particle-matrix interface.

With increasing plastic strain, the existing microvoids combine and hence eventually enlarge. These become close enough so that the thin ridge, or membranes, separating them rupture, and fracture occurs. The resultant fracture surfaces have numerous cup-like depressions or dimples.

Beacham (24) has shown that, from the shape of dimple, ^{one can deduce} the relative stress directions operating to make the microvoid grow. When the fracture is caused by simple tension, dimples usually have an equiaxial appearance. An elongated dimple is obtained when a shearing motion takes place as in shear lip or torsion fracture.

4. METHODS FOR EVALUATION OF FRACTURE TOUGHNESS

4.1 Previous and Recent Work for Measuring Fracture Toughness

It has been shown by Irwin that the radius of the plastic zone around a crack tip in plane strain is approximately $(K_{IC}/\sigma_{ys})^2 / 6\pi$, where K_{IC} is the plane strain critical stress intensity factor (fracture toughness) and σ_{ys} is the yield strength in tension.

LEFM approaches to measuring K_{IC} require a large specimen width and thickness compared to the crack tip plastic zone radius.

The ASTM E399-74 method for measuring plane strain fracture toughness requires ligament width and initial crack length to be at least as large as $2.5(K_{IC}/\sigma_{ys})^2$. This has made it difficult to measure K_{IC} of many high toughness materials by ASTM (Fig. 16).⁽²⁵⁾

$$B \approx (w-a) \approx 2.5 \left(\frac{K_{IC}}{\sigma_{ys}} \right)^2$$

A modified criterion was developed on an empirical basis for the minimum thickness of plane strain fracture toughness test specimen.

$$B_{\min} = 400 \frac{K_{IC}^2}{E\sigma_y}$$

Many models have been developed with attempts to relate ξ_i and K_{IC} to material characteristics. Krafft⁽²⁶⁾ proposed a model in which an onset of unstable fracture coincides with attainment of plastic instability in the process zone of fixed size. The process envisaged is

that of necking and tensile rupture of small fracture cells initiated at inclusion/matrix interfaces, lying along the crack front. The relationship be proposed is expressed as follows:

$$K_{IC} = En(2\pi L)^{\frac{1}{2}} \dots\dots\dots(10)$$

where K_{IC} is the plane strain intensity factor when a plastic instability strain, n , is attained in a process zone L , in a material of Young's Modulus E .

Furthermore, a fracture toughness measurement ⁽²⁷⁾ is based on the use of specimen configuration for which the initial crack growth is stable under controlled force conditions. The concept was demonstrated on a specimen configuration consisting of a short rod/bar with narrow longitudinal slots for crack guides.

A new method ⁽²⁸⁾ was presented for measuring the plane strain fracture toughness of ductile materials. This method is much more simple than the other method which was mentioned before in this report for measuring the K_{IC} . The advantage of this new technique is that the specimen can be much smaller than is normally required for a valid K_{IC} test.

is selected
 short rod/bar specimen configuration for
 which the material along the crack tip is well constrained
 to the plane strain state. From the measurement and
 elastic plastic analysis of the load/displacement curve is
 determined the energy per unit crack area which is required
 to slowly advance a steady-state crack under plane strain
 condition.

Two methods may be used to load the short rod/bar specimens:

- a. Shallow grip grooves are machined into the face of
 the specimen and claw grips provide the loading,
 as indicated in Fig. 17, the peak load is used to
 calculate K_{IC} :

$$K_{IC} = AF_c / (V^{3/2} (1-\nu)^{1/2}) \dots\dots\dots (11)$$

$$A^2 = G_{IC} EB^3 / F_c$$

$$G_{IC} E = K_{IC}^2 (1-\nu^2)$$

A = 20.8 dimensionless calibration constant

ν = Poisson's ratio

F_c = the peak load (force) applied to the specimen
 in the test

B = specimen diameter

- b. By using a thin inflatable bladder called a flat
 jack ⁽²⁹⁾, Fig. 18.

Additionally, the ASTM technique for evaluating the fracture toughness ⁽²¹⁾, is independent of the test specimens design. One of the difficulties which arises in applying ASTM E399-74⁽¹⁰⁾, is that the test validity requirements sometimes require a specimen size which is so large that it precludes the fracture toughness measurements. Another difficulty concerns fatigue pre-cracking requirements.

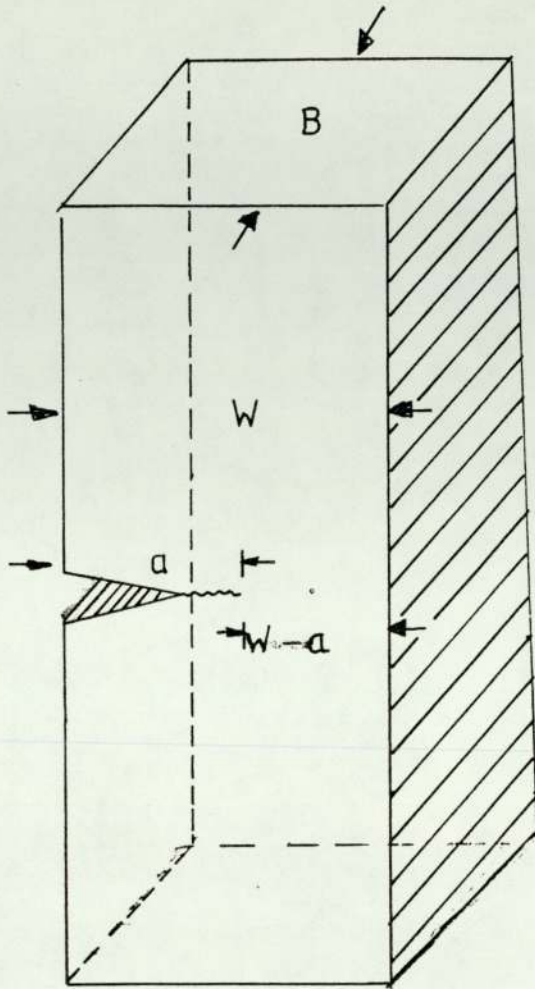


FIGURE 16 Relation between the geometry (25;61) and the ratio of crack length

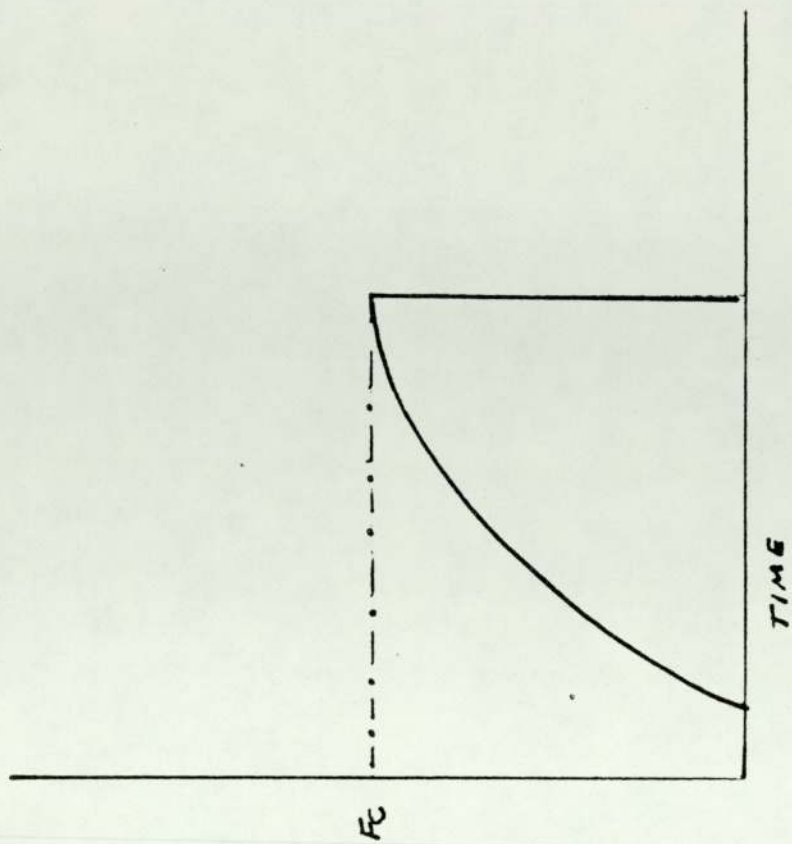
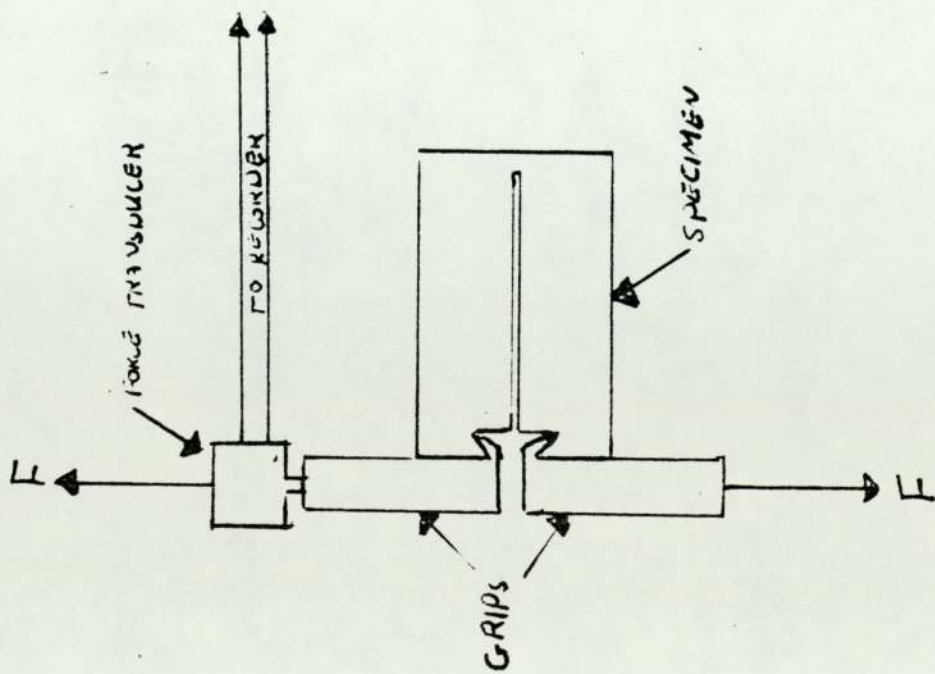


Figure 17 Grip method of loading the short rod specimen

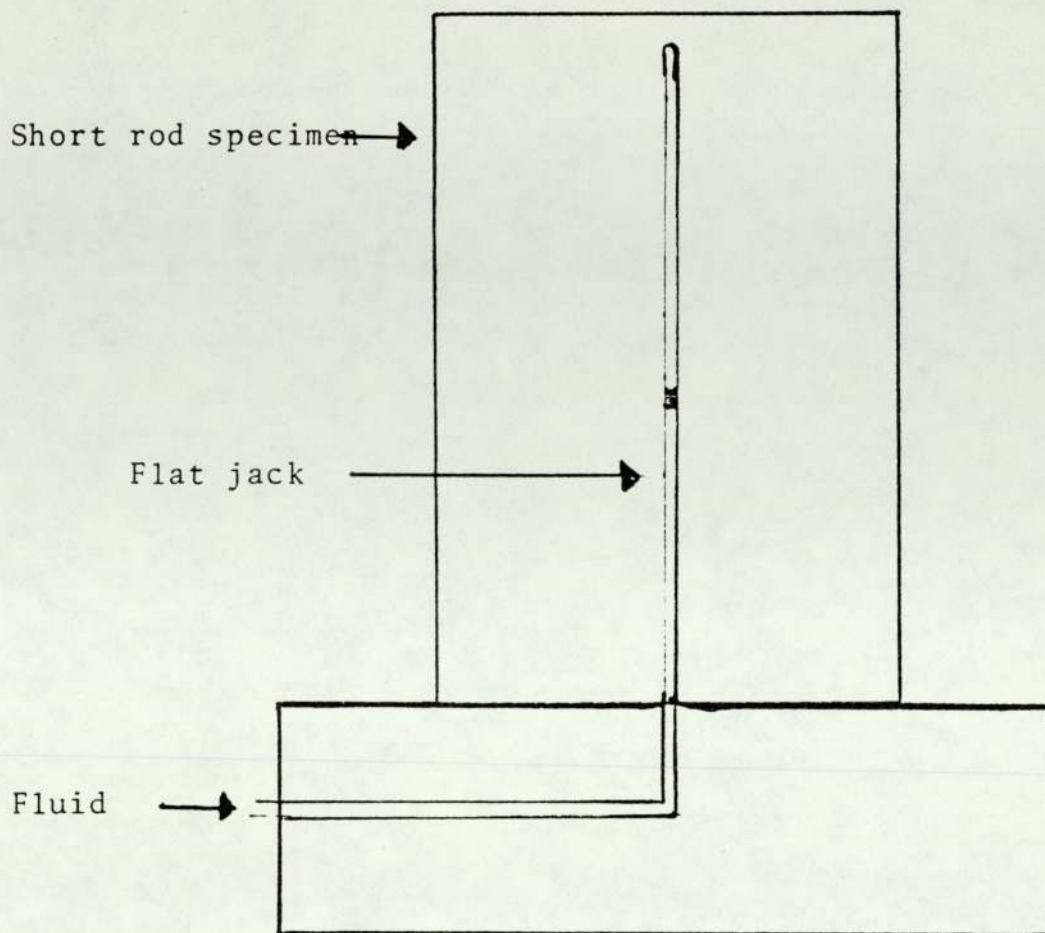


Figure 18 Fractometer method of loading short rod specimens.

4.1.1 Short Rod/bar Technique for Measuring Fracture Toughness

The method which was suggested by Barker (27) enables the determination of fracture toughness of brittle materials using calibrated specimens requiring neither fatigue pre-cracking nor measurements of critical crack length which cause failure of the specimen in an unstable manner. Thus the fracture toughness can be determined from the equation below by measuring only the maximum load, as the scaled dimensions

$$K_{IC} = \frac{P_{max}^A}{B^{3/2}} \dots\dots\dots(12)$$

This equation is only valid for material which behaves in a linear elastic fashion. For materials which exhibit non-linear elastic behaviour or a rising crack resistance curve during testing due to extensive plastic deformation ahead of the crack tip, Barker (28) suggested a plasticity correction factor p which can be determined during the testing. Thus the above equation can be written in the following way

$$K_{ICSB} = \frac{F_c A}{B^{3/2}} (1+p/1-p)^{1/2} \dots\dots\dots(13)$$

- where:
- F_c = average load between two unloading-reloading cycles
 - A = constant
 - p = plasticity correction
 - B = specimen width or diameter

4.1.2 Crack Opening Displacement "COD" Technique

British Standard (30) specifies the method for carrying out crack opening displacement (COD) test of metallic materials. A test piece in which a sharp crack has developed by fatigue from a machined notch is subjected to loading. Test results are obtained from plots on an x-y recorder (Fig.20).

Calibration of the clip gauge should be made ideally prior to each test.

For the test presented in terms of plane strain fracture toughness (K_{IC}) the fatigue pre-cracking procedure is presented in the British Standard 5447. Values of fatigue pre-cracking force (p_f) are calculated by using the following equations:

$$K_f = \frac{Y P_f}{B w^{\frac{1}{2}}}$$

$$Y = \left(\frac{a}{w}\right)$$

$\frac{a}{w}$ ratio should be in the region 0.45 to 0.55, i.e.

$$0.45 < \frac{a}{w} < 0.55.$$

4.1.3 The 5% Secant, LEFM

In the recent publishing of BS.5447.1977 proposed method for plane strain fracture toughness K_{IC} , a notched machined specimen is used and the sharpest possible crack is produced at the notch root by fatiguing the specimen in a low cycle. The initial crack length is the sum of

the notch depth and the fatigue crack length. The thickness of the test piece (B) should be

$$B > 2.5 \left(\frac{K_{IC}}{\sigma_{ys}} \right)^2$$

K_{IC} is fracture toughness, σ_{ys} is the yield stress.

The test must be carried out in a testing machine which provides for a continuous autographic record of load P and relative displacement across the open end of the notch.

Four types of load-crack displacement curves are shown in Fig. 19. The type I load displacement curve represents the behaviour of a wide variety of ductile metals in which the crack propagates by a tearing mode with increasing load. This curve contains no characteristic features to indicate the load corresponding to the onset of unstable fracture. The BS.5447 and the ASTM.399-72 suggest the following procedure. Firstly, draw the secant line Op_s from the origin with a slope that is 5 percent less than the tangent OA. A horizontal line (V_1) at a load equal to 80 percent of P_5 has to be drawn (see Fig. 19). If V_1 exceeds one fourth of the corresponding distance V at P_5 , the material is too ductile to obtain a valid K_{IC} value. If the material is not too ductile, then the load P_5 is designated p_Q and used in the calculation at the end of this section.

The type II load displacement curve has a point where there is a sharp drop in load followed by a recovery of load. The load drop represents a "pop in" which arises from sudden unstable rapid crack propagation before the crack slows down to a tearing mode of propagation. The same criterion for extensive ductility (as for type I) was applied to type II curve, but in this case p_Q is the maximum recorded load. The type III curve shows complete "pop in" instability where the initial crack propagates rapidly to complete failure. This type of curve is characteristic of a very brittle elastic material.

The value of p_Q determined from the load displacement curve is used to calculate a conditional value of fracture toughness K_{IC} . The equations relating the specimen geometry, Fig. 34,35, crack length (a), and critical load p_Q are:

For bend specimens

$$K_{IC} = \frac{p_Q Y}{B w^{\frac{1}{2}}}$$

$$Y\left(\frac{a}{w}\right) = \left[1.93 \left(\frac{a}{w}\right)^{\frac{1}{2}} - 3.07 \left(\frac{a}{w}\right)^{\frac{3}{2}} + 14.55 \left(\frac{a}{w}\right)^{\frac{5}{2}} - 25.11 \left(\frac{a}{w}\right)^{\frac{7}{2}} + 25.8 \left(\frac{a}{w}\right)^{\frac{9}{2}} \right]$$

The crack length (a) used in the above equation has to be measured after fracture at 25% B, 50% B and 75% B, and the factor $B > 2.5 (K_{IC}/\sigma_{ys})^2$ has to be calculated also.

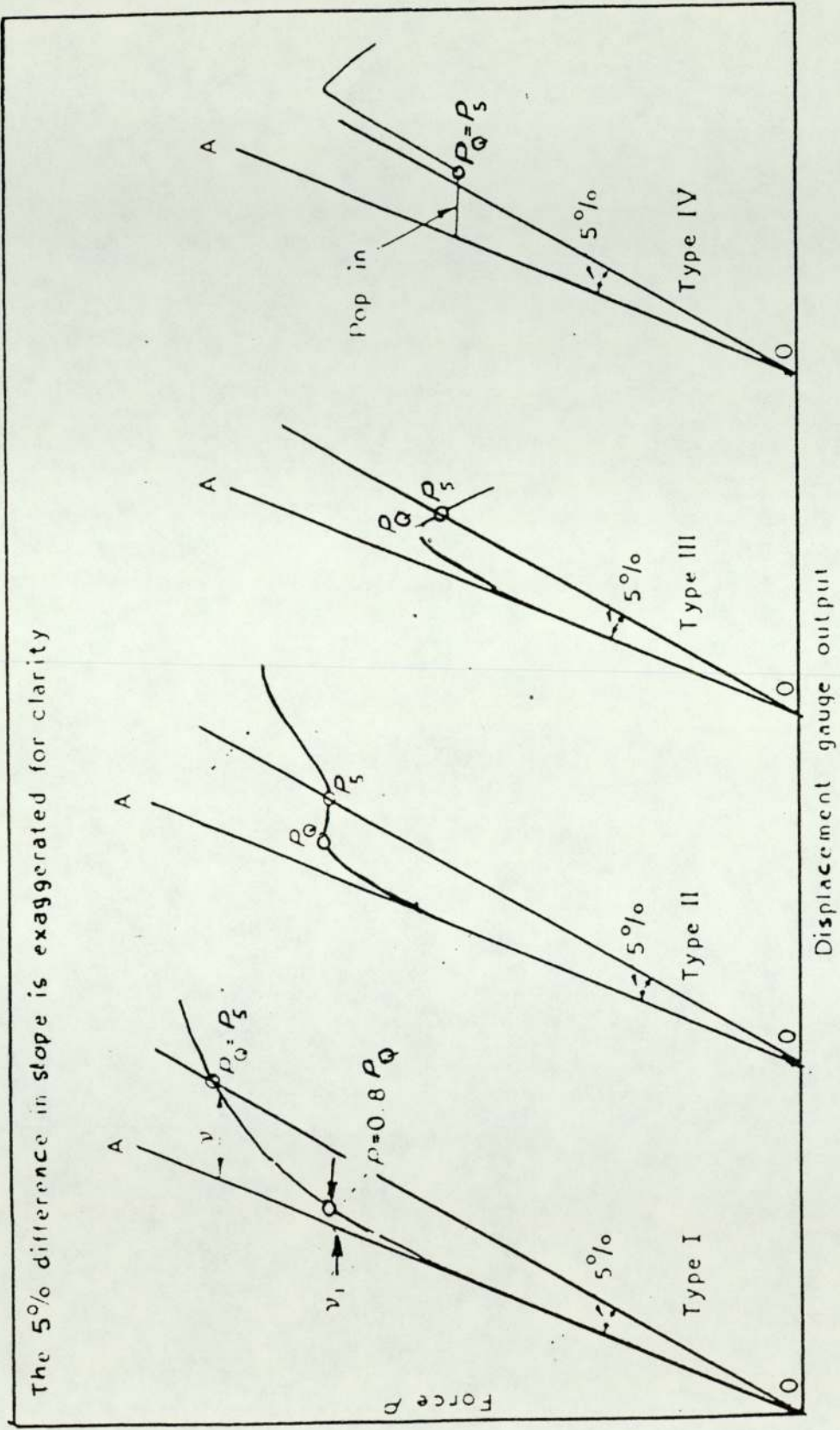
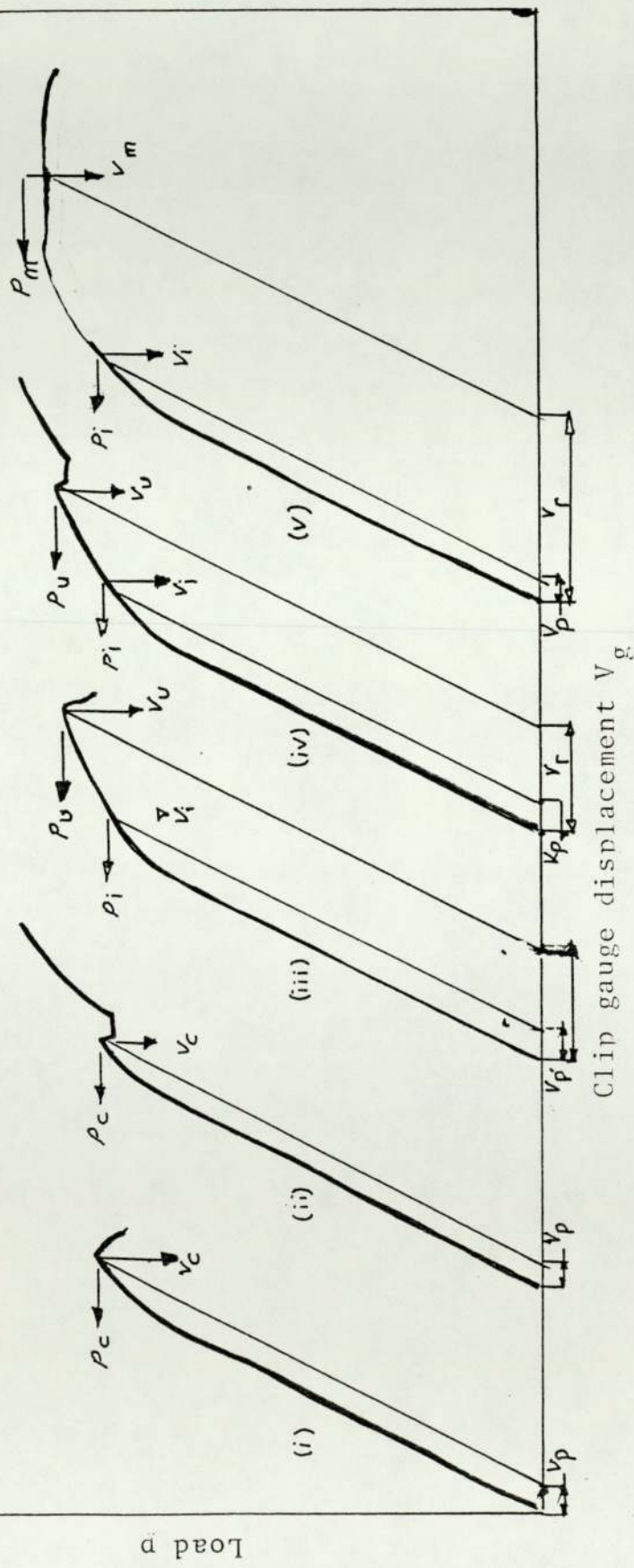


FIGURE 19 Principle types of force/displacement record



Clip gauge displacement V_g

FIGURE 20 Types of load clip gauge displacement graphs for calculation of COD (30, 37)

4.2 General Yield Fracture Mechanics

4.2.1 The Crack Opening Displacement (COD)

The concept of crack opening displacement (COD) is used to extend the basic linear elastic fracture mechanics theory to a situation where the fracture process is accompanied by significant plastic deformation.

Wells (31) and Cottrell (32) worked on the principle that the amount by which a sharp crack opens previous to fracture depends only on the local fracture ductility of the material, and does not depend on whether the fracture occurs before or after general yield. This opening, the (COD), is therefore as fundamental a material property as, for example, yield stress.

The recognition of the consequences of yielding at a crack tip giving rise to a physical displacement of the crack surfaces at the tip, was first applied as a possible fracture criterion by Wells and Cottrell.

Burdekin and Stone (33) found from the theoretical analysis that the crack opening displacement δ , at the tip of the real crack is using the model employed by Dugdale (34), Fig. 21, given by the displacement at the point $x = \frac{1}{2} a$ within the elastically stressed crack of length $2a$, this displacement was shown by (33):

$$\delta = \frac{8e\gamma a}{\pi} \log_e \operatorname{Sec}\left(\frac{\pi\sigma}{2\sigma_y}\right) \dots\dots\dots(14)$$

where $\epsilon_y = \frac{\sigma_y}{E}$ (elastic yield strain)
 a = half length of real crack
 σ, σ_y = applied or yield stress

Expanding the expression for COD as a series in $\left[\frac{\pi\sigma}{2\sigma_y}\right]$

$$\delta = \frac{8\sigma_y a}{\pi E} \left\{ \frac{1}{2} \left(\frac{\pi\sigma}{2\sigma_y}\right)^2 + \frac{1}{12} \left(\frac{\pi\sigma}{2\sigma_y}\right)^4 + \frac{1}{45} \left(\frac{\pi\sigma}{2\sigma_y}\right)^6 + \dots \right\} \dots\dots (15)$$

taking the first term

$$\delta = \frac{\pi\sigma^2 a}{E\sigma_y} \dots\dots\dots (16)$$

From the analysis of a centre cracked plate that the strain energy release rate G was found as

$$G = \frac{\pi\sigma^2 a}{E}$$

From equation (16)

$$\delta = \frac{G}{\sigma_y}$$

From first and second terms from equation (14)

or $G = \delta \sigma_y \dots\dots\dots (17)$

$$\delta = \frac{\pi\sigma^2 a}{E\sigma_y} \left\{ 1 + \frac{\pi^2}{24} \left(\frac{\sigma}{\sigma_y}\right)^2 \right\} \dots\dots\dots (18)$$

Comparing this with ASTM treatment for small plastic zone (35)

i.e. $\frac{G}{\sigma_y} = \frac{\pi\sigma^2 a}{E\sigma_y} \left\{ 1 + \frac{1}{2} \left(\frac{\sigma}{\sigma_y}\right)^2 \right\} \dots\dots\dots (19)$

Thus, it can be seen that for $\frac{\sigma}{\sigma_y} \ll 1$, which corresponds to a requirement for a crack tip plastic zone which is small compared to the crack length, extension force G is given by equation no. (17).

The model that employed this analysis is shown in Fig. 21, which is based on a real crack of length $2a$ in an infinite plate. Under a uniform stress, σ , applied in the y direction at infinity, plastic zones produced at the tip of the crack extending (x -axis extending along the line of the crack) to $x = \pm a$. This situation is represented for the purpose of analysis by a crack of length $2a$ which is surrounded by an entirely elastic stress field when under load, but which is stressed not only by externally applied stress, σ , but also by a series of internal tensile stresses in the y direction of magnitude σ_b at $x = b$ in the region $\pm a < \pm b < \pm a$.

The stress applied within the crack length $2a$ represents the stresses in the plastic zone at the tip of the real crack.

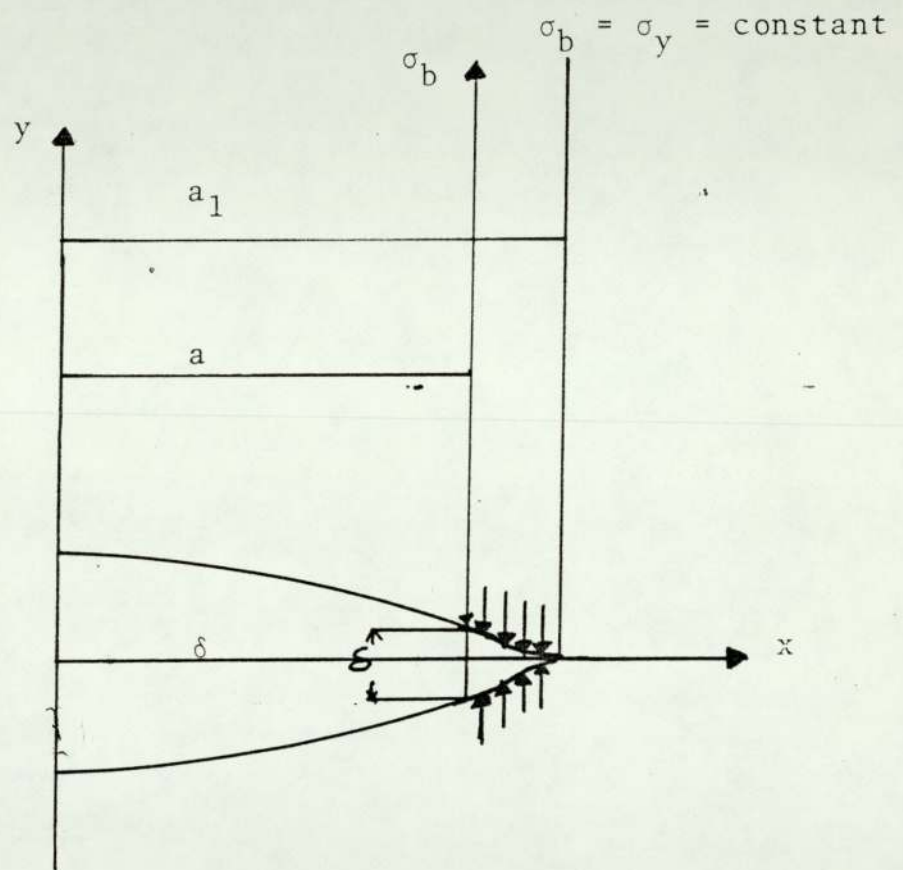
Burdekin and Stone have confirmed experimentally the validity of ^{the} basic concept of critical crack opening displacement prior to fracture using notched tensile and bend specimens of mild steel over a wide temperature range. Equation (17) indicates the physical nature of the relationship between crack extension force and crack opening displacement. That is, as loading progresses the plastic zone develops at the crack tip which permits the faces of the crack to move apart. If the COD is large enough for a specified value of yield stress such that the product $\sigma_y \delta$ exceeds the critical crack extension force for the material, then fracture follows.

This expression does not consider the triaxiality near the tip region.

Measurement of COD requires the use of equipment capable of recording the opening at a crack tip during loading. In early results a "codmeter" was used. The separation of the crack is detected by rotation of small blades, which provide a continuous direction measurement of the COD.

A photographic technique was used by Fearnehough ⁽³⁶⁾ to record the crack opening displacement. The displacement measurements were taken from a series of photographs using microhardness indentations made on either side of the slits. The indentation being made close to the crack surface projected an image via the objective lens from a microscope into a ground glass screen. The magnified image is photographed at various loads during the test and the COD can subsequently be determined from the displacement of indentation.

Crack opening displacements have been measured also by using a clip gauge attached to the specimen with sharpened cracks. A sketch of typical gauge in position is shown in Fig. 17 (page 43). This method is proposed as standard in draft ⁽³⁷⁾. Recently, British Standard ⁽³⁰⁾ specified a new method for carrying out crack opening displacement. The specimen configuration and test method are similar to those specified for K_{IC} testing in BS 5447.



$$\frac{a}{a_1} = \cos\left(\frac{\pi\sigma}{2\sigma_y}\right)$$

$$\delta = \left[\frac{8\sigma_y a}{\pi E} \right] \log_e \text{Sec} \left[\frac{\pi\sigma}{2\sigma_y} \right]$$

FIGURE 21 Schematic representation of local plasticity and crack tip for theoretical analysis (9)

4.2.2 J-Integral

The J-integral, defined by Rice ⁽³⁸⁾ has been proposed by Rice and Begley and Landes ⁽³⁹⁾ as a fracture criterion for elastic-plastic behaviour in metals. This criterion attempts to extend linear elastic fracture mechanics concepts, where only small scale plasticity is permissible, to cases where large scale plasticity is involved. Begley and Landes showed by experiment that the J-integral is a successful fracture criterion for two steels.

The J-integral as defined by Rice is a path independent energy line integral.

$$J = \int_{\Gamma} (w dy - \bar{T} \cdot \frac{\partial \bar{u}}{\partial x} ds)$$

where w is the strain energy density

\bar{T} traction vector on the path Γ

\bar{u} displacement vector

Γ any contour surrounding the crack tip.
 s is path length

It has been further shown by Rice that the J-integral may be interpreted as the potential energy difference between two dimensional bodies having neighbouring crack size a and $a + d_a$

$$J = \frac{\partial u}{\partial a}$$

where u is the potential energy per unit thickness and a is the crack length. Using this energy Begley and Landes proposed the J-integral as a fracture criterion.

McClintock (40) has shown that by combining the work of Hutchinson (41) and Rice (38), the crack tip elastic stress and strain singularities can be expressed as a function of J . Therefore, fracture will be governed by a characteristic crack tip singularity in the plastic range. This aspect is analogous to the role of stress intensity factor, K_I , in linear elastic fracture with singularity at the crack tip.

The strength of the crack tip singularity is the stress intensity factor, K . The crack tip region can then be characterised by the single parameter " K " with fracture occurring at a critical value of K .

4.2.2.1 Limitation of J-Integral as a Fracture Criterion

A failure criterion which could predict failure at cracked bodies would be a useful engineering tool for both evaluation of structural integrity and the selection of materials. LEFM provides a parameter failure criterion for a limited class of problems, those of cracked bodies with small-scale yielding, where the crack tip plastic region is at least smaller than the physical dimensions of the component.

It is desirable to have a failure criterion which could predict fracture in structure in cases of both small and large-scale plasticity. The fracture mechanics are based on the elastic analysis of the crack tip region which shows a unique stress-strain field with a singularity of the crack tip. The strength of the crack tip singularity is the stress intensity factor K .

A characterisation of the crack tip area by a parameter calculated without focussing attention directly at the crack tip would provide a more practical method for analysing fracture.

The path independent J-integral^{has been} proposed by Rice (38), its value depends upon the near tip stress-strain field. However, the path independent nature of the integral allows an integration path taken sufficiently far from the crack tip region.

For linear elastic behaviour the J-integral is identical to G, the energy release rate per unit crack extension. Therefore a J-failure criterion for the linear elastic case is identical to K_{IC} failure criterion.

5. INFLUENCE OF ALLOY CONSTITUENT ON THE PROPERTIES OF STEELS

The primary purpose of adding alloying elements to steel is to shift the curves on a TTT diagram to longer times. In heat treating this allows the steel to be cooled more slowly and still retain its austenitic structure down to M_s temperature. In a piece of steel being quenched the cooling rate decreases with depth from the surface. Thus, alloying means that the centre of thicker pieces of austenite can be cooled down to M_s in a given quenchant without prior transformation.

For a given carbon content ⁽⁴²⁾ the hardness of steel of given intercarbon spacing is largely independent of the amount of alloying elements. The depth of hardening varies with alloy. Various alloying elements, and combination of elements, can have a notable effect on the rate of nucleation and growth of pearlite and bainite (Fig. 22).

In the commercial treating of steel the peak almost always transforms while being continuously cooled. Because of this it is desirable to consider a TTT diagram for continuously cooled specimens (a C-T diagram).

5.1 Heat Treatment and Isothermal Transformation

The transformation of austenite below the eutectoidal temperature can be represented by isothermal transformation diagrams in which the beginning and end of

transformation is plotted as a function of temperature and time temperature transformation or TTT curves form one of the important sources of quantitative information for the heat treatment of steels.

The effect of carbon ⁽⁴³⁾ on both M_s and M_f is shown in Fig. 23, from which it can be seen that 1% C by weight lowers the M_f by over 300°C, that above 0.7% C the M_f temperature is below room temperature and consequently higher carbon steels quenched into water will normally contain substantial amounts of retained austenite. Carbon has also an effect on the range of temperature over which upper and lower bainite occurs. The B_s , the start of bainite transformation temperature, is depressed by many alloying elements but the carbon has the greatest influence, the carbon concentration also influences the temperature of transition from upper to lower bainite,

Alloying elements ⁽⁴³⁾ have a great influence on the proportion of austenite retained on quenching.

Typically, a steel with 4% molybdenum, 0.2% C, in the martensitic state contains less than 2% austenite. From 0.2% molybdenum in steel containing 0.4% carbon to 2% molybdenum and 0.3% carbon, then the whole C-curve is raised and reaction substantially slowed, so that the nose is above 700°C, the reaction starting after four minutes (Fig. 23-1 and 23-2). Two typical cooling

curves for the surface and the centre of an oil quenched 95 mm diameter bar are shown in Fig. 24-1 and 38 mm Electem and Somdie block (Figs. 24-2 and 24-3). In the case of chromium which is a strong carbide former, the strength of the steel rises by 8-10 kg/mm² per 1% chromium. The yield point is likewise increased, however not at the same rate but the notch impact value is lowered. Additionally, adding a certain percent of manganese to steel improves the strength properties while only slightly impairing its elasticity. Furthermore, manganese has a favourable influence on the forging property. With up to 3% manganese the tensile strength of steel is increased by about 10 kg/mm² for every percent of manganese. The yield point behaves in a similar manner (43). Molybdenum has a considerable effect on steel; it improves the tensile strength and especially the heat resistance. When used in alloy steels in combination with chromium and nickel, molybdenum may produce high yield point^{and} tensile strength values. Molybdenum also has a strong tendency to form carbide. Furthermore, molybdenum reduces the tendency to "temper brittleness" in low nickel, low chromium steels (44).

Isothermal transformation and cooling curves for Electem, Somdie and Thermodie steel are shown in Figs. 25-1, 25-2 and 25-3 (45).

5.1.1 Bainite Transformation

To develop the best combination of strength, ductility, impact toughness and fatigue resistance, a steel with good hardenability has to be chosen to ensure the formation of a fully martensitic structure before tempering. Many components, however, are not subjected to the high stress which requires the use of tempered martensitic structure, and in this case it is possible to use steel of lower hardenability given a completely hardened structure which is partly or wholly bainitic. It must be emphasised, however, that incompletely hardened structures often have poor toughness and low resistance to fracture. The location of the bainite range with respect to cooling rates, treatment time and treatment temperature is also important.

Bainitic transformation ⁽⁴⁶⁾ results in the formation of a mixture of α -phase and carbide, which is called bainite. Unlike pearlitic carbide, which has a lamellar structure, the carbide in bainite is in the form of very disperse particles detectable by electron microscopy only. A distinction is usually made between upper and lower bainite to show that bainitic transformation has taken place in either upper or lower regions of intermediate temperature ranges. Upper bainite has a feather-like structure, whereas lower bainite has a martensitic-like acicular structure. The microstructure of the lower bainite may sometimes be hardly distinguishable from that of tempered martensite. These microstructural

features of bainite, which should be linked with the shape of ferritic crystals, may be absent in some steels. For instance, the shape of ferrite in bainite may be other than acicular, granular and columnar forms of bainite are sometimes possible. A stricter distinction between upper and lower bainite can be made by the pattern of distribution of carbide phases. As has been shown by electron microscopic examination, carbide particles in upper bainite may be present between ferritic plates or at grain boundaries and inside plates, whereas in lower bainite the carbides are always present inside platelets of α -phase.

In many alloy steels the bainitic transformation has a feature very typical of martensitic transformation, i.e. it does not proceed to full disappearance of austenite. As the transformation temperature departs from that for the start of the bainite transformation, B_s , the amount of bainite increases, while the amount of retained austenite decreases. Alloying elements may have a different effect on the speed of break down of austenite in the pearlitic and bainitic regions. In some steels, the bainitic transformation may be shifted considerably to the right because of alloying effects (Fig. 26).

5.1.2 Martensitic Transformation

Martensitic formation temperatures have some influence on the response of low and medium carbon alloy steels to conventional quenching treatment. From the practical

viewpoint, the rate at which the martensite expansion occurs in various parts of complex components made from different steels is a factor affecting distortion. The dependence of the martensite formation reaction on chemical composition has been recognised for many years.

Novikov ⁽⁴⁶⁾ pointed out that martensitic transformation can occur in carbon steel heated to a temperature above A_1 if the steel is quickly quenched, for instance, in water. For each steel grade, the austenite to martensite transformation starts at a definite temperature M_s . The M_s temperature is independent of cooling rate within a very wide range of cooling rates, the formation of martensite takes place within martensitic point M_s and the lower point M_f . The M_s point can be lowered appreciably by increasing the carbon, in steel with less than one percent carbon it is above 200°C . The M_s point may be changed through variations in the steel composition. In particular, alloying additions which increase the elastic modulus of matrix (austenite) can hinder the martensitic transformation.

The content of carbon in austenite is not always the same as that in steel, since the carbon may be present in carbides. These carbides, which exist in the metal along with austenite, cannot by themselves affect the M_s point, but can produce an indirect effect. For instance, on increasing the hardening temperatures, the carbides dissolve in the austenite, the latter becomes higher in carbon, and thus the M_s point is lowered.

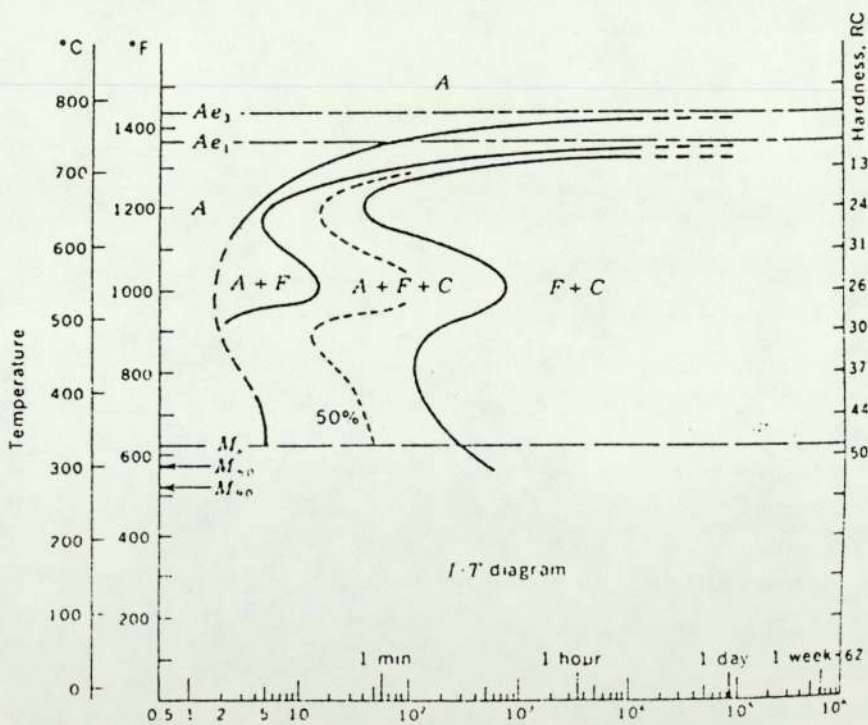
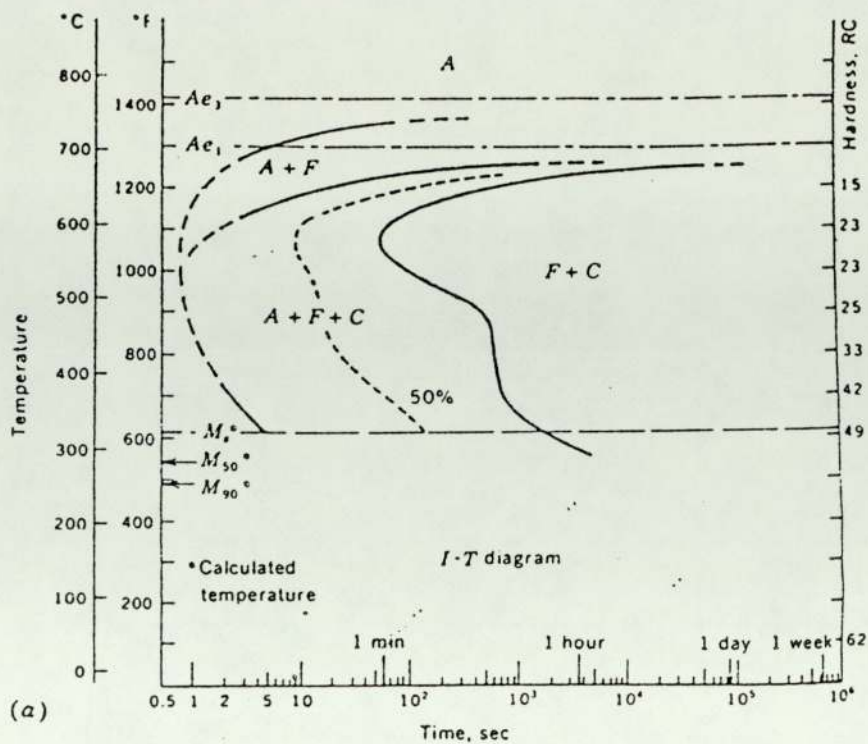


FIGURE 22-1 TTT diagrams of Cr commercial low alloy steels, containing
 a. 0.4% C, 1% Mn,
 b. 0.4% C, 1% Mn and 0.9% Cr

(From Atlas of Isothermal Transformation diagram, U.S. Steel Company)(42)

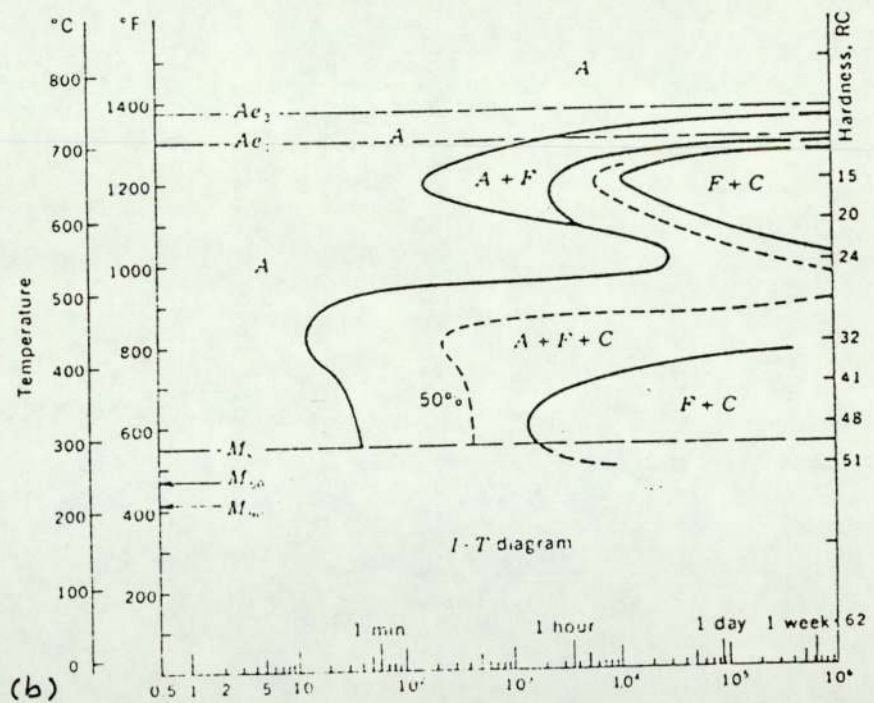
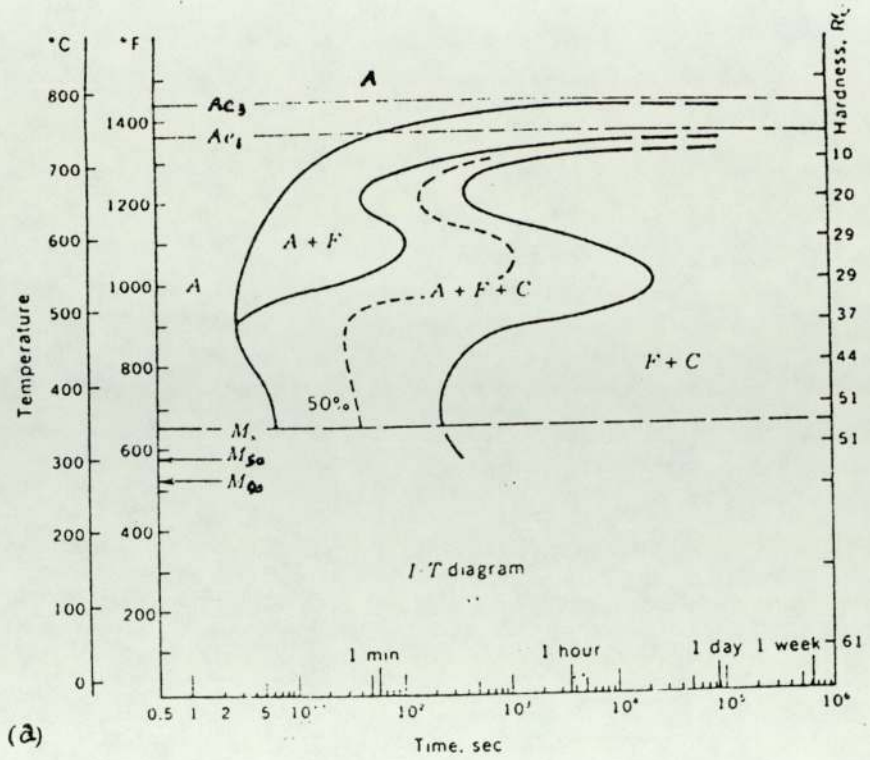


FIGURE 22-2

TTT Diagram for low alloy steels which contain

a. 0.4% C, 1% Mn, 1% Cr and 0.2% Mo

b. 0.4% C, 1% Mn, 0.8% Cr, 0.3% Mo and 1.8% Ni

(From Atlas of Isothermal Transformation diagram, U.S. Steel Company)

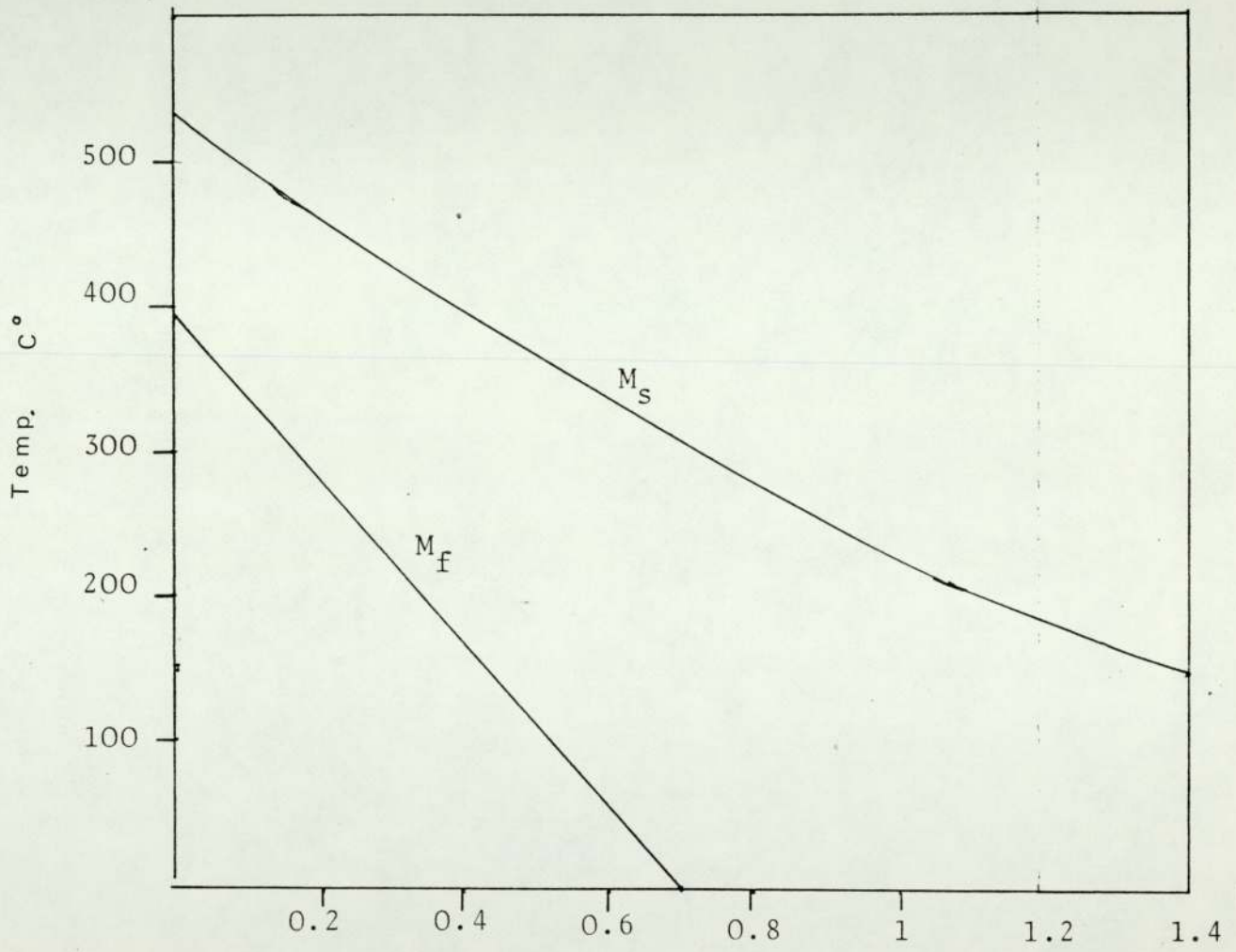


FIGURE 23. The effect of carbon on M_s and M_f (43)



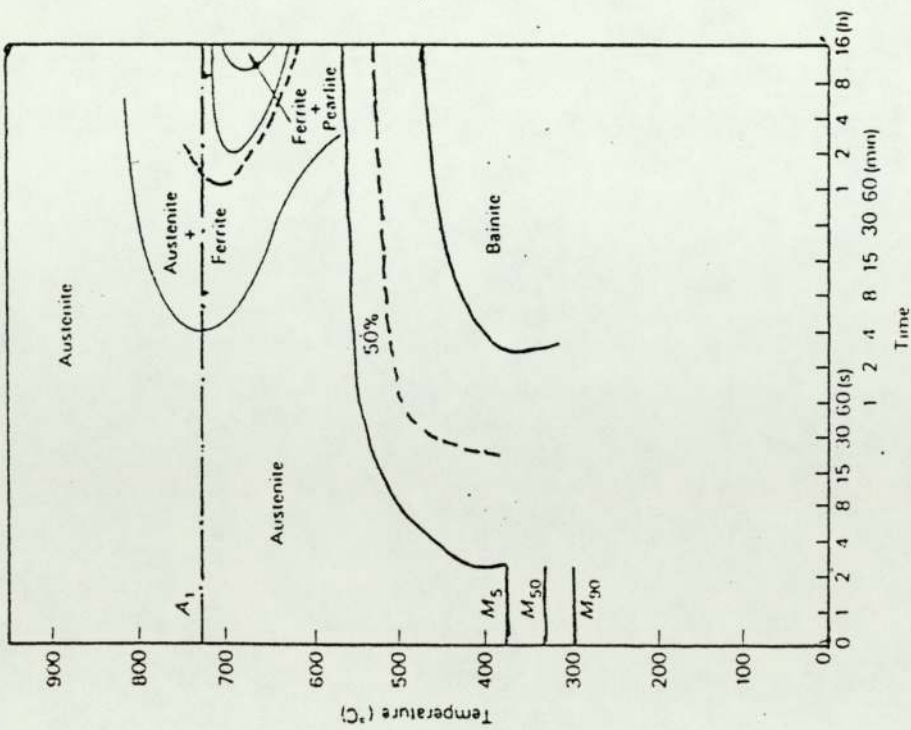


FIGURE 23-1 TTT diagram of a molybdenum steel (43) 0.3% C, 2.0% Mo

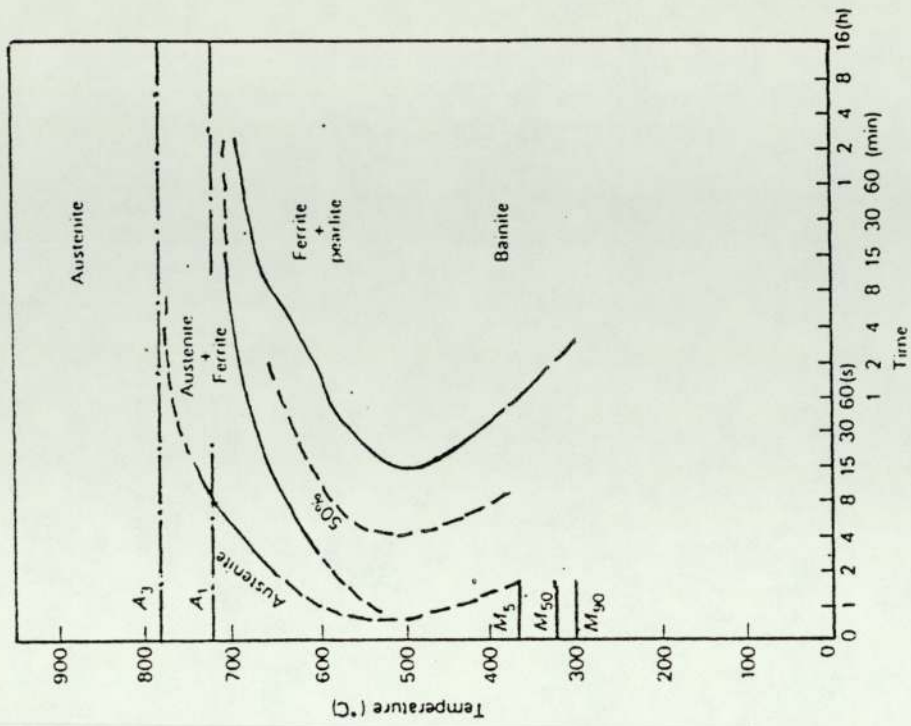


FIGURE 23-2 TTT diagram of a molybdenum steel (43) 0.4% C, 0.2% Mo

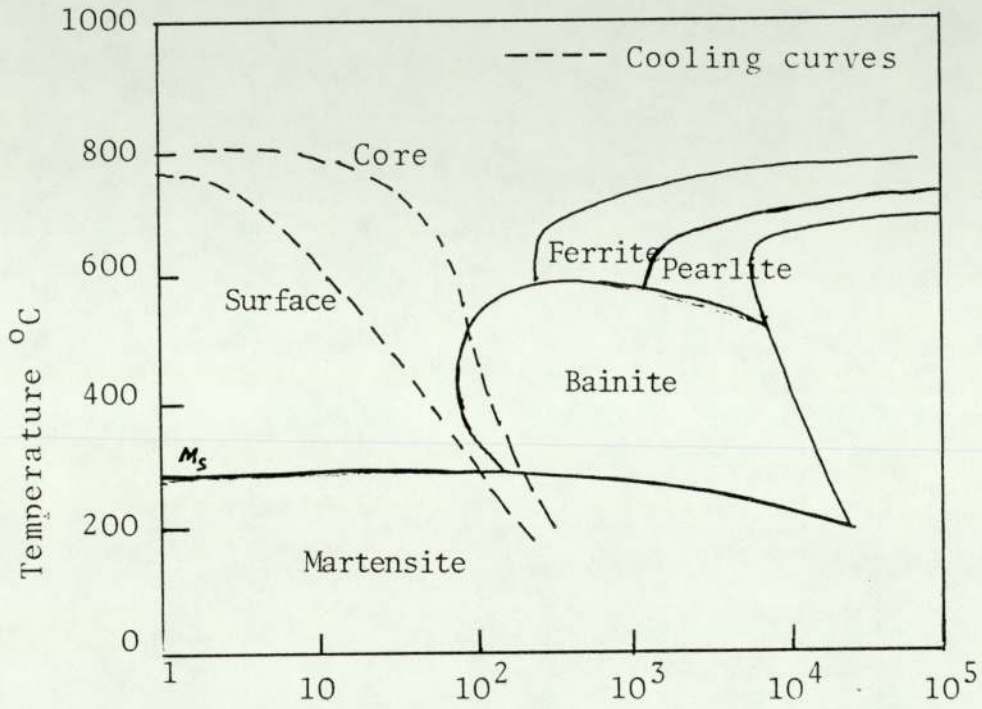


FIGURE 24-1 Relation between cooling curves for the surface and core of an oil-quenched 95 mm diameter bar and the microstructure. The surface is fully martensitic.

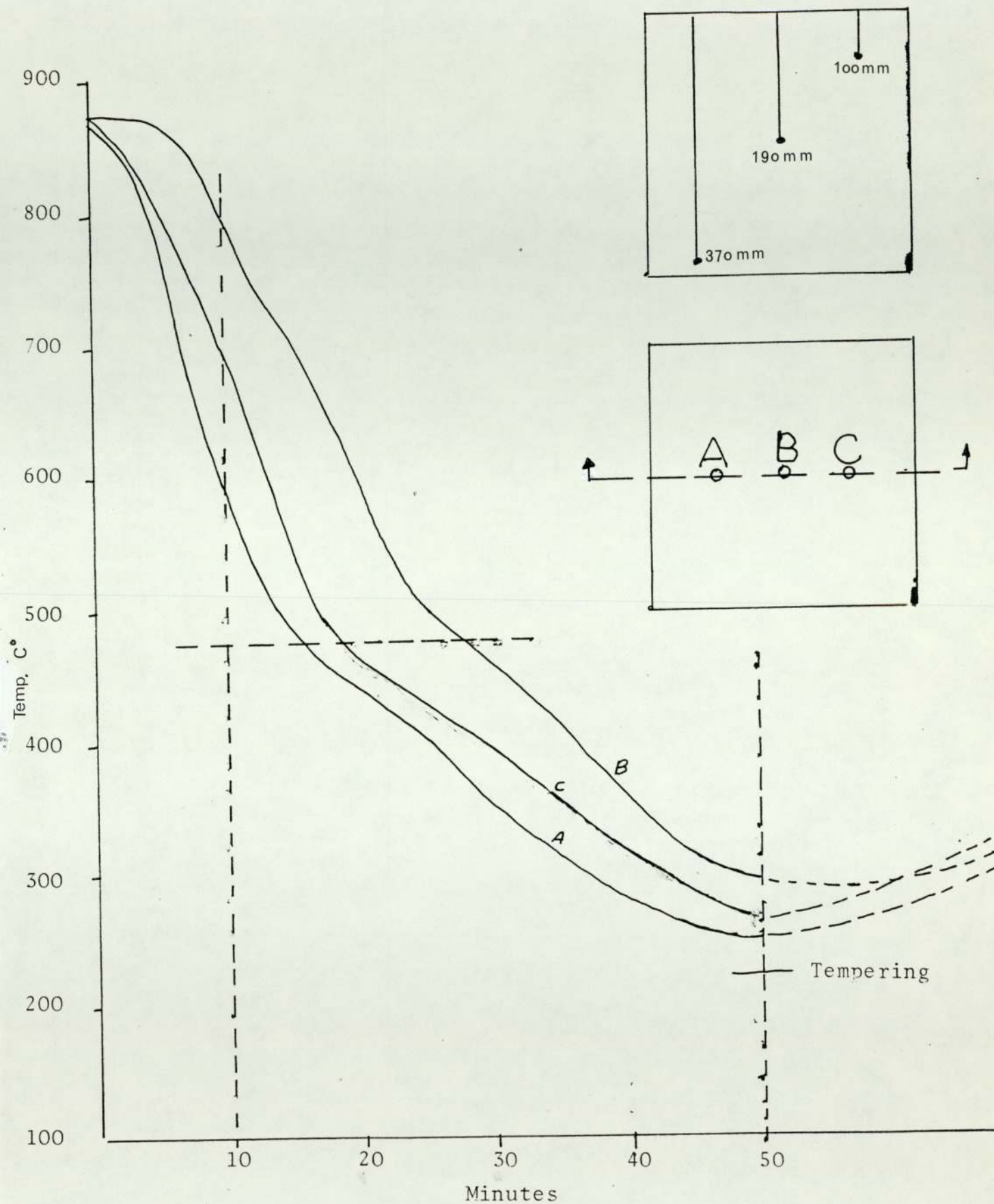


FIGURE 24-2 Typical cooling curves of quenching Electem die blocks 380 mm² water and oil quench. Quenching time 50 minutes.⁽⁴⁵⁾

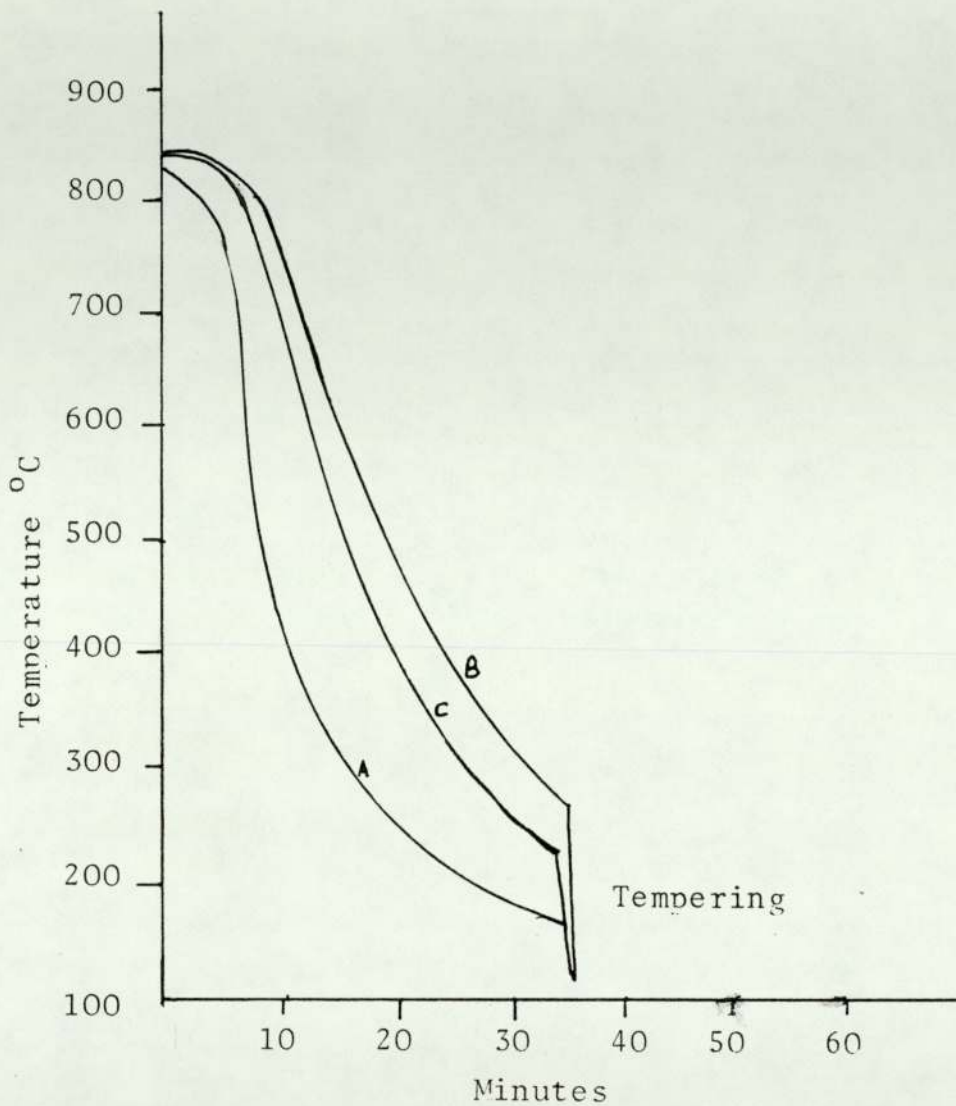


FIGURE 24-3 Typical cooling curves of 380 mm² of Somdie block, quench time 35 minutes (45)

ISOTHERMAL TRANSFORMATION DIAGRAM

ELECTEM	C	Si	S	P	Ni	Cr	Mn
	5.7	29	0.25	0.10	1.5	79	30

AUSTENITIZED AT 840 C FOR 30 MINS.

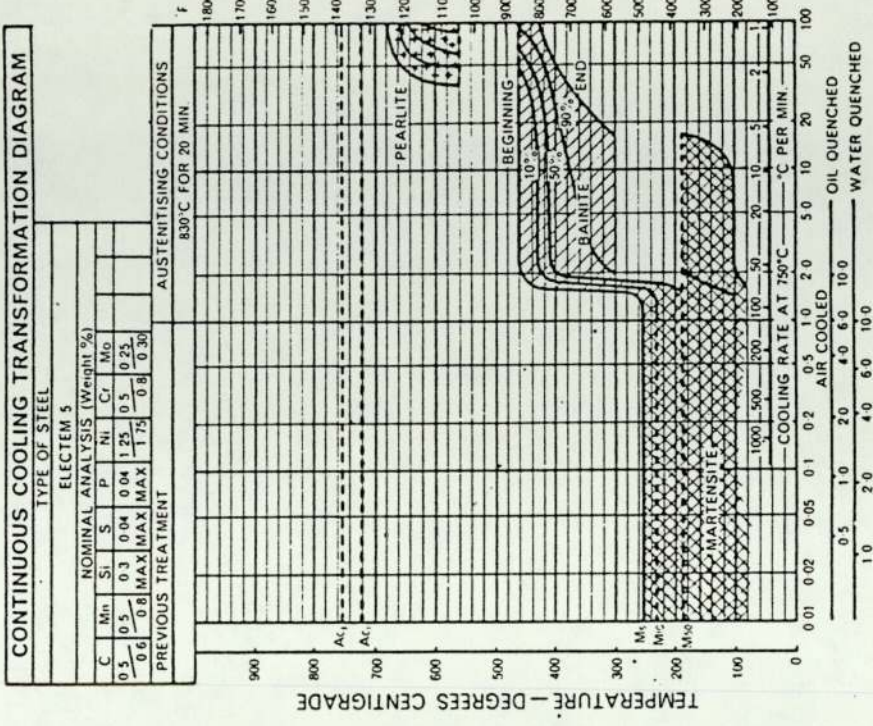
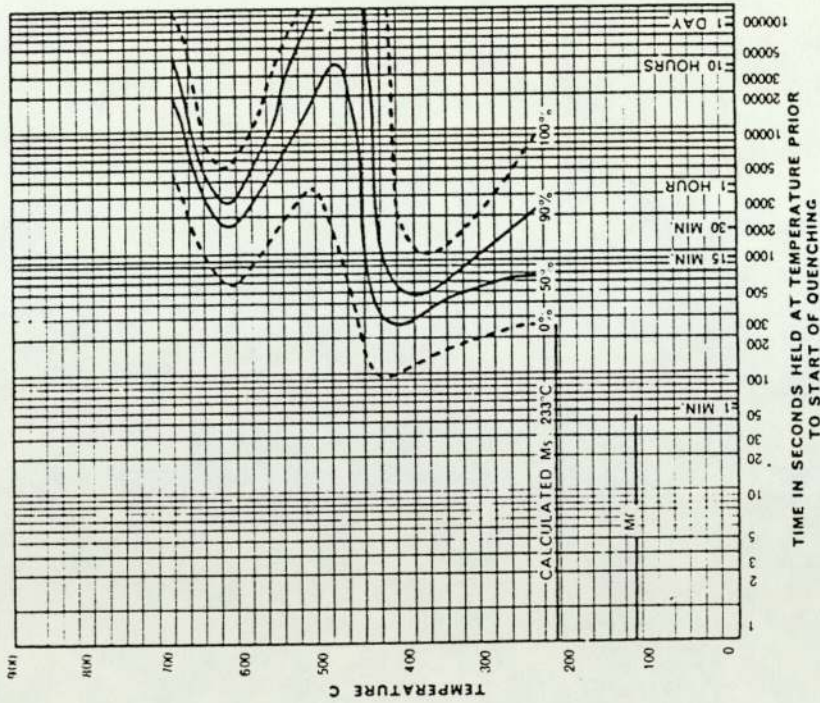


FIGURE 25-1 Continuous cooling diagram and isothermal transformation diagram for Electem die steel (45)

THERMODIE CONTINUOUS COOLING DIAGRAM

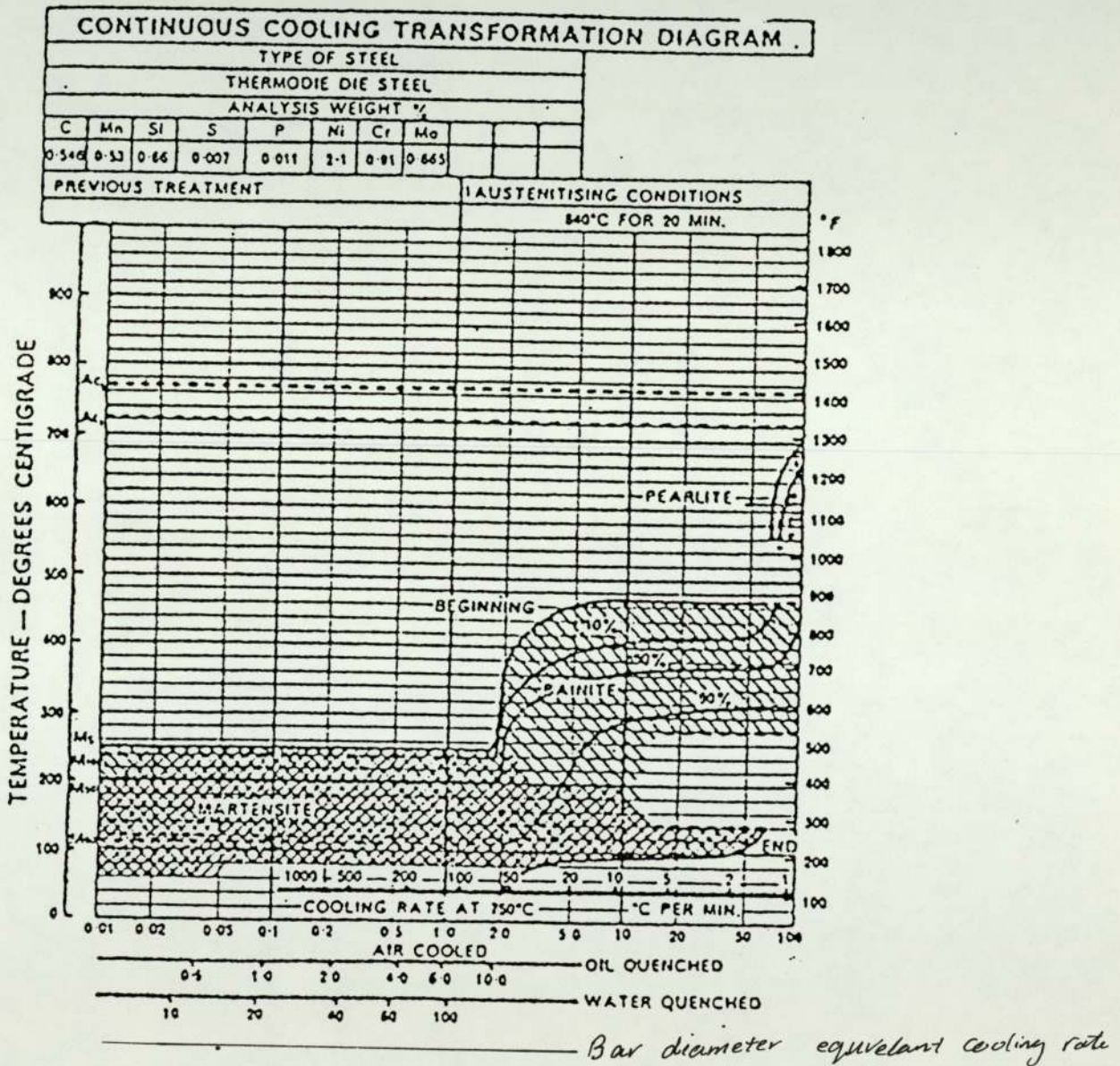


FIGURE 25-2 Continuous cooling transformation diagram of Thermodie die steel (45)

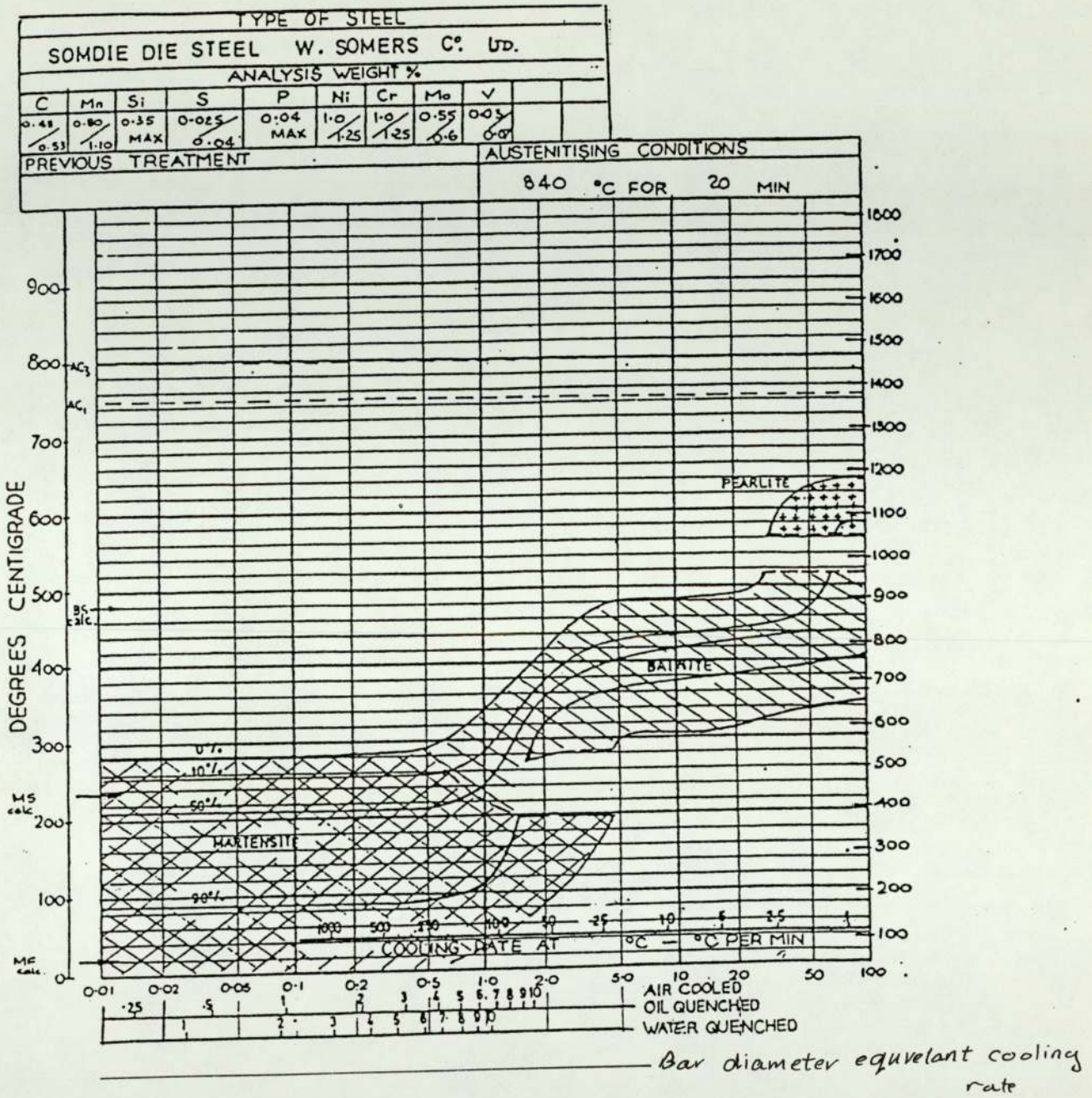


FIGURE 25-3 Continuous cooling transformation diagram of Somdie die steel (48)

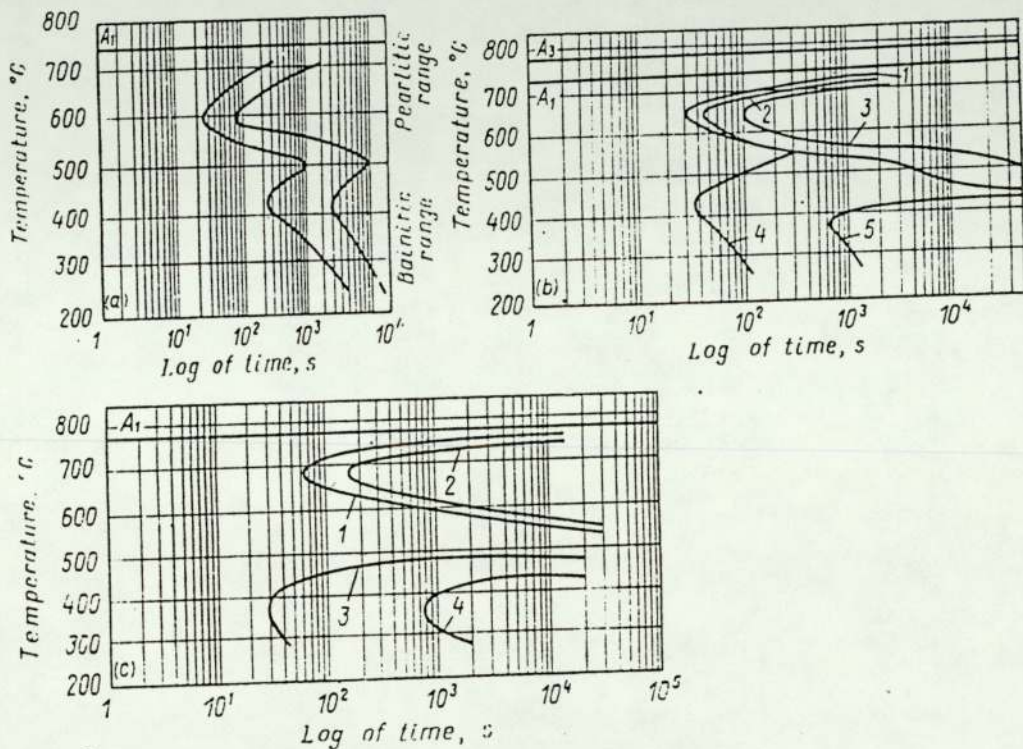


FIGURE 26 Diagrams of isothermal decomposition of austenite in alloy steels with separate C-curves for pearlitic and bainitic transformation

- a. steel with 1.07% C and 1.52% Cr
- b. steel with 0.43% C, 1.22% Cr,
0.82% Mn and 0.11% V
- c. steel with 0.43% C and 3.52% Cr

5.1.2.1 Deformation Induced Martensitic Transformation and Transformation Induced Plasticity in Steel

The martensitic transformation is induced by deformation in metastable austenitic steel. This is called the deformation induced martensitic transformation. In order to understand the general nature of deformation, applied stress and plastic strain on martensitic transformation has to be considered, since the martensitic transformation is achieved by the co-operative shear movement of atoms, therefore, applied stress aids the transformation.

Tamura (47) suggested that the deformation induced martensitic transformation can be understood only in terms of the effect of applied stress rather than effect of strain. A remarkable increase in elongation[↑] when a martensitic[↑] structure is formed during deformation.

5.1.2.1.1 Deformation Induced Martensitic Transformation

Fig.27 shows the change in the chemical free energies of martensite and austenite with the temperature, where:

T_0 is the temperature at which the austenite and martensite are in equilibrium

M_s temperature at which the transformation starts by cooling

$\Delta G_{M_s}^{\gamma \rightarrow \bar{\alpha}}$ free energies difference between austenite and martensite which is equal to the critical chemical driving force for start of martensitic transformation.

\bar{u} is the critical mechanical driving force

$$\bar{u} = \Delta G_{M_s}^{\gamma \rightarrow \bar{\alpha}} - G_{M_{T_1}}^{\gamma \rightarrow \bar{\alpha}} \quad (\text{See Figure 27})$$

This is necessary for the stress induced martensitic transformation at T_1 . The mechanical driving force, u , is a function of stress and the orientation of transformation martensite plate, this was explained by Patel and Cohen et al (48).

H. Onodera, Hgoto and F. Tamura (49) pointed out that when the specimen is stressed by σ_1 , as shown in Fig. 28, therefore τ and σ are expressed

$$\begin{aligned}\tau &= 0.5\sigma_1 \sin 2\theta \cos \alpha \\ \sigma &= + 0.5\sigma_1 (1 + \cos 2\theta)\end{aligned}$$

where σ_1 is the absolute value for applied stress/tension or compression, θ is the angle between the axis of applied stress and the normal to plane p ; α is the angle between the shear direction of the applied stress on plane p ; + and - correspond to tension and compression respectively.

Tamura (47) also pointed out that for the martensite formation the critical stress increases linearly with increasing temperature between M_s and M_s^σ below the yield stress of austenite, as shown in Fig. 29.

The complex inter-reactions between applied stress, plastic strain and martensite transformations have been studied extensively by Bolling and Richman (50). They defined a temperature M_S^σ (above M_S), below which yielding under applied stress is initiated by the onset of martensite formation and above which yielding under applied stress is initiated by regular slip processes in the parent phase, these relations as given in Fig. 29.

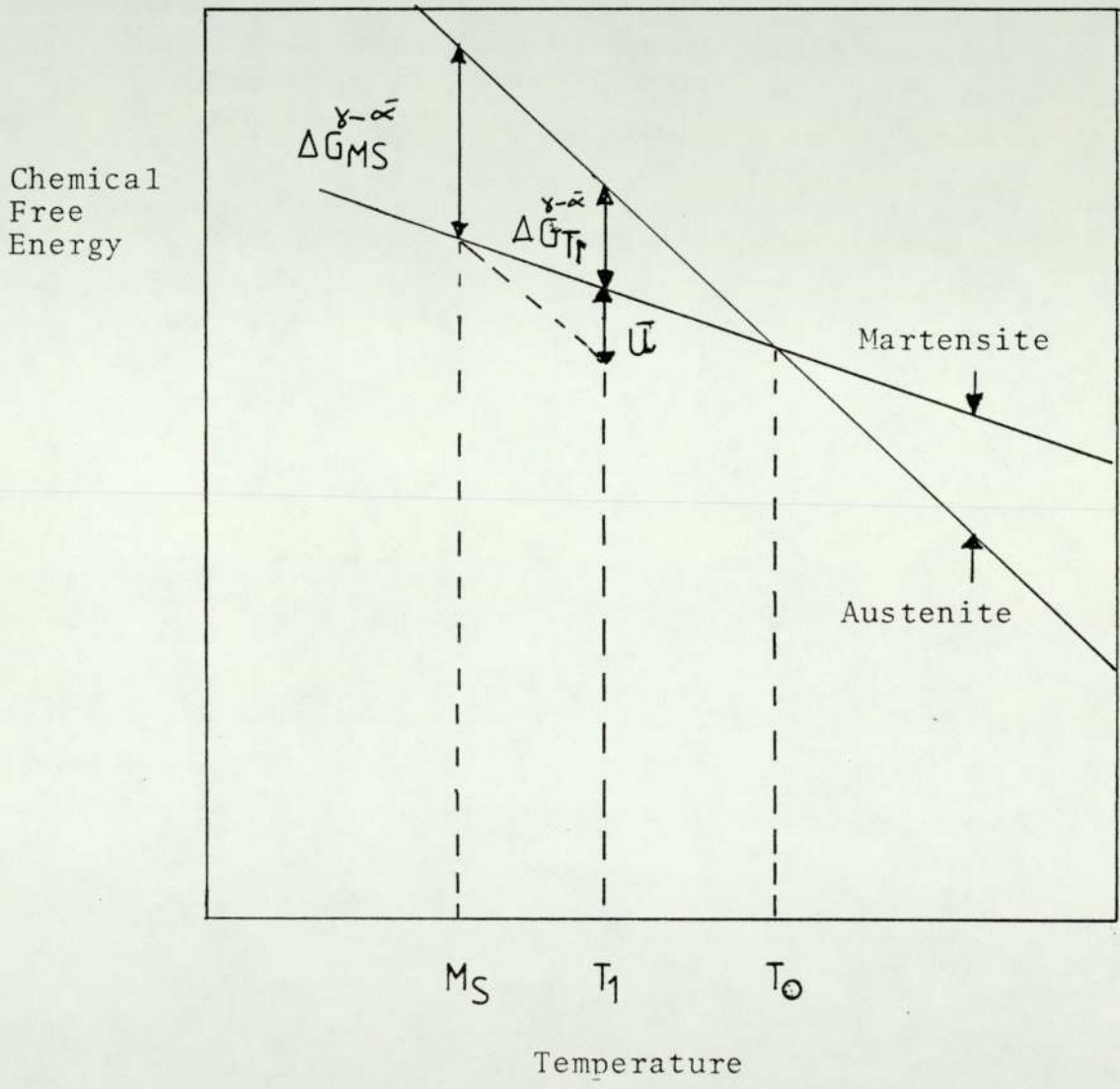


FIGURE 27 Chemical Free Energy of austenite and martensite as a function of temperature.(47)

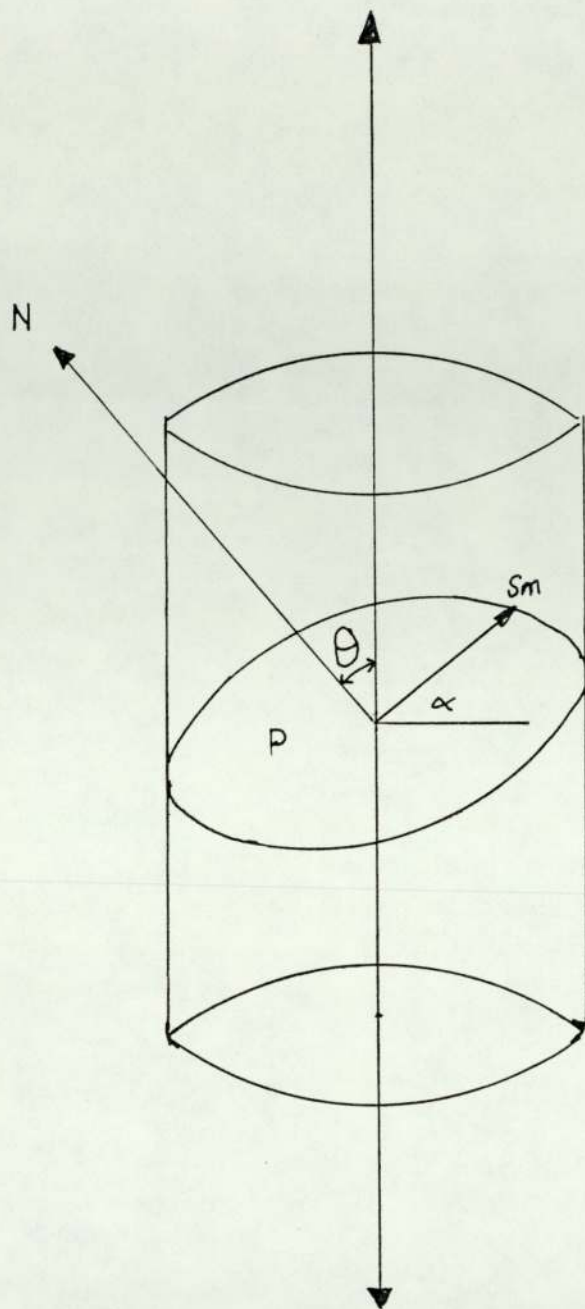


FIGURE 28 Relation between applied stress axis, A, θ and α , N normal direction to plane p, S is shear direction of martensitic transformation and S_m is maximum shear direction on p (47)

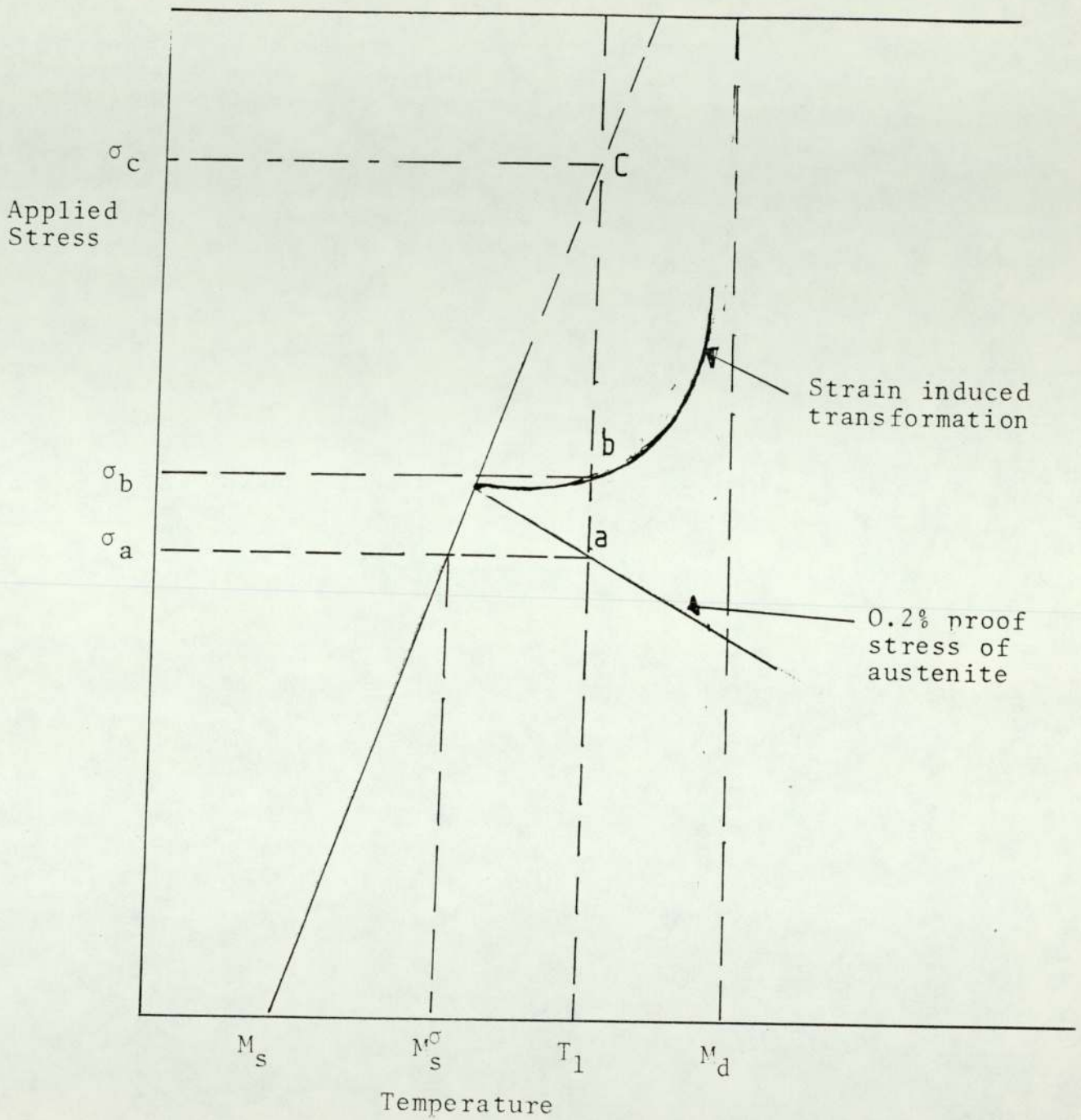


FIGURE 29 Critical stress for martensite formation as a function of temperature.⁽⁴⁷⁾

6. EXPERIMENTAL WORK

6.1 Material Used

Four types of die steel were tested:

1. Electem
2. Thermodie
3. Hydie
4. Somdie.

Each of these materials were forged into 10" x 10" size blocks; specimens were provided by Walter Somers Limited, representing top, middle and centre of a die block. All these specimens were machined after heat treating the block, as shown in Table 1. The chemical analysis also has been tabulated in Table 2.

6.2 Specimen Preparation and Dimensions

6.2.1 Short Rod/Bar

Specimens were machined from forged die blocks for each material, Fig. 30. The dimensions of these specimens include slot length, slot thickness, grip and grooved depth, as shown in Fig. 31.

The specimens taken from 10" x 10" blocks were to be used for determining the effect of microstructure on fracture toughness from outside to centre of the block, as shown in Figs. 32, 33. A spark machine was used for producing the slot, each specimen was measured before being tested. Figure 30 shows short rod/bar which has been used for

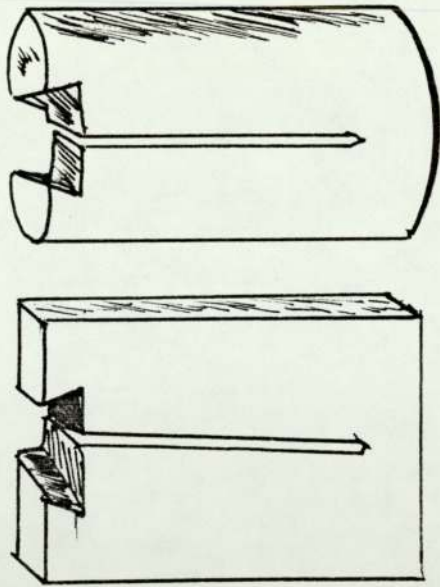
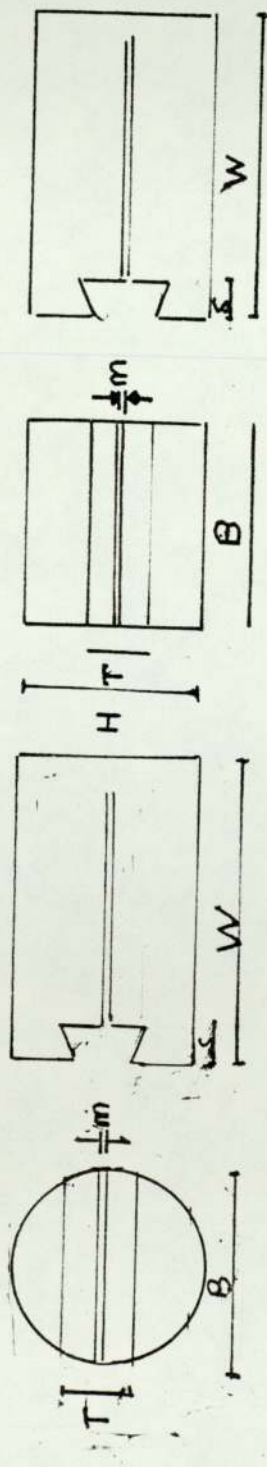


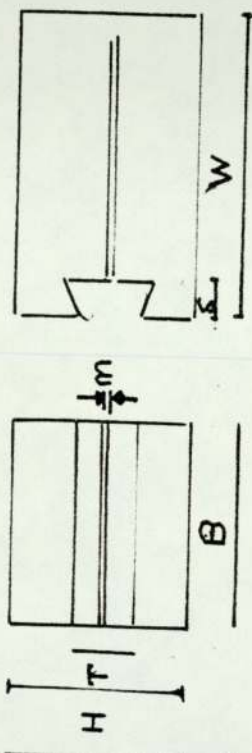
FIGURE 30 Short Rod/Bar Specimen

(a)



$B = 25.4$
 $W = 38.1$
 $H = 25.4$
 $T = 8.0$
 $S = 4.0$
 $m = 0.25$
 $a_o = 10.70$
 $L = 1.75$
 $\theta = 58.0^\circ$

(b)



$B = 25.4$
 $W = 38.1$
 $H = 22$
 $T = 8.0$
 $S = 4$
 $m = 0.25$
 $a_o = 13.10$
 $L = 1.75$
 $\theta = 55.0^\circ$

FIGURE 31 (a) short rod dimensions "mm"
 (b) short bar dimensions "mm"

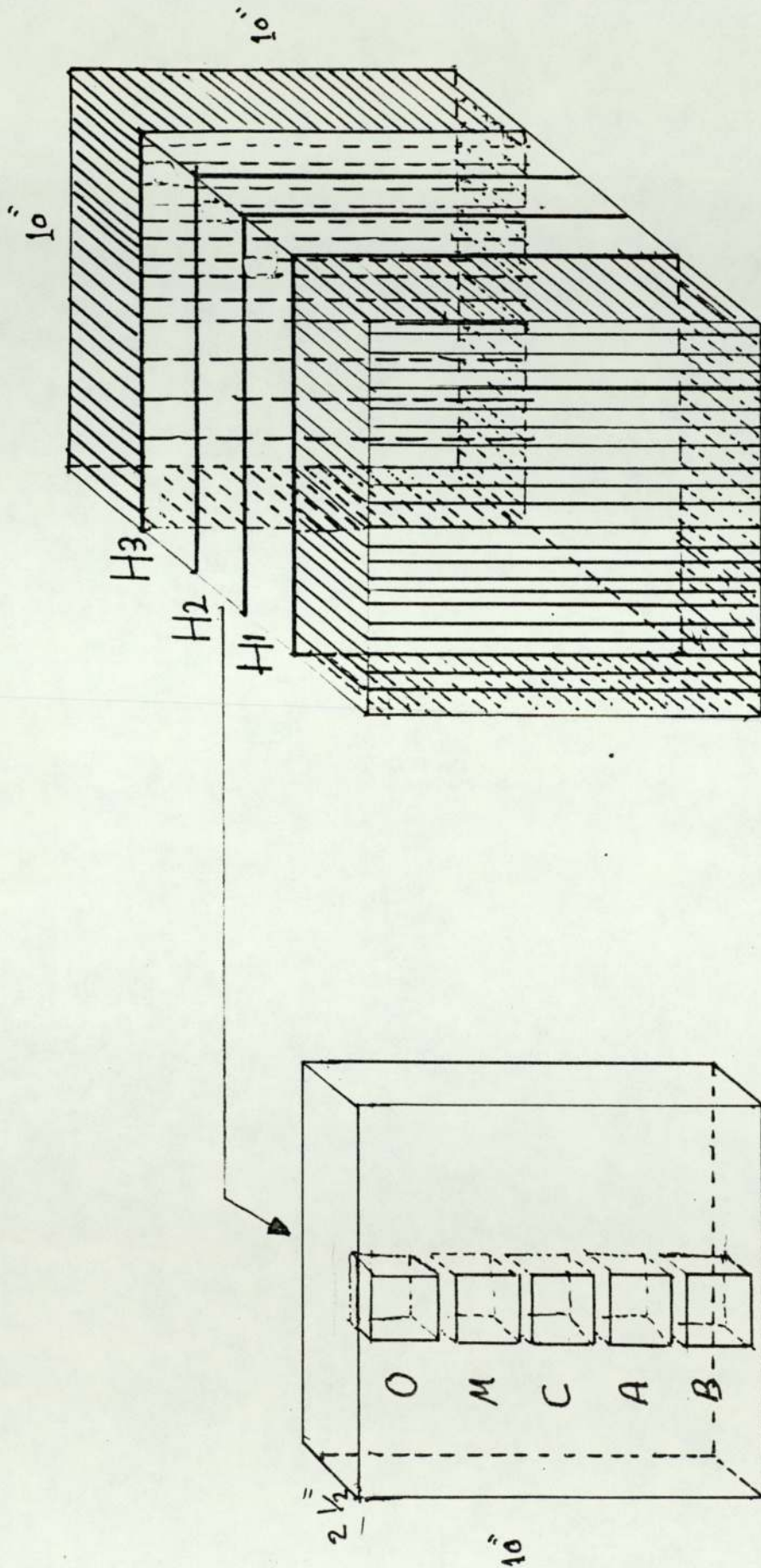


FIGURE 32 Schematic plan of work for 'Hydie' Steel/Short Bar.

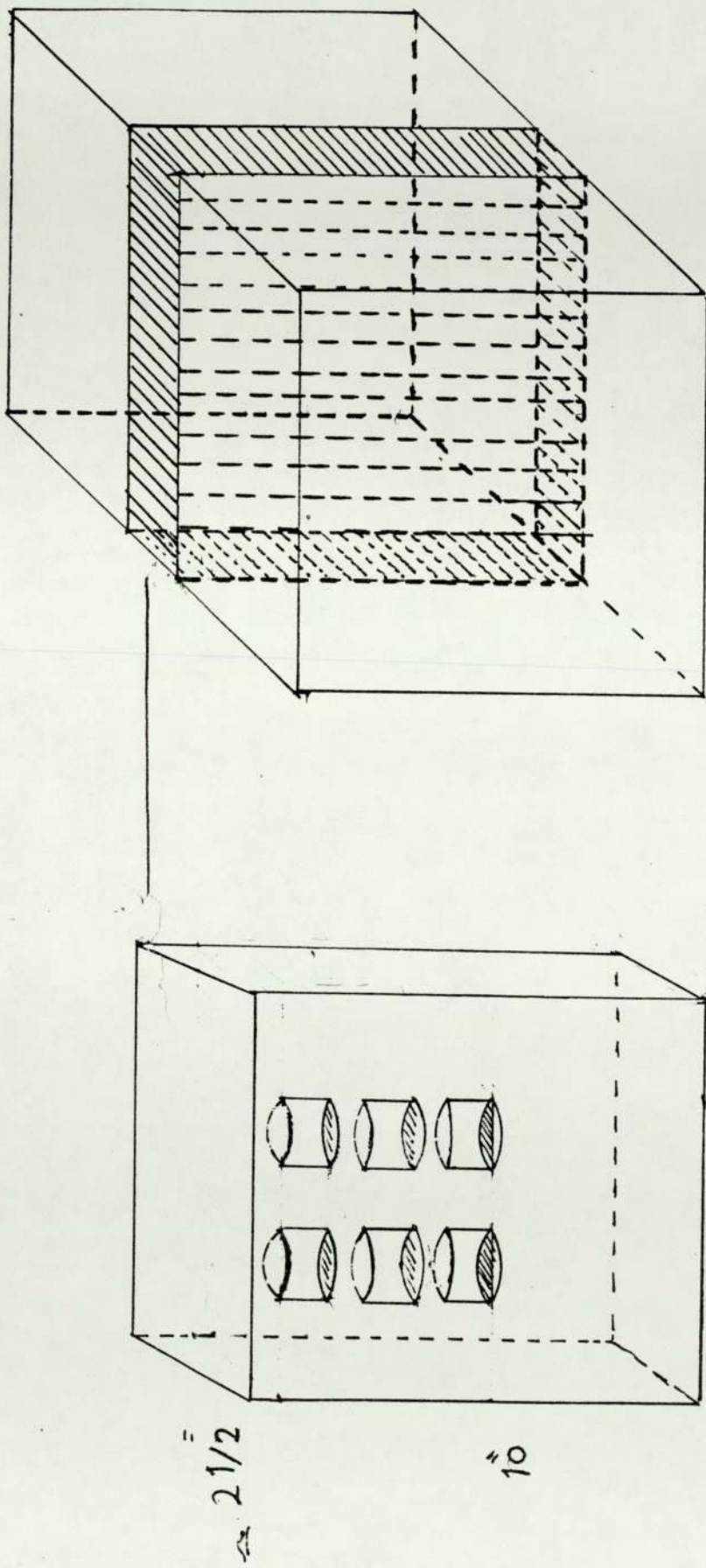


FIGURE 33 Schematic plan of work for Eiectem, Somdie and Thermodie/Short Rod.

determination of fracture toughness.

Barker (51) pointed out in his recent work that the specimen geometry has to do with the configuration of the slot bottoms. It was also shown in his previous work that if the plastic zone is not extremely small, the slots should be either very thin or they should have pointed bottoms to minimise errors from non-plane strain effect at the end of the crack.

The specimen dimensions for short rod/bar used in this experimental work are shown in Tables 5, 7 and 10.

6.2.2 Three Point Bend

The fracture toughness testing programme followed strictly the procedure for the K_{IC} test. The basic observations as a function of load ~~was~~ made for each fracture toughness specimen, ^{were} the amount of crack opening displacement and the extension of crack growth.

The fracture toughness testing specimens were made to meet the recommendations of the standard for plane strain fracture toughness testing, BS 5447. The specimens, as shown in Fig. 34 and dimensions in Table 12, were cut from the forged block in direction shown in Fig. 35. One specimen for each type of die steel was tested with the notch on an edge surface in the plane parallel to the top surface of the block. The first step in preparing the specimen for testing was to polish both faces, normal to

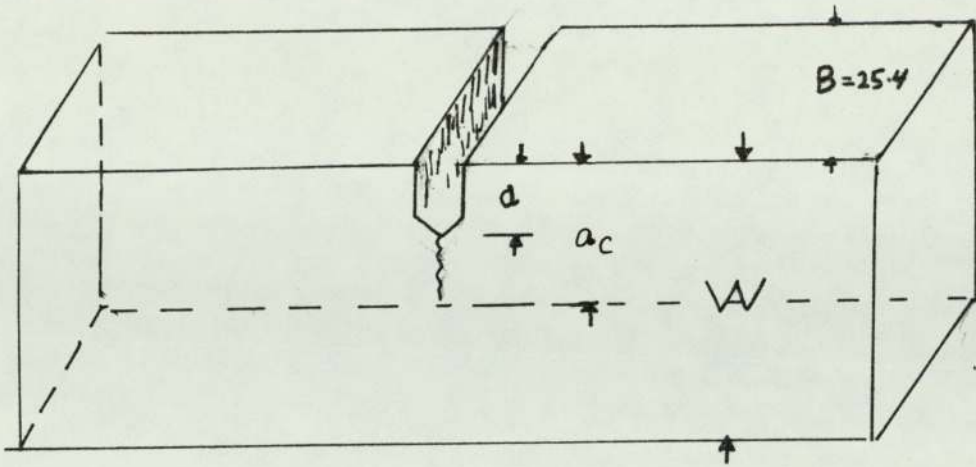


FIGURE 34 3-point bend specimen

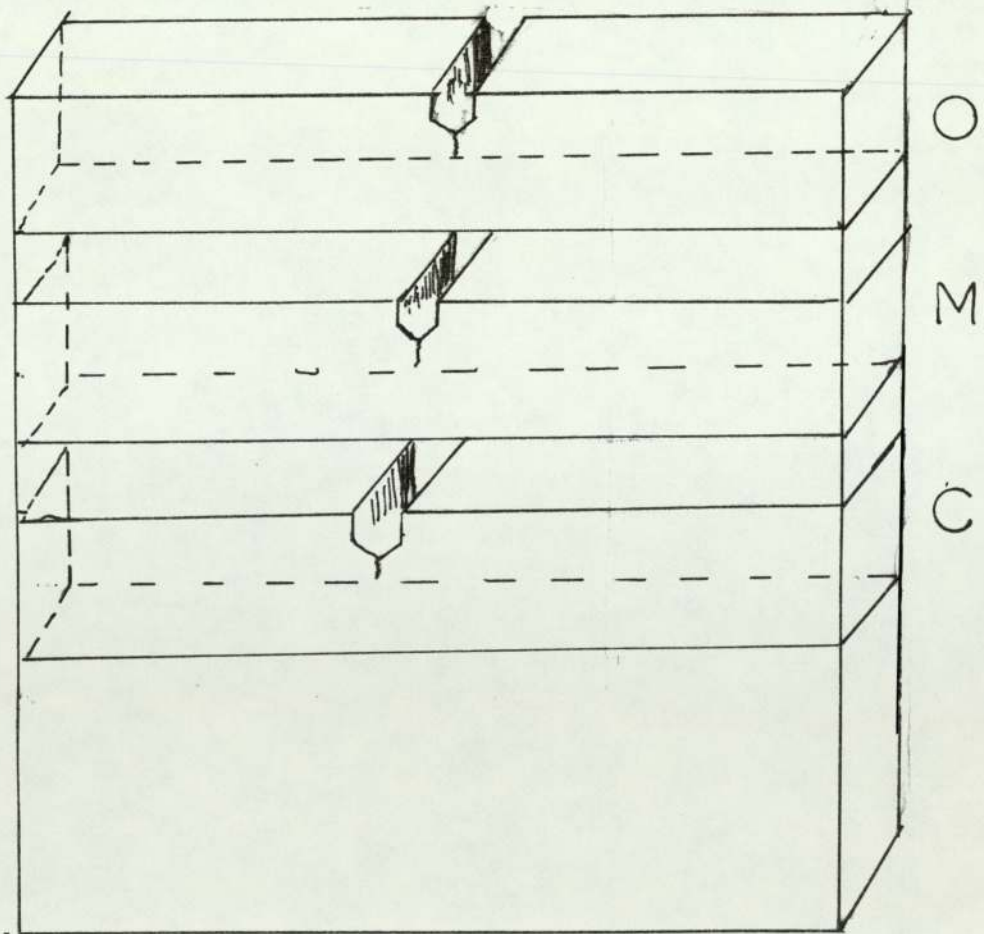


FIGURE 35 Schematic plan of work for a 3-point bend test specimen

the cracking plane to allow optical examination and surface measurement of the fatigue pre-crack. The fatigue pre-cracking was carried out under fully controlled conditions using an Amsler Vibrophore having a 2-tonne maximum capacity dynamometer. The preliminary test specimens were fatigue pre-cracked to obtain the crack length to width ratio, as shown in Table 12.

Estimating the K_{IC} of the materials from short rod/bar (average value), the K_{Fmax} at the end of initiation stage was calculated by using the following equation:

$$P_{Fmax} = \frac{K_{Fmax} Bw^{\frac{1}{2}}}{Y}$$

6.3 Short Rod/Bar Fracture Toughness Testing

Fracturing of the specimen was carried out on 5000 kgf capacity Instron testing machine using a cross-head speed of 0.01 cm/min. Claw grips with clip gauge were mounted across the centre of the mouth of the crack.

The loading was accomplished by pulling on grips fitted into grip grooves in the face of each specimen (Fig. 17 page 43). A clip gauge was used to monitor the specimen mouth opening, and ^{a record} was made of the applied load vs. the mouth opening.

In each experiment on a short rod, three unloading slopes were drawn for measurement of p (plasticity) at different average crack lengths, which indicated the variation of p with crack length. The linear unloading slopes in Fig. 36(1-12) have been extrapolated to the zero load axis

for the graphical determination of ΔX_0 . Likewise the horizontal F line was drawn at the average load between the unloading slopes. The plasticity "p" was then the ratio ($\Delta X_0/\Delta X$). The average value for each specimen is listed in Table 6.

The test record was used to determine the load versus displacement crack mouth opening, diagrammatic illustrations of these test records are shown in Figs. 36(1-12), 37(1-15) and 38(1-14).

The appropriate fracture toughness results incorporated in this thesis were obtained in order to assess the following:

1. The effect of material, test method and size of test specimen on fracture toughness.
2. The effect of material condition on fracture toughness.
3. The effect of crack length on fracture toughness.
4. The effect of microstructure on fracture toughness.

All these results are incorporated in Tables 1-9.

6.4 Three Point Bend Test

Three point bend tests were carried out on Thermodie, Hydrie and Somdie hot work die steel. The specimens were machined from the forged block according to BS.5447.

Dimensions of these specimens including notch depths, root radii and crack length are incorporated in Table 12. After machining the specimens were electro-spark machined to ensure straight crack fronts (Professor J.T. Barnby conversation). Fine notches were produced by using a thin copper foil. Following production, each specimen was measured before being tested. In order to determine the notch depth a shadow-graph was used. Fatigue pre-cracking of the specimens was performed on Amsler vibrophore, crack lengths were measured after the test using a travelling microscope.

A schematic diagram of the test set up is shown in Fig. 34. All the specimens were tested on an Instron testing machine using the 5000 kgf load cell and 10,000 kgf load cell at constant cross-head speed 0.1 and 0.2 mm/min. The three point bend rig illustrated in Plate 1 was used. Span length^{was} four times that of the width and the specimens were supported on free rollers. Before starting any tests, recorder and Instron were warmed up for at least $\frac{1}{2}$ hour, then the load cell was calibrated prior to experiments, a clip gauge was seated on the test piece supported by two knife edges each side of the notch. The test clip gauge was calibrated also.

The test record was used to determine the load versus displacement crack mouth opening, diagrammatic illustrations of these test records are shown in Fig. 39(1-6).



PLATE 1 : General View of Specimen on Machine (Three point bend test)

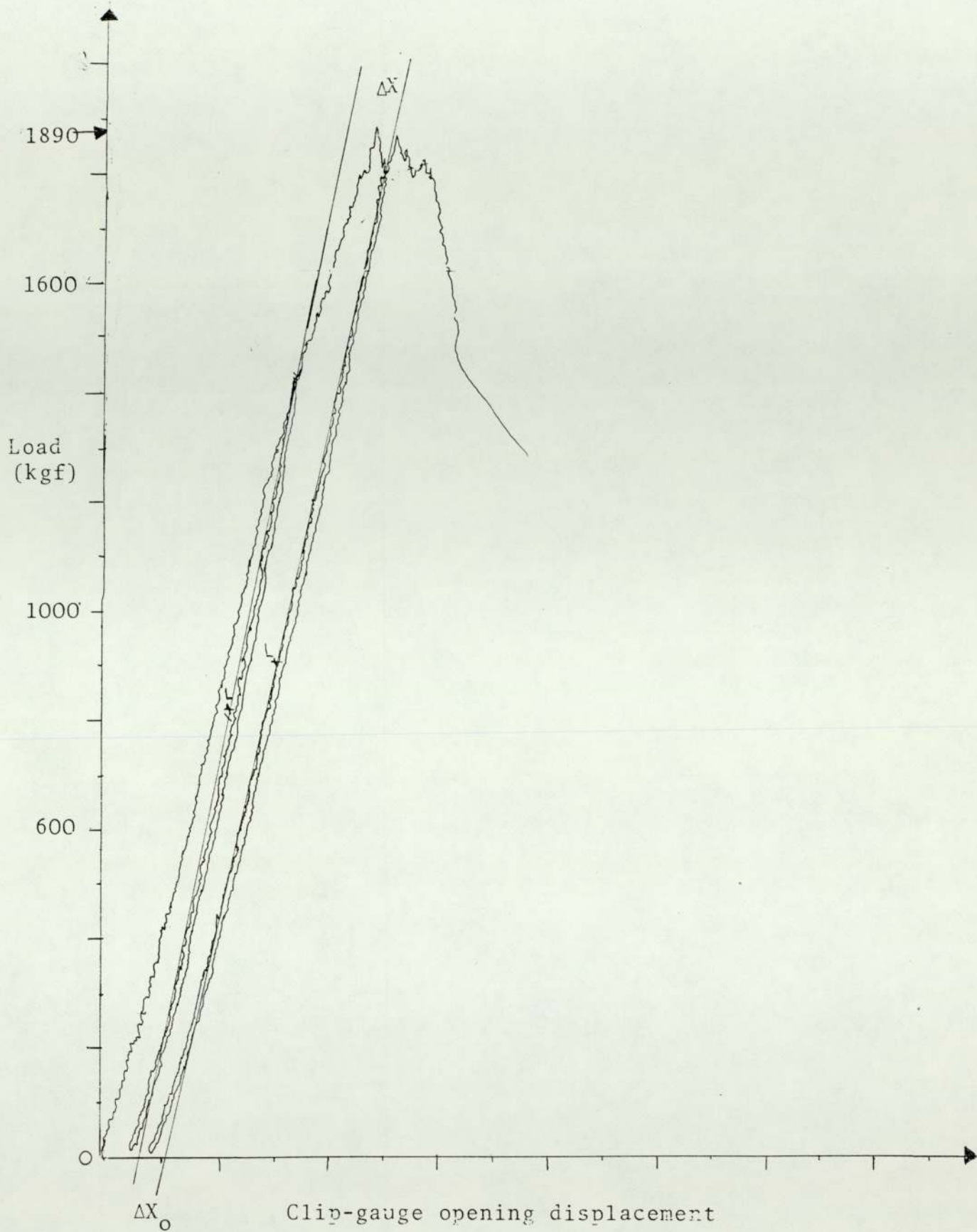


FIGURE 136-1 Force/clip-gauge opening displacement test record for "Electem" steel A0

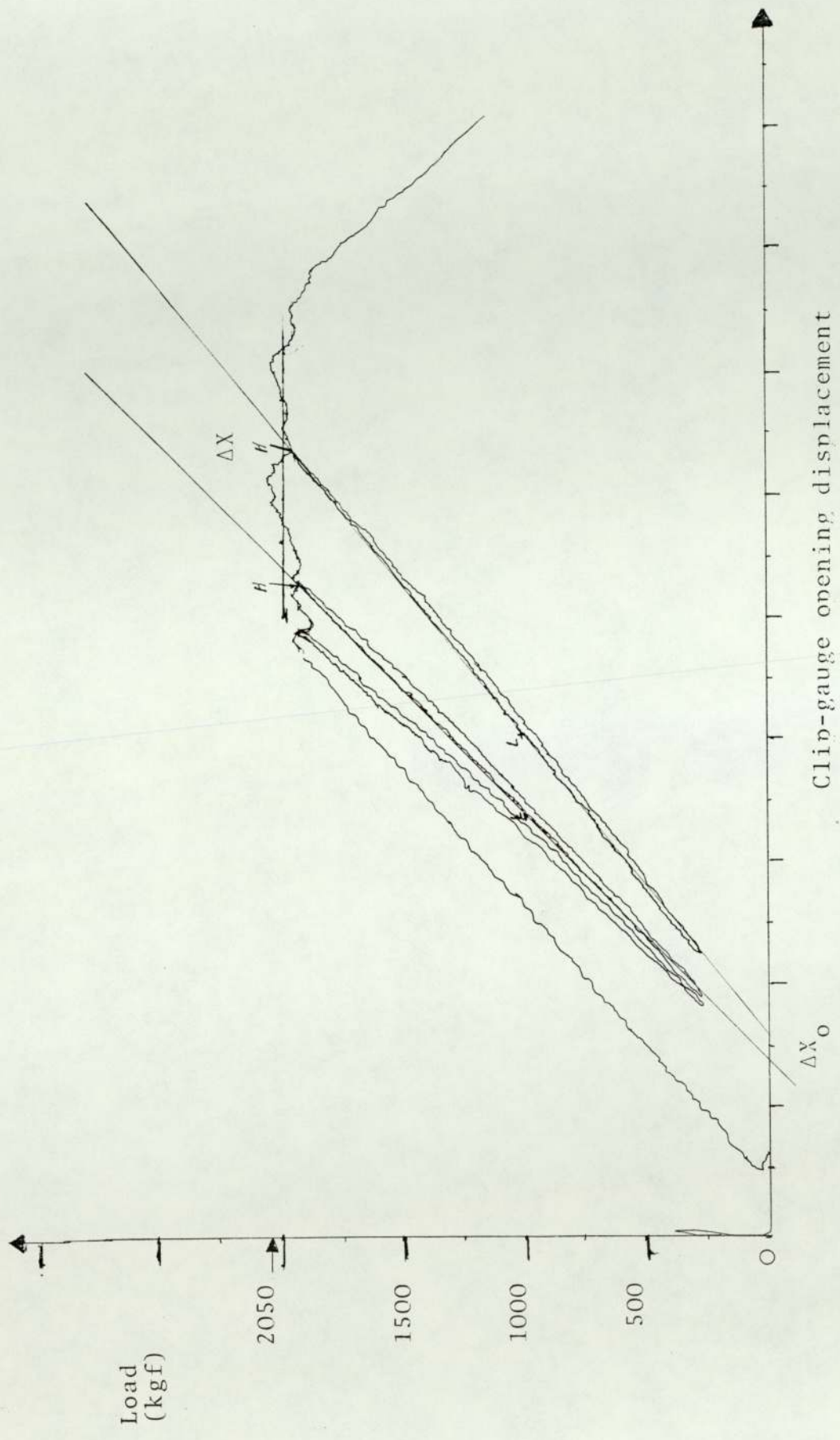


FIGURE 36-2 Force/clip-gauge opening displacement test record for "Electem" BO

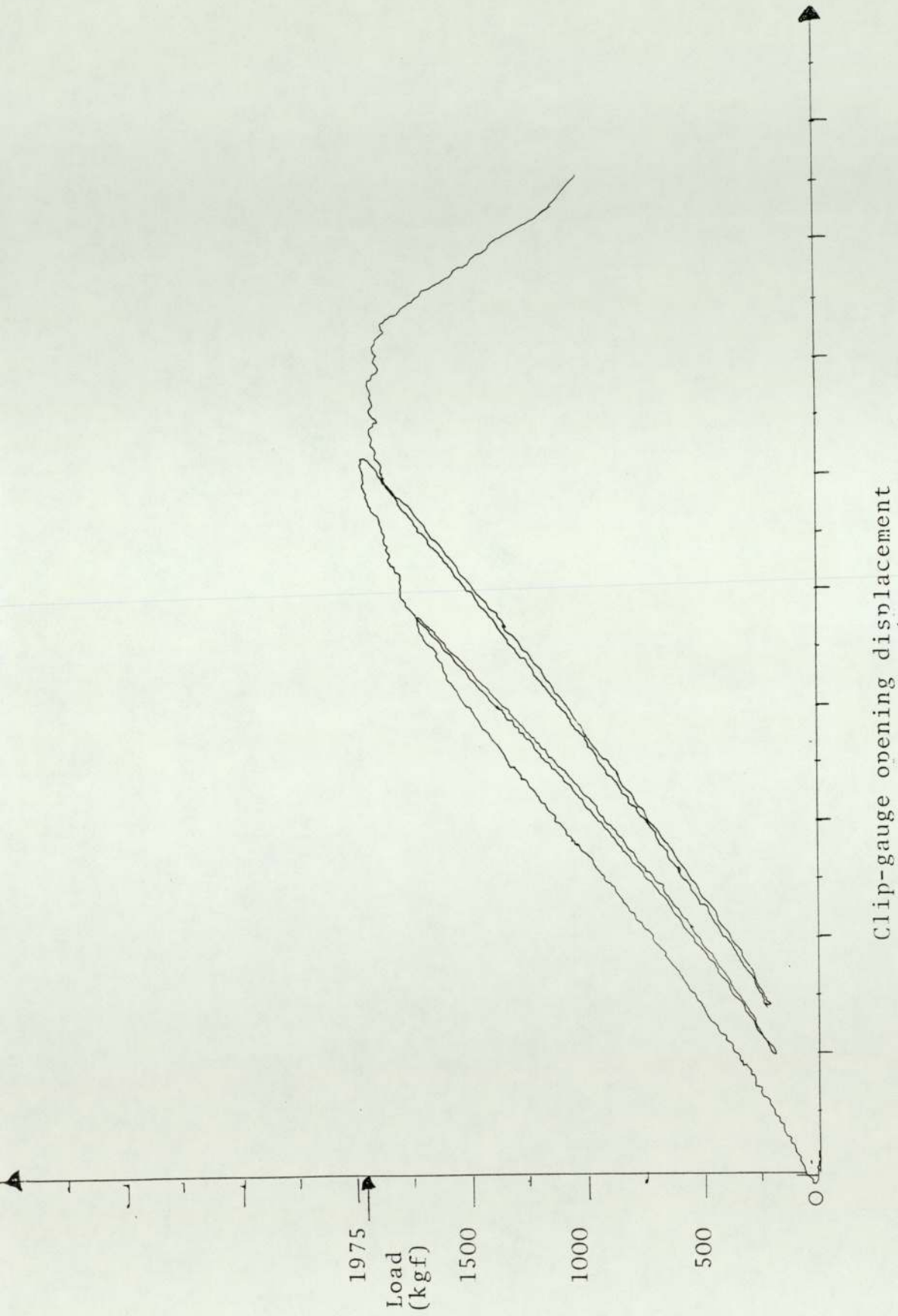


FIGURE 36-3 Force/clip-gauge opening displacement test record for "Somdié" steel CO

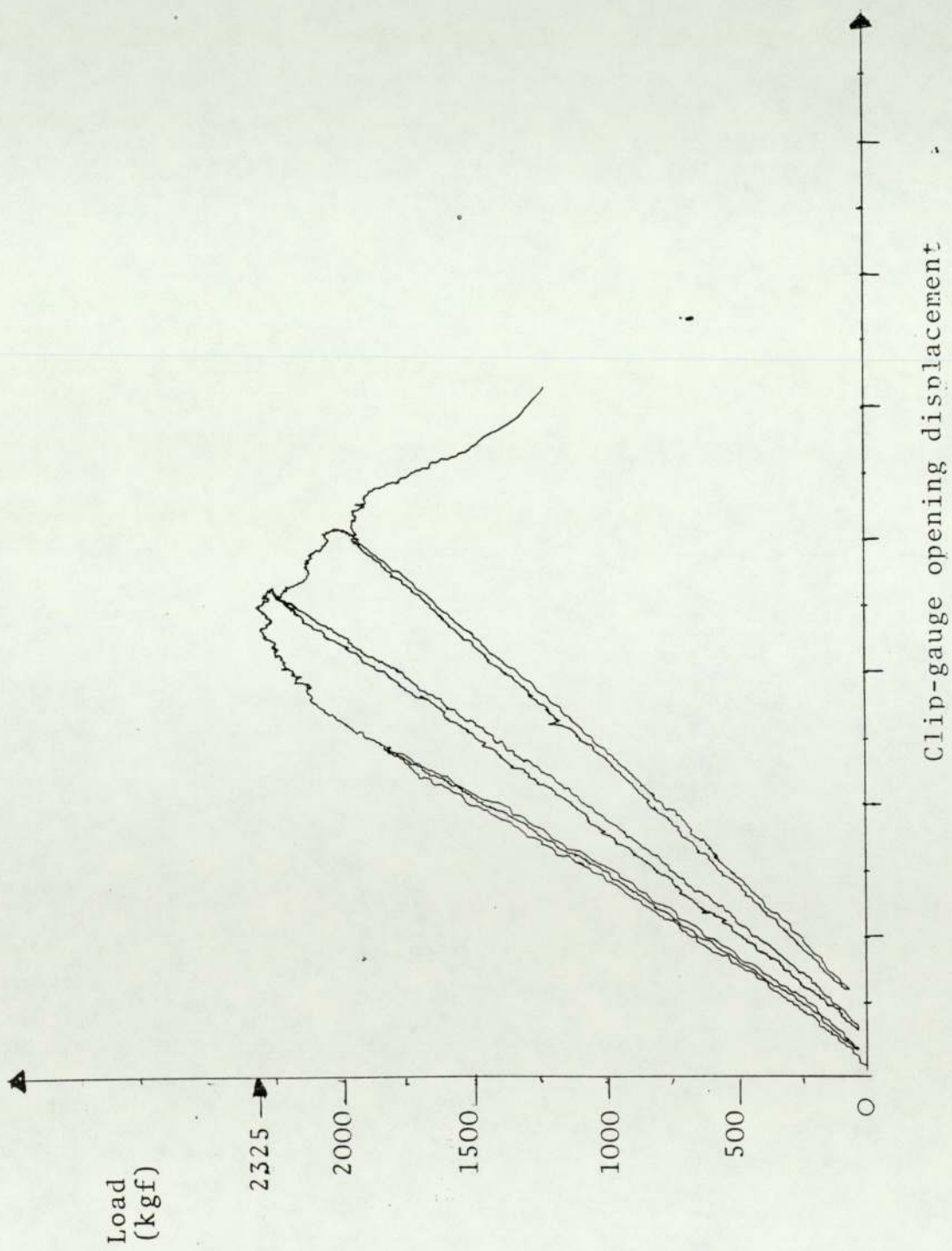
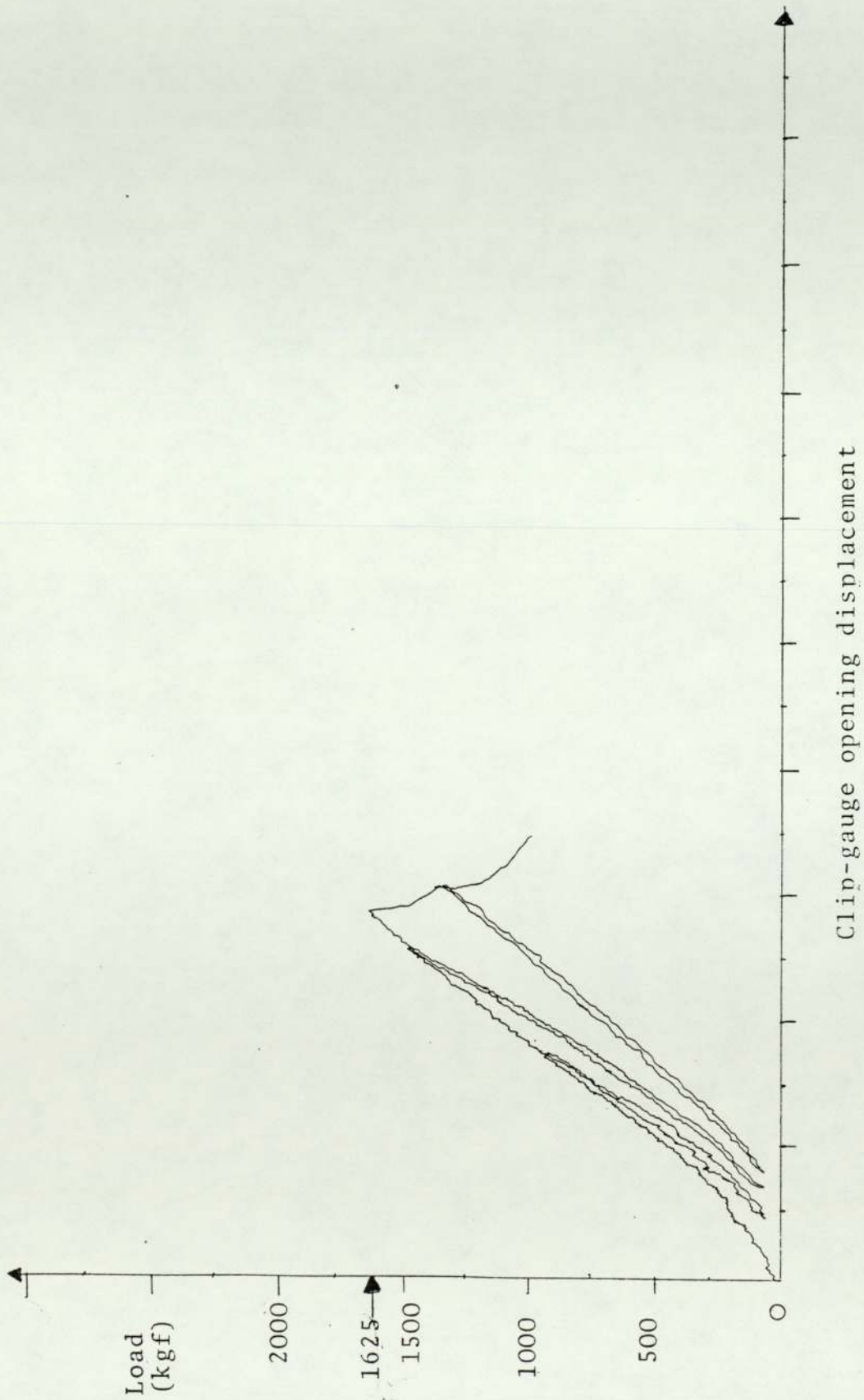
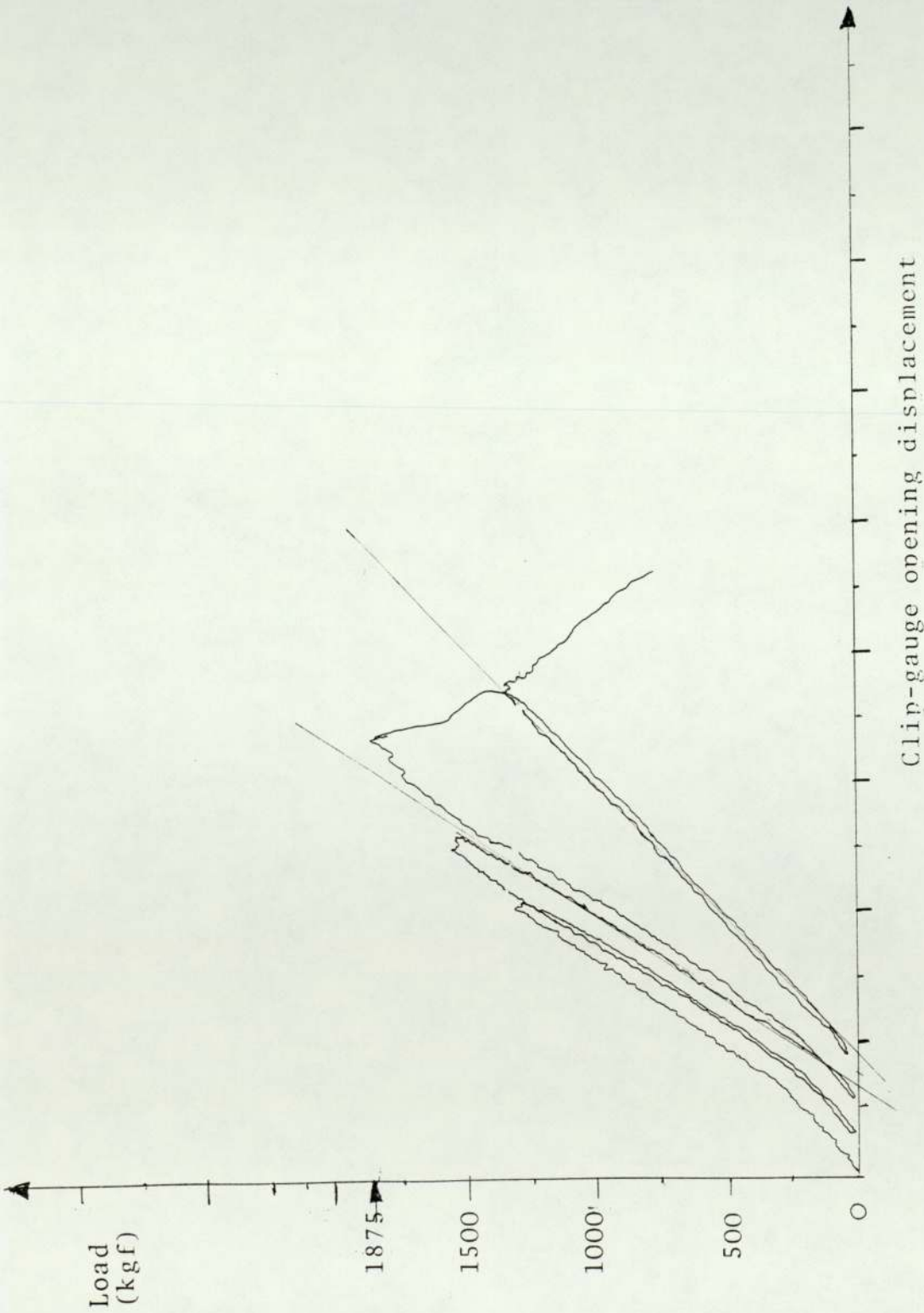


FIGURE 36-4 Force/clip-gauge opening displacement test record for "Somdie" steel D0



Clip-gauge opening displacement

FIGURE 36-5 Force/clip-gauge opening displacement test record for "Electem" steel BM



Clip-gauge opening displacement

FIGURE 36-6 Force/clip-gauge opening displacement test record for "Somdic" steel CM

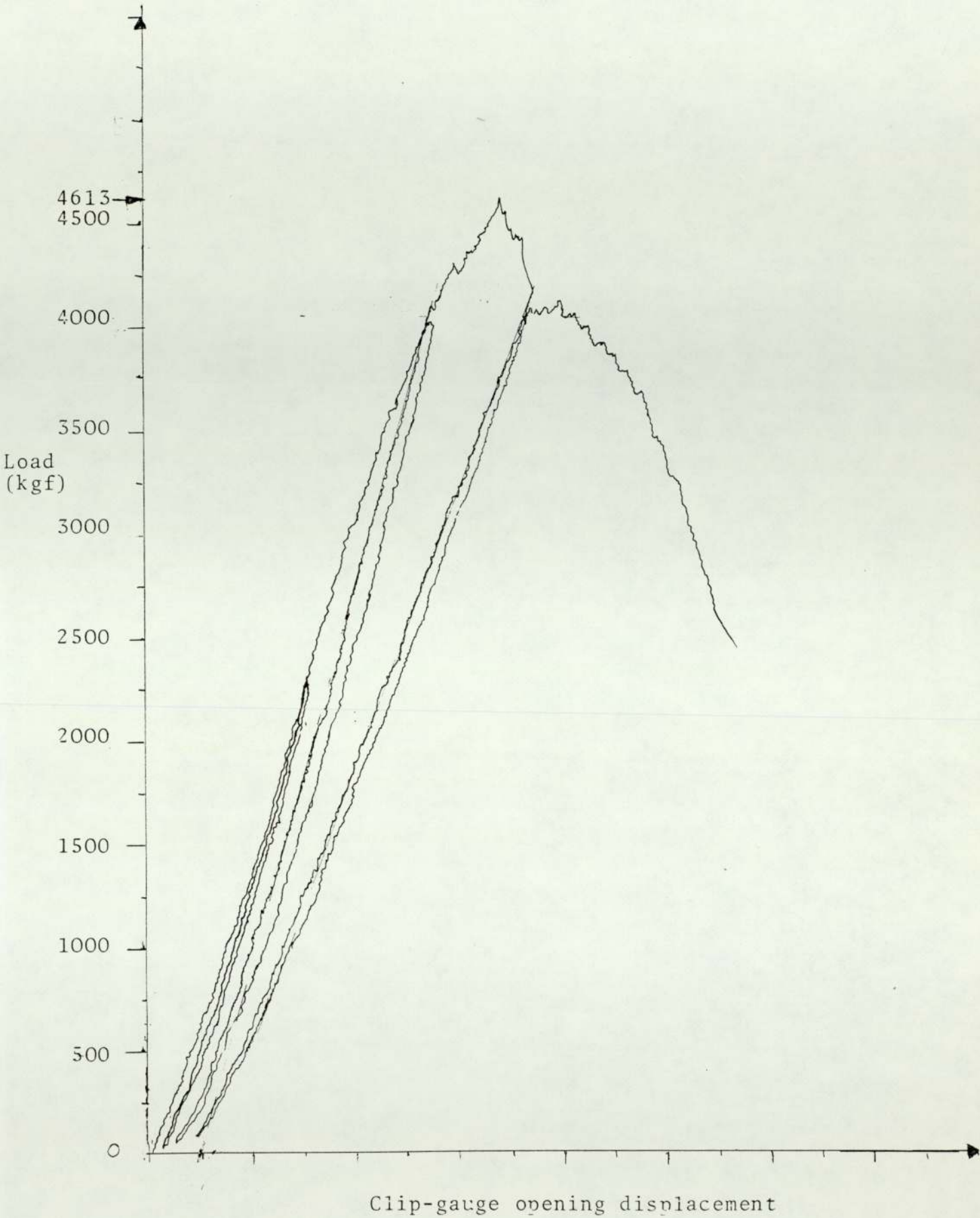


FIGURE 36-7 Force/clip-gauge opening displacement record test for "Somdie" steel DM

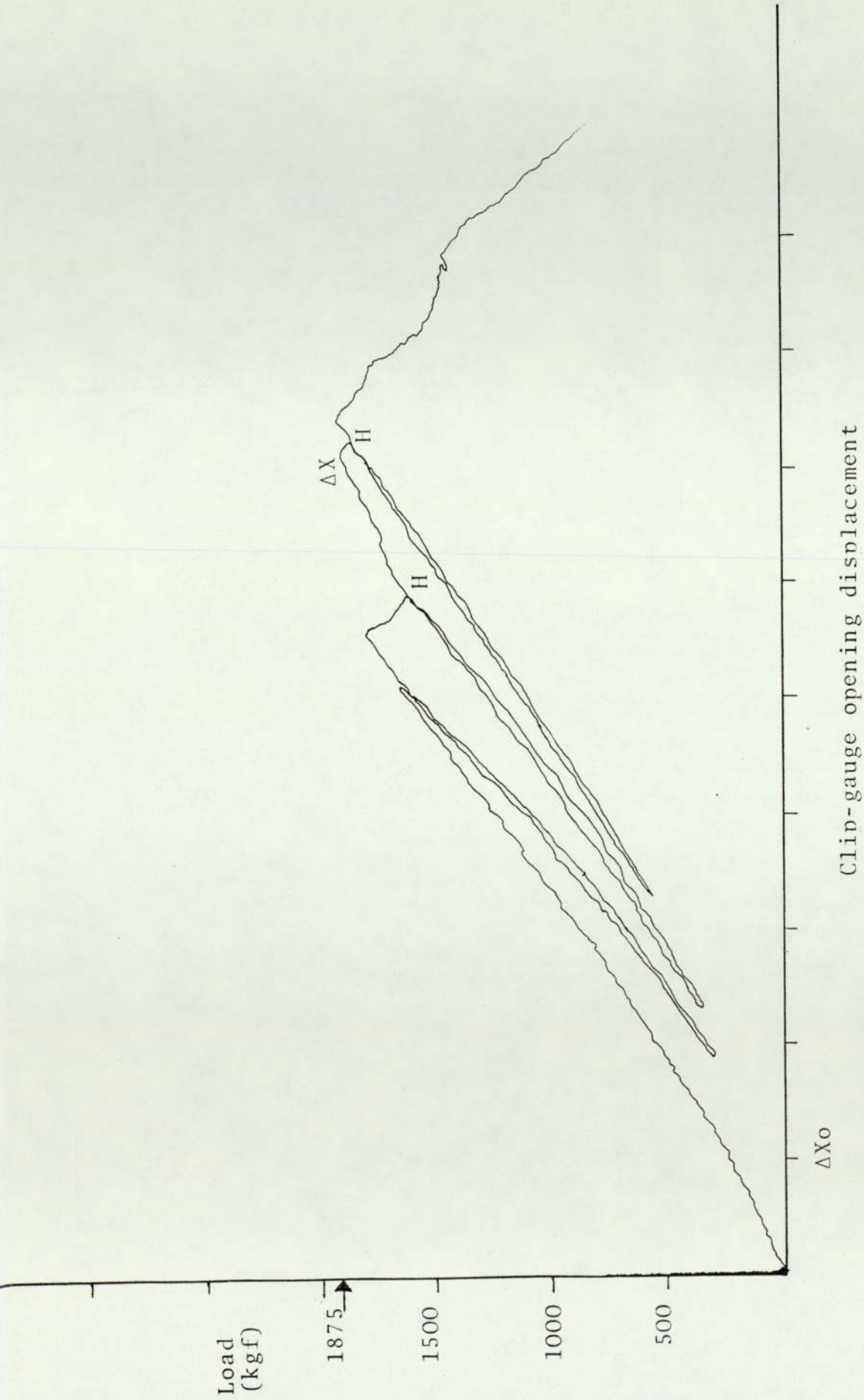


FIGURE 36-8 Force/clip-gauge opening displacement test record for "Electem" steel AC

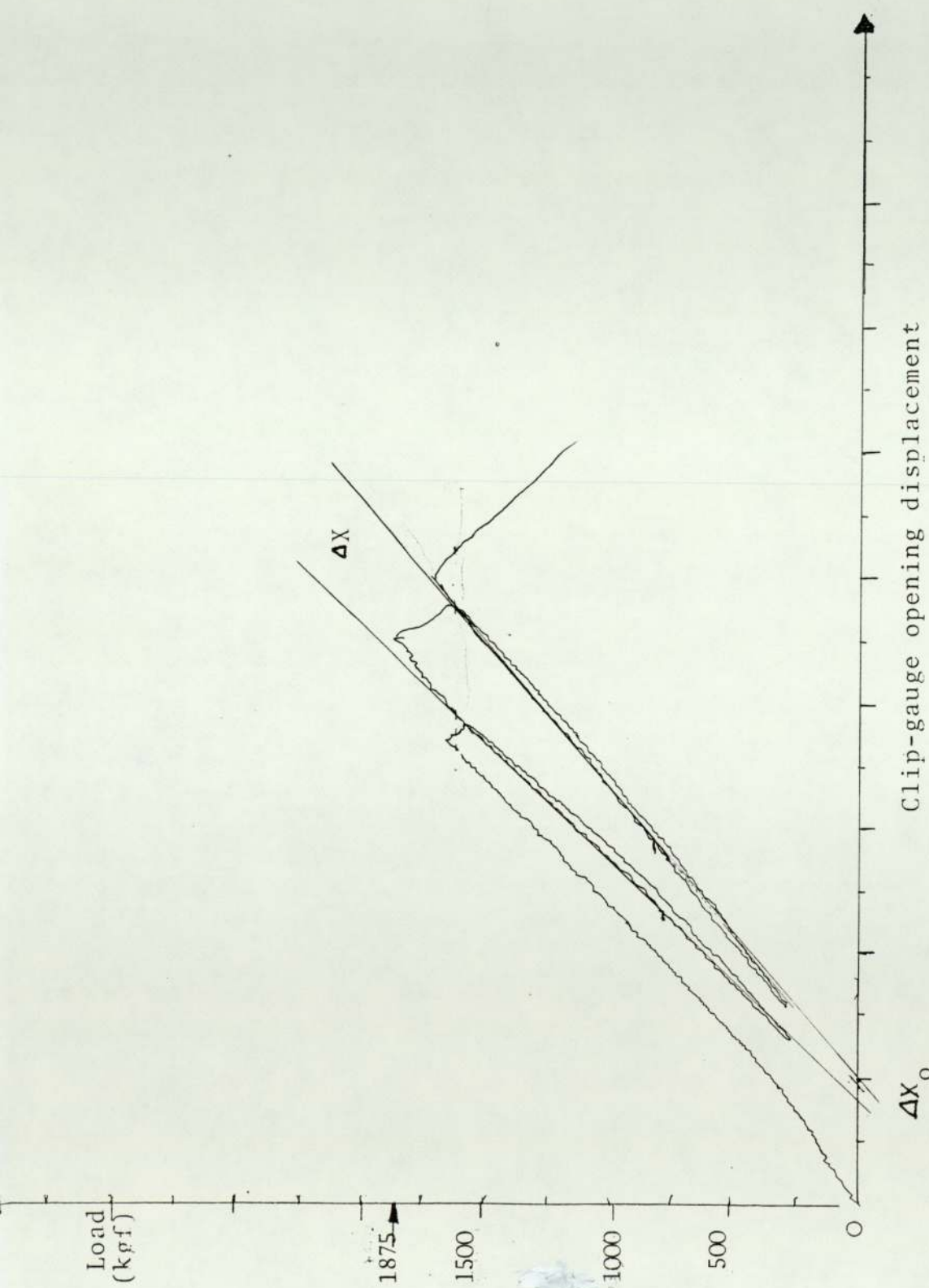
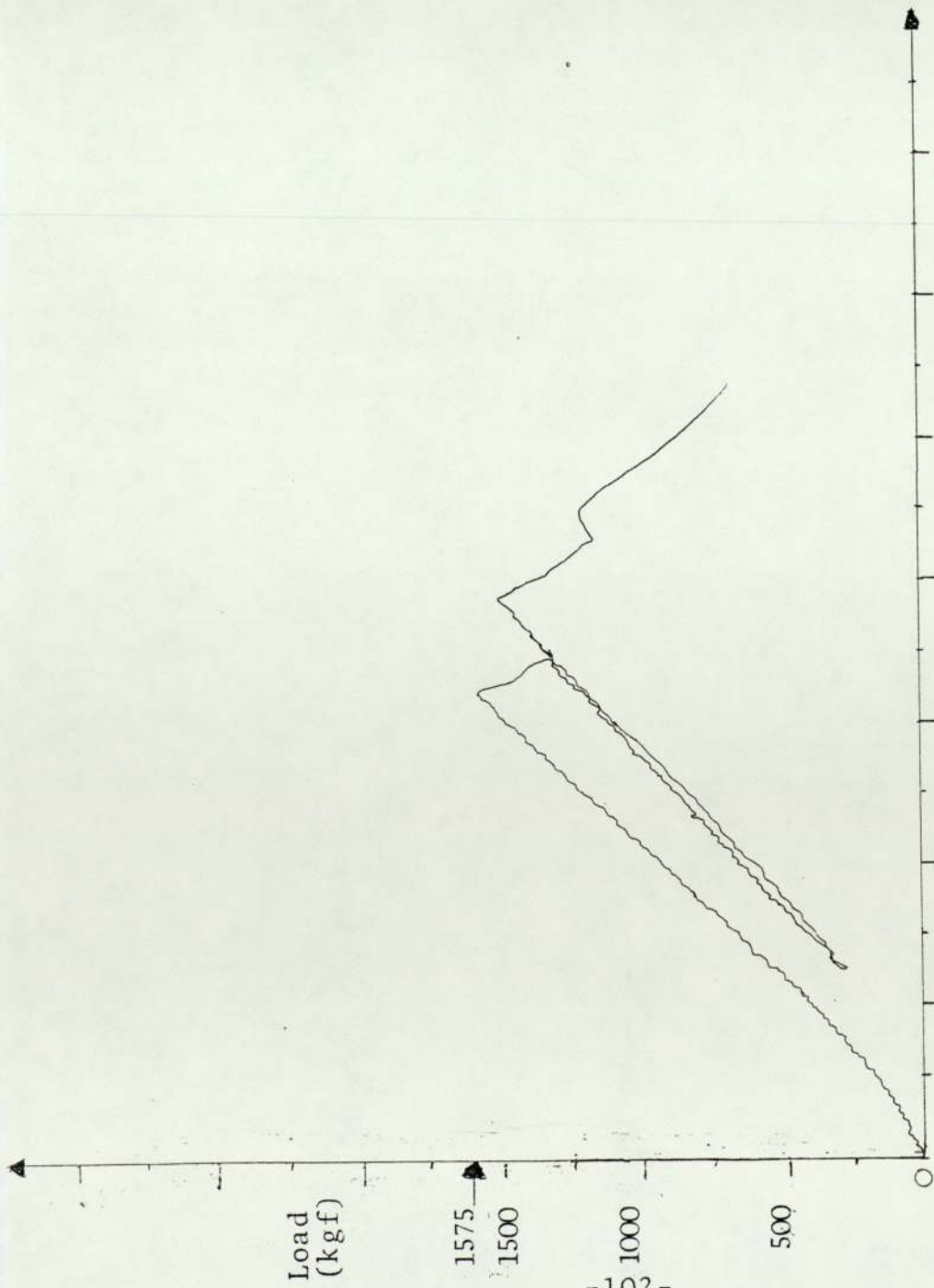
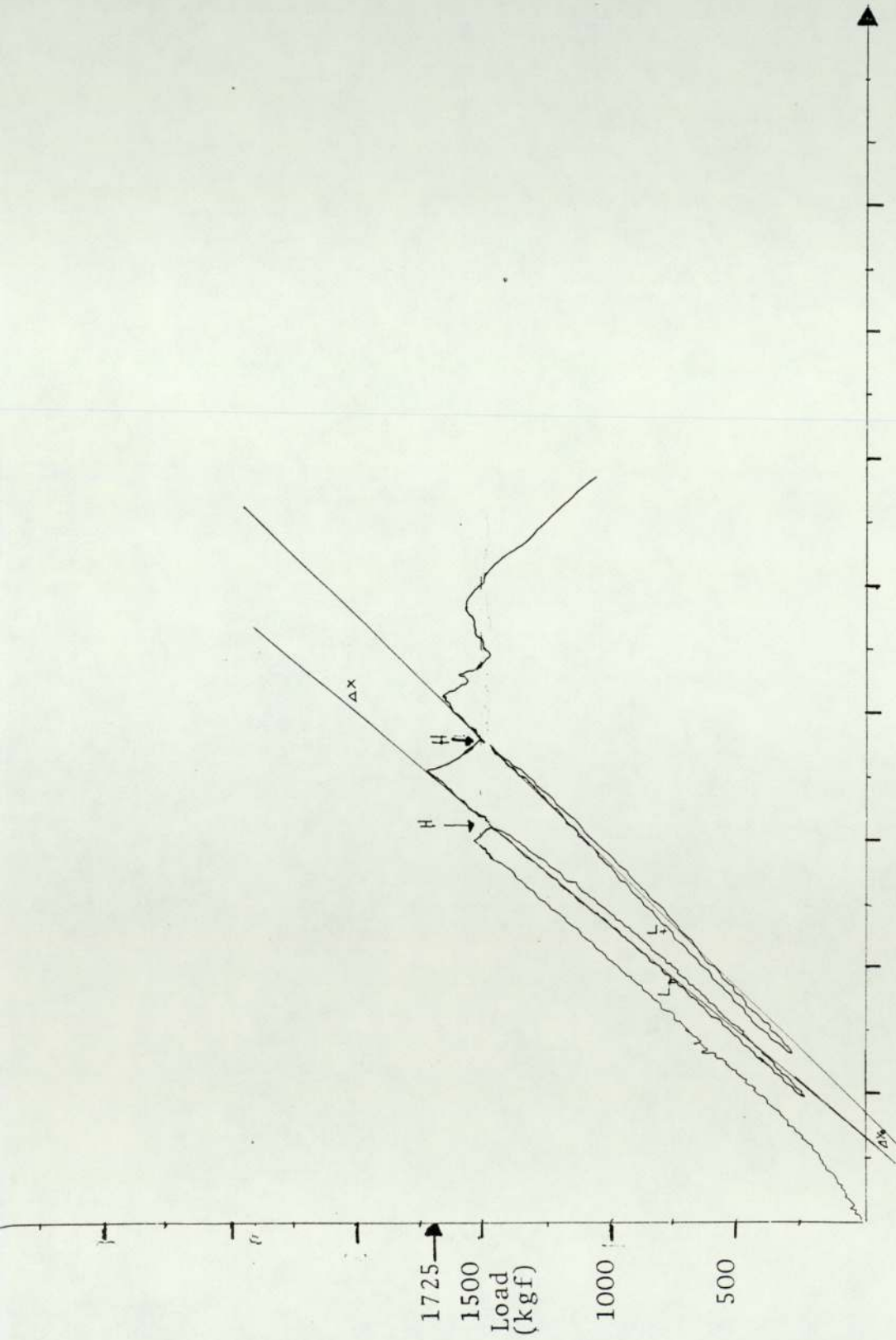


FIGURE 36-9 Load/clip-gauge opening displacement test record for "Electer" steel BC



Clip-gauge opening displacement

FIGURE 36-10 Force/clip-gauge opening displacement test record for "Somdie" steel CC



Clip-gauge opening displacement

FIGURE 36-11 Force/clip-gauge opening displacement test record for "Somdie" steel DC

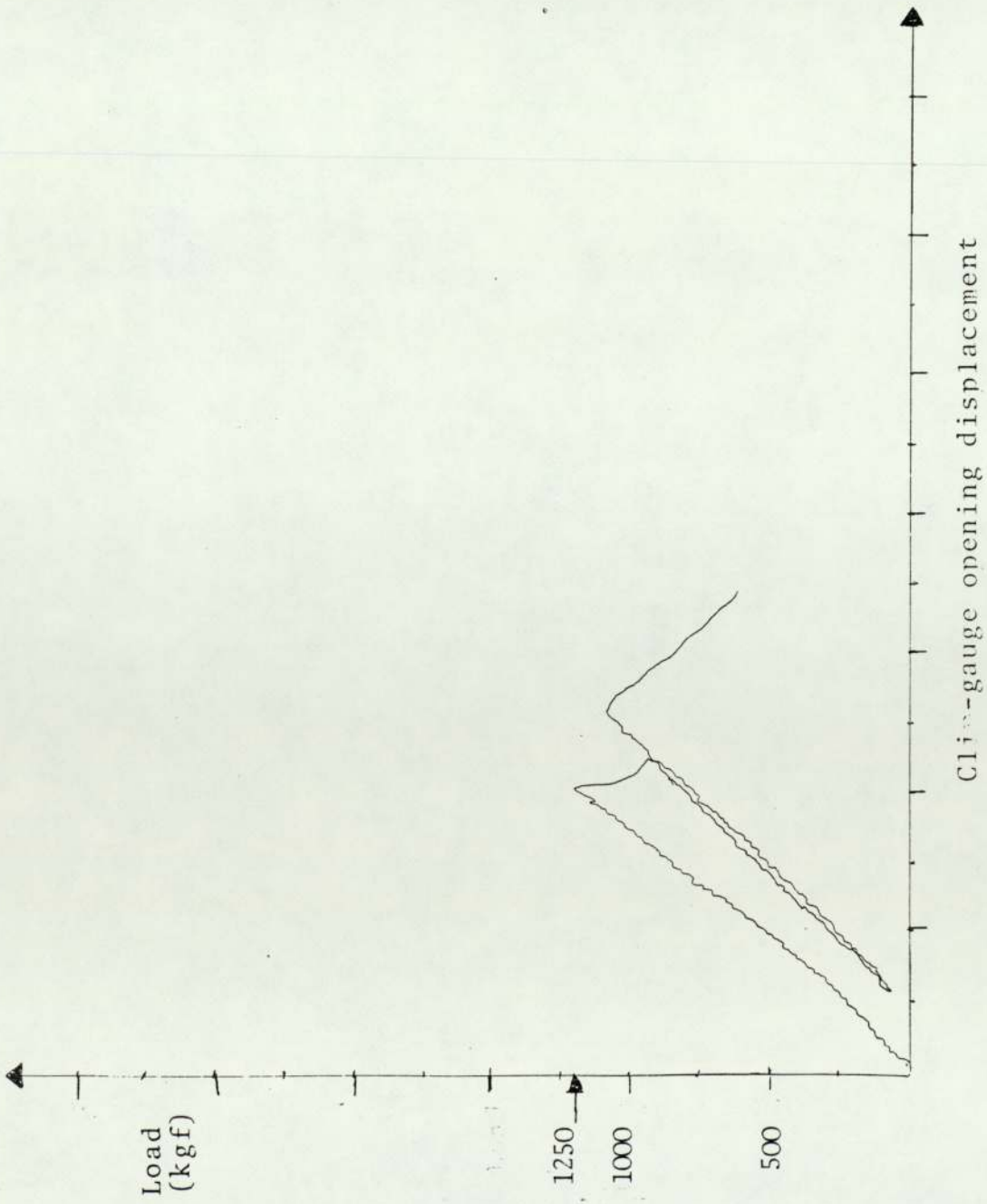


FIGURE 36-12 Force/clip-gauge opening displacement test record for "Thermodie" steel EC

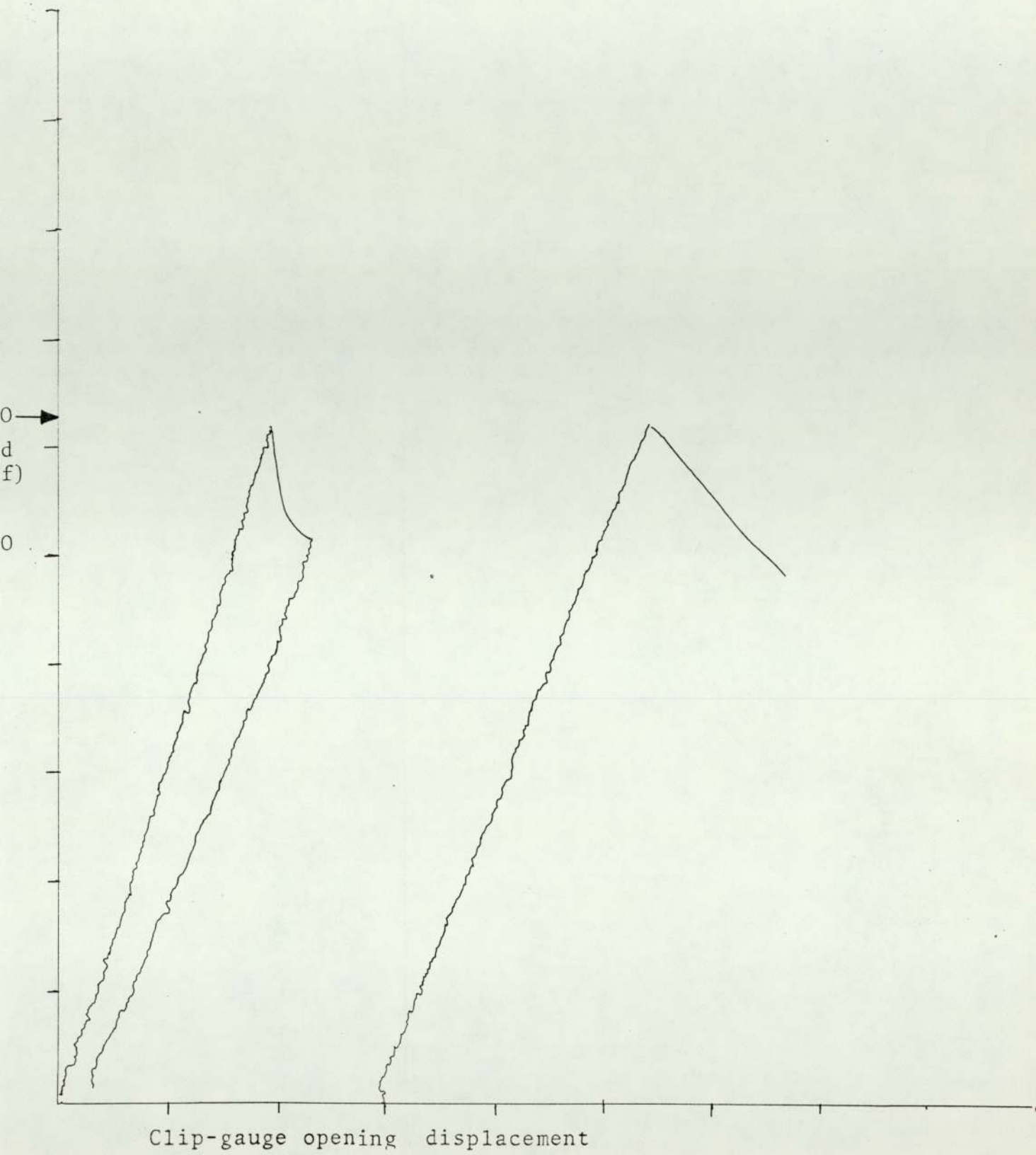


FIGURE 37-1 Force/clip-gauge opening displacement test record for "Hydie" H10

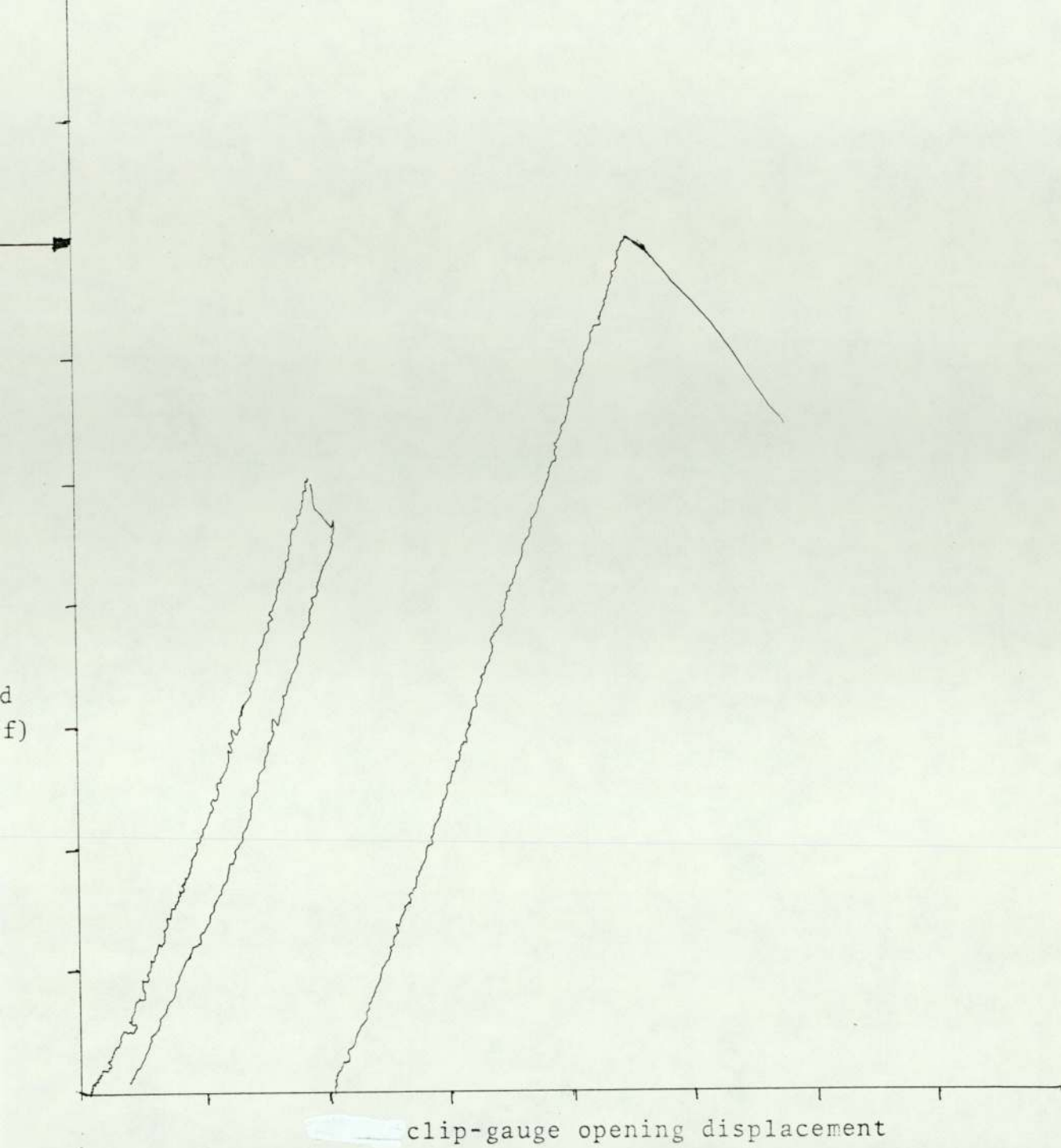


FIGURE 37-2 Force/clip-opening displacement test record for "Hydie" steel H1M

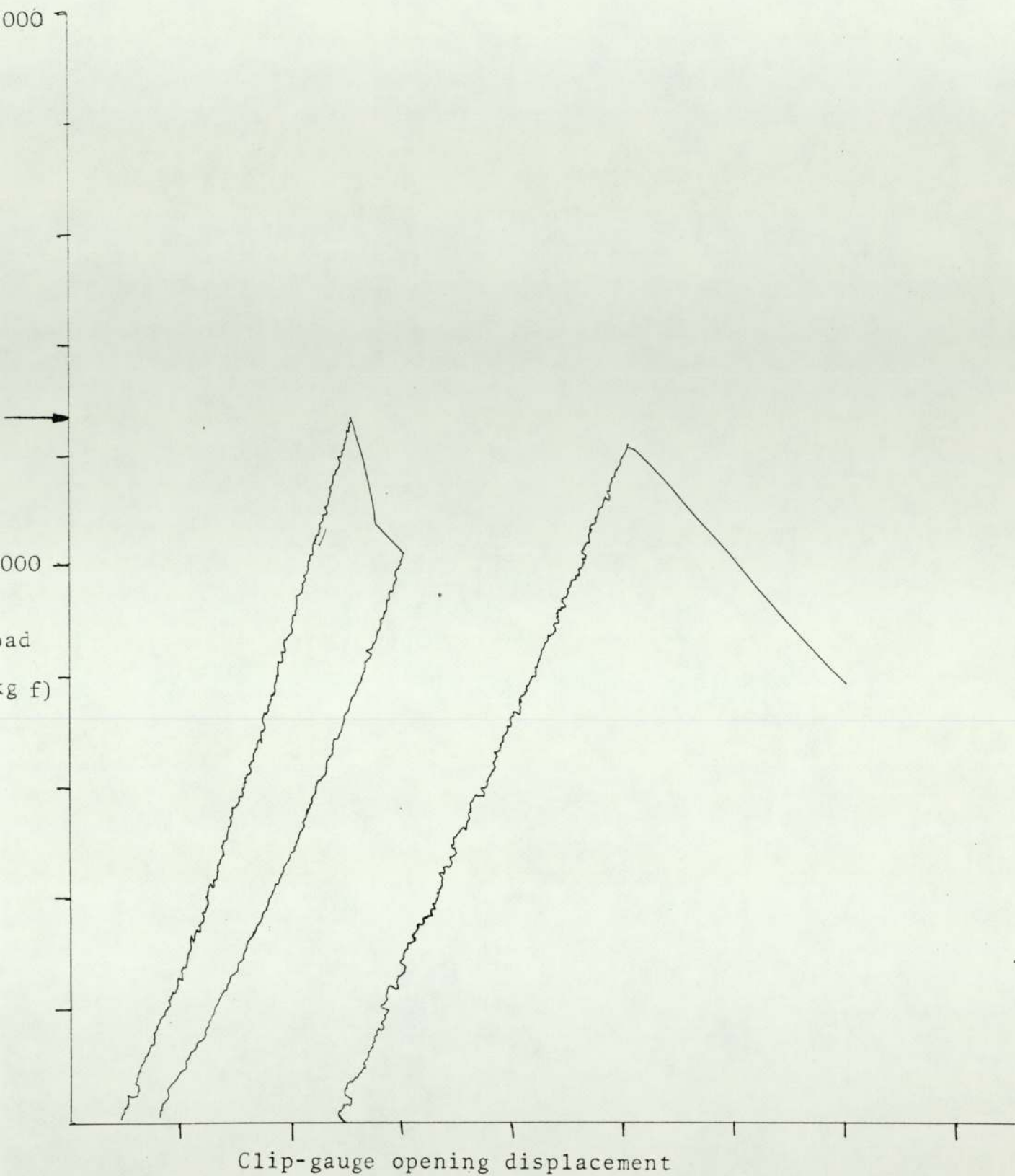


FIGURE 37-3 Force/clip-gauge opening displacement test record for "Hydie" steel H1C

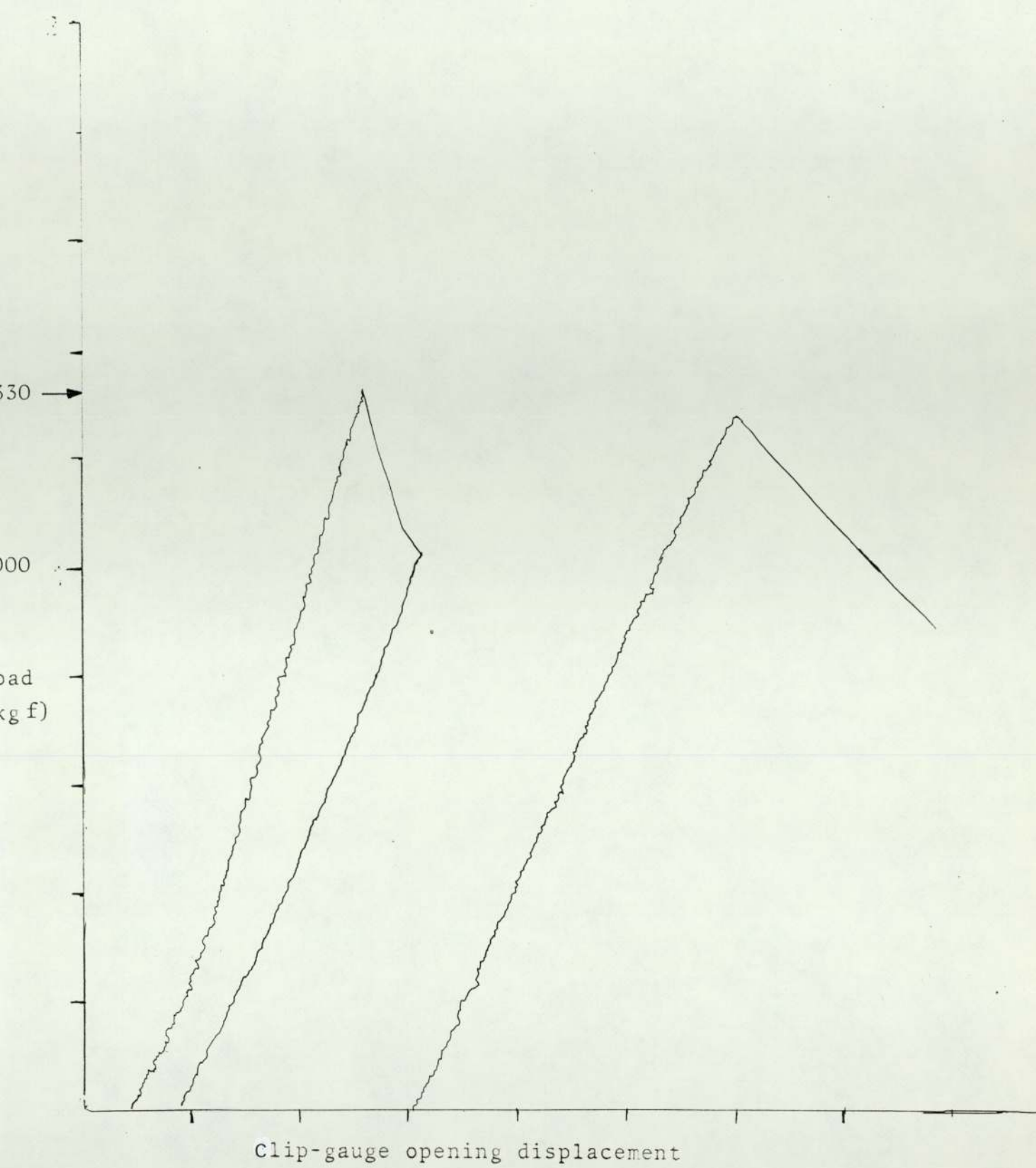


FIGURE 37-4 Force/clip-gauge opening displacement test record for "Hydie" steel H1A

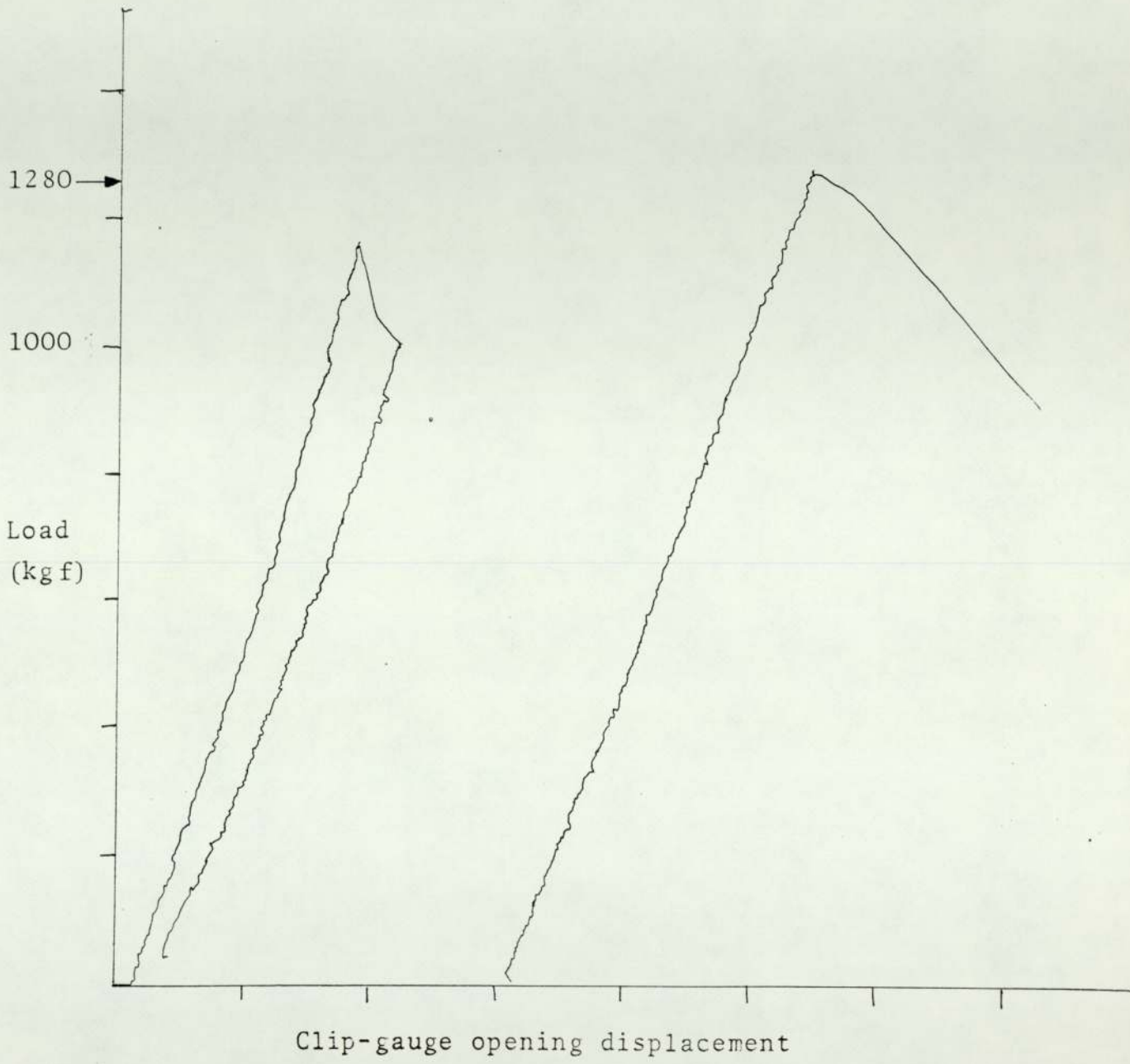


FIGURE 37-5 Force/clip-gauge opening displacement test record for "Hydie" H1B

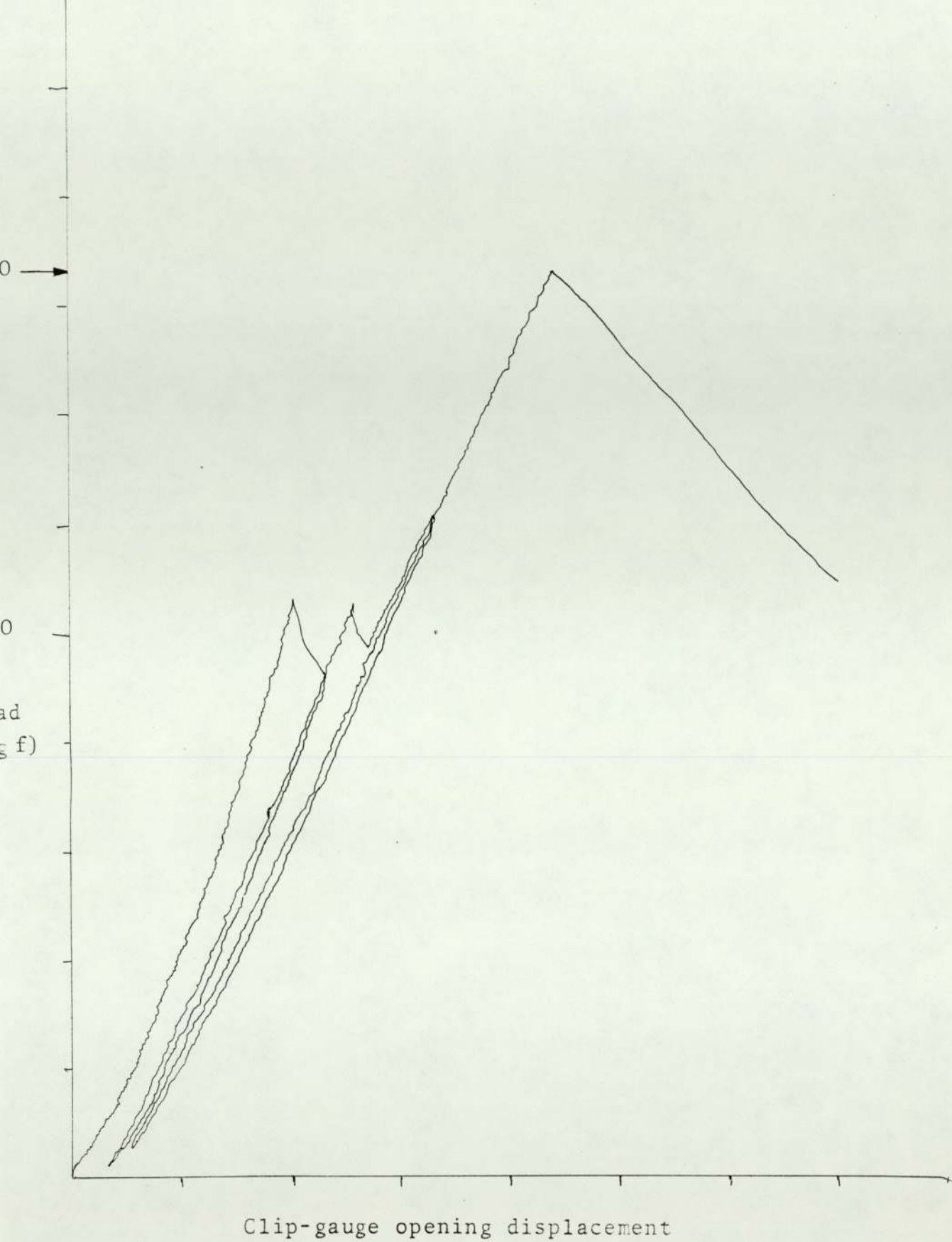


FIGURE 37-6 Force/clip-gauge opening displacement test record for "Hydie" steel H20

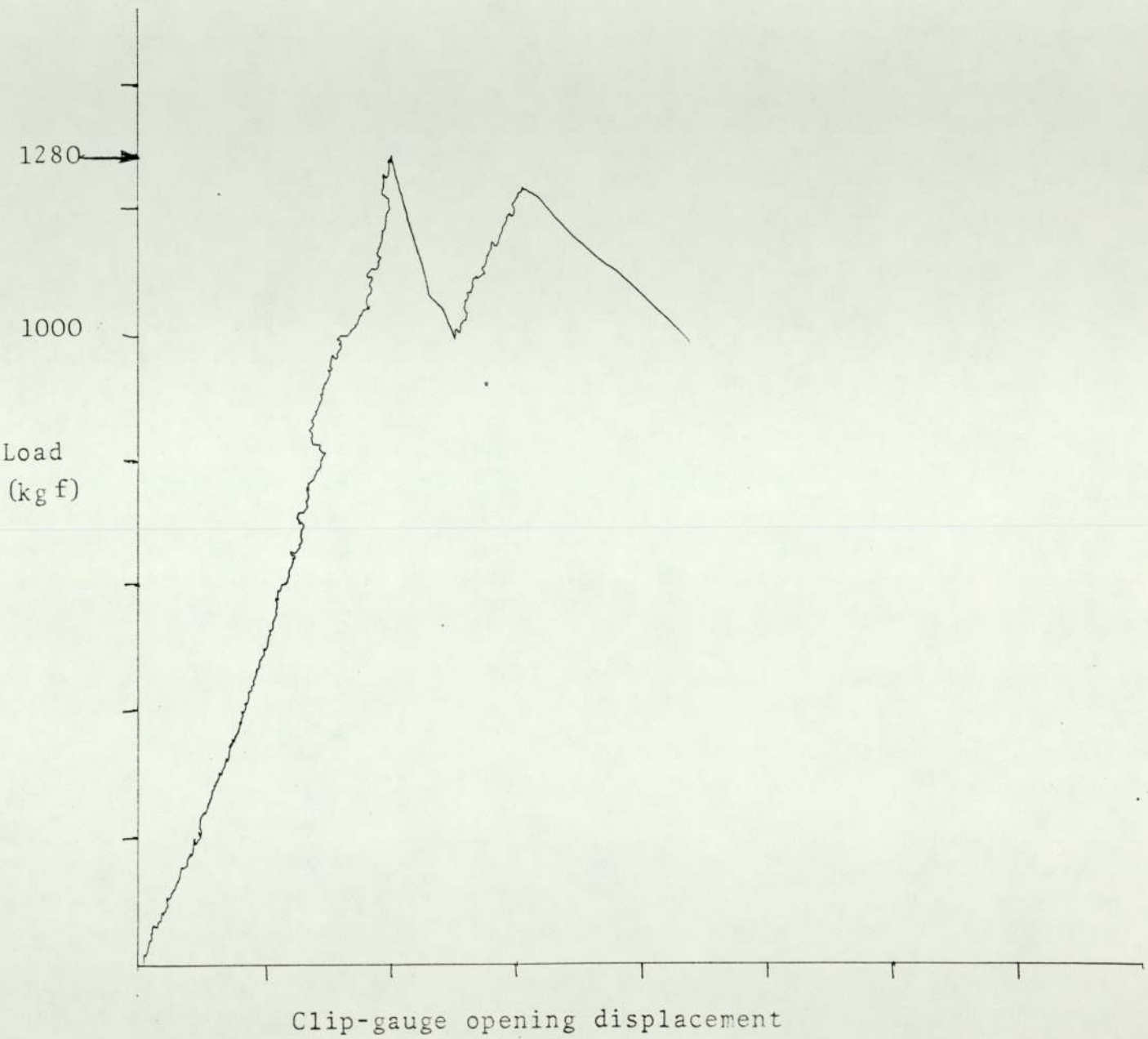


FIGURE 37-7 Force/clip-gauge opening displacement test record for "Hydie" Steel H2M

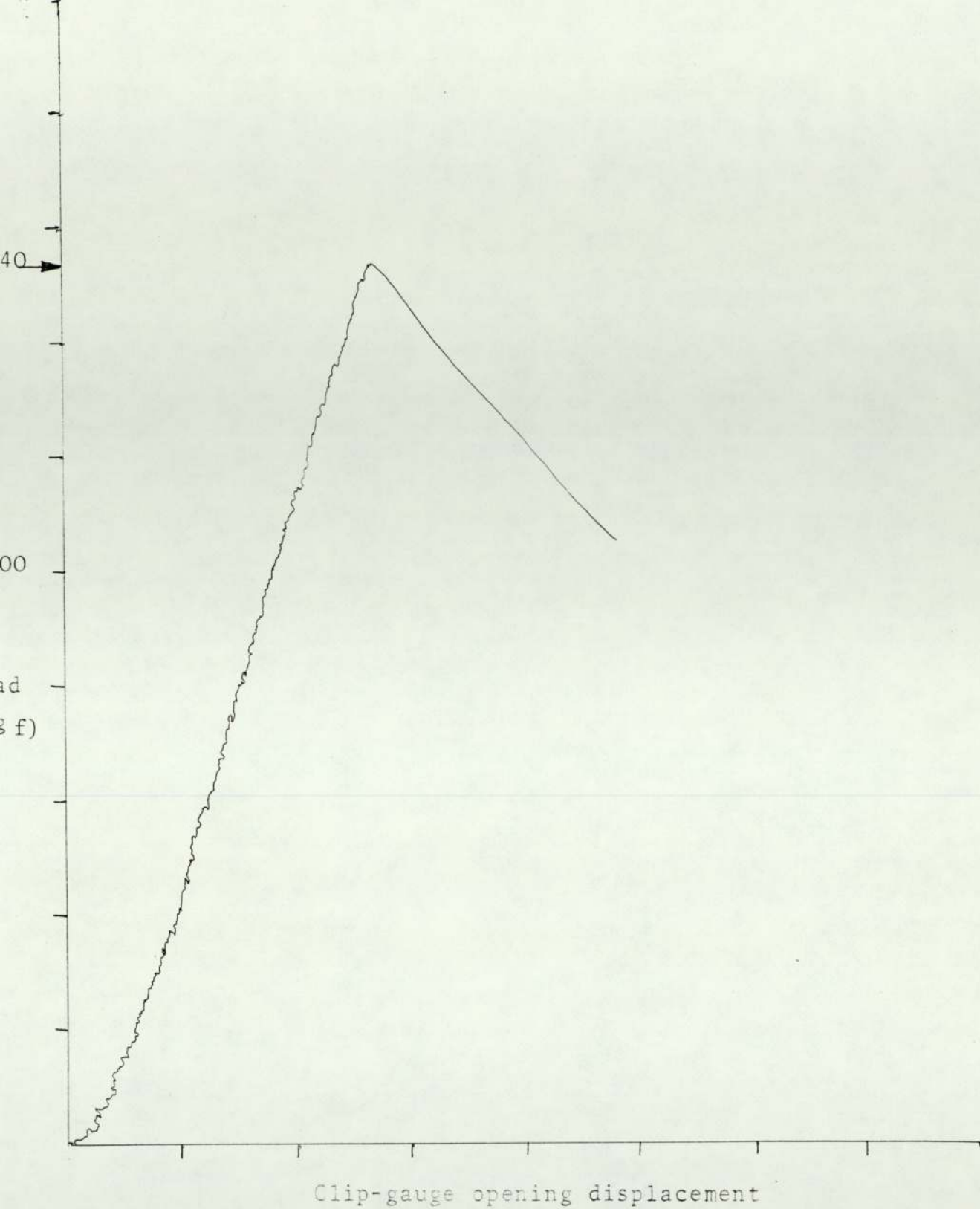


FIGURE 37-8 Force/clip-gauge opening displacement test record for "Hydie" steel H2C

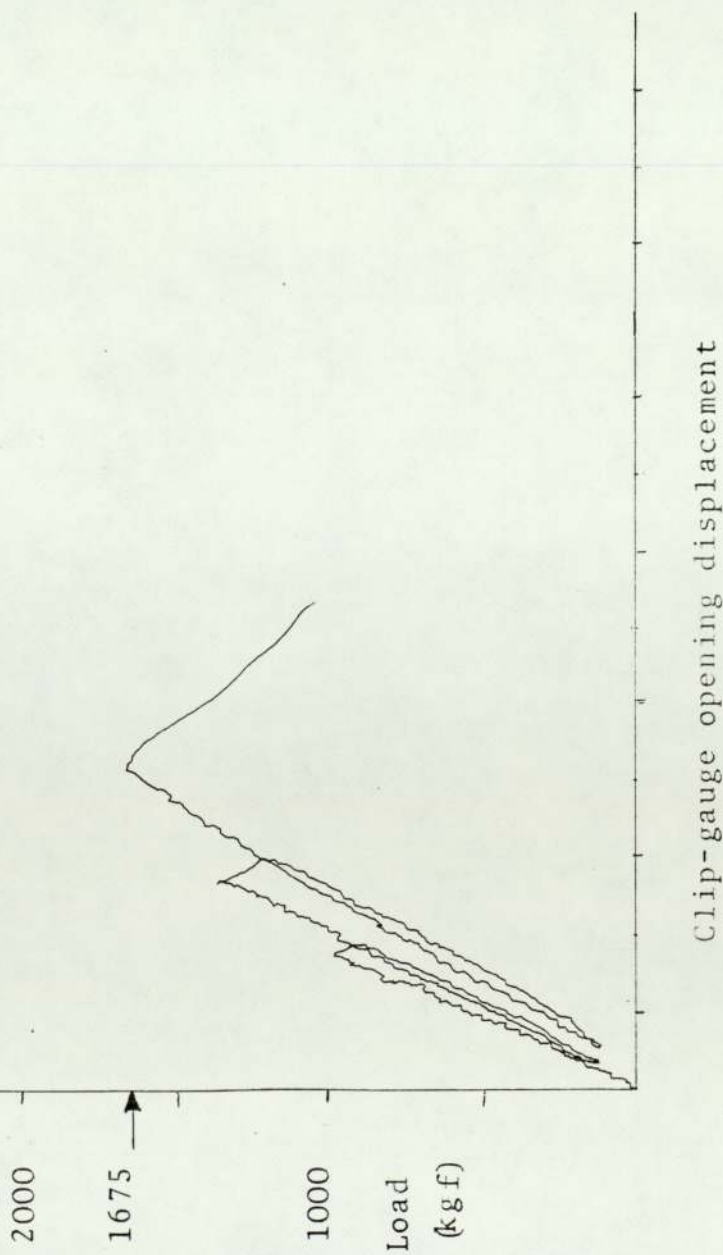


FIGURE 37-9 Force/clip-gauge opening displacement test record for "Hydie" steel H2A

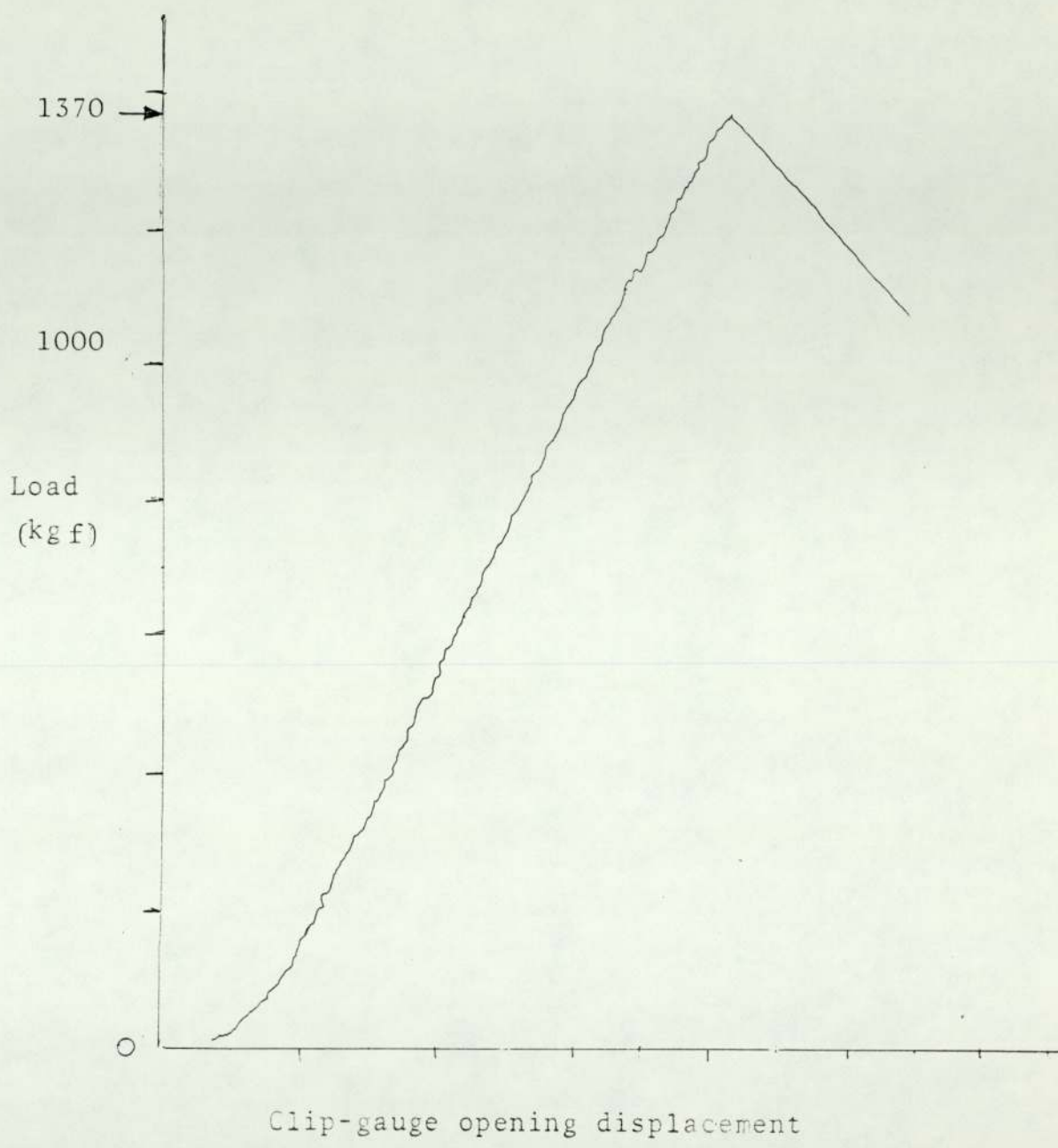
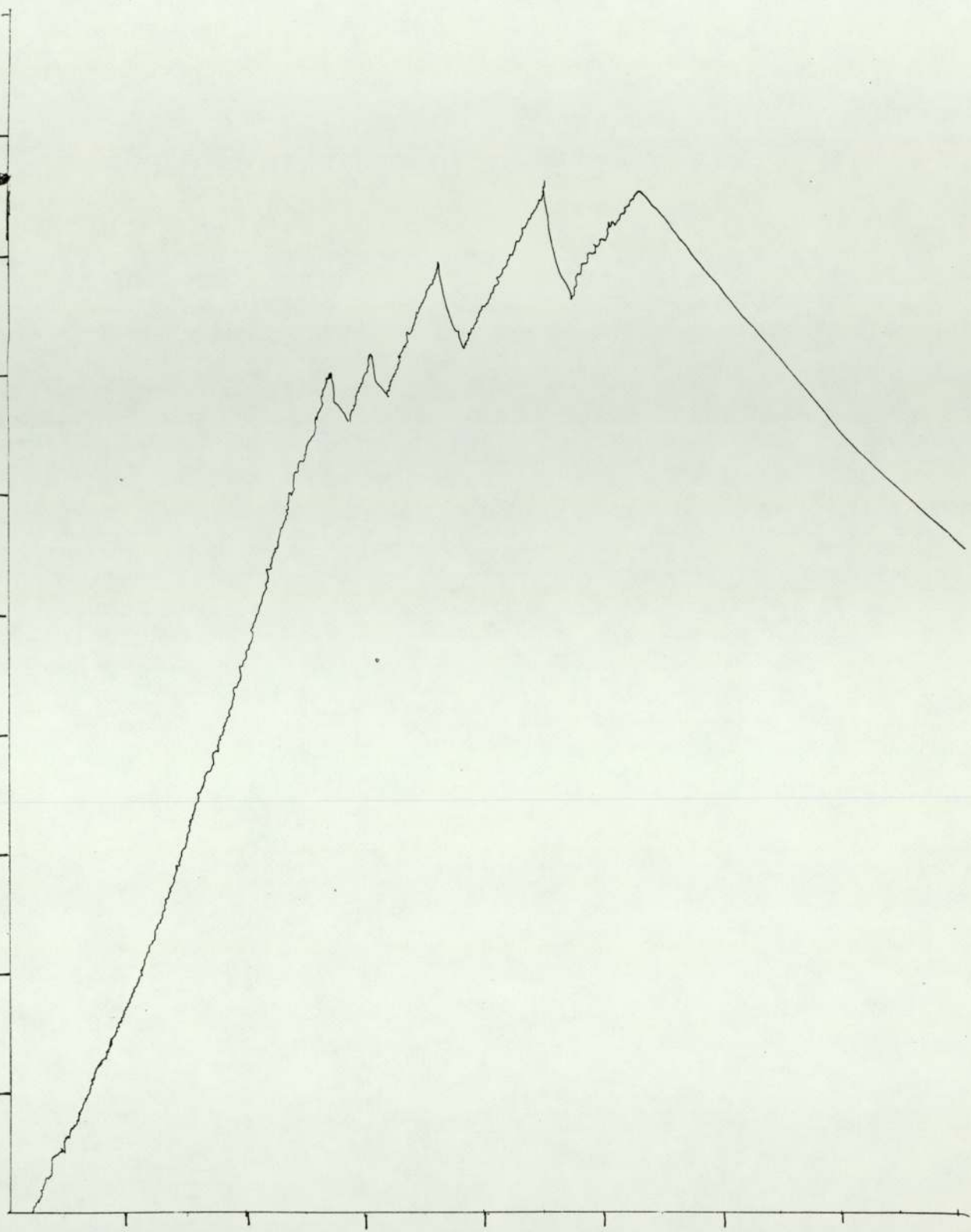


FIGURE 37-10 Force/clip-gauge opening displacement test record for "Hydie" steel H2B

1710

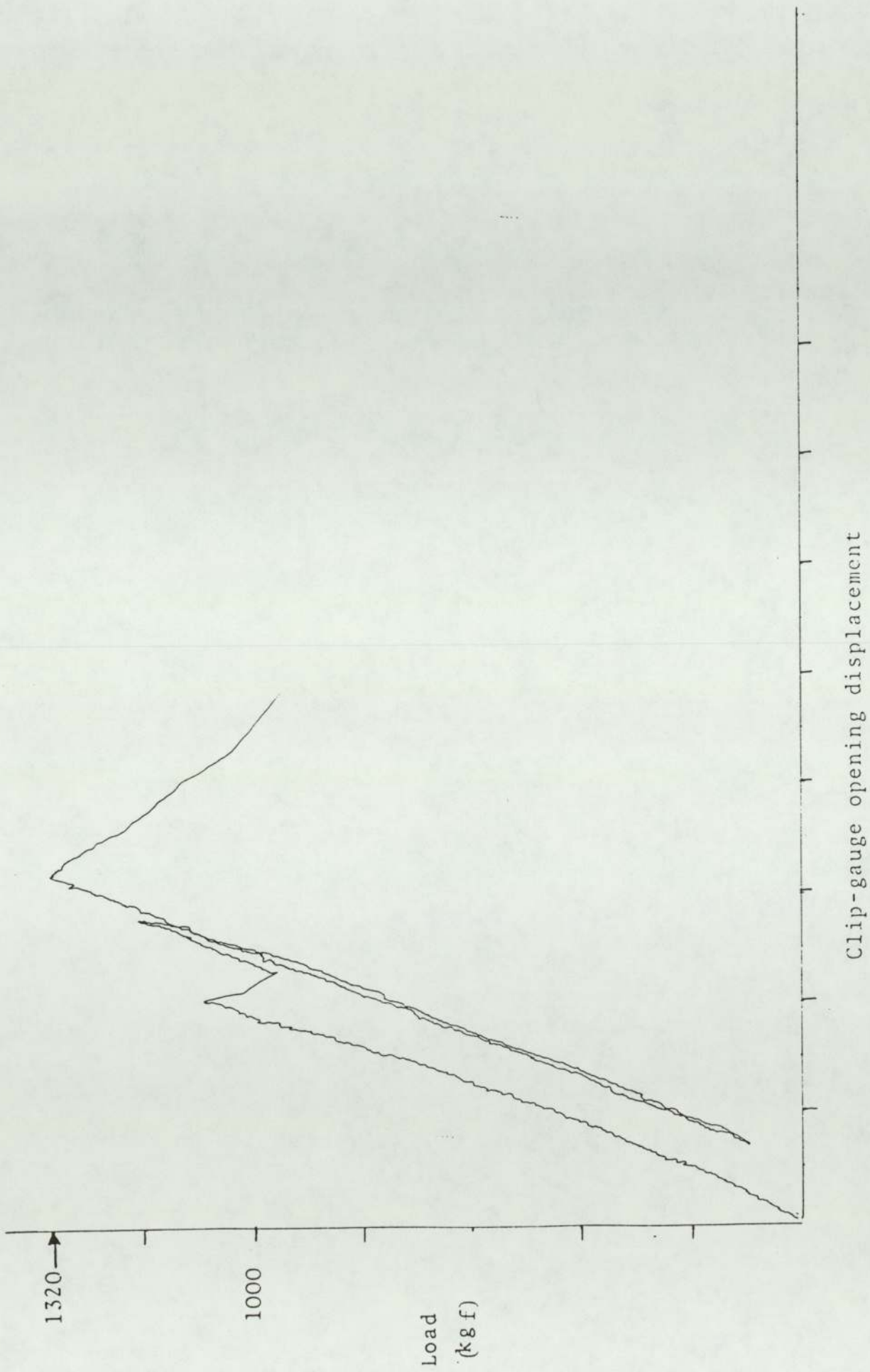
1000

oad
(kg f)



Clip-gauge opening displacement

FIGURE 37-11 Force/clip-gauge opening displacement test record for "Hydie" steel H30



Clip-gauge opening displacement

FIGURE 37-12 Force/clip-gauge opening displacement test record for "Hydic" steel H3M

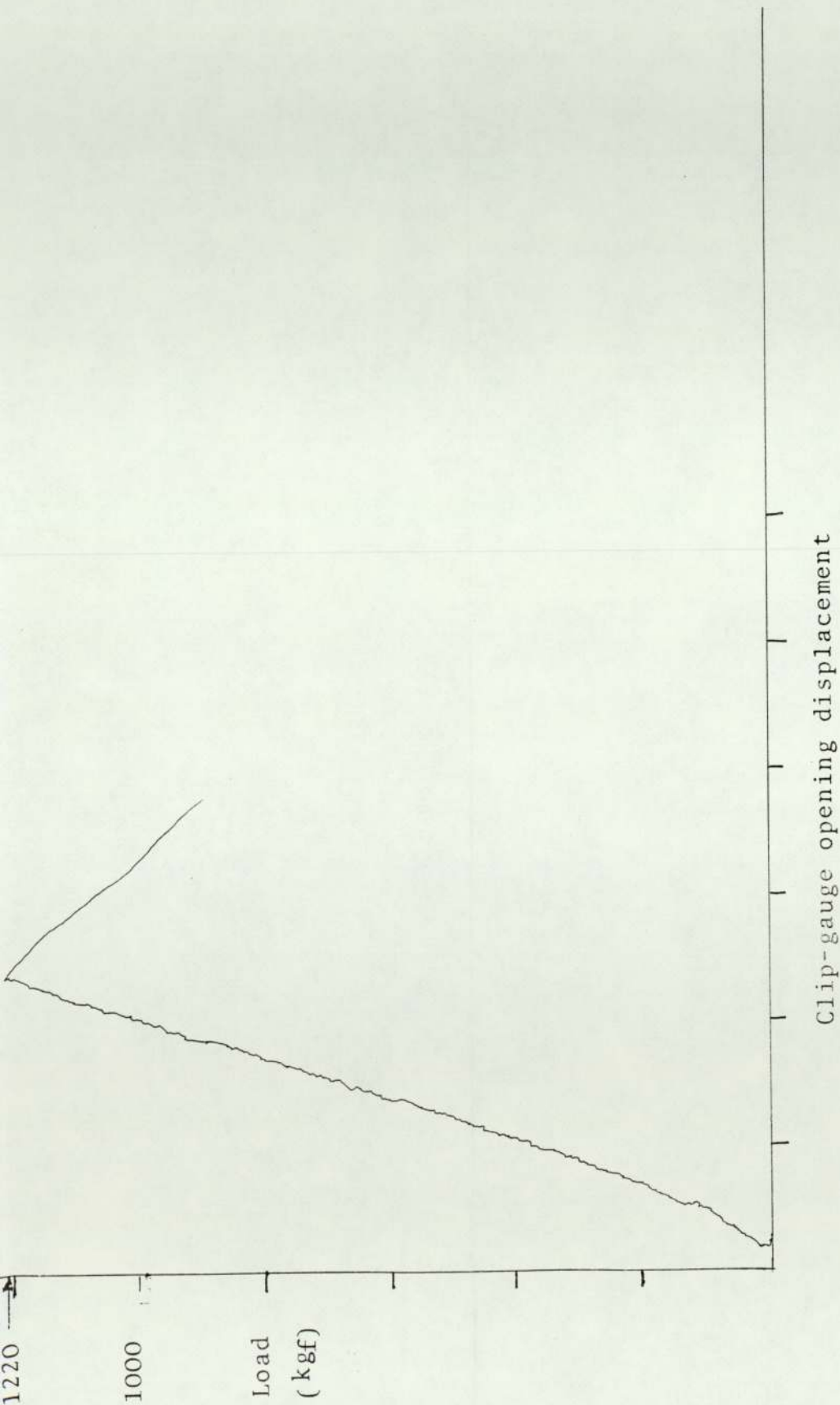


FIGURE 37-13 Force/clip-gauge opening displacement test record for "Hydie" steel H3C

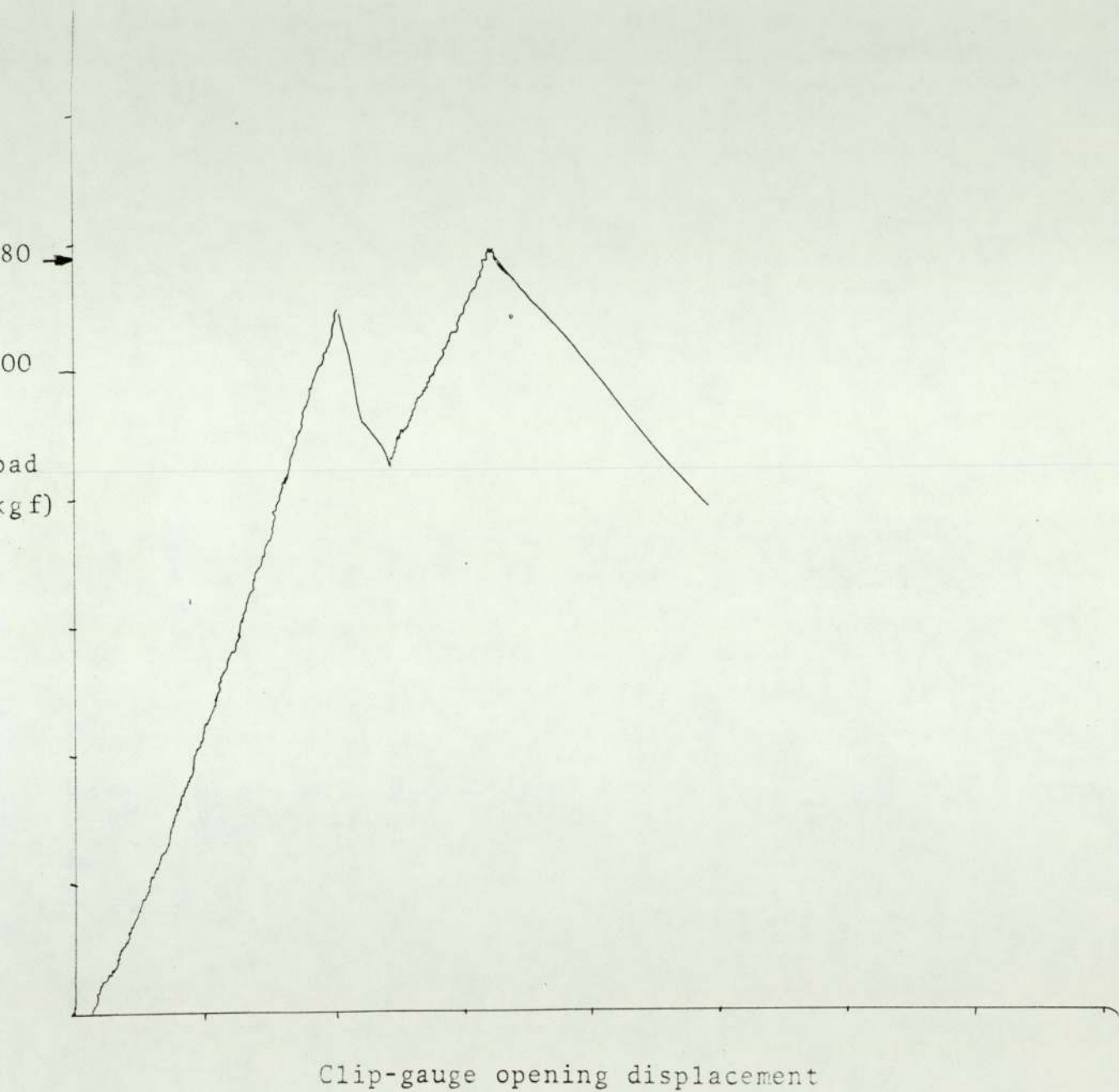


FIGURE 37-14 Force/clip gauge opening displacement test record for "Hydie" steel H3A

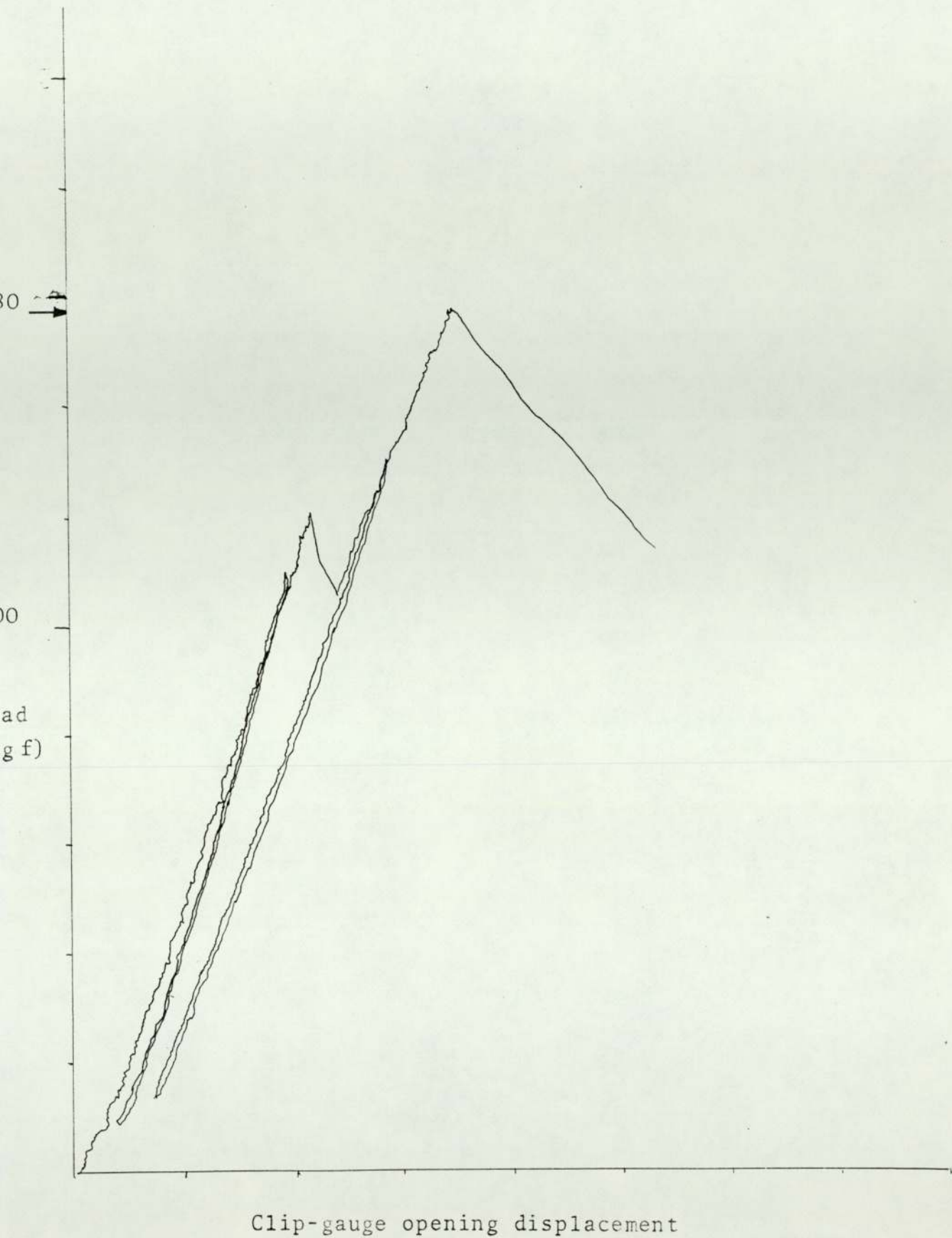
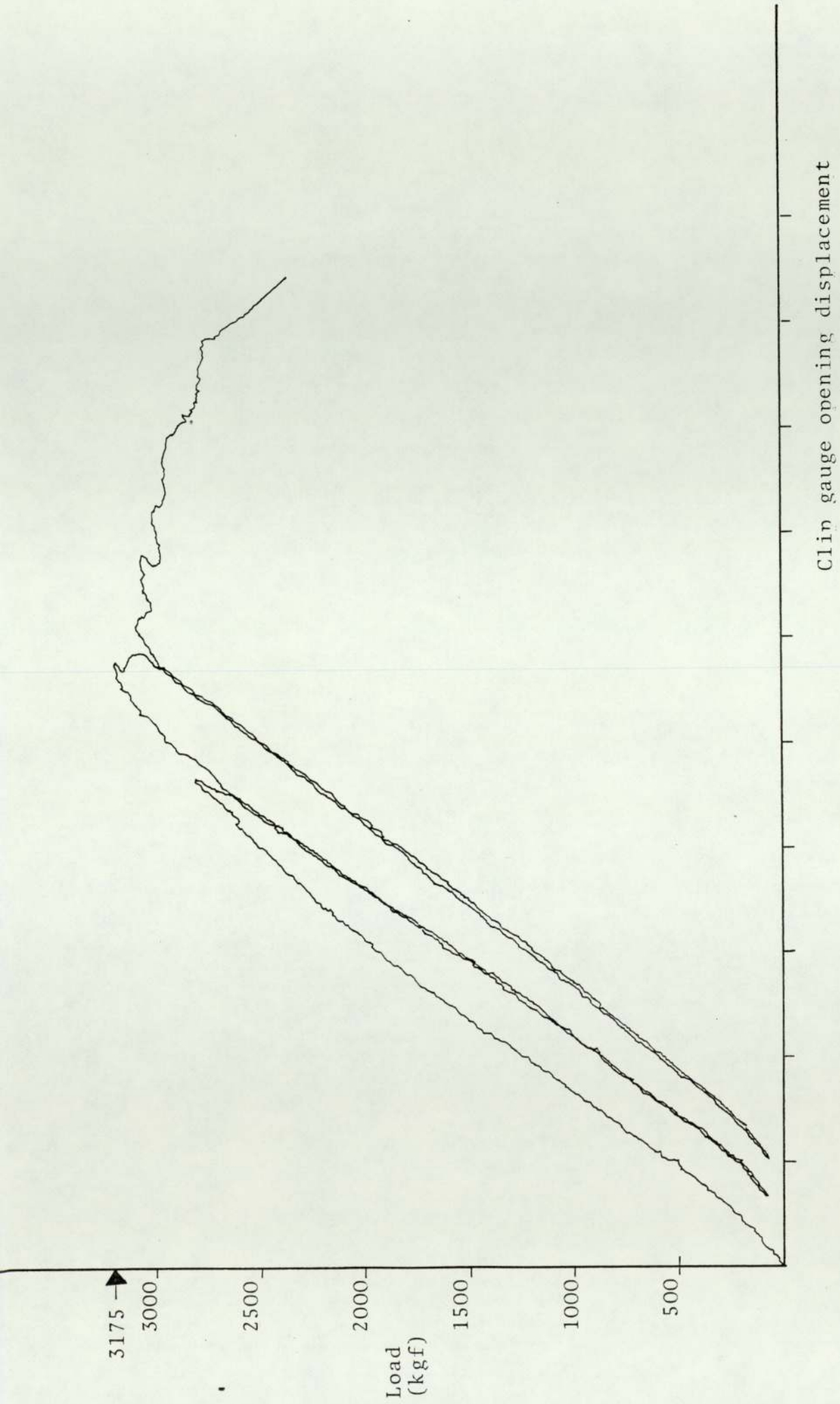


FIGURE 37-15 Force/clip-gauge opening displacement test record for "Hydie" steel H3B



Clip gauge opening displacement

FIGURE 38-1 Force/clip-gauge opening displacement record for S10

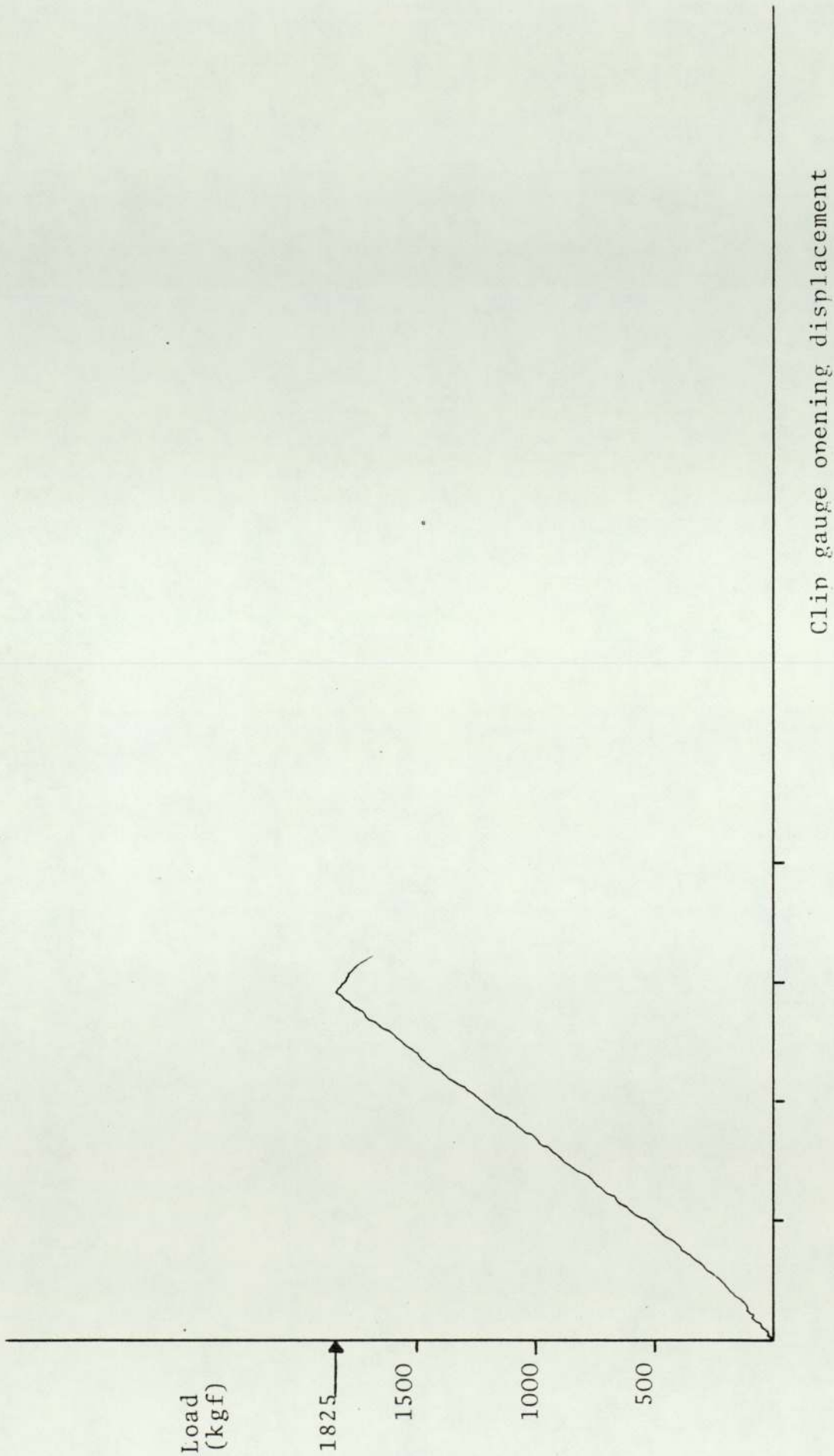


FIGURE 38-2 Force/clip-gauge opening displacement record for SIM

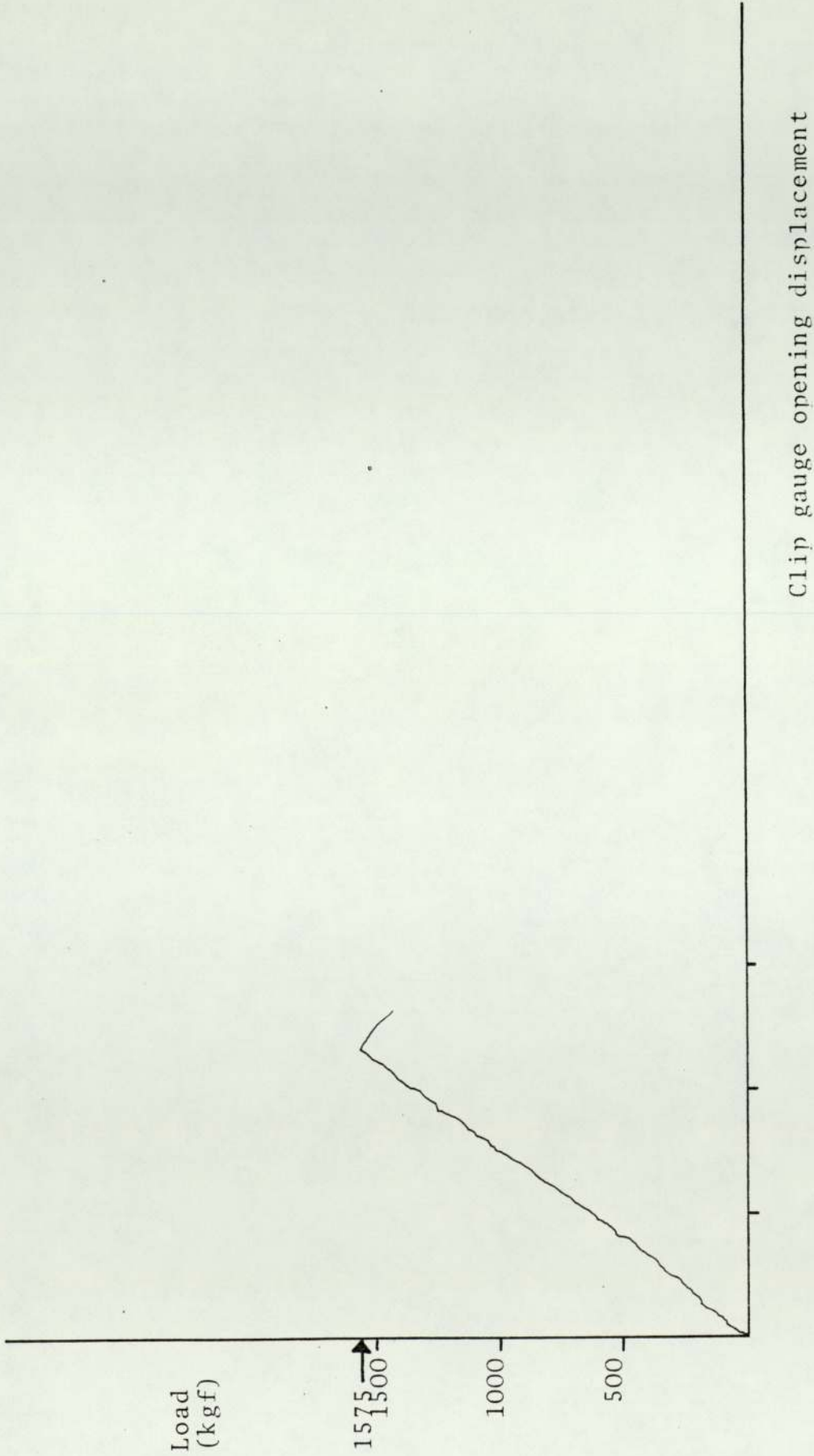


FIGURE 38-3 Force/clip-gauge opening displacement record for SIC

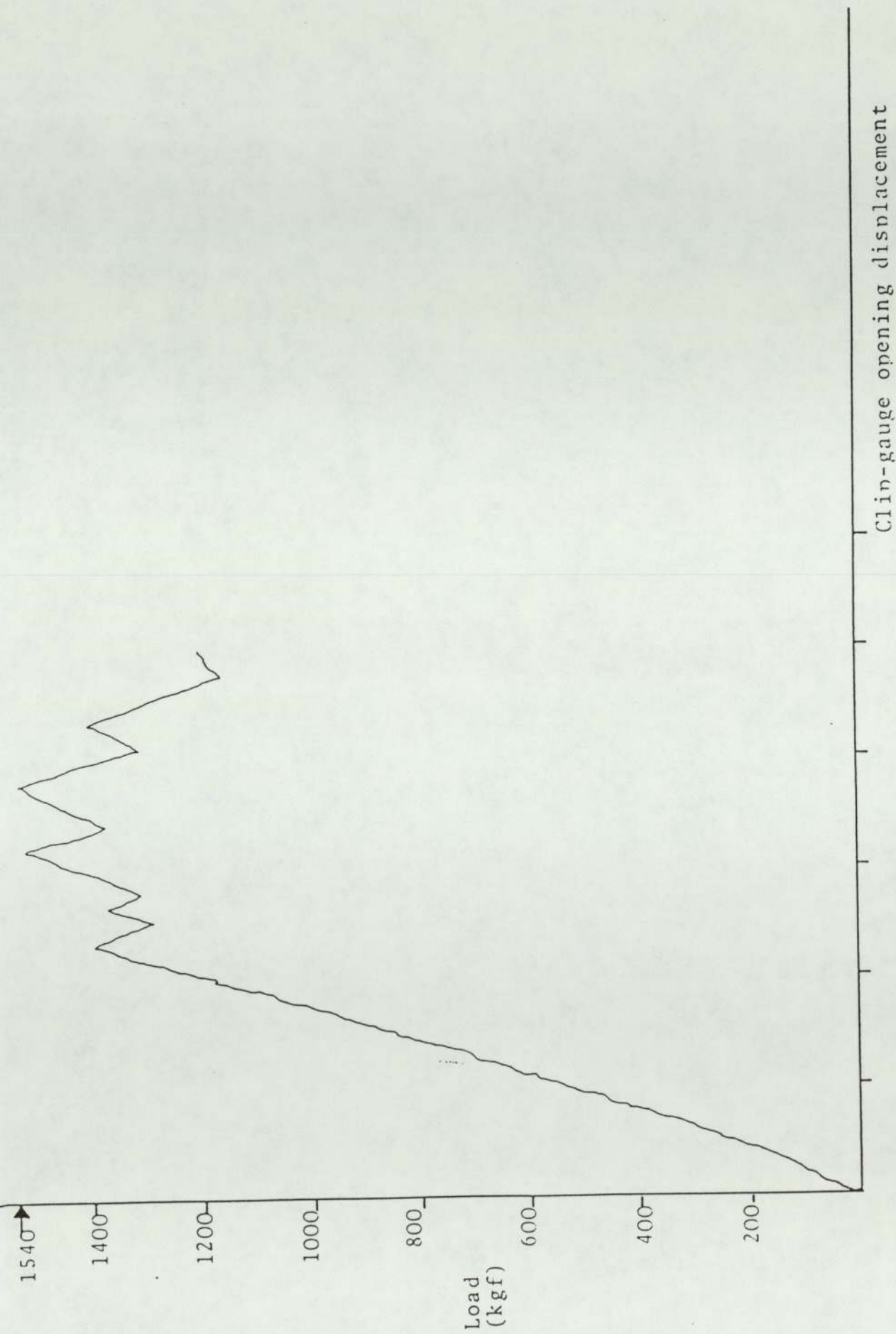


FIGURE 38-4 Force/clip-gauge displacement record for S1A

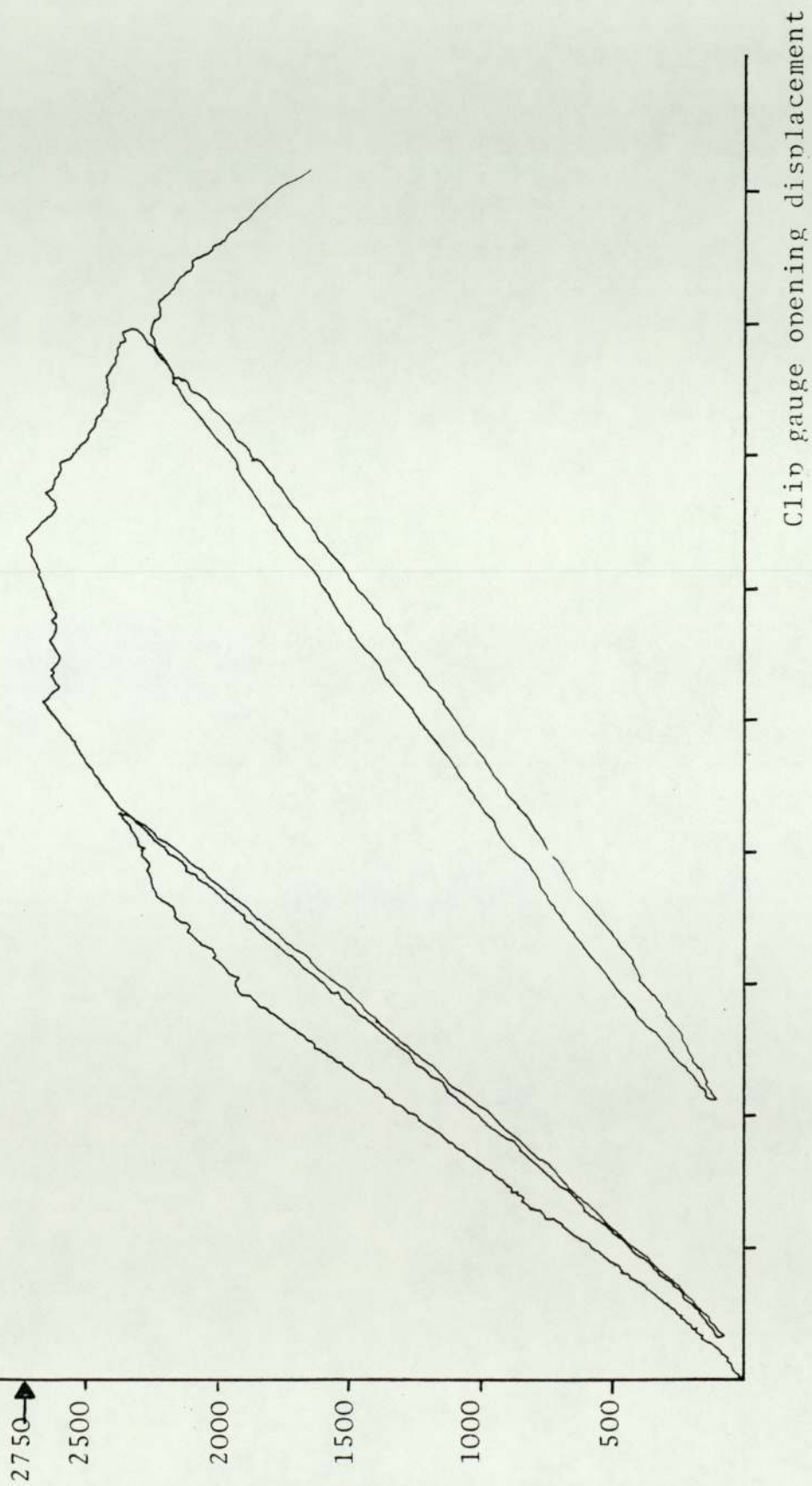


FIGURE 38-5 Force/clip-gauge displacement record for S1B

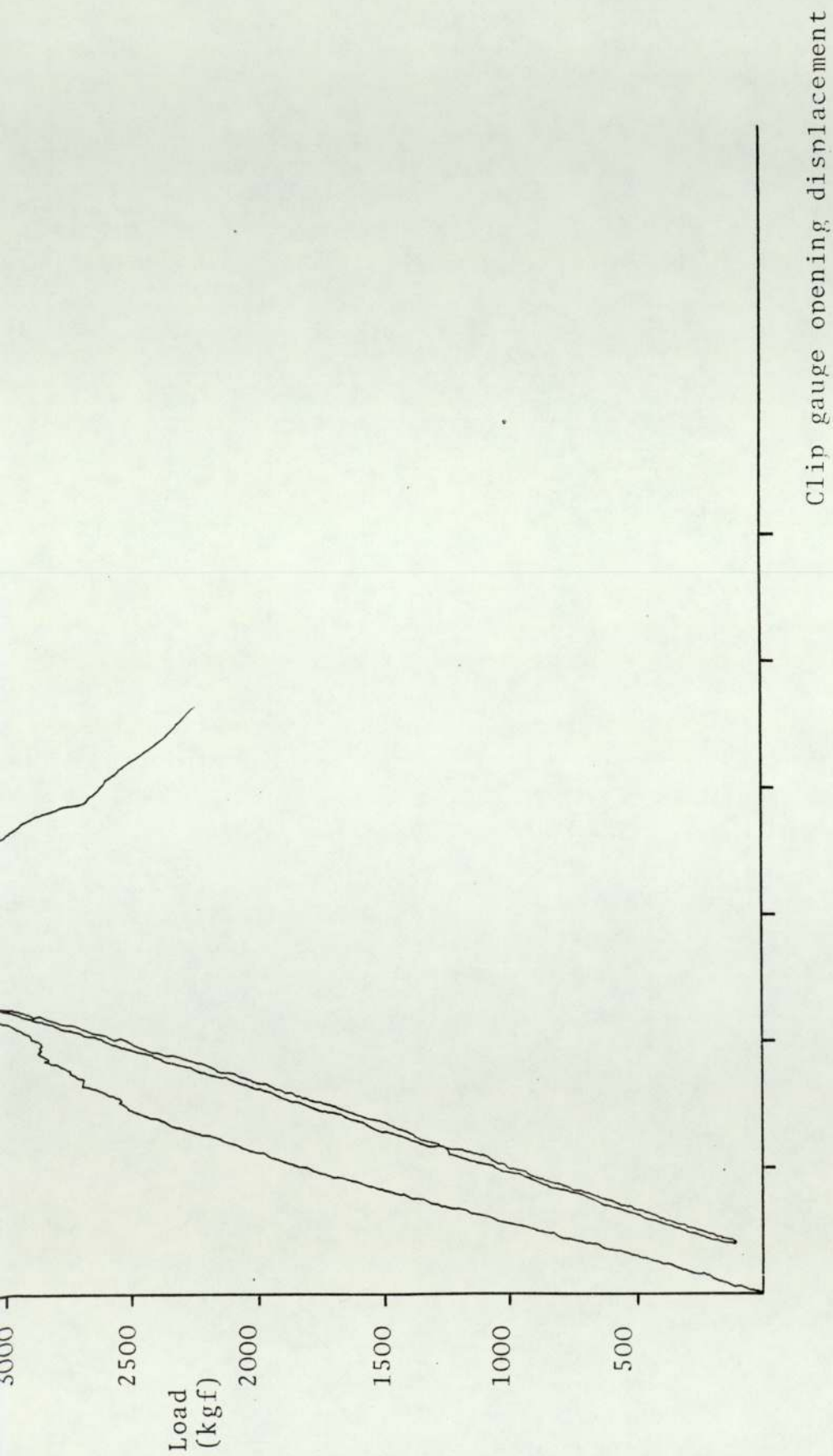


FIGURE 36-6 Force/clip-gauge opening displacement record for S20

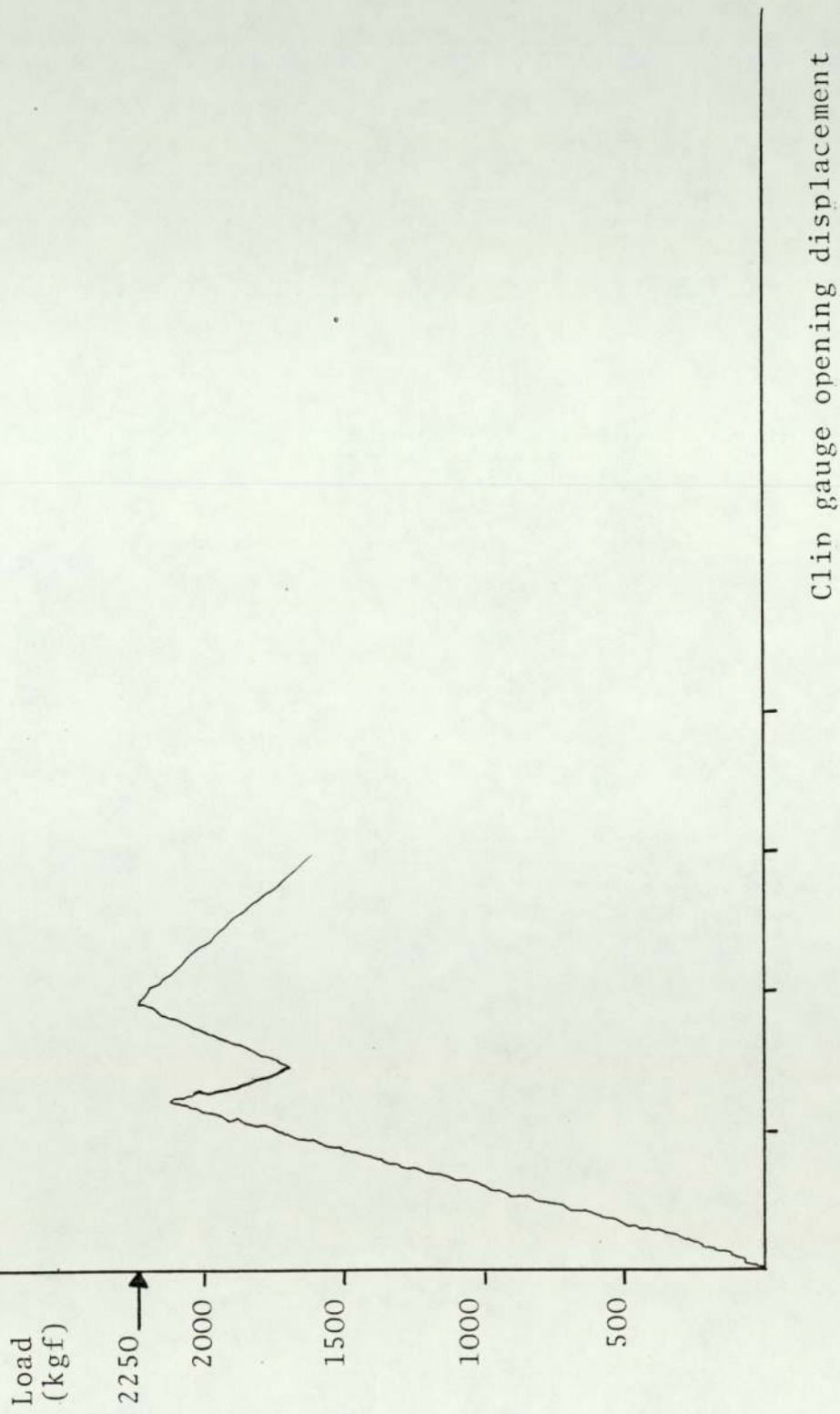


FIGURE 37-7 Force/clip-gauge opening displacement record for S2M

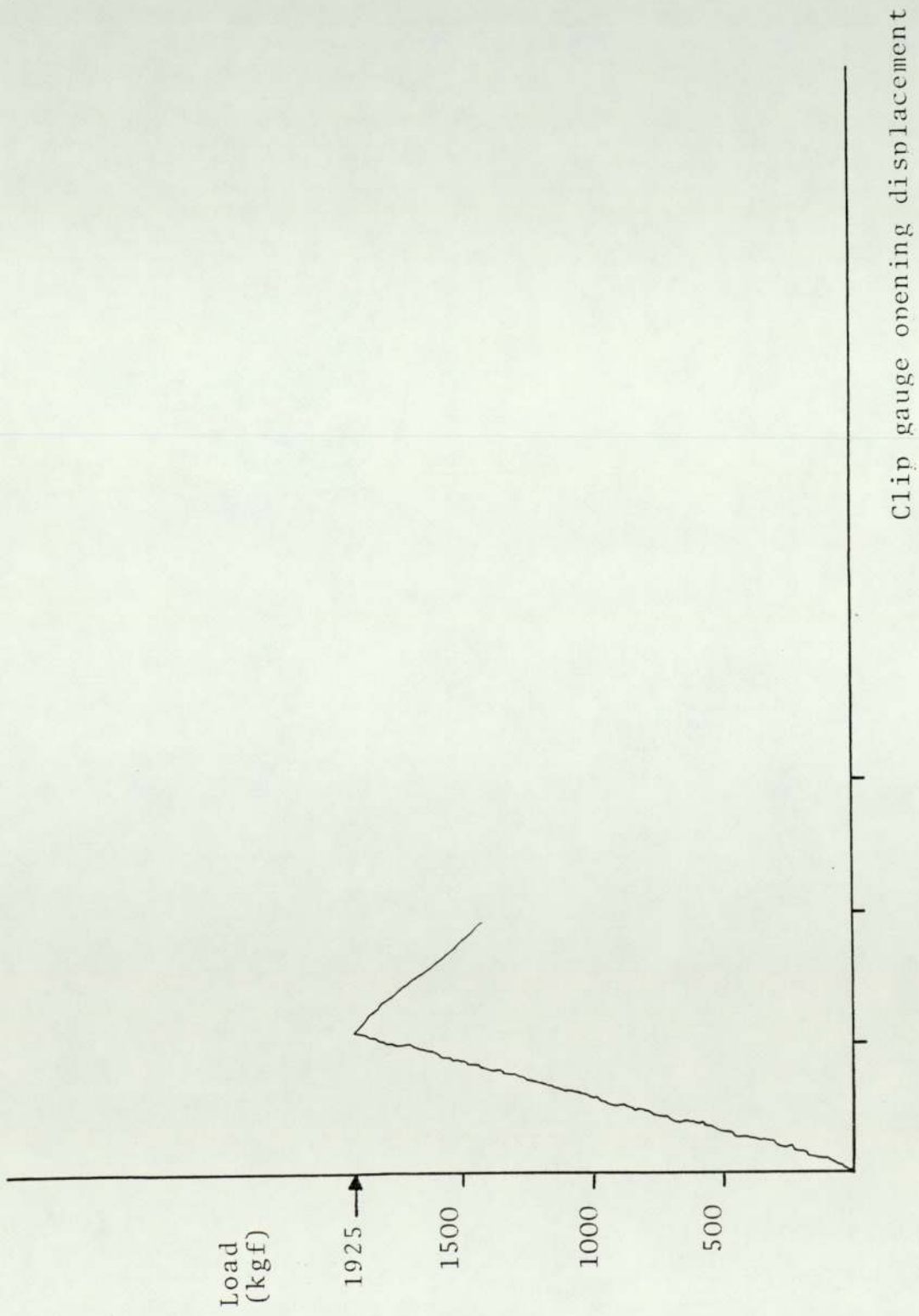


FIGURE 38-8 Force/clip-gauge opening displacement record for S2C

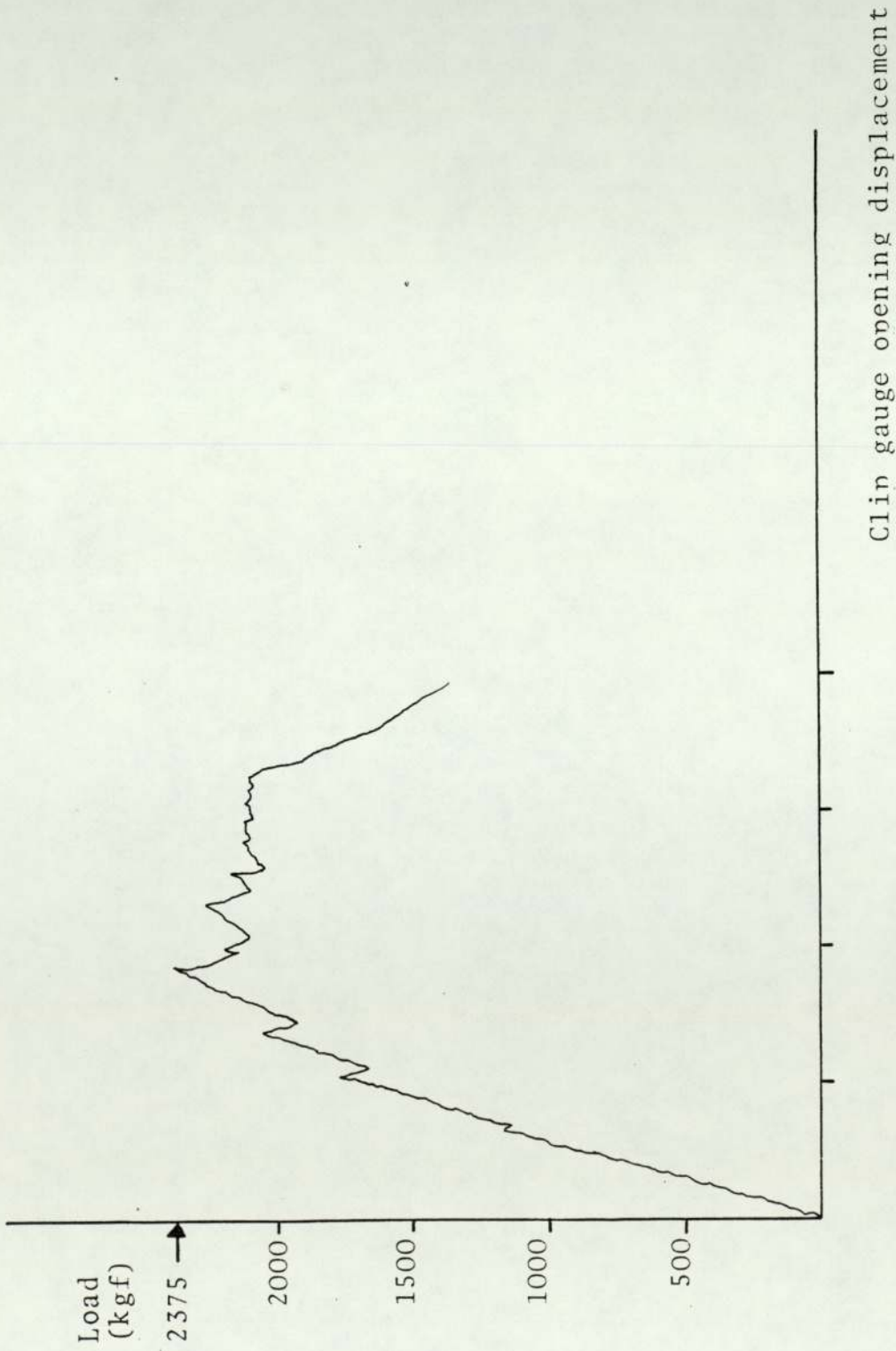


FIGURE 38-9 Force/clip-gauge opening displacement for S2A

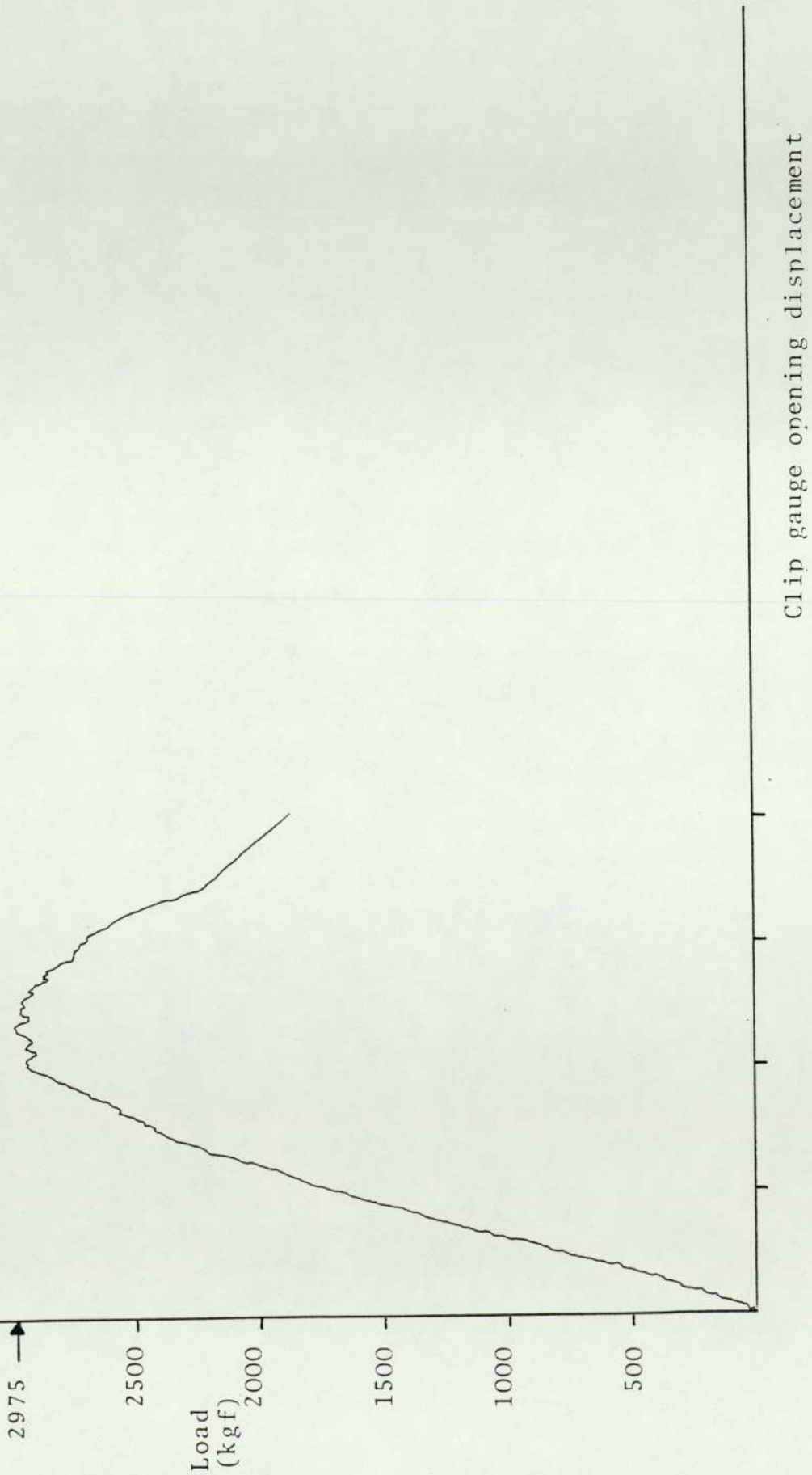


FIGURE 38-10 Force/clip-gauge opening displacement
for S2B

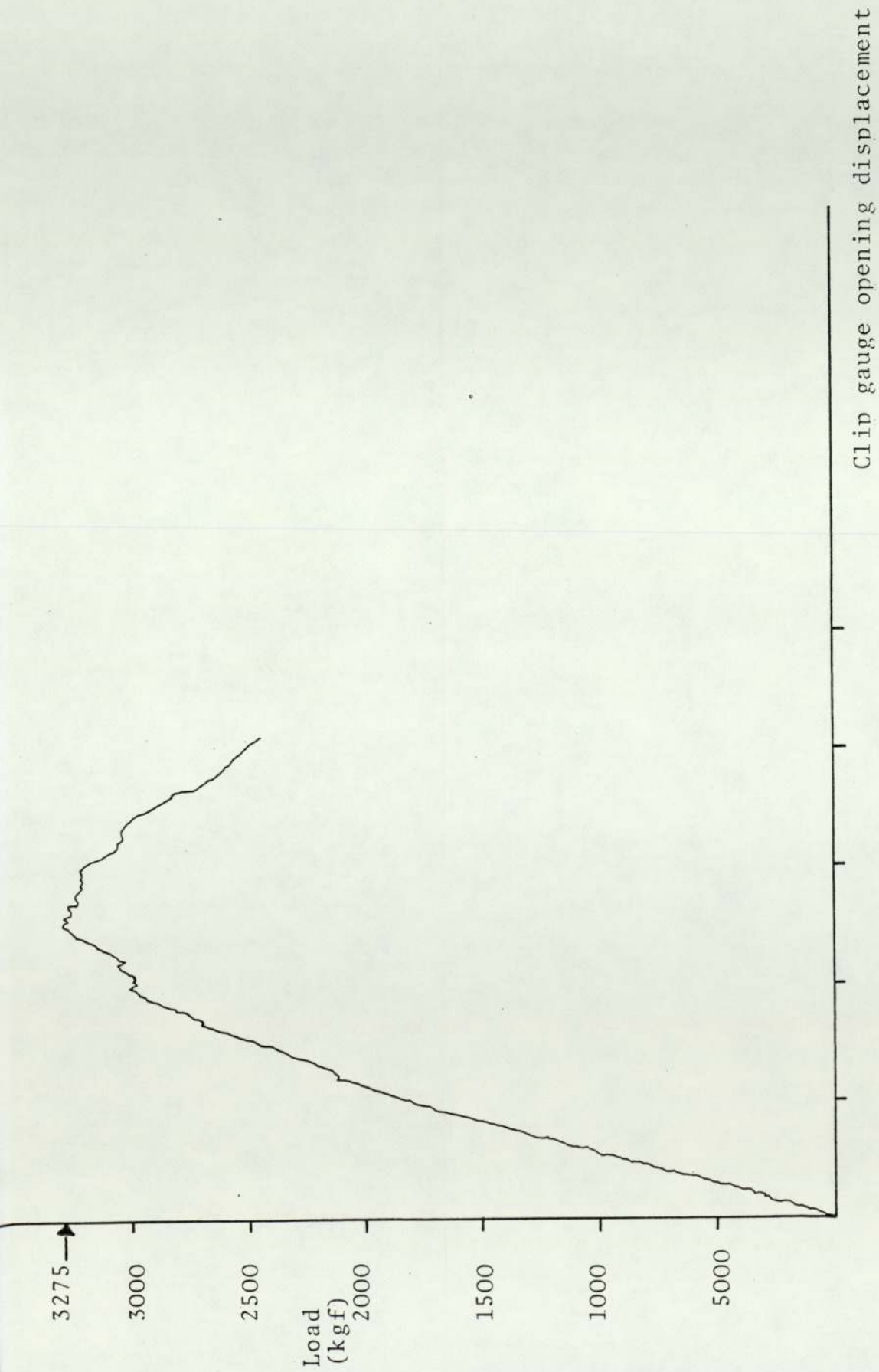


FIGURE 38-11 Force/clip-gauge opening displacement record (S30)

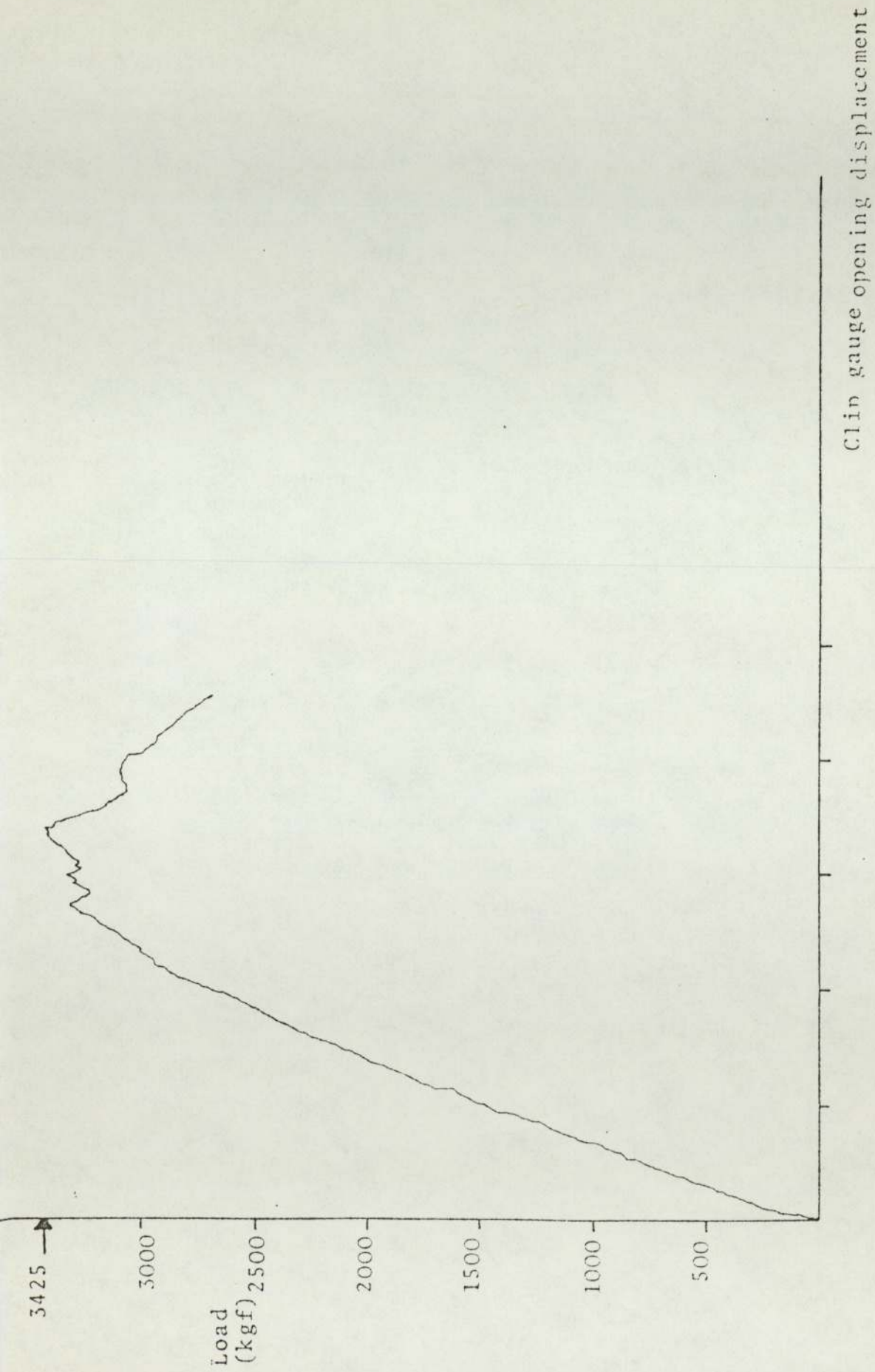


FIGURE 38-12 Force/clin-gauge opening displacement record (S3M)

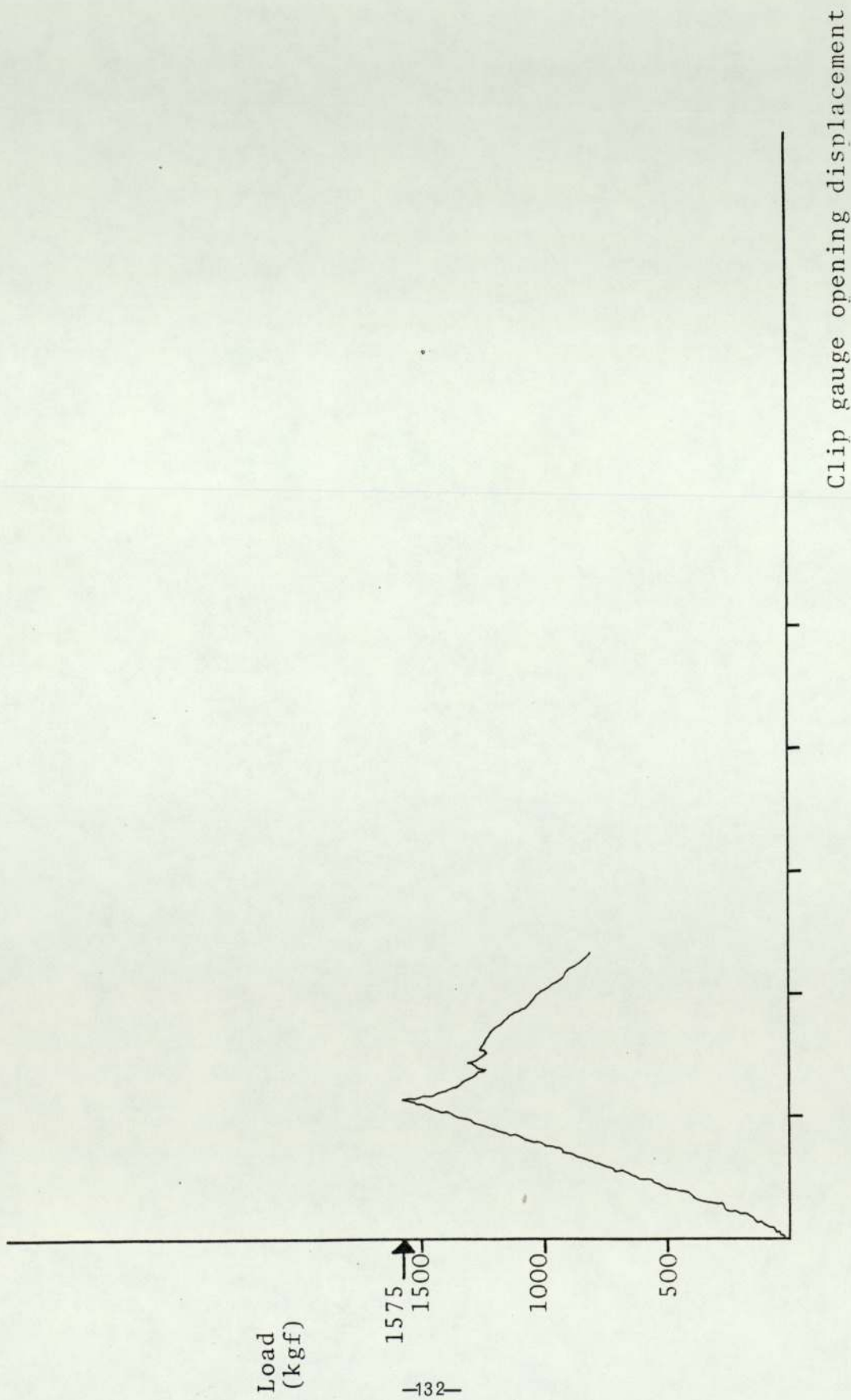


FIGURE 38-13 Force/clip-gauge opening displacement record (S3C)

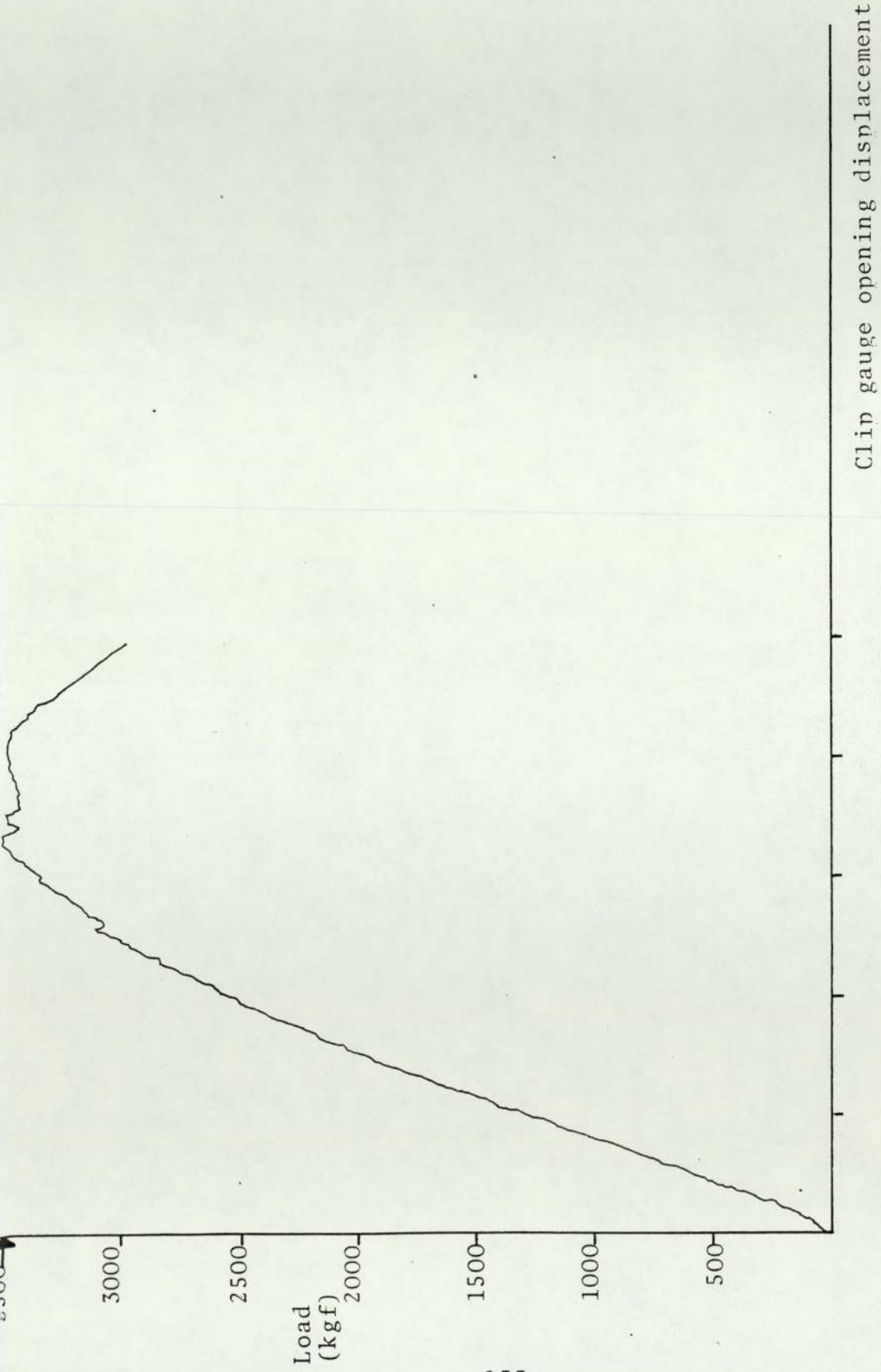


FIGURE 38-14 Force/clip-gauge opening displacement record (S3B)

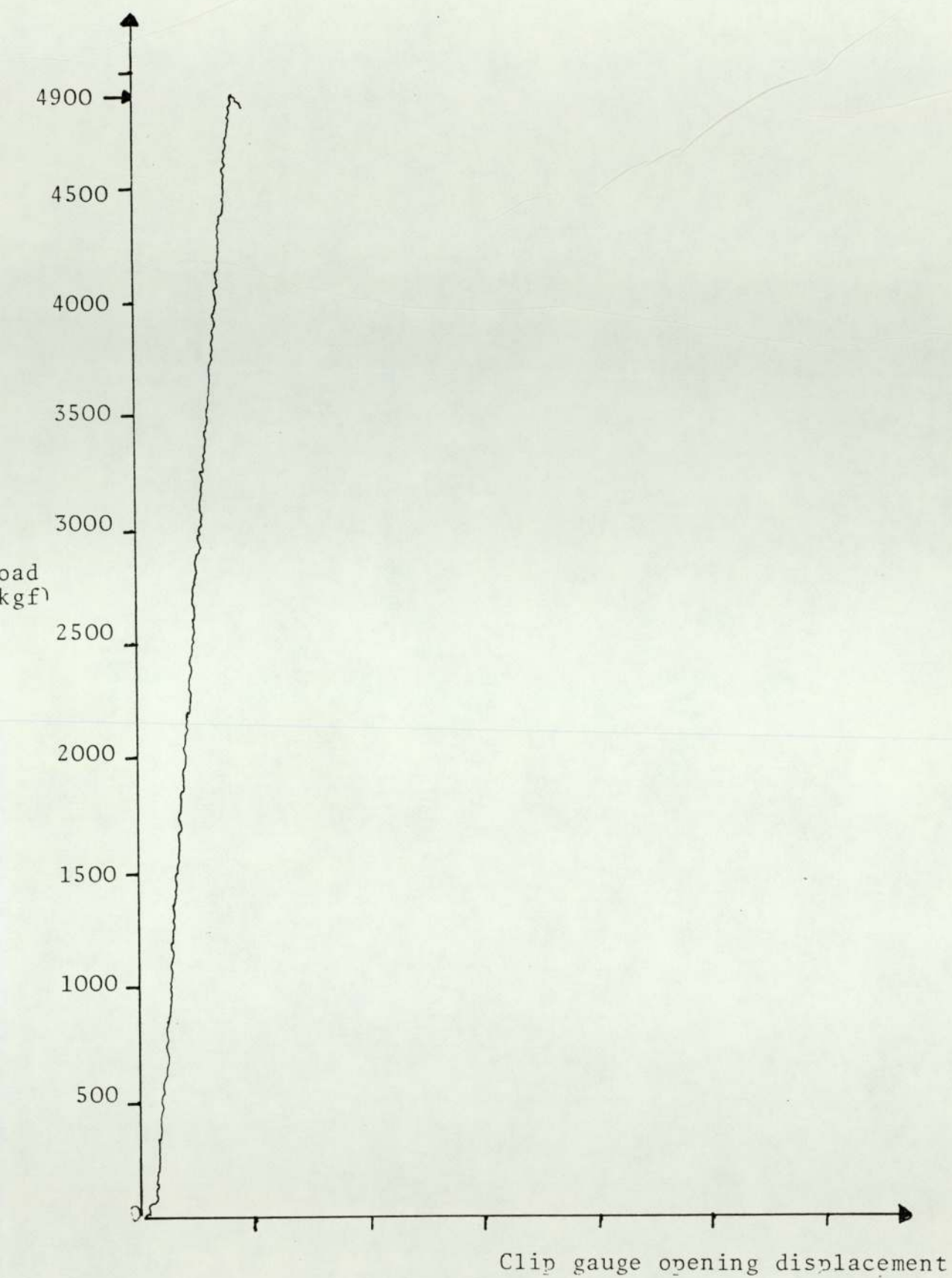


FIGURE 39-1 Load/clip-gauge opening displacement test record (three-point bend) for H0

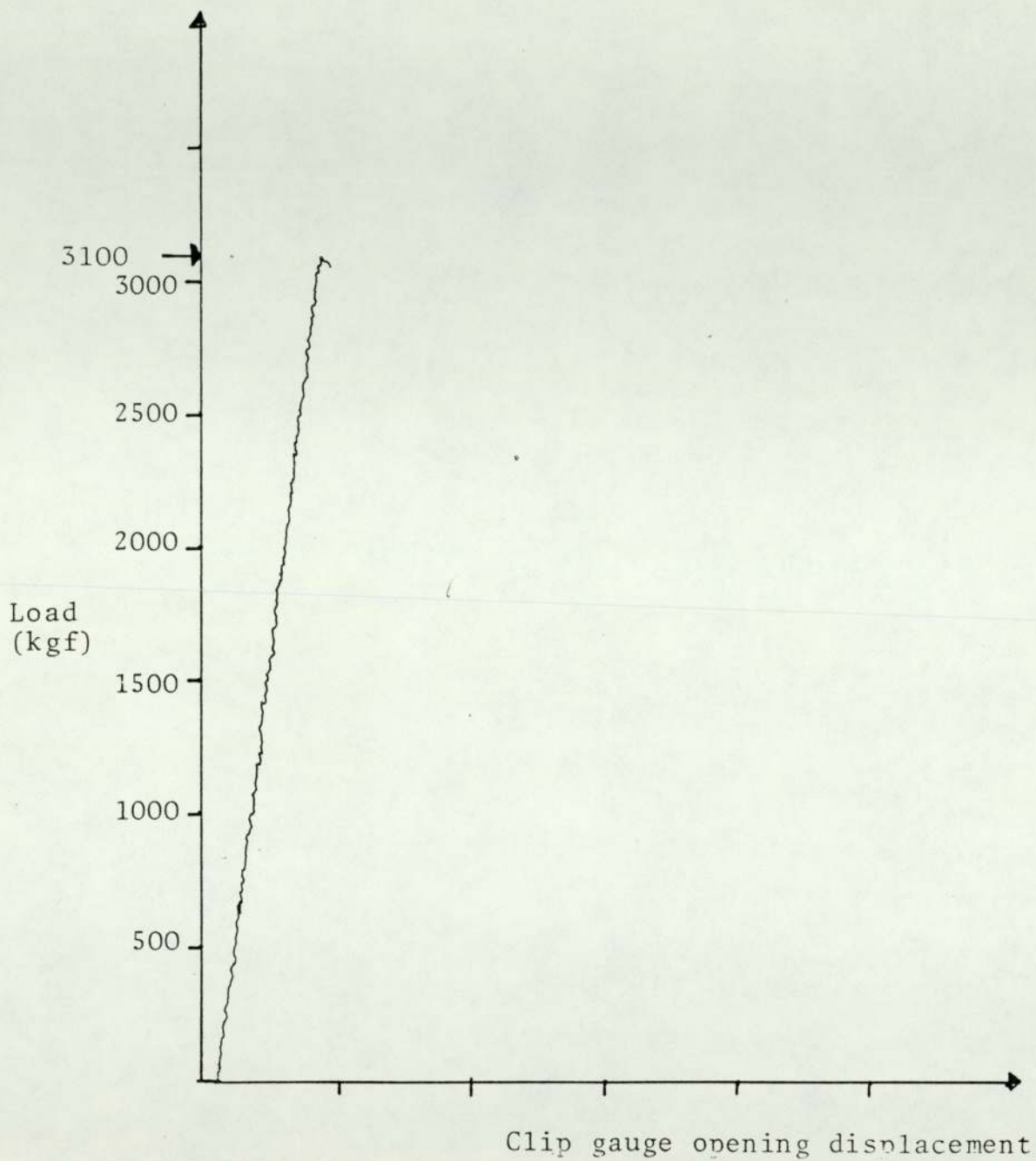


FIGURE 39-2 Load/clip-gauge opening displacement test record (three-point bend) for HM

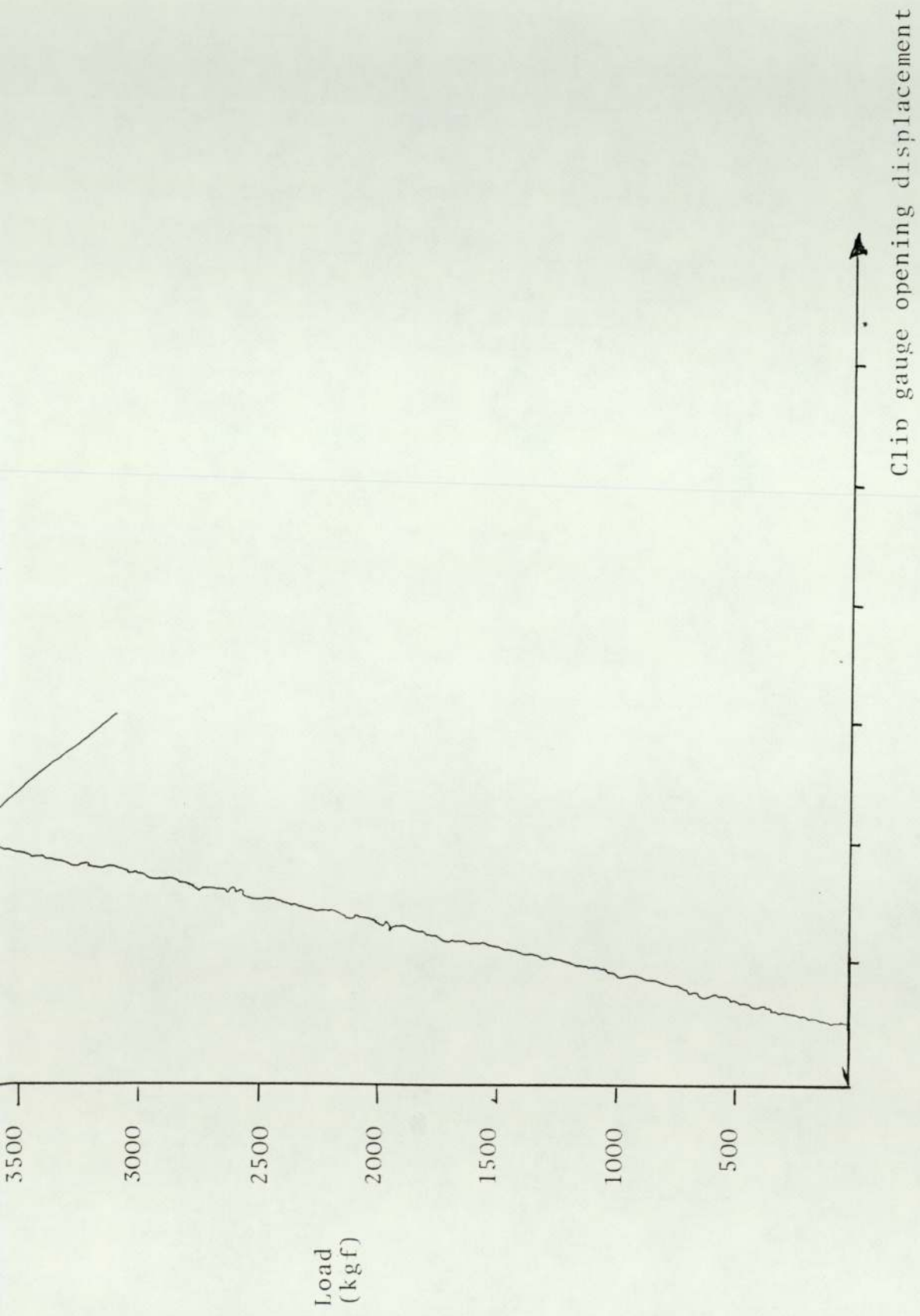


FIGURE 59-3 Load/clip-gauge opening displacement test record (three-point bend) for HC

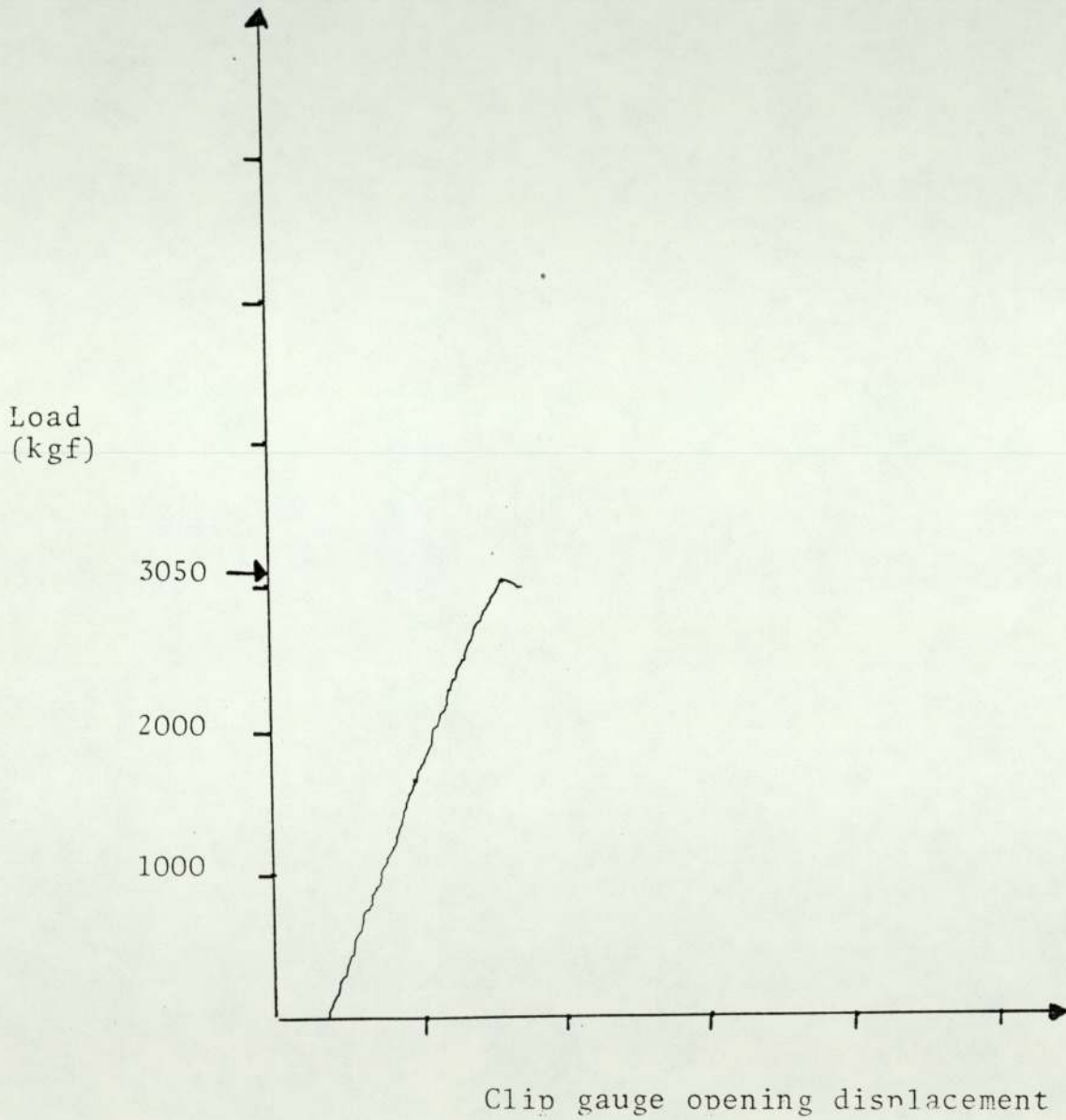


FIGURE 39-4 Load/clip-gauge opening displacement record, 3-point bend (S1)

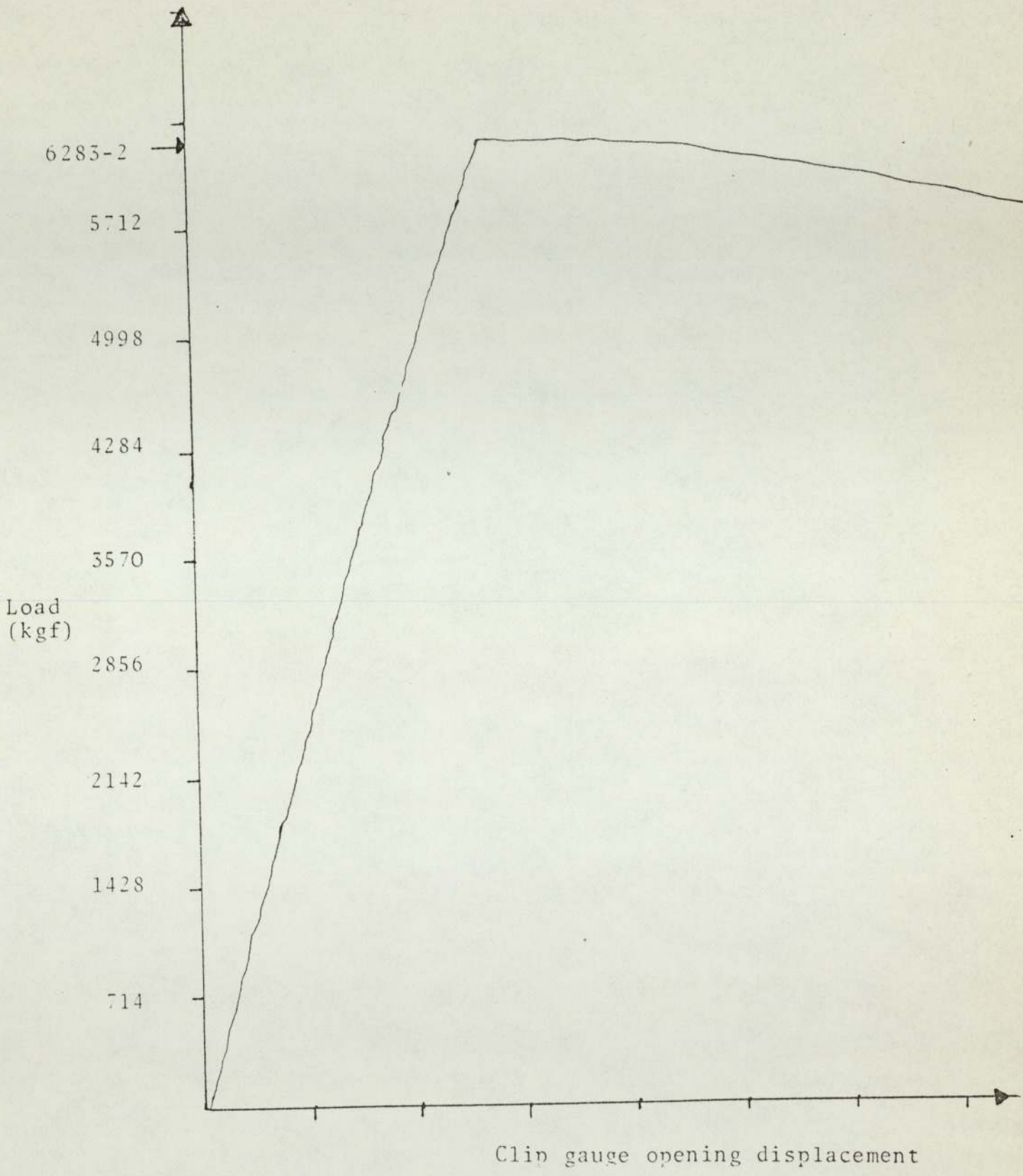


FIGURE 39-5 Load/clip-gauge opening displacement record, 3-point bend (S2)

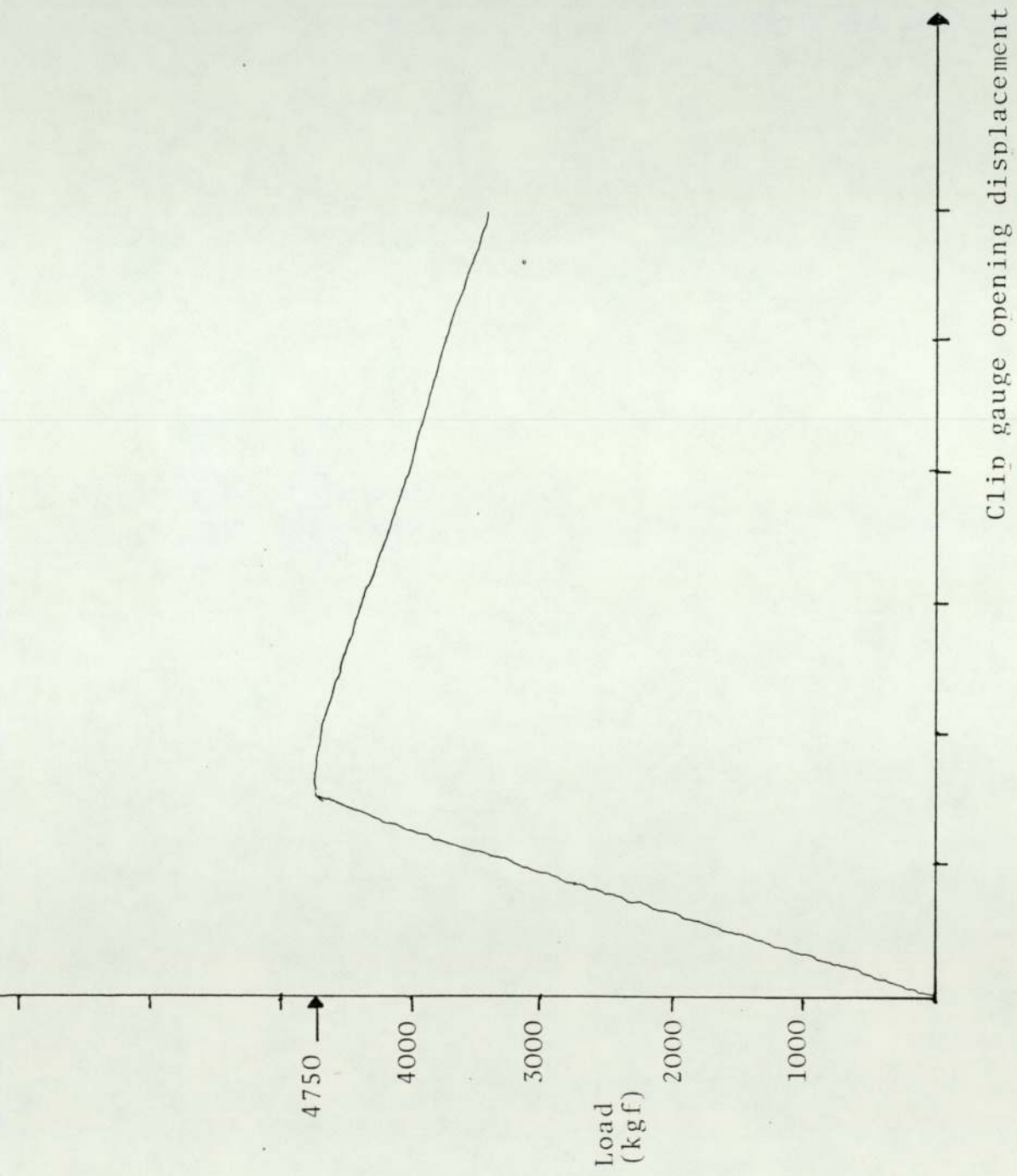


FIGURE 39-6 Load/clip-gauge opening displacement record, 3-point bend (S3)

6.5 Mechanical Testing

6.5.1 Tensile Testing

Tensile testing was carried out on Electem, Thermodie, Hydrie and Somdie steel specimens.

No. 12 tensile specimens (Fig. 40) were used in this test, and testing was carried out on 5000 kgf capacity Instron testing machine with various cross-head speeds of 0.02 and 0.05 cm/min. and chart speed 1 cm/min.

The conditions applied to these specimens are as shown in Table 1; the room temperature, mechanical properties, incorporated in Table 3, are obtained from load/extension record, as shown in Figs. 41-43. The conventional measures of ductility that are obtained from the tension test are the engineering strain at fracture (e_f) (usually called the elongation); the reduction of the area at fracture, q , both of these properties are obtained by putting the specimens back together after fracturing and taking measurements of L_f and A_f .

$$e_f = \frac{L_f - L_o}{L_o} \dots\dots\dots (20)$$

$$q = \frac{A_o - A_f}{A_o} \dots\dots\dots (21)$$

Both elongation and reduction of area are usually expressed as a percentage. The value of (e_f) depends on the gauge length (L_o). The smaller the gauge length the greater will be the contribution to overall elongation from the necked region and the higher will be the value (e_f).

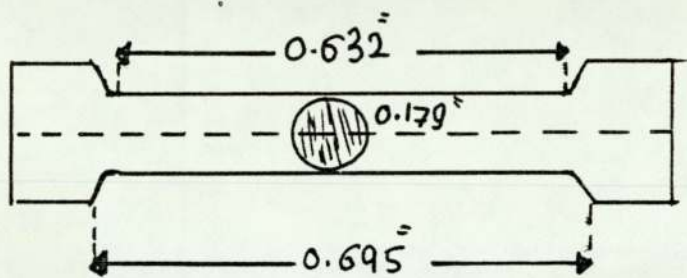


FIGURE 40 Test piece tensile test specimen No. 12" showing the dimensions and the cross-sectional area "A"

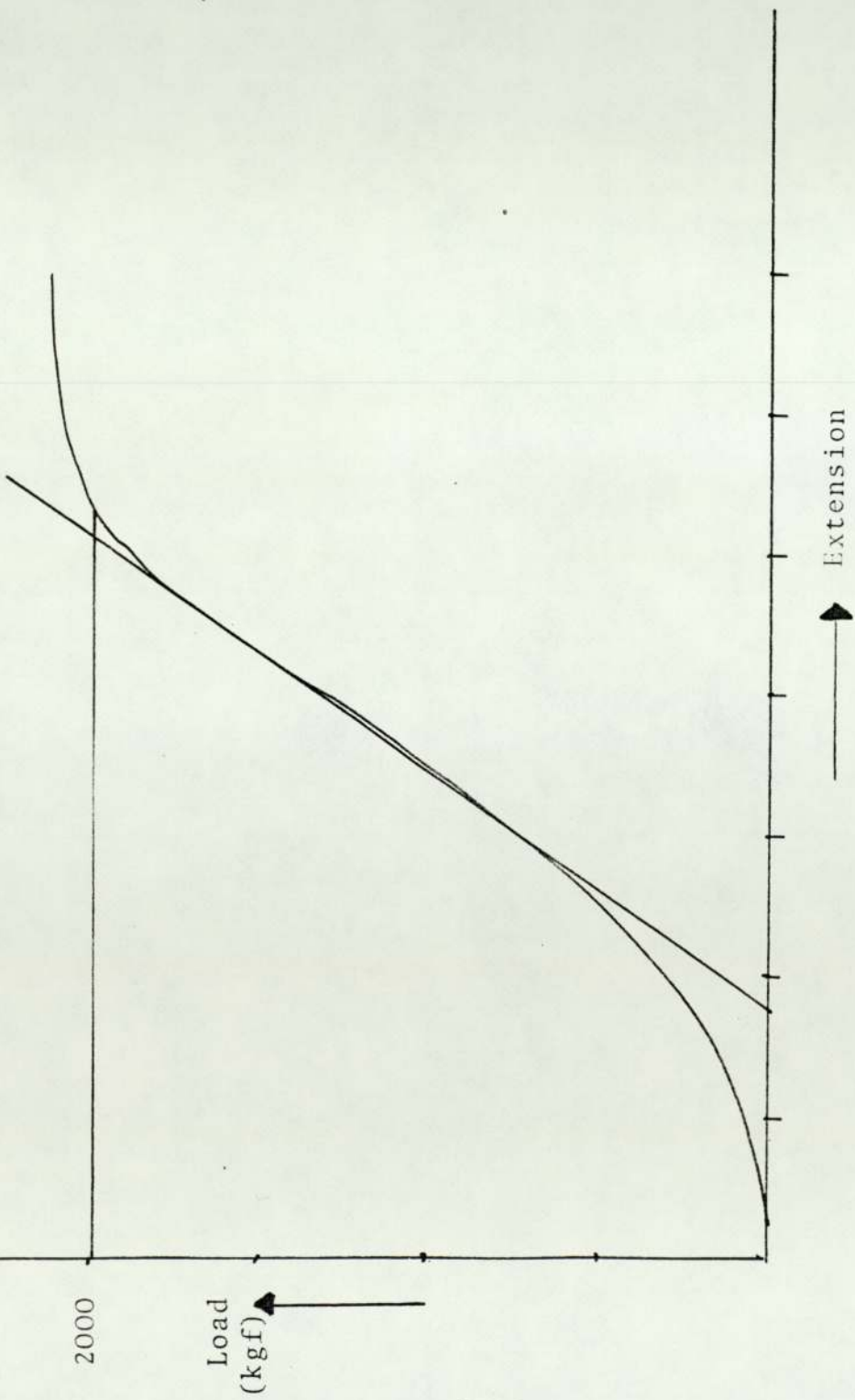


FIGURE 41-1 Load/Extension curve for H.W. Die Steel "Thermodie" A0

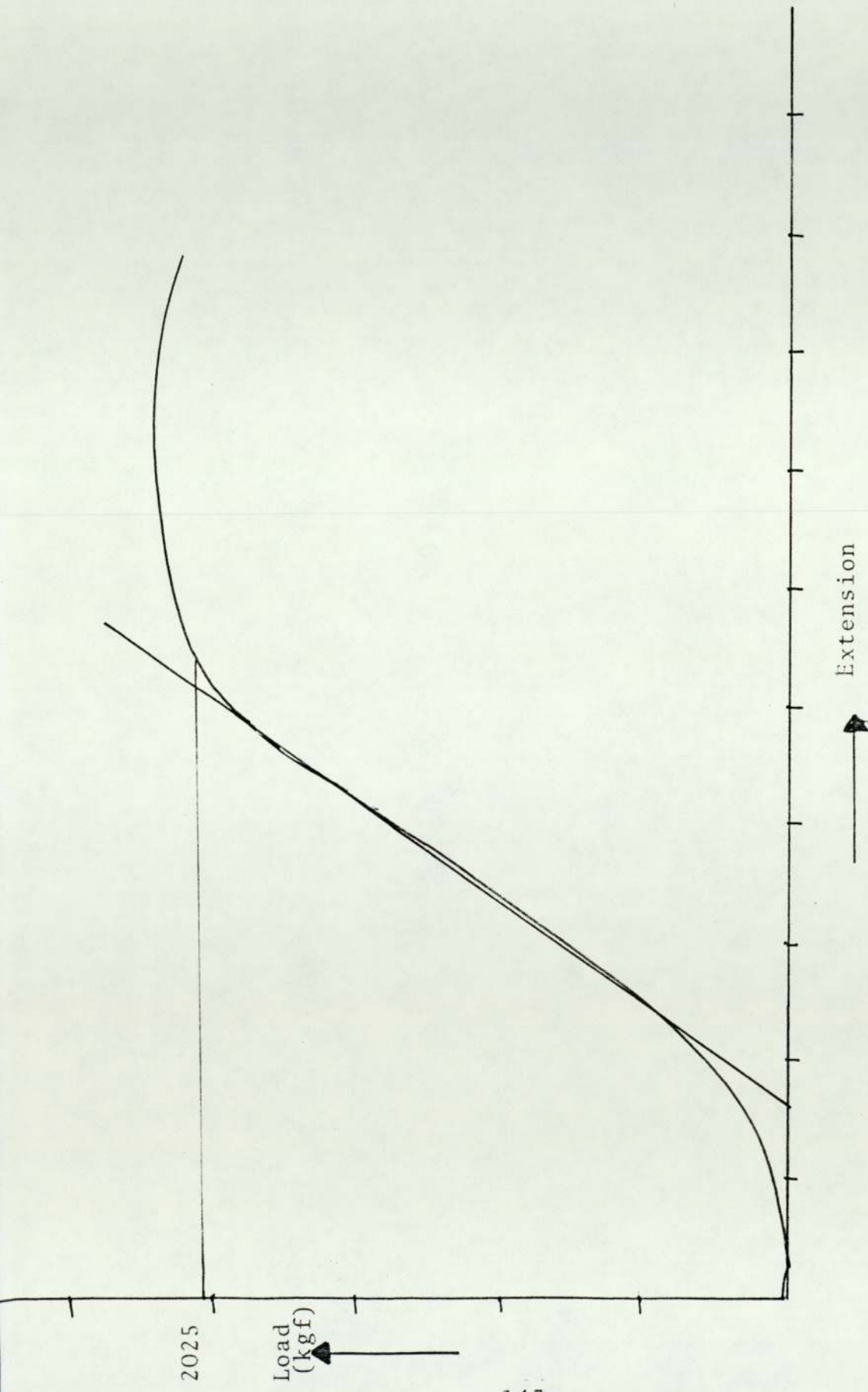


FIGURE 41-2 Load/Extension curve for H.W. Die Steel "Thermodie" Co

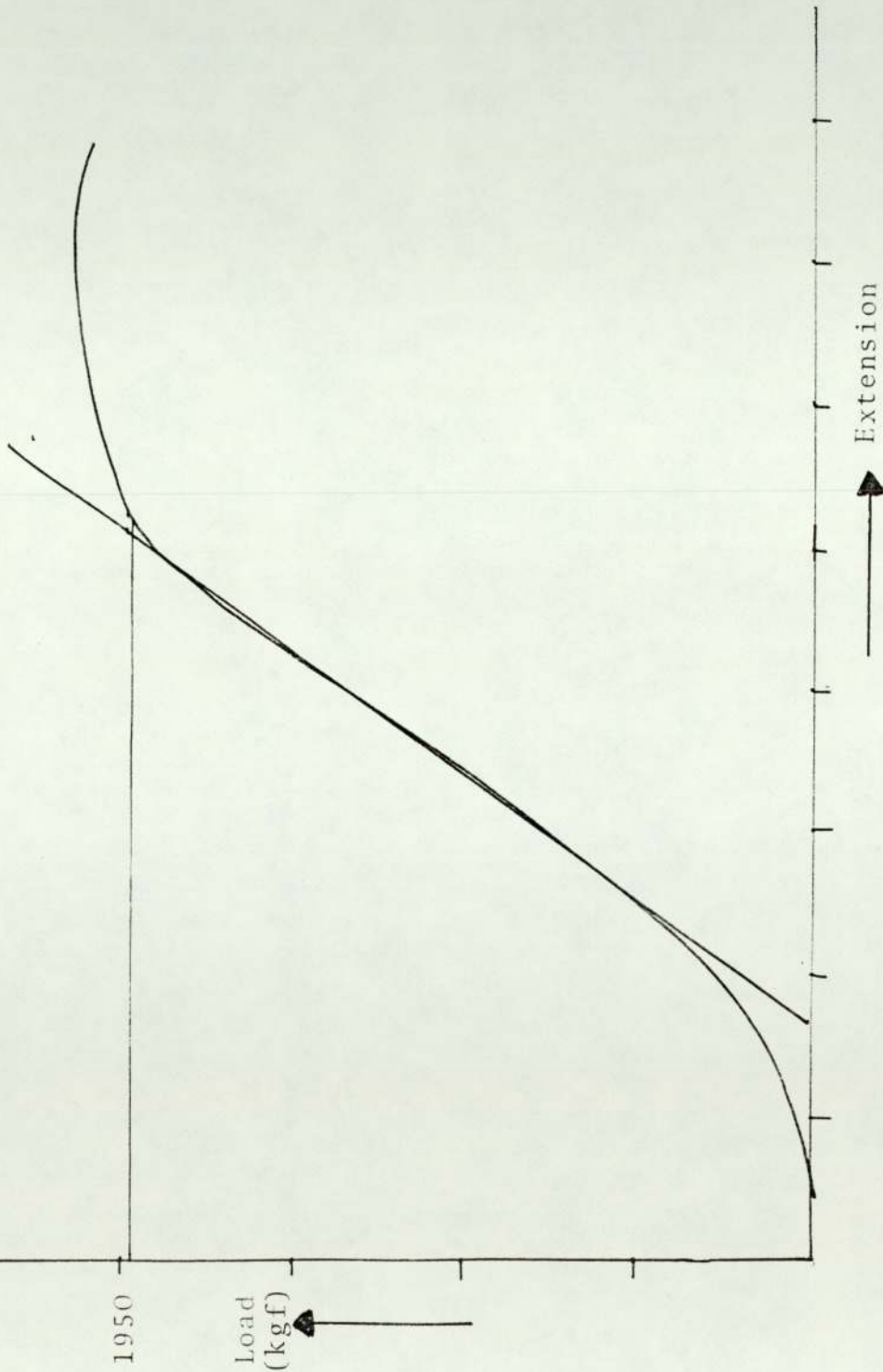


FIGURE 41-3 Load/Extension curve for H.W. Die Steel "Thermodie" Do

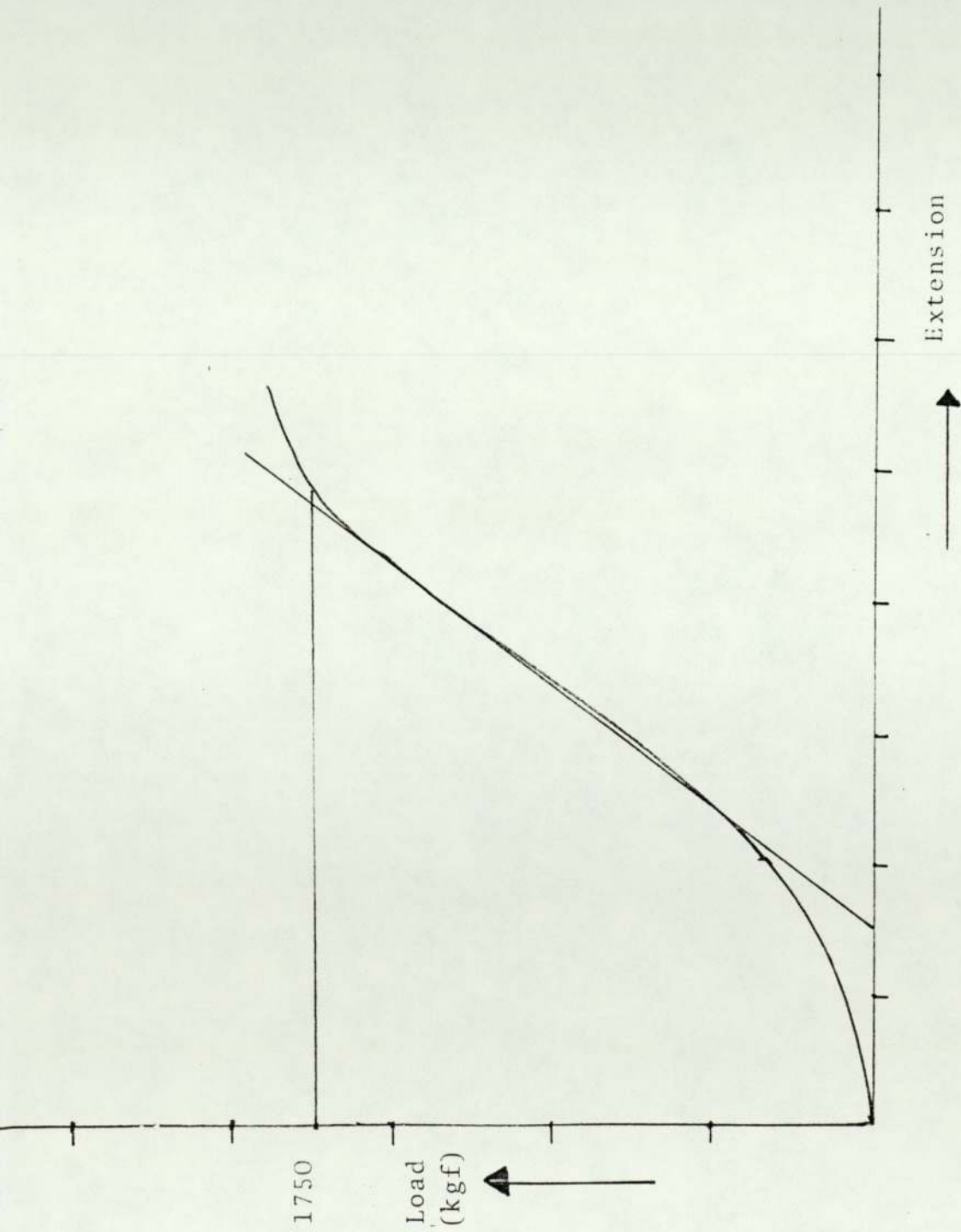


FIGURE 41-4 Load/Extension curve for H.W. Die Steel "Thermodie" AM

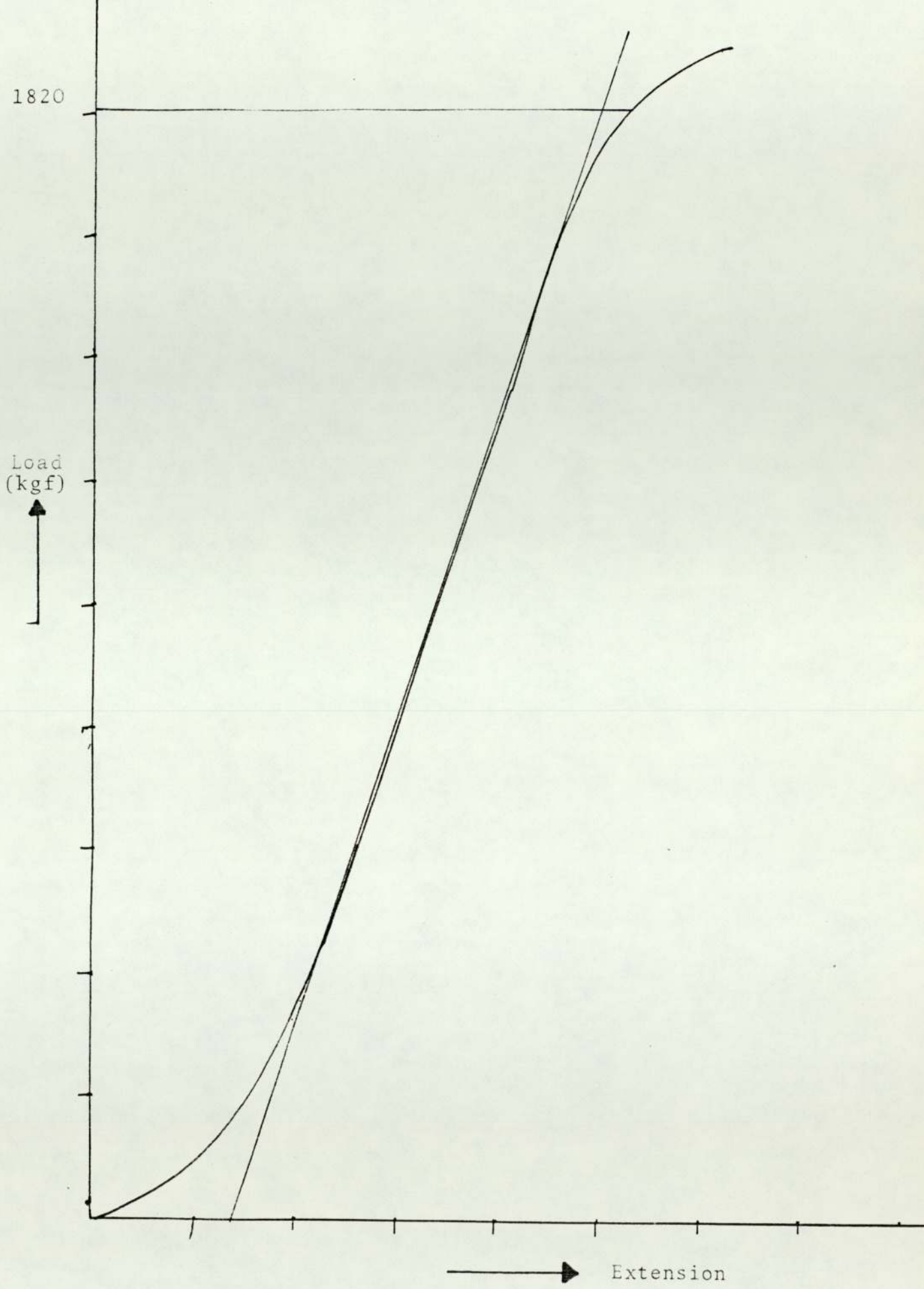


FIGURE 41-5 Load/Extension curve for H.W. Die Steel "Thermodie" BM

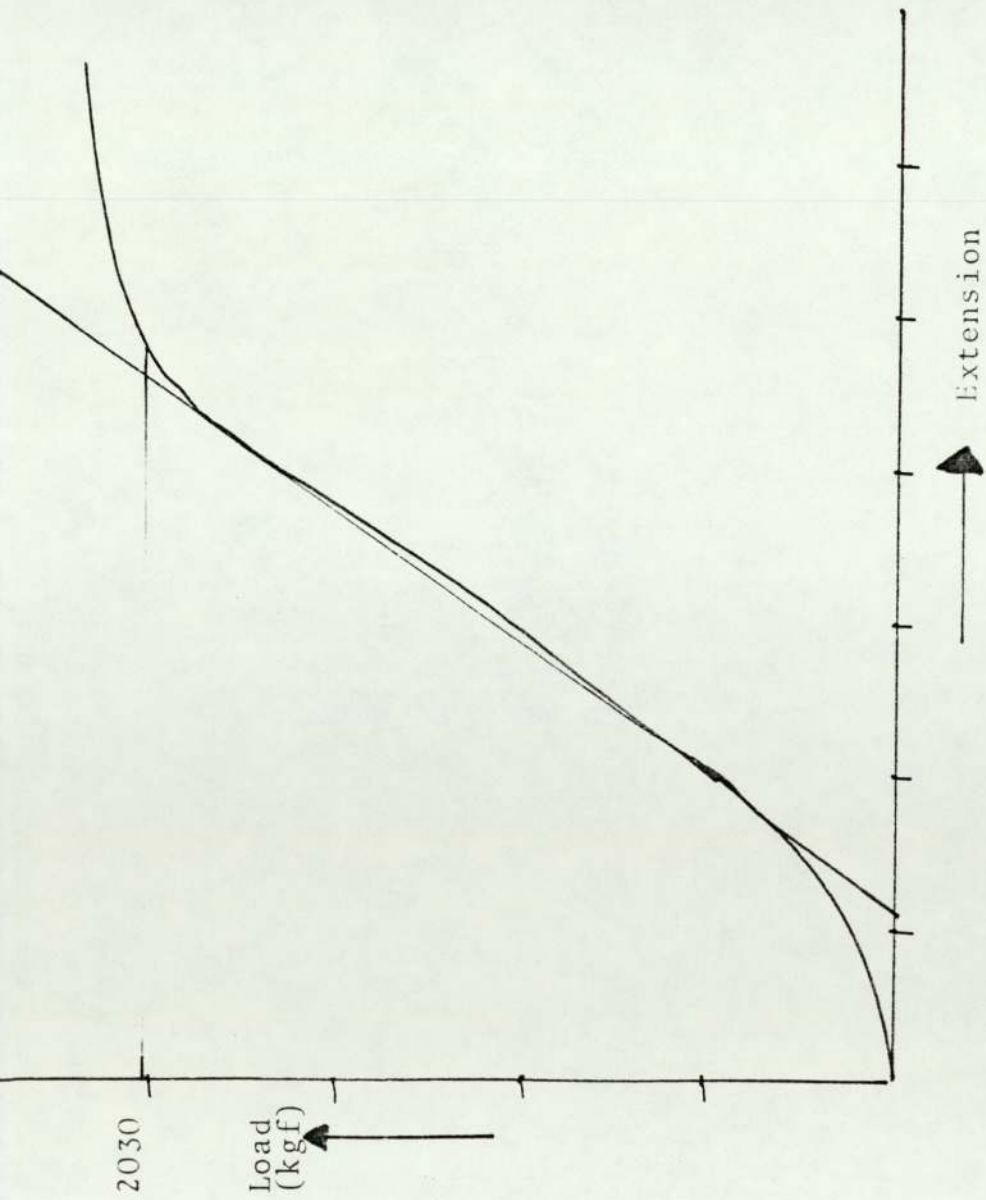


FIGURE 41-6 Load/Extension curve for H.W. Due Steel "Thermodie" DM

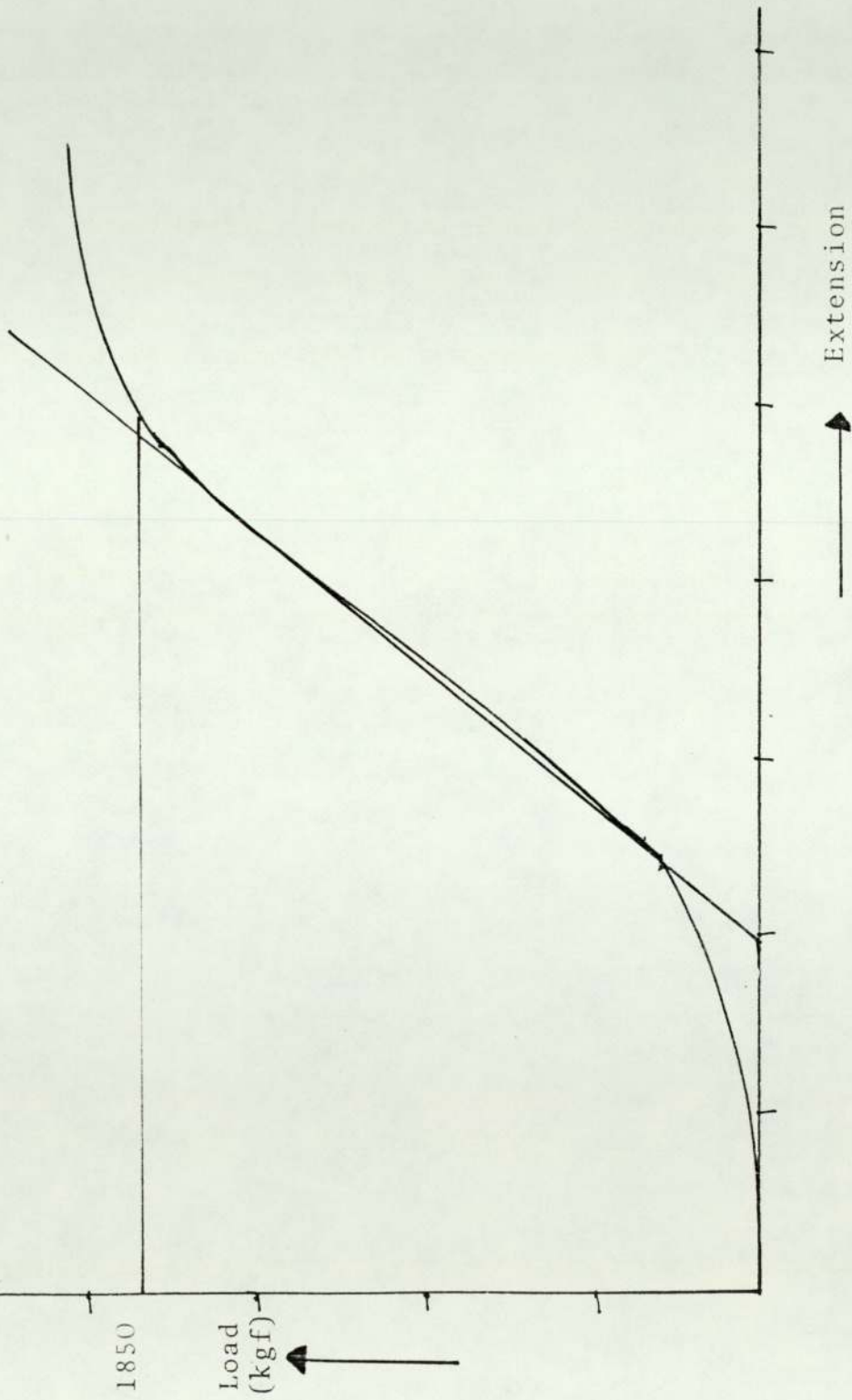


FIGURE 41-7 Load/Extension curve for H.W. Die Steel "Thermodie" BC

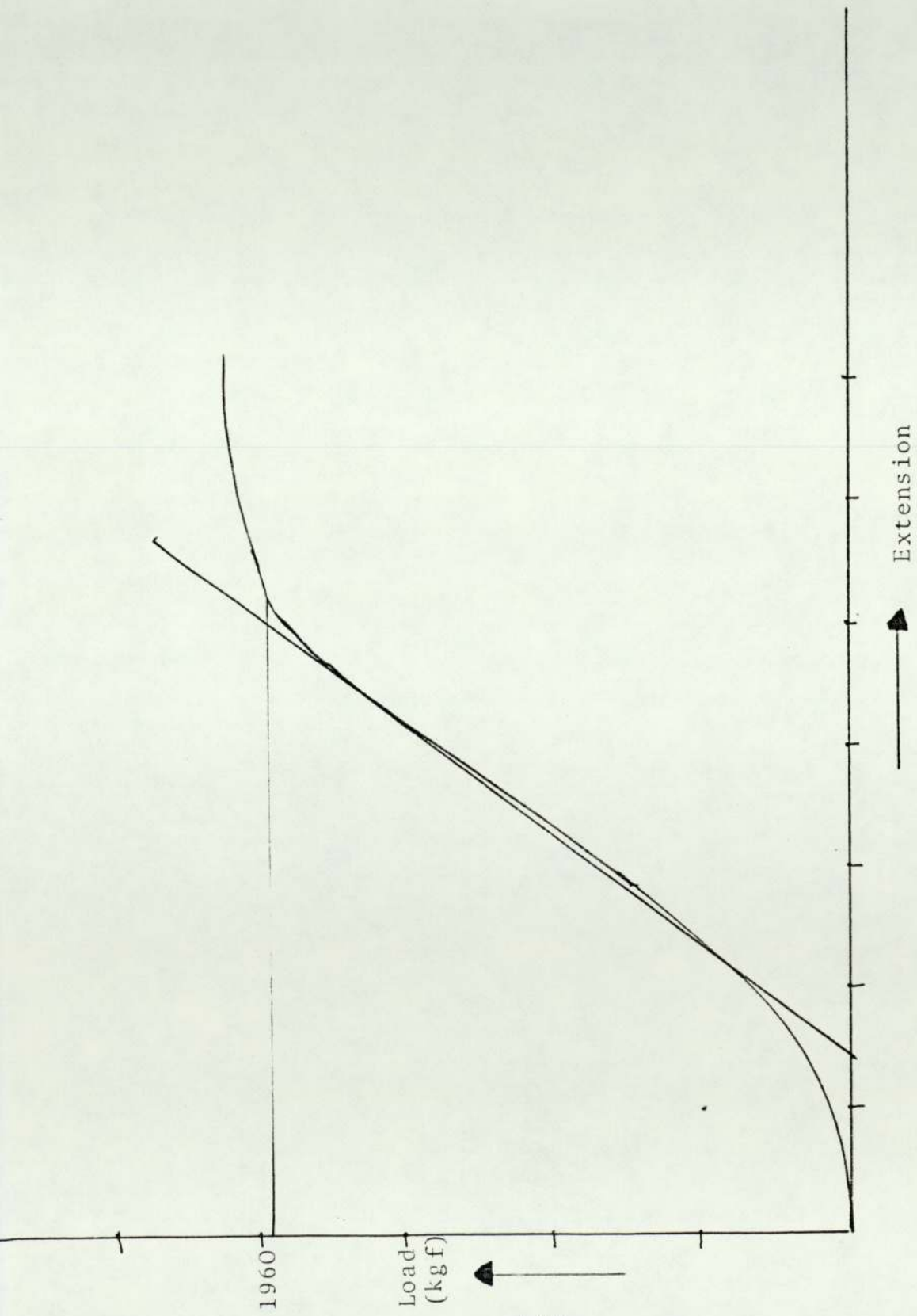


FIGURE 41-8 Load/Extension curve for H.W.
Die Steel "Thermodie" DC

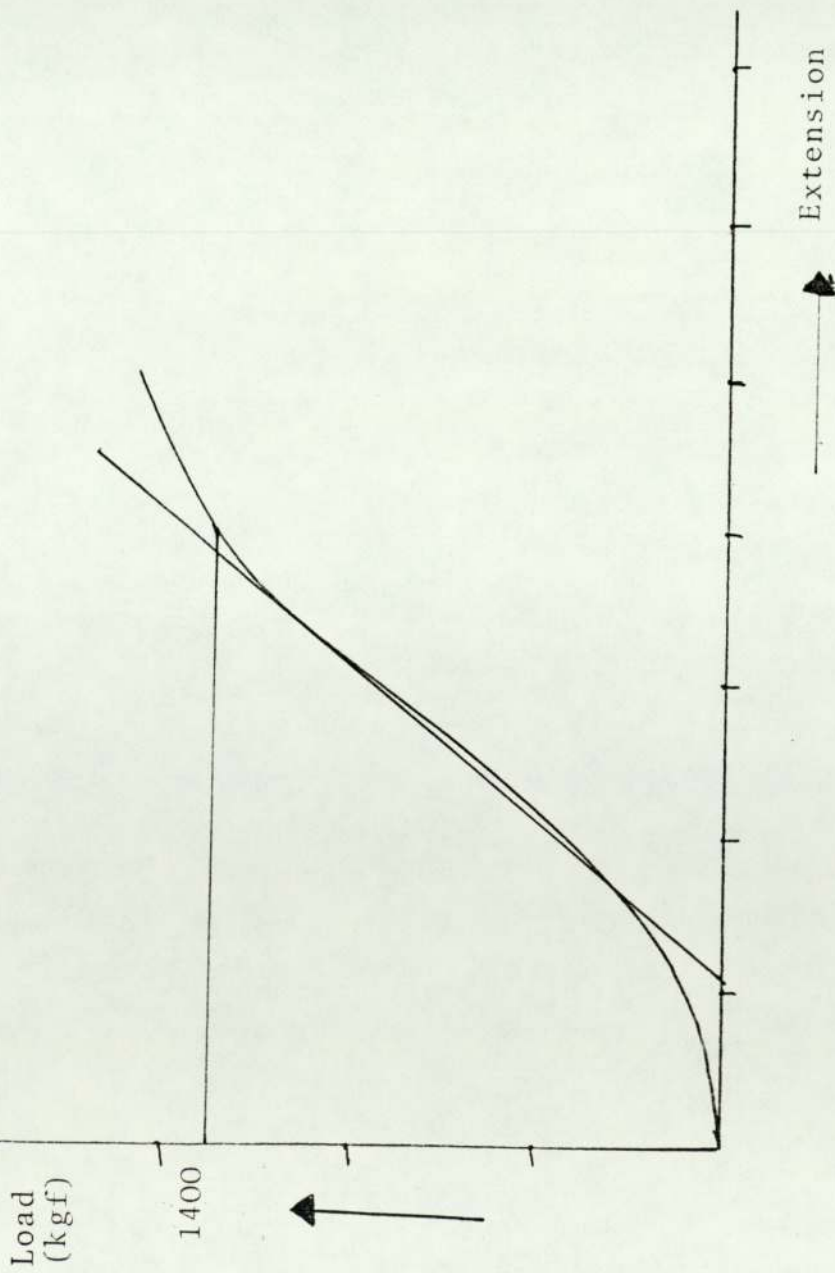


FIGURE 41-9 Load/Extension force for H.W. Die Steel "Thermodie EC

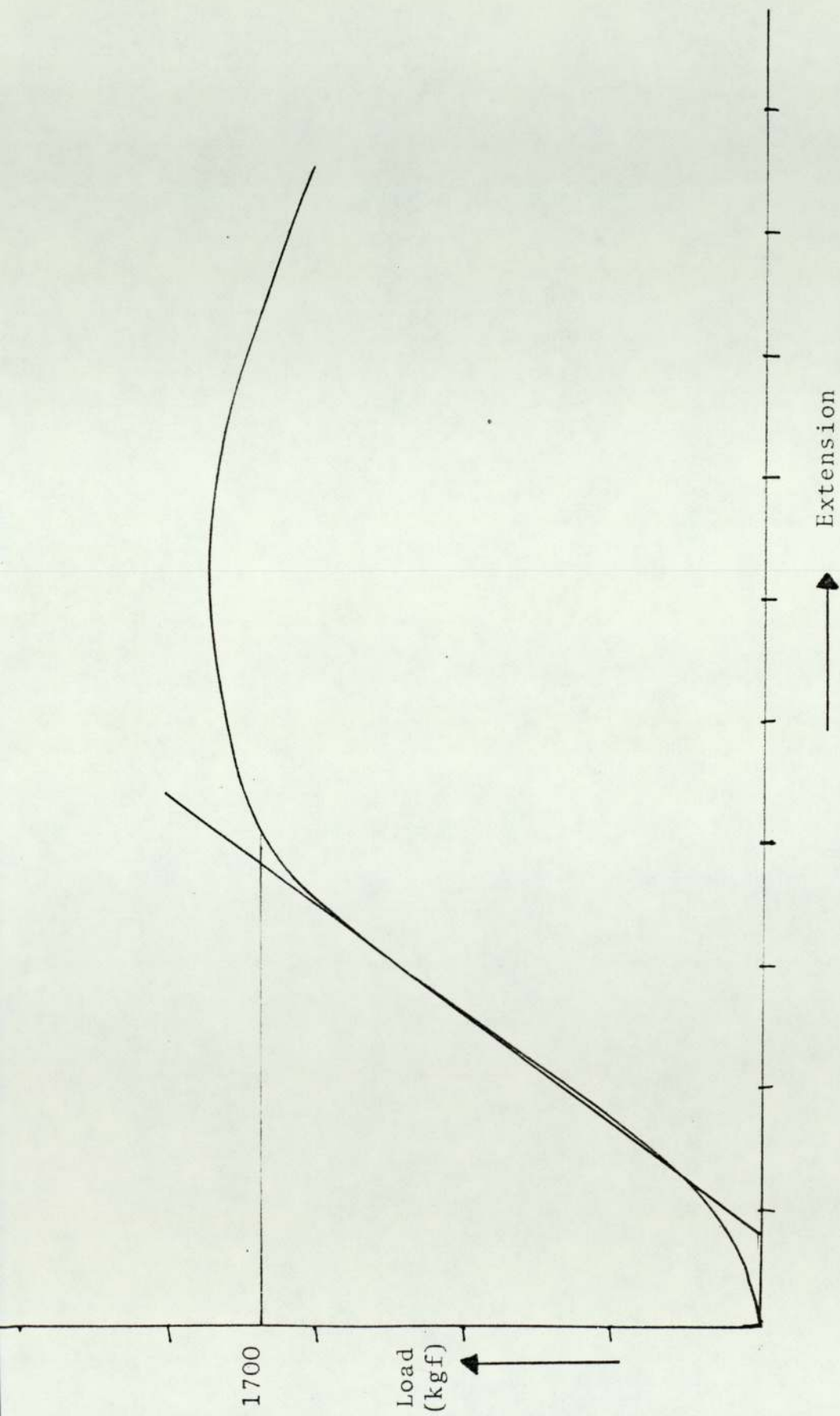


FIGURE 42-1 Load/Extension curve for "Hydie" Steel H10

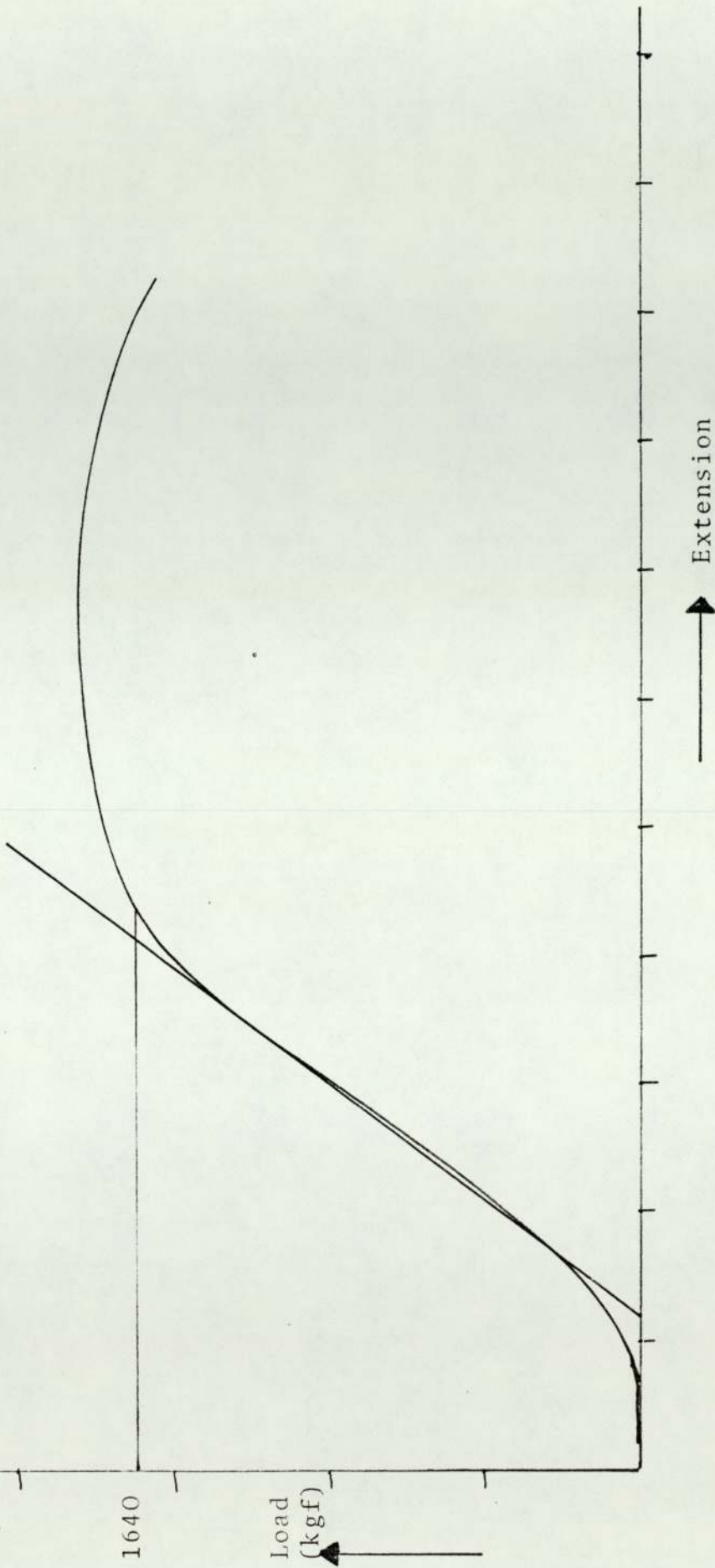


FIGURE 42-2 Load/Extension curve for "Hydie" Steel HIC

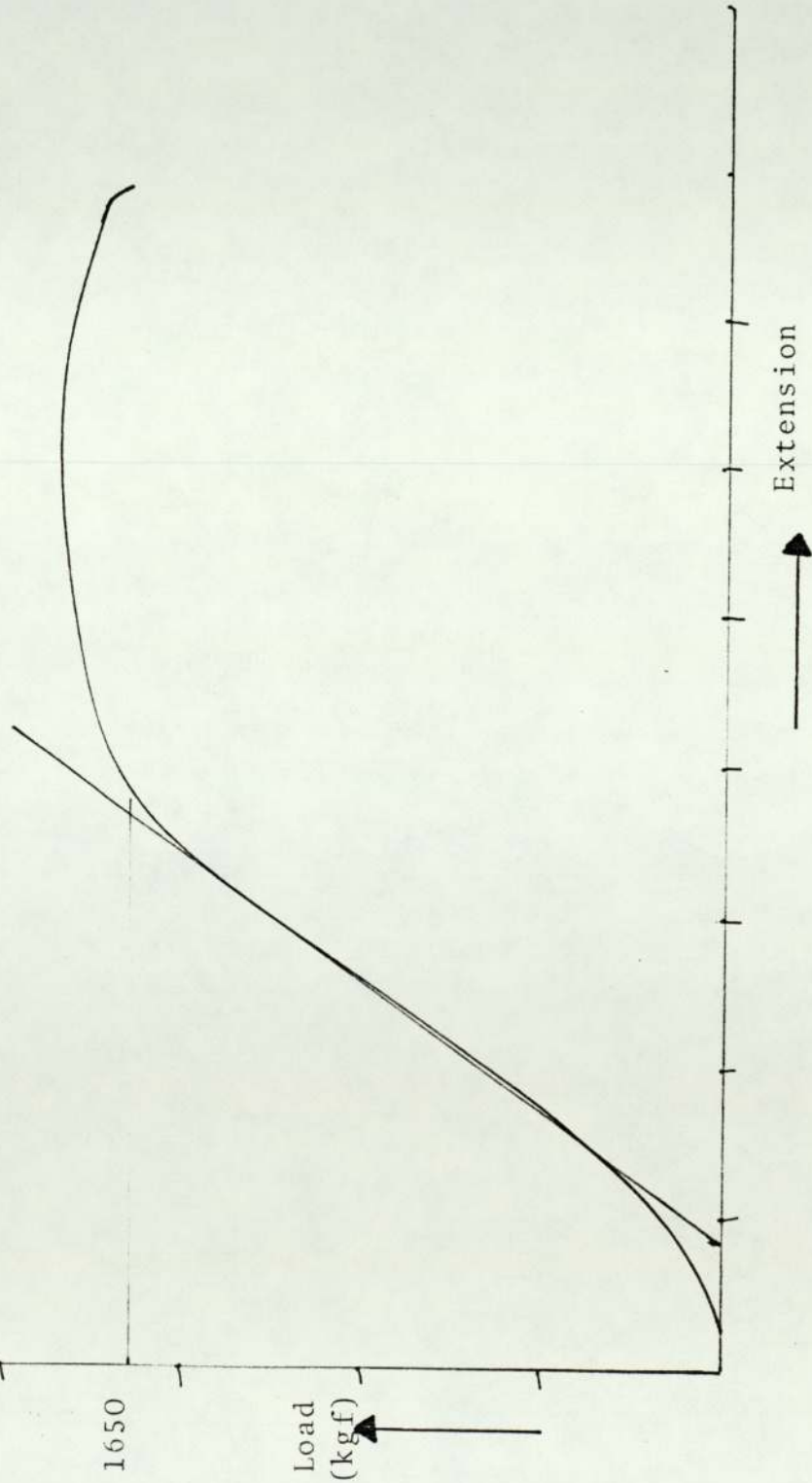


FIGURE 42-3 Load/Extension curve for "Hydie" steel HIB

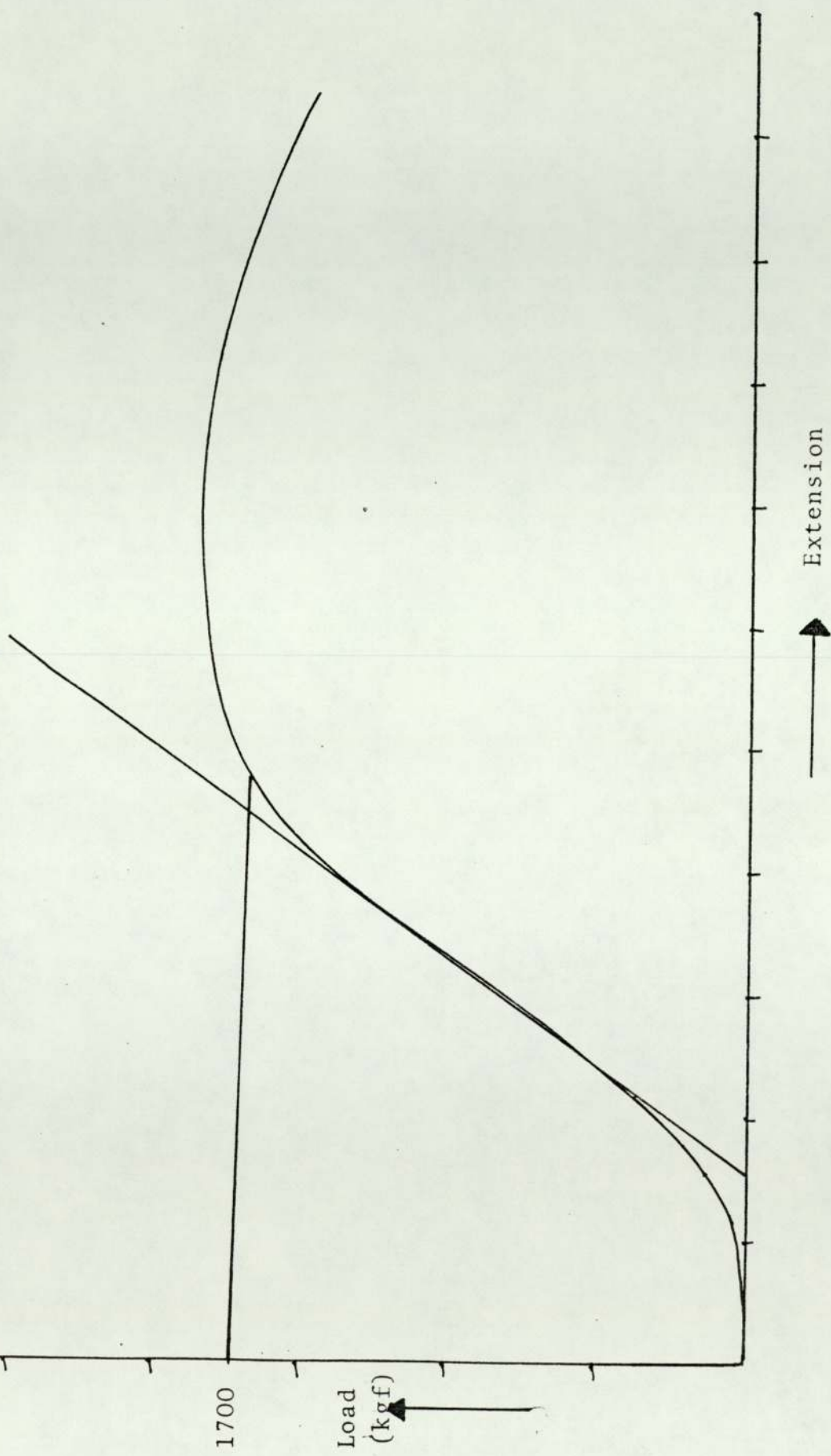


FIGURE 42-4 Load/Extension curve for "Hydie" steel H20

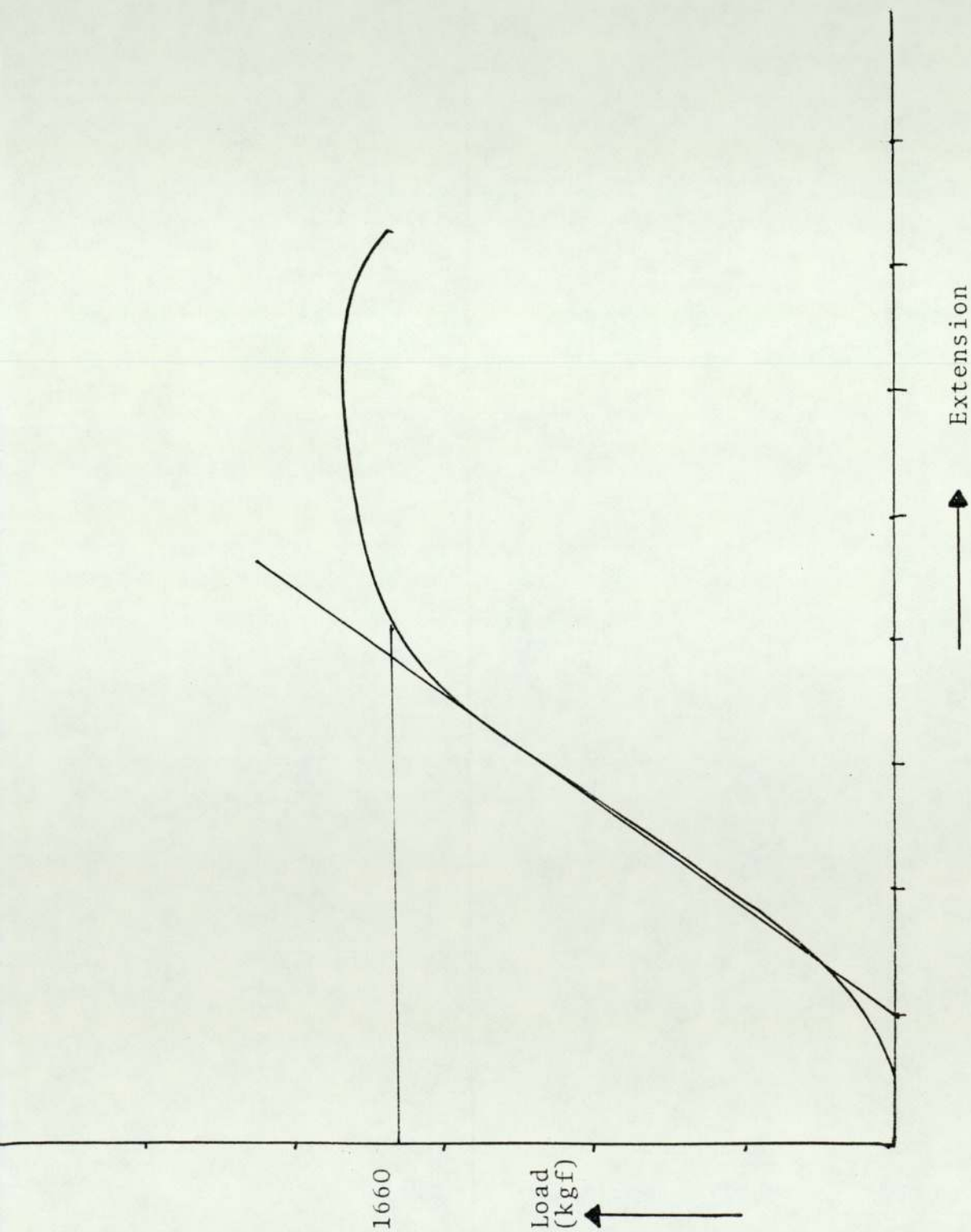


FIGURE 42-5 Load/Extension curve for "Hydie" steel H2C

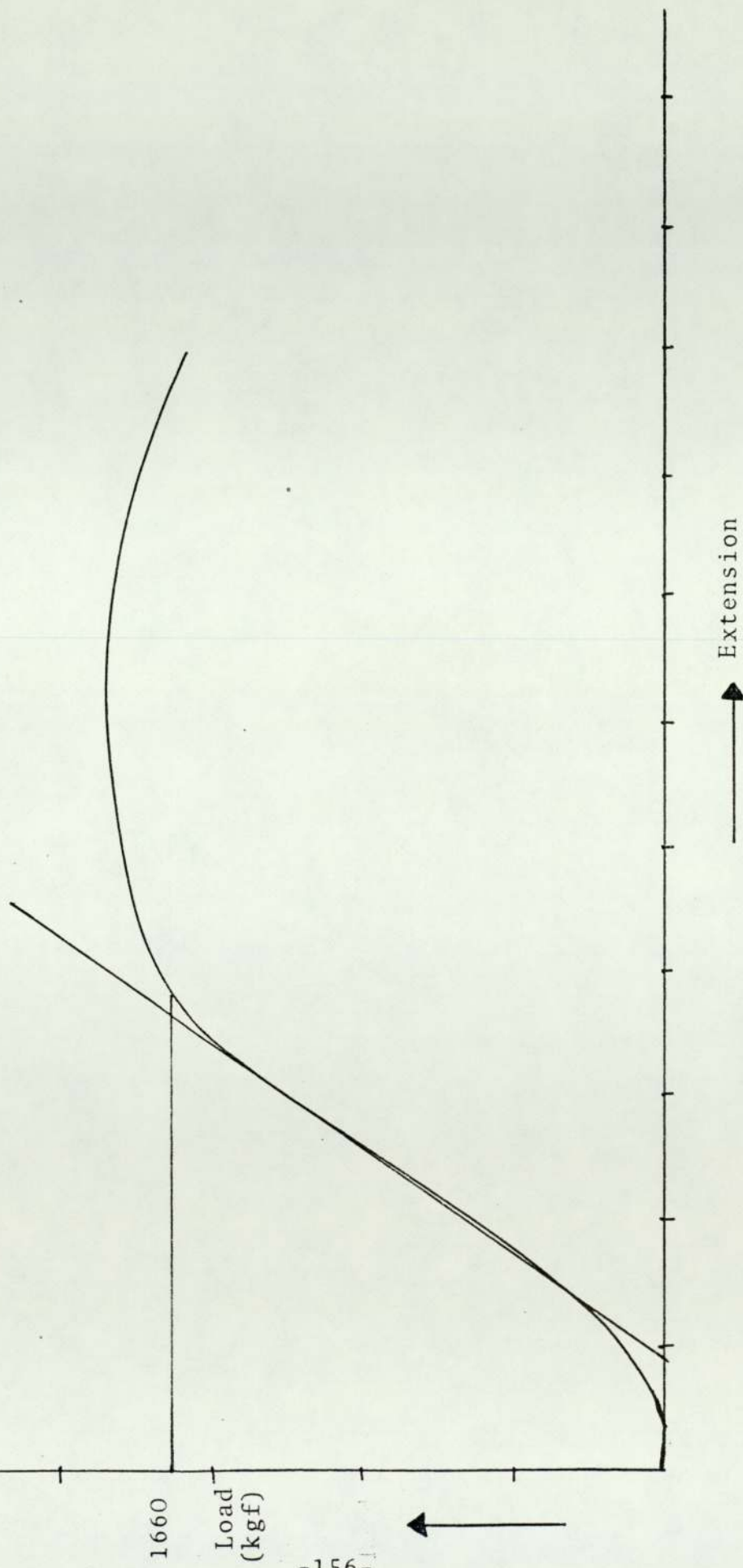


FIGURE 42-6 Load/Extension curve for "Hydie" steel H2B

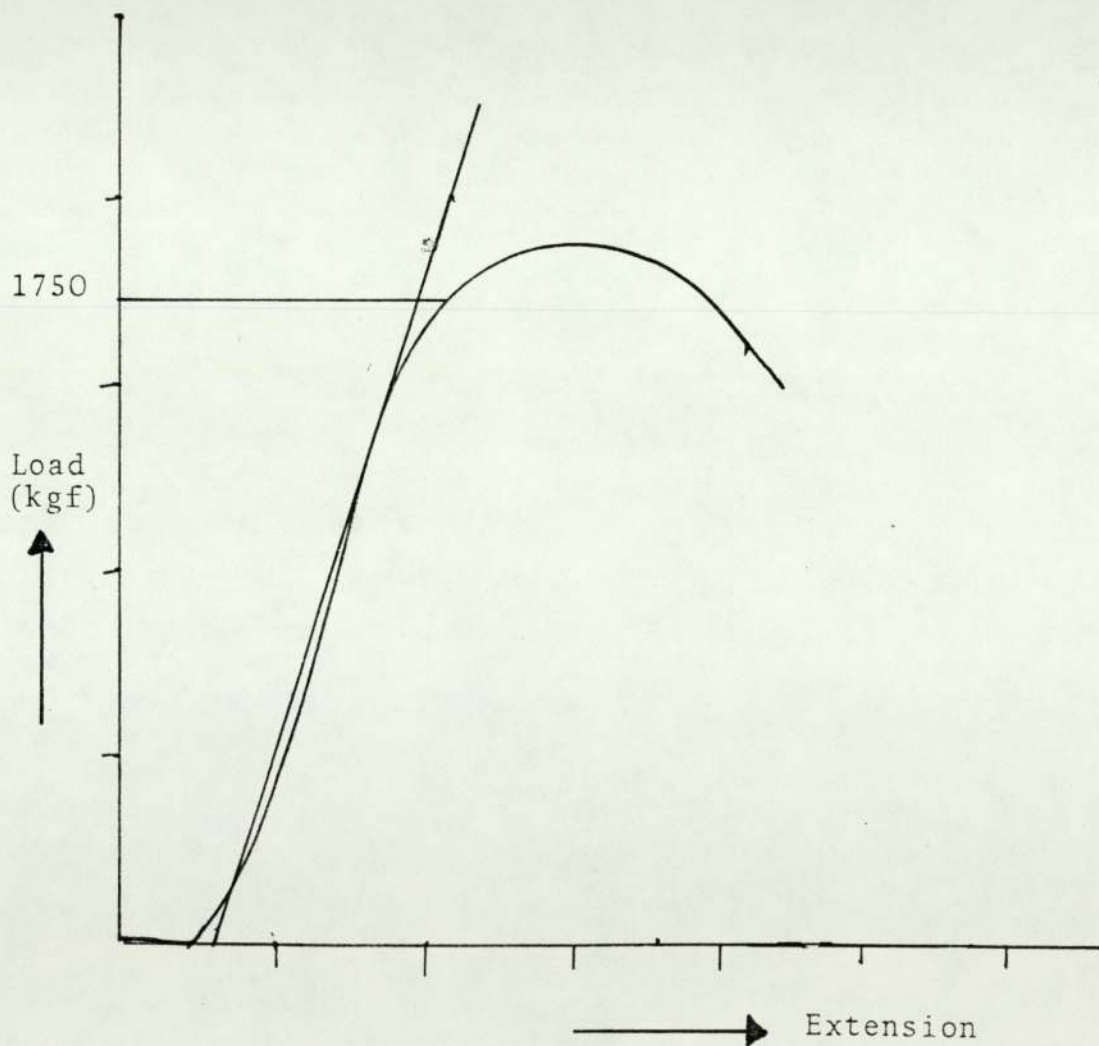


FIGURE 42-7 Load/Extension curve for
"Hydie" Steel H30

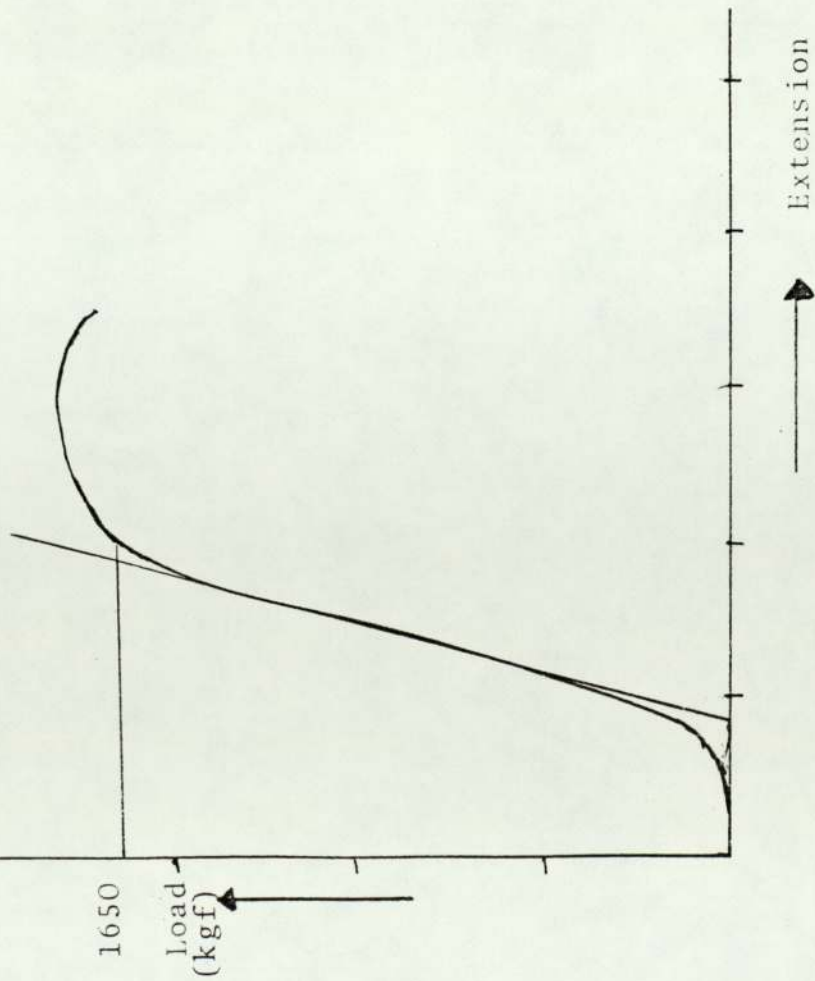


FIGURE 42-8 Load/Extension curve for "Hydie" steel H3C

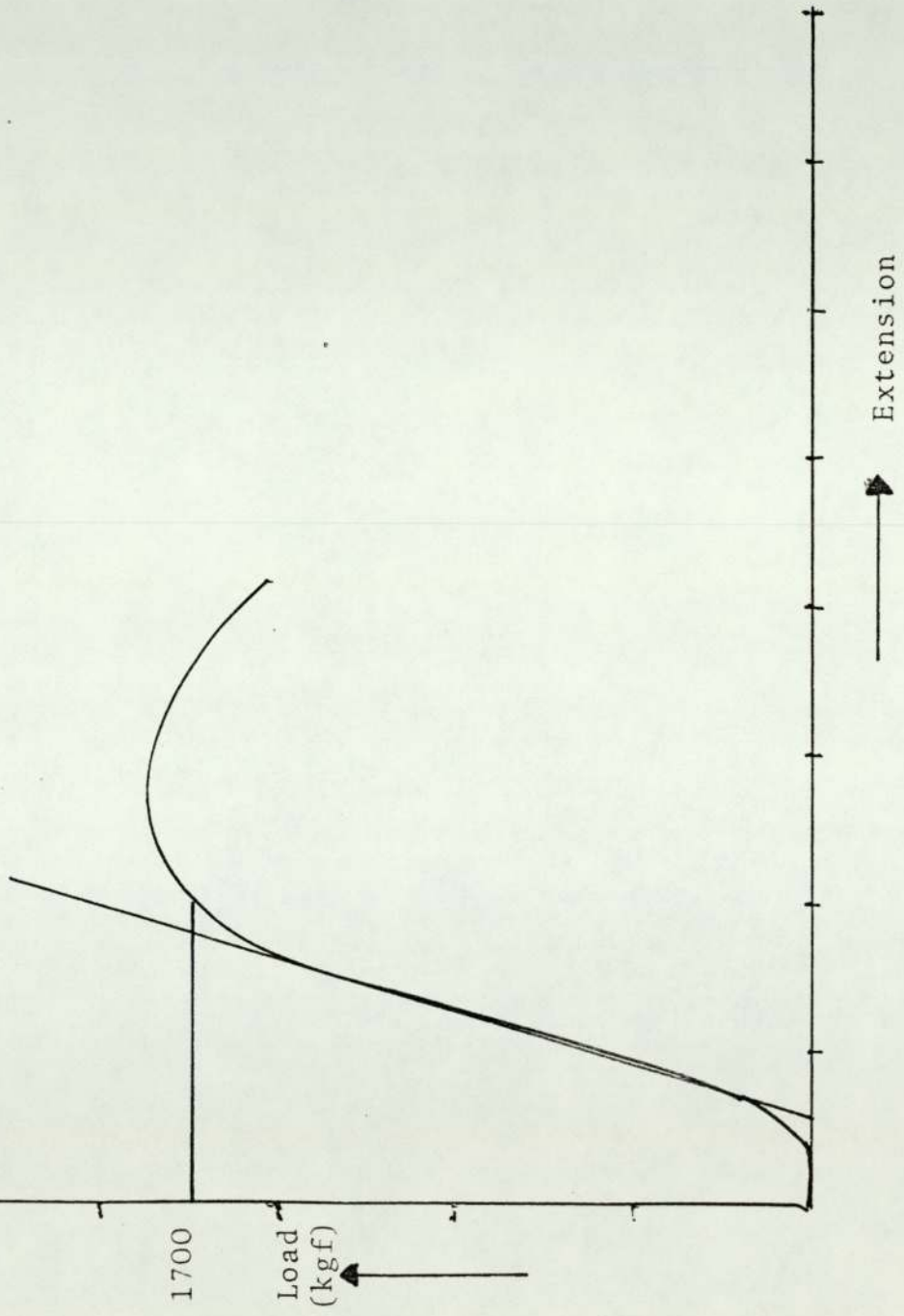


FIGURE 42-9 Load/Extension curve for "Hydie" Steel U3B

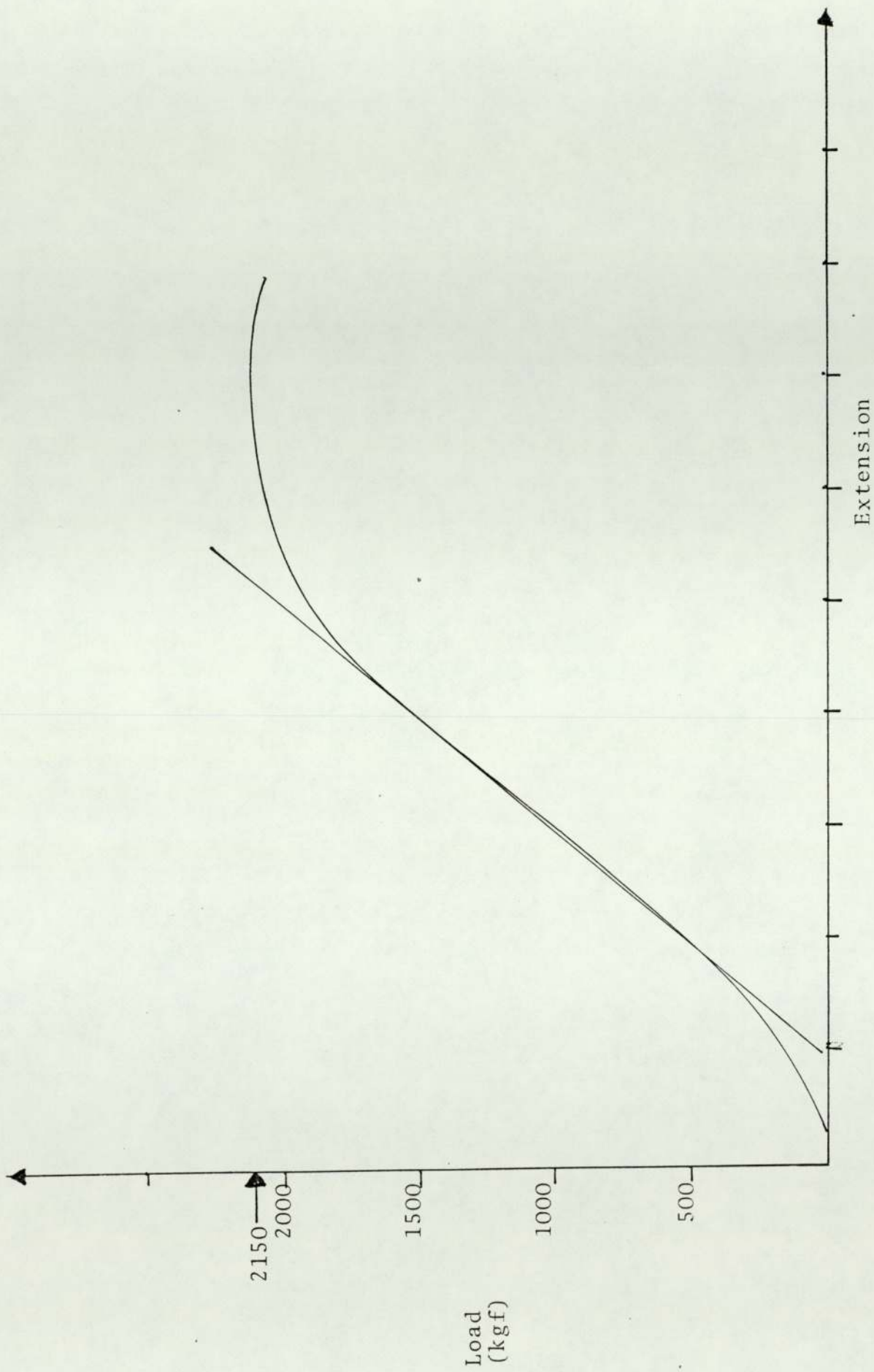


FIGURE 43-1 Load/extension curve of Somdie steel S10

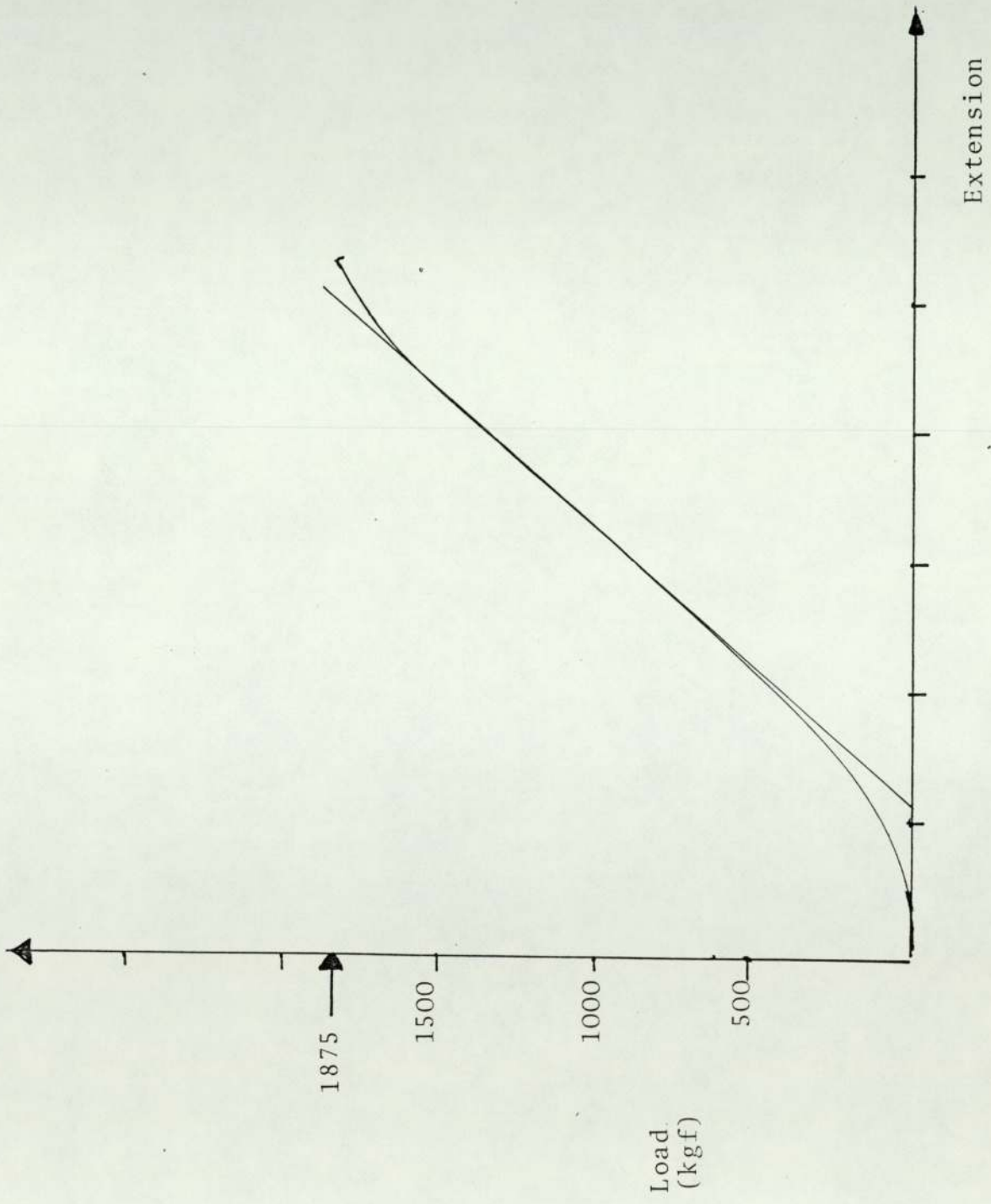


FIGURE 43-2 Load/extension curve of Somdie steel SIC

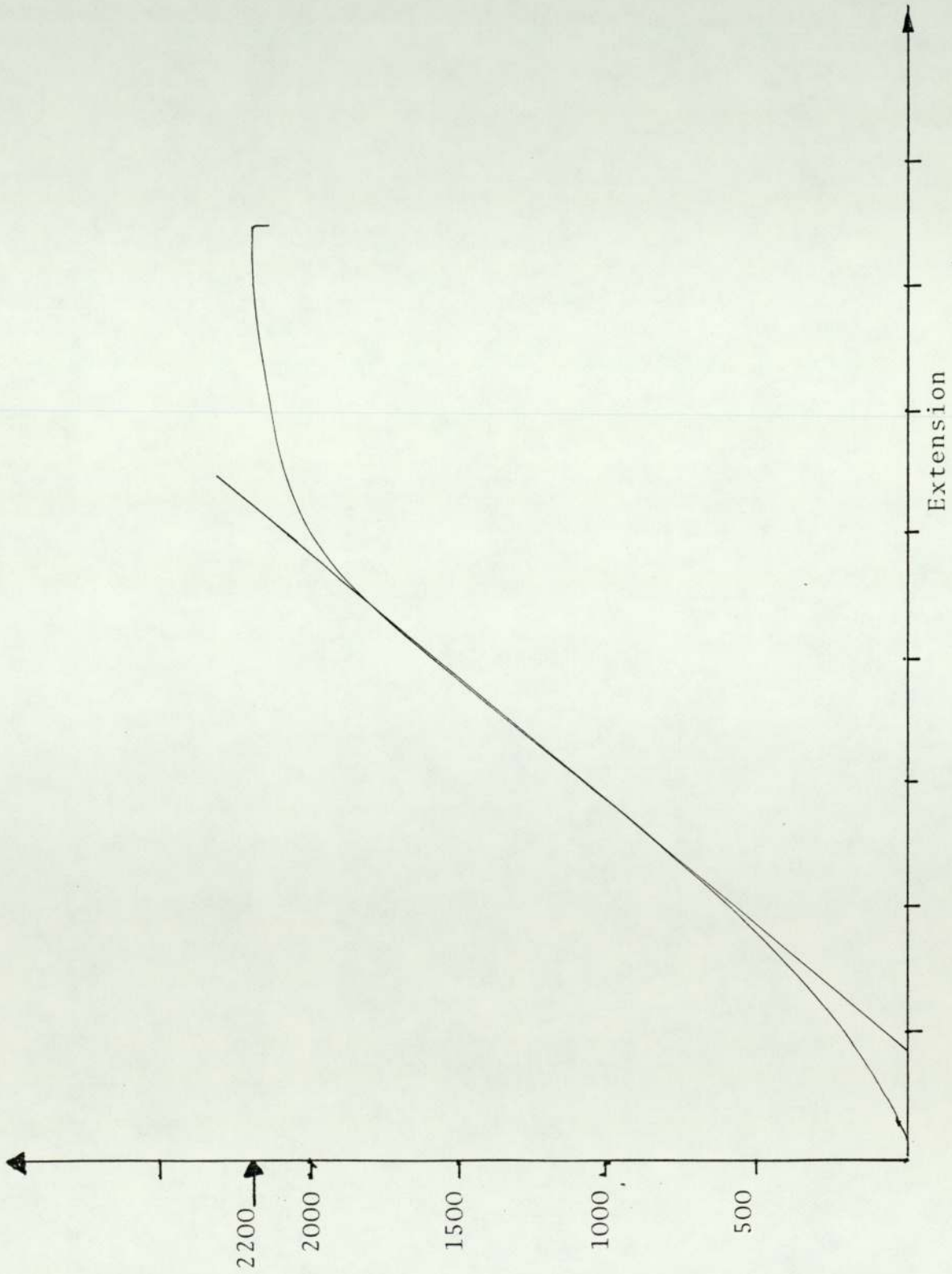


FIGURE 43-3 Load/extension curve of Somdie steel S1B

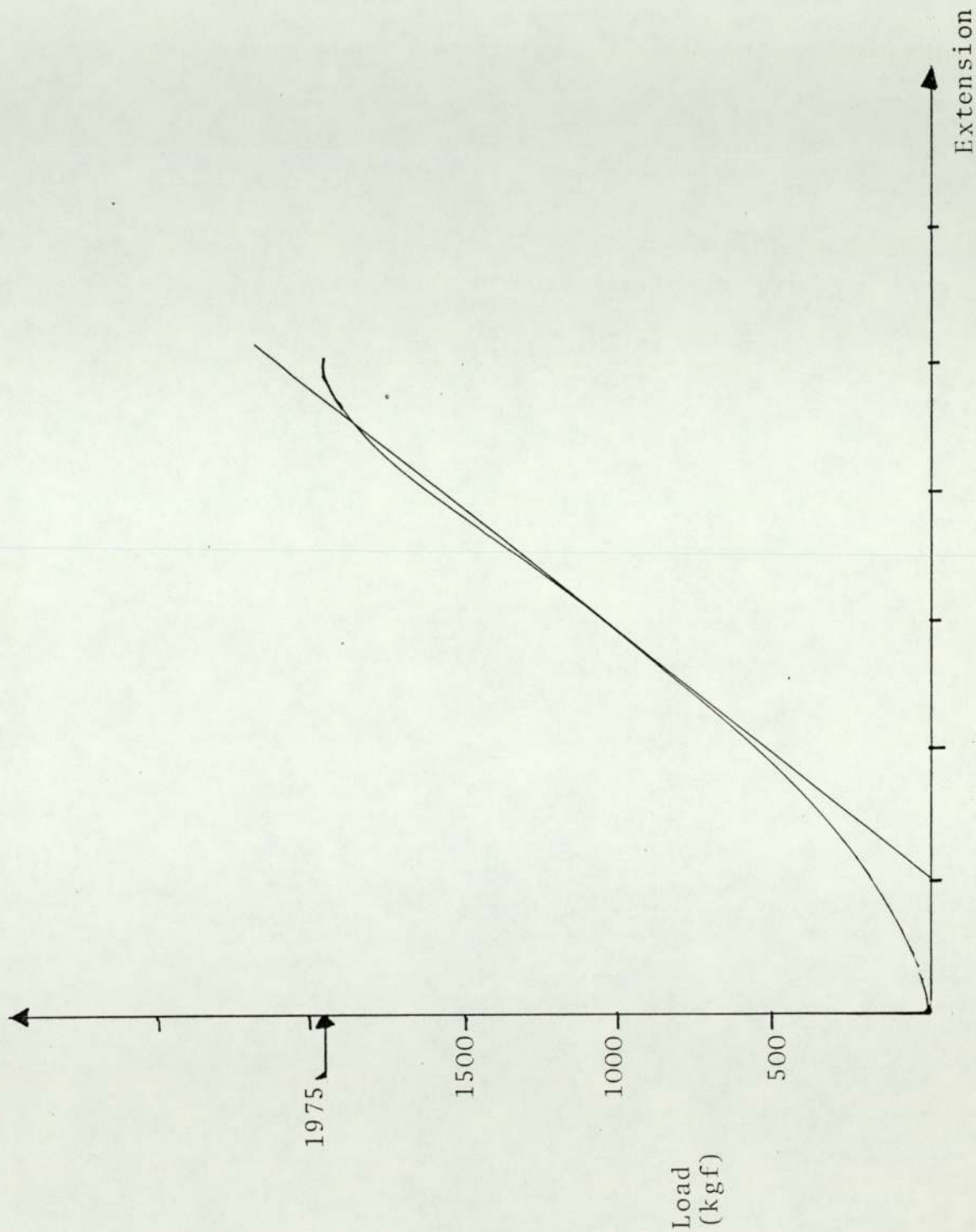


FIGURE 43-4 Load/extension curve for Somdie steel S20

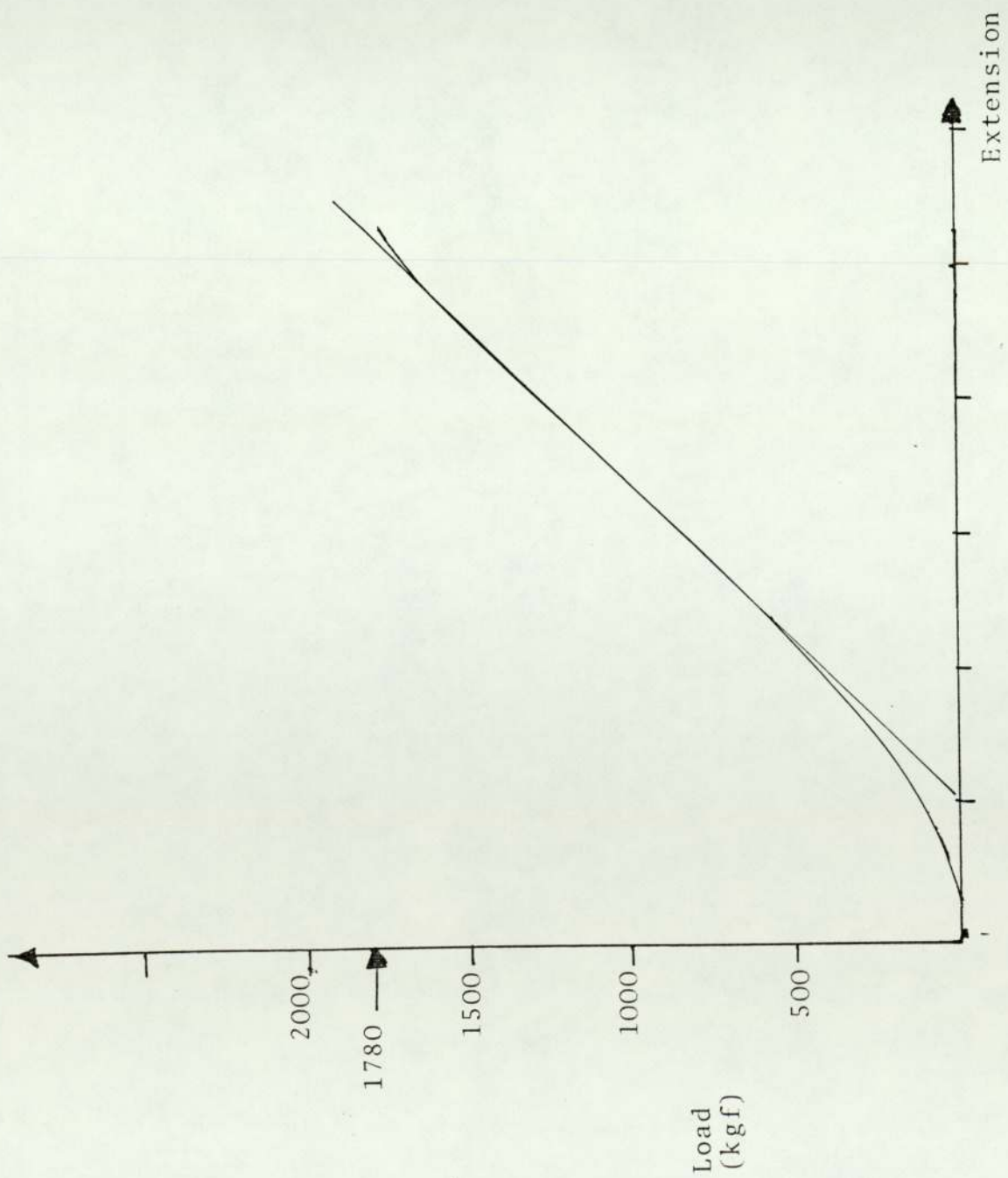


FIGURE 43-5 Load/extension curve for Somdie steel S2C

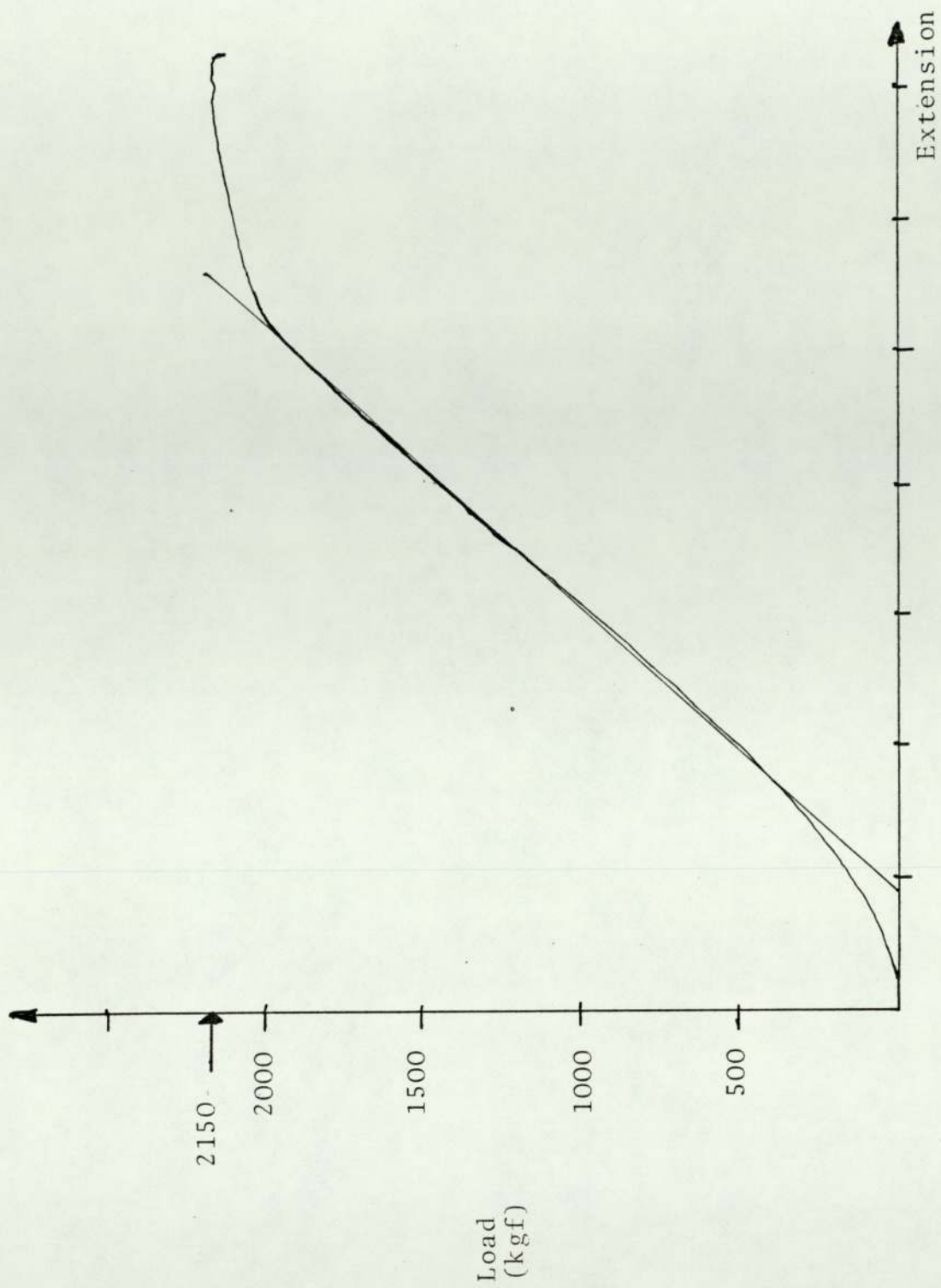


FIGURE 43-6 Load/extension curve for Somdie steel S2B

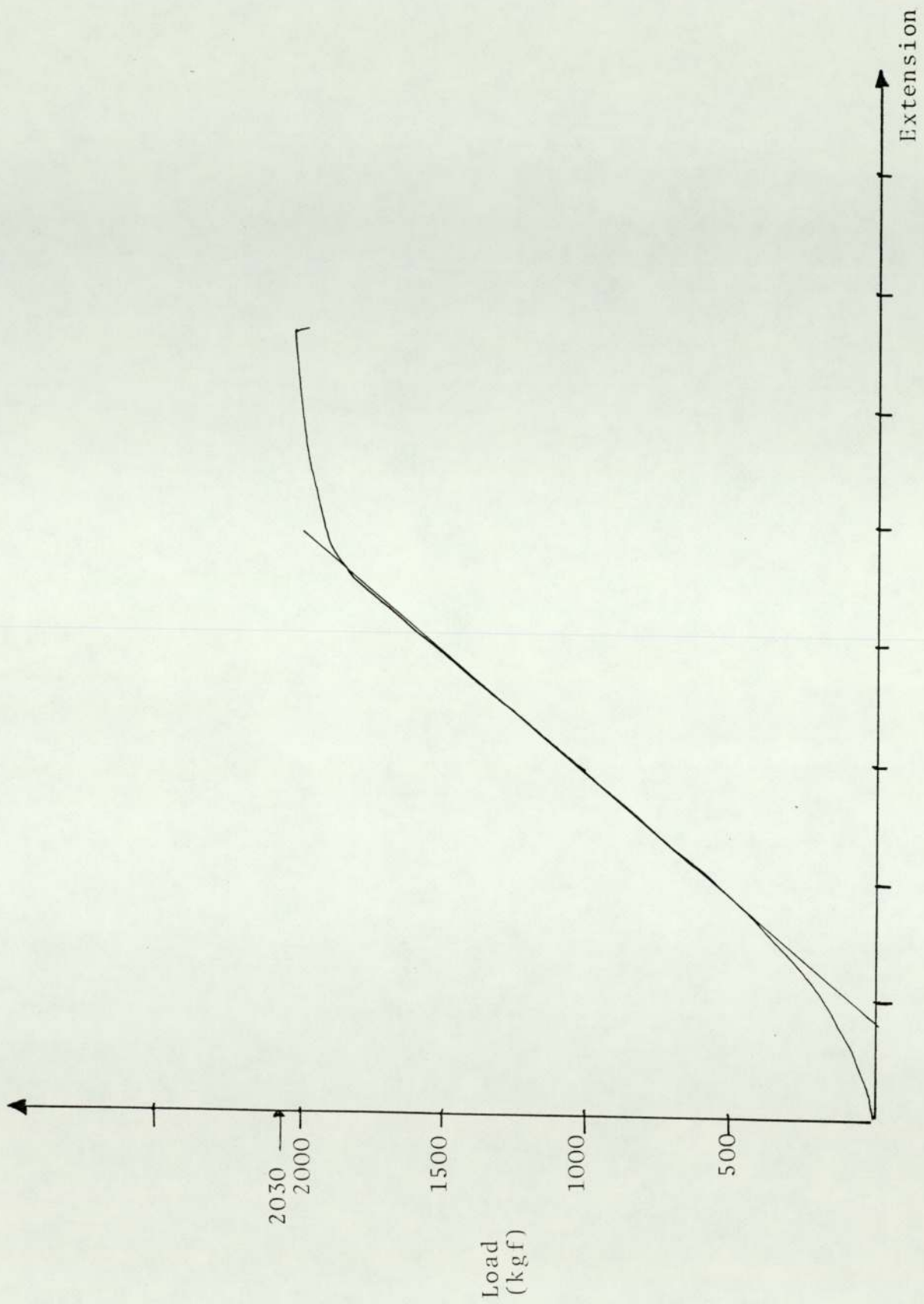


FIGURE 43-7 . Load/extension curve of Somdie steel S30

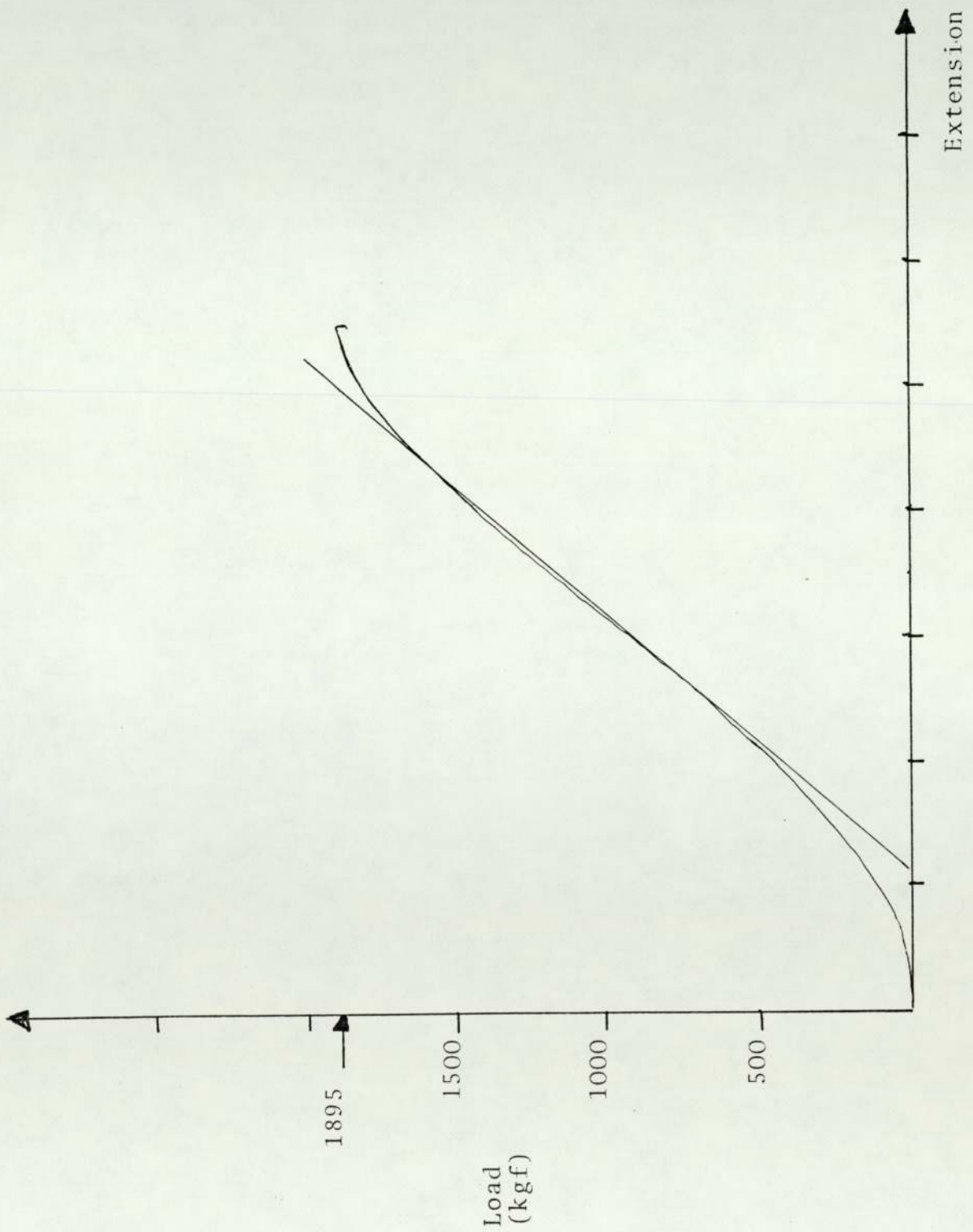


FIGURE 43-8 Load/extension curve of Somedie steel S3C

Reduction of area is more a measure of the deformation required to produce fracture, and its contribution results from the necking process. Because of the complicated stress state in the neck, the values of reduction of area are dependent on specimen geometry and deformation behaviour. They should not be taken as the material properties. Some mechanical properties of the material have been investigated, such as tensile strength, yield stress and the maximum load to fracture, as shown in Tables 3 and 4.

6.5.2 Hardness Testing

Hardness can be defined as the property of a material which causes it to resist the penetration of another body.

Hardness tests are carried out by using a diamond pyramid (Vickers method). Hardness was determined by using 20 kg force; results are incorporated in Tables 3-4, the values given are an average of at least ten readings.

6.5.3 Metallography and Fractography

From each of the alloys specimen halves were taken. The fracture surface at each half along the crack was examined by using the scanning electron microscope. Three photographs were taken from three positions on the fracture surface along the centre at (V), shown as A, B, and C in Plates 2 to 39.

A section along the crack surface was mounted in transparent moulding powder, ground and polished in the normal metallurgical manner and examined in etched conditions (etchant 4% nital). Photographs taken for the microsections in the etched condition from the top, middle and edge along the crack surface are as shown in Plates 40 to 77 inclusive, by using an optical electron microscope, photographs have also been taken along the fatigue/front surface for (Hydie and Somdie) three point bend test, as shown in Plates 78-83

6.6 Heat Tinting Process

Since the heat tinting has long been successful, it was used to obtain baseline data. In the heat tinting method specimens are:

1. Loaded to some predetermined displacement to obtain an estimated crack length,
2. Unloaded,
3. Heat tinted to mark the crack advance,
4. Cooled and broken apart by further loading in order to expose the heat tinted surface for the actual measurement of crack length.

A series of heat tinting tests were carried out on 'Hydie' steel H1 "Short Bar", as shown in Table 8, by placing the specimens in a furnace at 300°C for a minimum of 4 hours and then following the same procedure as above.

7. DATA ANALYSIS

7.1 K_{ICSB} Analysis

By measuring the plane strain fracture toughness of short rod/bar specimens, several specimen test behaviour types have been observed.

One data analysis was valid for most types but when the specimen material displayed the crack jump behaviour during the test a different procedure was appropriate.

The plasticity correction factor for some of the short rod steels and the critical load has been determined from the load/crack mouth opening displacement, as shown in Table 6.

The plasticity correction factor and critical load were determined as follows:-

1. Two or more unloading and reloading paths are drawn when the load is near its maximum value.
2. The high and low points on each unloading-reloading cycle were determined ("H" and "L" points in Fig. 36 (2-8)). A high point is the point at which the grips started moving together to relax the load on the specimen, and the corresponding low point is on the reloading part of the unloading path at half of the high point.

Through the high and low point of each unloading-reloading cycle, an ideal elastic release path is drawn.

3. The average load line represents the average load between the two unloading-reloading cycles. However, this was just before and after the maximum.
4. ΔX was measured (the distance between the release path approximation at the average load line) and ΔX_0 (the distance between the release path approximation at the zero load line).

The value of the plasticity correction was calculated from the equation below:

$$p = \frac{\Delta X_0}{\Delta X}$$

5. K_{ICSB}^{III} value was obtained using the equation (53)

$$K_{ICSB}^{III} = p_Q \frac{AC}{B^{3/2}} \left(\frac{1+p}{1-p} \right)^{1/2}$$

The value of A was obtained from:

$$A = Y_{\min}^* / \sqrt{W/B}$$

$$Y^* = \frac{1}{2} \left[\frac{a_1 - a_0}{a - a_0} \frac{dCEB}{dC^a / W} \right]^{1/2}$$

Biner and Barnby (54) found that "A" for standard specimen used by Barker has to be 18.62.

The value of K_{ICSB} was calculated in three different ways, as follows:

$$1. \quad K_{ICSB}^I = \frac{P_{\max} \cdot A_s}{B^{3/2}}$$

where P_{\max} = maximum load at fracture

A_s = 18.62 as standard

B = specimen diameter or breadth
plasticity correction $p = 0$

$$2. \quad K_{ICSB}^{II} = \frac{P_{\text{first}} A_s}{B^{3/2}}$$

P_{first} = load for the first crack jump

A_s = dimensional constant (18.62)

B = specimen diameter or breadth

p_c = 0

$$3. \quad K_{ICSB}^{III} = \frac{P_Q \cdot A_c}{B^{3/2}} \left(\frac{1+p}{1-p} \right)^{\frac{1}{2}} \text{ estimated fracture toughness}$$

P_Q = average load after loading and re-loading

A_c = calculated dimensionless constant

$p = \frac{\Delta X_0}{\Delta X}$ plasticity correction factor

A representative trace of applied load versus clip gauge opening is reproduced for each material and such curves give an indication of type of fracture behaviour exhibited by the material.

7.2 K_{IC} (Three Point Bend Testing Specimens)

The data obtained from the load-crack opening displacement were used to calculate the stress intensity factor

(K_{IC}). By using the following equation

$$K_{IC} = \frac{P_{\max} Y}{B w^{\frac{3}{2}}}$$

$$Y = \frac{a}{w}$$

where Y is the specimen compliance function dependent on the crack length (a) and the width of the specimen (w), P_{\max} is the maximum load to fracture. B and w are thickness and width of the specimens.

The compliance function that was used to determine Y in this work is given in the following equation:

$$Y = 1.93 - 3.07 \left(\frac{a}{w}\right) + 14.53 \left(\frac{a}{w}\right)^2 - 25.11 \left(\frac{a}{w}\right)^3 - 25.8 \left(\frac{a}{w}\right)^4$$

In the preliminary test programme, the stress intensity factors were calculated according to the plane strain fracture toughness stated in BS.5445.

The crack length was measured after fracturing the specimens by using the shadow graphs as a notch length plus a fatigue crack length of $\frac{1}{4}$, $\frac{1}{2}$, $\frac{3}{4}$ of B along the end of fatigue crack front.

Two criteria were put forward to check the validity of K_{IC} value, these are:

1. P_{\max}/P_Q ratio must not exceed 1.1
2. Limiting thickness criterion is

$$B > 2.5 (K_{IC}/\sigma_{ys})^2$$

8. RESULTS

The test results obtained are summarised in Tables 1 to 12 for fracture toughness short rod/bar and three point bend tests.

General appearance of the test specimens are shown in Plates 84-87. Photographs from the top of the fracture surface down to the edge, as A, B and C respectively have been taken as shown in Plates 2-83

TABLE 1

CONDITION USED FOR TREATMENT OF SHORT
ROD/BAR H.W. DIE STEEL

<u>MATERIALS</u>	<u>CONDITION</u>
Electem and Somdie (short rod)	Water quench from 850°C for 5 minutes, and then OQ down to room temperature. Tempering between 630-640°C.
Thermodie (short rod)	O.Q. from 850°C, cool 150°C before tempering between 630-640°C.
Hydie (short bar)	O.Q. from 900-920°C and tempering immediately.
Somdie (short bar)	W.Q. and tempered

TABLE 2

CHEMICAL ANALYSIS OF SHORT ROD/BAR TEST SPECIMENS

Elements	Electem w/o	Somdie w/o	Thermodie w/o	Hydie w/o
Carbon	0.53	0.53	0.56	0.31
Sulphur	0.028	0.025	0.029	0.021
Silicon	0.30	0.31	0.560	0.24
Phosphorus	0.013	0.023	0.022	0.011
Manganese	0.90	1.04	0.590	0.56
Nickel	1.30	1.17	1.99	0.38
Chromium	0.97	1.30	0.83	2.78
Vanadium	ND	ND	0.01	0.16
Molybdenum	0.28	0.53	0.73	0.18
Cobalt	0.09	0.07	0.03	0.02
Copper	0.15	0.13	0.24	0.18
Tin	ND	ND	0.019	0.24
Aluminium	ND	ND	0.010	ND
Iron	Remainder	Remainder	Remainder	Remainder

TABLE 3

MECHANICAL PROPERTIES OF INVESTIGATED ALLOYS AT ROOM TEMPERATURE UNDER CONDITIONS SET IN TABLE 1 (SHORT ROD SPECIMENS)

Material	Specimen No.	Vickers Hardness	Yield Strength MN/m ² Proof Stress 0.2%	U.T.S. MN/m ²	Reduction in Area %	Elongation %
Electem A	O	420	1205	1284	5	8.3
	M	415	1058	1088	1	5.0
	C	394	1127	1284	0.4	6.5
Electem B	O	426	1137	1205	4	5.0
	M	420	1107	1166	1	5.0
	C	401	1166	1284	5	7.0
Somdie C	O	435	1225	1333	10	10.0
	M	438	1215	1313	5	7.0
	C	412	1235	1362	4	7.5
Somdie D	O	447	1186	1303	8	7.5
	M	441	1210	1323	6	8.0
	C	418	1245	1352	5	6.0
Thermodie E	O	391	1058	1215	5	7.5
	M	337	1019	1166	10	15.0
	C	397	866	990	3	4.0

TABLE 4

MECHANICAL PROPERTIES OF INVESTIGATED ALLOYS AT ROOM TEMPERATURE UNDER CONDITIONS SET IN TABLE 1 (SHORT BAR)

Specimen No.	Vickers Hardness	Yield Strength MN/m ² Proof Stress 0.2%	U.T.S. MN/m ²	Reduction in Area %	Elongation %
H10	381	1029	1127	35	15
H1M	371	1029	1117	25	11
H1C	371	990	1107	34	16
H1A	371	1000	1088	32	14
H1B	381	1000	1117	24	12
H20	388	1039	1137	40	15
H2M	383	1029	1127	6	7
H2C	381	1009	1127	18	12
H2A	358	1000	1107	28	13
H2B	376	1009	1117	32	14
H30	388	1054	1147	40	15
H3M	374	1059	1156	20	12
H3C	362	1029	1117	20	12
H3A	362	1029	1117	30	14
H3B	362	1029	1127	40	16
S10	528	1205	1294	15	7
S1M	420	1137	1176	2	4
S1C	418	1117	1127	2	2
S1A	528	1107	1127	2	1
S1B	432	1254	1323	4	5
S20	528	1235	1254	2	2
S2M	460	1029	1039	1	2.5
S2C	435	1088	1088	1	2
S2A	429	1156	1176	3	3
S2B	435	1264	1274	6	5
S30	411	1205	1225	5	5
S3M	432	1176	1176	2.5	2.5
S3C	426	1225	1125	2.5	3
S3A	438	-	-	-	-
S3B	438	1303	1323	4	3

TABLE 5

SPECIMENS DIMENSIONS OF H.W. DIE STEEL SHORT ROD

Specimen No.	B mm	W mm	a ₀ mm	a ₁ mm	θ	AC	AS	
Electem	AO	25.41	38.27	14.17	0.50	58	19.23	18.62
	AM	25.48	38.27	14.37	0.70	58	18.92	18.62
	AC	25.47	38.28	13.23	1.52	55	17.96	18.62
	BO	25.46	38.23	14.32	0.00	55	19.63	18.62
	BM	25.40	38.16	14.46	0.45	58	19.60	18.62
	BC	25.44	38.14	14.76	0.00	55	20.13	18.62
Somdie	CO	25.46	38.13	13.93	0.45	56	19.12	18.62
	CM	25.45	38.18	13.78	0.00	55	19.12	18.62
	CC	25.45	38.09	13.89	0.01	55	19.27	18.62
	DO	25.47	38.12	17.32	0.30	65	23.12	18.62
Thermodie	DM	25.45	38.08	14.72	0.25	58	20.02	18.62
	DC	25.44	38.10	13.40	0.003	55	18.79	18.62
	EO	25.43	38.14	12.84	0.40	57	18.12	18.62
	EC	25.32	38.17	14.67	1.735	58	19.22	18.62

TABLE 6

H.W. DIE STEEL FRACTURE TOUGHNESS TEST RESULTS
SHORT ROD SPECIMEN

Specimen No.	P _{max} kg	P _Q kg	P _c	K _{ICSB} ^I MN/m ^{3/2}	K _{ICSB} ^{II} MN/m ^{3/2}
AO	1890	1862	-	85	87
AM	1625	-	-	73	74
AC	1875	1781	-	84	81
*BO	2050	2000	0.18	92	97
BM	1625	-	-	73	77
BC	1875	1742	-	84	91
CO	1975	1883	-	89	91
CM	1875	-	-	84	87
CC	1575	-	-	71	73
DO	2325	2219	-	104	130
DM	4613	4293	-	208	223
DC	1725	1631	-	78	78
EO	2800	-	-	126	123
EM	2775	2722	0.11	125	-
EC	1200	-	-	54	56

* Fracture toughness for specimen BO is also calculated by using the plasticity correction factor

$$K_{ICSB} = 113 \quad \text{calculated by } K_{ICSB} = \frac{P_0 \cdot AS}{B^{3/2}} \left(\frac{1+p}{1-p} \right)^{\frac{1}{2}}$$

$$K_{ICSB}^I = \frac{P_{max} \cdot AS}{B^{3/2}} \quad P_{max} = \text{max. load to fracture}$$

$$K_{ICSB}^{II} = \frac{P_{max} \cdot AC}{B^{3/2}} \quad P_Q = \text{average load}$$

AS = standard constant (18.62)

AC = calculated constant

TABLE 7

SPECIMEN DIMENSIONS OF "HYDIE" STEEL SHORT ROD

Specimen No.	B mm	W mm	a ₀ mm	a ₁ mm	θ	AS
H10	25.48	38.29	12.59	0.85	55.17	18.62
H1M	25.48	38.46	12.86	0.40	54.04	18.62
H1C	25.40	38.29	12.69	0.85	55.88	18.62
H1A	25.48	38.29	12.39	0.60	54.05	18.62
H1B	25.48	38.29	12.59	0.60	54.78	18.62
H20	25.47	38.29	12.58	0.30	54.20	18.62
H2M	25.48	38.29	12.39	0.60	54.33	18.62
H2C	25.45	38.29	12.39	0.65	54.74	18.62
H2A	25.47	30.28	12.58	0.60	53.80	18.62
H2B	25.47	38.29	12.59	0.55	53.90	18.62
H30	25.47	38.29	12.19	0.45	53.90	18.62
H3M	25.47	38.29	12.59	0.50	54.80	18.62
H3C	25.48	38.29	12.59	0.60	54.20	18.62
H3A	25.47	38.29	12.59	0.55	53.50	18.62
H3B	25.48	38.29	12.59	0.65	55.30	18.62

TABLE 8

"HYDIE" STEEL FRACTURE TOUGHNESS TEST RESULTS "SHORT BAR"
SPECIMENS

P_{\max} kg	P_{first}	$K_{IC(SB)}^I$ MN/m ^{3/2}	$K_{IC(SB)}^{II}$ MN/m ^{3/2}
1245	1240	55.89	55.67
1397	1000	62.72	44.90
1270	1270	57.29	57.29
1330	1330	59.71	59.71
1280	1170	57.47	52.53
1660	1060	74.57	47.62
1280	-	57.47	-
1540	-	69.26	-
1675	-	75.24	42.68
1370	-	61.54	-
1710	1710	78.30	64.12
1380	1100	63.19	49.41
1220	-	55.86	-
1180	1100	53.06	49.41
1580	1200	70.98	53.91

$$K_{IC(SB)}^I = \frac{P_{\max} \cdot AS}{B^{3/2}}$$

P_{\max} = maximum load to fracture

$$K_{IC(SB)}^{II} = \frac{P_{\text{first}} \cdot AS}{B^{3/2}}$$

P_{first} = first crack jump load

AS = 18.62 standard constant

TABLE 9

"HYDIE" CRACK LENGTH MEASUREMENT FOR SHORT BAR SPECIMEN

Spec. No.	W mm	B mm	Notch Depth mm	a mm	a _c mm	Crack Length after Heat Tinting mm	Crack Jump Load 1	Crack Jump Load 2	K _{IC} (SB) MN/m ^{3/2}
H10	38.29	25.48	12.59	22.59	18.71	20.84	1240	1245	55.89
H1M	38.46	25.48	12.86	18.86	18.80	17.11	1000	1397	62.72
H1C	38.29	25.40	12.69	22.79	18.71	21.04	1270	1220	57.29
H1A	38.29	25.48	12.39	24.46	18.71	22.71	1330	1280	59.71
H1B	38.29	25.48	12.59	21.54	18.71	19.79	1170	1280	57.47

$$a_c / (w - 1.75) = 0.512 \quad (57)$$

$$a_c = 0.512 (38.1 - 1.75)$$

$$= 18.6112 \text{ "for standard specimen"}$$

where

a_c is the critical crack length (mm)

w is the width (mm) of the test specimen

TABLE 10

SPECIMEN DIMENSIONS OF H.W. SOMDIE STEEL (SHORT BAR)

Specimen No.	B mm	W mm	a ₀ mm	a ₁ mm	θ	As
S10	25.28	38.19	12.59	0.55	53.8	18.62
S1M	25.28	38.19	12.29	0.50	53.9	18.62
S1C	25.28	38.18	12.88	0.85	53.8	18.62
S1A	25.29	38.19	12.59	0.70	54.0	18.62
S1B	25.28	38.20	12.50	0.35	53.6	18.62
S20	25.28	38.19	13.19	0.65	53.0	18.62
S2M	25.28	38.19	12.79	0.65	53.0	18.62
S2C	25.28	38.19	12.59	0.60	54.0	18.62
S2A	25.28	38.19	12.99	0.50	53.8	18.62
S2B	25.27	38.19	12.59	1.20	54.0	18.62
S30	25.29	38.18	12.48	1.0	53.0	18.62
S3M	25.28	38.18	12.68	1.5		18.62
S3C	25.28	38.19	12.69	0.5	53.0	18.62
S3A	25.28	38.19	-	-	-	-
S3B	25.27	38.19	12.79	1.0	53.7	18.62

TABLE 11

H.W. SOMDIE STEEL FRACTURE TOUGHNESS RESULTS
"SHORT BAR"

Specimen No.	P _{max} kg	K _{ICSB^I} MN/m ^{3/2}
S10	3175	143
S1M	1825	83
S1C	1575	72
S1A	1540	70
S1B	2725	124
S20	3250	148
S2M	2250	102
S2C	1925	88
S2A	2375	108
S2B	2975	135
S30	3275	149
S3M	3427	156
S3C	1575	72
S3A	-	-
S3B	3500	159

$$K_{ICSB^I} = \frac{P_{max} A_s}{B^{3/2}}$$

P_{max} = maximum load to fracture

TABLE 12

FRACTURE TOUGHNESS (K_{IC}) RESULTS FOR THREE POINT BEND TEST

Specimen No	Width 'W' mm	Breadth 'B' mm	Notch Depth mm	Crack Depth 'a' mm	a/w	Y	P _{max} kgf	$K_{IC}^{3/2}$ MN/m	$K_{ICSB}^{3/2}$ MN/m
HO	35.1	25.44	10.48	11.22	0.32	6.39	4900	64.46	74.57
HM	35.1	25.44	10.40	16.5	0.47	9.66	3100	61.62	57.47
HC	35.1	25.44	10.40	14.03	0.40	7.89	3725	61.0	69.26
S1	38.11	25.41	15.3	17.58	0.464	9.4	3050	57.1	148.0
S2	38.11	25.41	15.1	17.5	0.46	9.37	6285.7	116.0	102.0
S3	38.11	25.41	14.59	16.24	0.426	8.49	4750	80.0	88.0

TABLE 13

TEST RESULT OF SHORT ROD/BAR WITH STANDARD DEVIATION

Specimen No.	K_{ICSB} MN/m ^{3/2}	Average K_{ICSB} MN/m ^{3/2}	No. of Test	Standard Deviation	%
"Electem"	AO	85	1	4.95	5.6
	BO	92	2		
	AM	73	1	0	0
	BM	73	2	0	0
	AC	84	1		
	BC	84	2		
"Somdie"	CO	89	1	10.6	11
	DO	104	2		
	CM	84	1	87.68	60
	DM	208	2		
	CC	71	1	4.95	6.8
	DC	70	2		
"Hydie"	H10	56	1	8.44	12
	H20	75	2		
	H30	78	3		
	H1M	63	1	2.04	3.4
	H2M	58	2		
	H3M	63	3		
	H1C	57	1	2.98	4.9
	H2C	69	2		
	H3C	56	3		

9. DISCUSSION

General

Four types of die steel were investigated. The fracture properties of these steels were evaluated using short rod/bar and three point bend test specimens. The experimental testing was designed so that all measurements necessary for load/crack mouth opening displacement methods could be recorded during testing of a single specimen.

The fracture toughness was followed by macroscopic and microscopic observations of the broken specimens. For clarity of presentation, the discussion has been divided into sections.

9.1 Metallography and Fractography

Despite the differences in the four different types of die steels, the fracture surfaces exhibited similar features which could be categorised in the following way:

1. Fully Brittle

As shown in Plates 16, 17, 22 and 38, the fracture surface was made up almost entirely of cleavage facets, often with microcracks and stepped features associated with it. There was no evidence that change in orientation from one cleavage facet to another involved any substantial amount of ductile fracture.

2. Brittle but with isolated ductile regions, as shown in Plates 3, 4, 6, 10, ¹³18, 19, 20, 21, 22, 23, 24, 25, 28, 32, 33, 34.

Here, although the fracture surface was predominantly brittle, regions of ductile fracture, generally no larger than a grain, occurred randomly distributed along the crack. The dimpled features of these areas were always much finer than the main feature associated with ductile slow crack growth, were similar to that observed in the shear tip regions, as shown in Plates 11 and 12, but were never associated with inclusions.

3. Ductile slow crack growth ⁽³²⁾, as shown in Plates 5, 8, 11 and 14. These regions could be observed only for the shorter cracked specimens. Some of these tests probably failed entirely in the slow ductile mode while others started in the ductile mode but change eventually to fast brittle fracture could be observed within the slow crack growth areas and some ductile dimpling within the predominantly brittle regions. The dimpled regions tended to link one void with another, as shown in Plates 2, 5, 8, 11 and 14. The voids on the other hand, apart from containing inclusions, have similar appearance to the stretch zone. This similarity between the stretch zone suggests that voids are really a quasi-continuous extension of stretch zone ⁽⁵⁵⁾. Ductile tearing of this nature, that is void growth, generally around

inclusions linked by bridge of ductile dimples, as shown in Plates 2, 3, 5, 7, 8, 10, 14, 15, 26, 29, 30, 31, 35, 36, 37 and 39. These can occur either at plastic collapse or during slow stable crack growth. The crack growth is the crack tip controlled rather than controlled by dimensions of uncracked ligaments. Effects of these inclusions (type, shape) on fracture toughness are covered later.

Scanning electron microscopy of the fracture surface revealed for Electem, Thermodie, Hydrie and Somdie steels cleavage with no evidence of either ductile by tearing or intergranular fracture.

Lynch (63) considered that cleavage fracture usually occurred by tensile decohesion and, hence, proposed criteria for predicting cleavage which was based on the relative stresses required for slip and for decohesion at crack tips.

Fracture can involve such extensive deformation that specimens neck down to edge, or so little deformation that specimens are brittle on an atomic scale. Between these two extremes there are many cases where fracture involves nucleation, growth and coalescence of voids ahead of cracks, so that fracture surfaces are dimpled, Plates 30, 31, 36, 37 and 39. When deformation is extensive, dimples are quite large and deep and fractures are macroscopically ductile, S1M, S1C, S1A. However, when deformation is

highly localised at crack tips, dimples are very small and shallow and fractures are macroscopically brittle, examples S10, S2A, S2B and S3M. Therefore, formation of dimpled fracture surfaces (regardless of dimple size) involves intense dislocation activity around cracks.

For brittle materials such as H2M, H30, S1C, S2C and S3C steels, however, it is generally assumed that the crack growth occurs by tensile separation of atoms, then, in this case, dislocations should not generally intersect crack tips, voids should not form ahead of crack tips. Therefore, fracture surfaces are generally flat on an atomic scale.

Brittle cleavage was also observed in most of the die steel tested, which led to the conclusion that voids formed ahead of the cracks and that extensive slip intersected crack tip during cleavage. Small voids ahead of the crack tip could not be observed, but it is generally accepted that formation of dimpled fracture surface involved nucleation and growth of void ahead of cracks.

The river pattern observed on cleavage fracture surfaces results from propagation of crack on more than one level. The river patterns can also be formed (32):

1. After crack crosses a grain boundary
2. When the crack spreads from its nucleation site in the grain in which it was initiated

3. When a cleavage crack is restopped and restarted, large numbers of rivers are formed, as shown in Plates 3, 6, 9, 16-25, 28, 32, 33, 34 and 38.

Steps are produced when the main and new crack join together by tearing of materials between the crack cut from the movement of dislocations. These steps tend to be perpendicular to the crack front, in order to minimise their energy (area) and hence are roughly parallel to the direction of crack propagation. These steps also are able to coalesce gliding along the crack front, especially those with the same sign, therefore multiple steps are formed, Plate 3.

Scanning electron micrographs for four different types of die steel show that various fracture surfaces can be seen from the point of chevron down to the edge of the fracture surface. However, a concentrated area of manganese silicate inclusions surrounded with very fine dimples, which indicate that for microvoid to initiate and grow around the inclusion there must be a large amount of plastic strain resulting from loss of stress triaxiality. These considerations lead to a mechanism for slow crack growth based on that ductile crack propagation which occurs when a critical plastic strain is exceeded over a characteristic distance associated with the microstructure inclusion spacing, examples: Plates 2, 26, 30, 35, 36, 37 and 39.

The formation of fine dimples in some areas of the fracture surface of test specimens lead to the suggestion that grain size plays an important role in the fracture properties of these alloys.

Thompson and Zinkman ⁽⁵⁶⁾ support the above suggestion, as shown in Fig. 10, page 27), that the coalescence of microvoid causes crack propagation.

Macroscopic observation of the broken specimen was done also. Specimen S10, S1B, S2A, S30 and S3B showed a fibrous fracture characteristic of ductile materials. The macroscopic observation of a representative set of specimens are shown in Plate 34 and Plate 38, both reveal fibrous fracture surfaces reflecting possible banding in the microstructure, as shown in Plates 74 and 77.

Fatigue fracture surfaces are clearly distinguished by their flatter appearance.

9.2 Relation between Fracture Toughness and Microstructure of Electem, Thermodie, Hydie and Somdie Steels

9.2.1 Toughness and Microstructure

Engineering fracture mechanics describes fracture of a body in terms of critical stress intensity factor or fracture toughness. The body fails when the ^{critical} stress intensity is exceeded at the crack tip ⁽⁵⁷⁾.

McMahon and Cohen ⁽⁵⁸⁾ have shown also that cleavage failure initiates when brittle grain boundary particles

of cementite fracture to provide incipient microcracks that can subsequently propagate catastrophically through the steel. According to the above explanation there is assumed to be nuclei initiation when the brittle grain boundary cracked under the influence of dislocation pick-up or under plastically deforming matrix. The size of carbide particles ~~is~~ has considerable effect on fracture toughness ^{does} as [↑] the inclusion distribution. From the consideration of ductile fracture, as shown in Plates 3, 7, 8, 13, 14, 26, 27, 36-39, ^{it is clear} [↑] that the inclusions play a predominant role in the ductile fracture process. The effect of inclusions on behaviour and cleavage resistance is not clearly defined. Therefore, fracture ductility can be determined to a large extent by a complex function involving inclusion spacing and volume fraction.

Inclusion shape has a dominating influence on the fracture properties. However if ^a thin film of impurity elements ~~is~~ formed the toughness may be severely reduced. It can be predicted also that the only microstructural parameter affecting the fracture and the stress distribution. Although tensile strength values of the fracture have been investigated in these die steels it is not proven here that cleavage fracture obeys a critical tensile criterion.

From microstructure point of view the crack will always follow the easiest path and so local regions of the microstructure through which the crack passes may be

responsible for the overall behaviour of the material. The corrugated macroscopic appearance of the fracture surfaces however indicates that the relative distribution of phases and their crystallographic orientation did play a role in the microscopic processes of ductile fracture. The macroscopic appearance of specimens shows much smoother fracture, although the layer of material still visible, parallel to the crack front. The most direct insight into the effect of microstructure can be gained if one compares Plates 64, 65 and 66, specimens having the same orientation but different in fracture toughness value, such as 143, 83 and 72 MN/m^{3/2} respectively. However, there is a steep rise in fracture toughness value from central block to outside surface. This is because of different cooling rates along the block which reflect to give different microstructures.

The microstructure of the die block exerts also a marked influence on the appearance of steps and river patterns formed in cleavage fracture. The fracture path follows the cleavage plane of the ferrite through several bainite colonies. Many small cleavage facets were noted in these die steels and may be related to bainite or martensite needle size. The variation of strength levels was found in these die steels, however at higher strength levels the fracture surface exhibited smaller river patterns and more irregular tearing than in the structures corresponding to the lower strength levels.

Plate 88 (1-4) shows the variation of fracture toughness with distance from top surface to the centre of the die blocks.

Deformation appears much more difficult in most of these die steels ahead of crack tip. The onset of plasticity controlled slow crack growth is delayed and conditions of high tensile stress build up ahead of the crack leading to rapid failure. This is reflected in the load/crack mouth opening displacement curves, Figs. 37-39, which rather resemble those of a brittle material.

In order ⁽⁵⁷⁾ to incorporate micromechanisms of fracture toughness it is needed to look to the stress field characterising role of the stress intensity factor.

Cracking of spheroidised carbides ⁽¹⁾ is more difficult because dislocation in the ferrite matrix can cross slip around them more easily than for plate-like carbide, and the build-up of high stresses at pile-up.

In the case of spheroidised carbides there is a smaller contact area with the matrix, therefore the tensile stress in the particles will be less than the lamellar carbide. The very fine carbides are very resistant to void formation and this accounts for the good ductility of this structure at high strength, Plates 2, 4, 7, 8, 9, 12, 26, 30, 31, 35, 36, 37 and 39, also see Tables 3 and 4 - Mechanical properties.

Systematic investigation by Karl Heinzsche ⁽¹⁷⁾ has shown that the effect of grain size on K_{IC} is comparable to that ^{of} loading ratio \dot{K} . Increasing inclusion concentration has probably the same effect as increasing particle dimension and the loading ratio.

The hot working parameters such as temperature, strain and type of inclusion have a considerable effect on the way the inclusions deform into elongated stringers, break-up and disseminate through the steel ⁽⁵⁹⁾. This was emphasised in the present investigation of hot work die steel such as shown in Plates 2-77.

The appreciation of the importance of inclusion plasticity and fracture has led to attempts to control the plasticity, particularly of sulphide inclusion shape control employing addition of zirconium, titanium, calcium or rare earth ⁽⁶⁰⁾.

The above discussion leads to the conclusion that processing variables during hot working are very effective in controlling inclusion plasticity for both sulphide and silicate.

Finally, fracture toughness increases with increasing material purity, i.e. increasing inclusion distance.

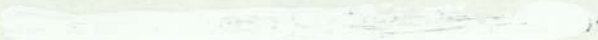
As shown in plate (89), it was very difficult to distinguish the fatigue crack tip from the fast fracture area in Hydie and Somdie steels. The fracture surface characteristics, very close to the fatigue zone in these bend specimens, were identical to the fracture surfaces of Hydie and some of Somdie steels in short bar specimens (i.e. cleavage fracture surface).

Plate (34a) shows the crack branch propagated by mixed modes of fine dimpled linked with the inclusion cavities and quasi-cleavage.

Plate 36a shows crack path propagation through the ductile region with concentrated silicate inclusion at the crack tip. In this case the fracture occurs by the classical mechanism of microvoid coalescence involving the initiation, growth and coalescence of cavities formed at inclusion.

It can be seen from plate (70a) that the crack path preferentially followed the bainite plates and linked with the inclusion cavities.

9.2.2 Toughness and Fractography

The results that are presented in section 8 are for short rod/bar and three point bend test specimens of these die steels, variation of specimen position in the forged block, the cooling rate and subsequent heat treatments may well influence the fracture toughness. The rate of cooling for the whole block after heat treatments varies from outside to the centre of the die block. This can be related to the heat transfer through the solid body which is related to many factors. For this reason, microstructure studies have to be made for each set of specimens within the die block,  along the crack surface at the point (V) towards the edge of fracture surface.

It is worth noting that the cooling rate for specimens taken from centre of the block has considerable effect on microstructure and fracture, as shown in Plates 10, 12, 15, 23, 28, 33 and 38, with their microstructural appearance as shown in Plates 48, 51, 53, 61, 66, 71 and 76. The fracture surface of these specimens shows cleavage brittle fracture or cleavage with ductile dimpled area and microstructure of tempered bainite and some stringer of sulphide silicate inclusion. Fracture toughness of these specimens are 71, 78, 54, 56, 70, 88, 72 MN/m^{3/2} respectively. In view of these comments the micrographs shown in Plates 40-78 can be used to relate the various fracture toughness values obtained with their relevant microstructure.

The microstructures in Somdie steel specimens are mostly bainite. These transformations may be induced by deformation or an applied stress strongly promoting the transformation not only by its thermodynamical effect but also by its dynamical effect, which introduces a sort of local stress concentration, and thus acts to produce more stable sites for preferential nucleation of bainite and banded along inclusion with some of martensite structure inbetween as shown in Plates 65, 66, 70, 71, 75, 76

In most of Hydie and Somdie steels appreciable amounts of martensite remain in the centre of the grain, occasionally there is ferrite outlining the grain boundaries but for the most part black colonies of lower bainite outline the grains. The large light areas are martensite formed from austenite that remained when the region passed the M_s temperature, Plates 3, 6, and 9.

From the literature review, section 2.4, there are a number of compositional and structural factors that can influence the toughness of these materials, for example, Electem, Thermodie, Hydie and Somdie steels contain a considerable amount of sulphur which has an effect on toughness. Tables 6, 8 and 11 show that specimen position in the die block and the plasticity (p_c) value have a strong influence on the fracture toughness as well as sulphide and silicate inclusions.

Details of examination of the fracture surfaces for all the specimens have been discussed in the first part of this section.

The fractographic examination, does, in general provide confirmation of the toughness values obtained for the various specimens. For example, the fracture surface of specimen EC, Plate 15, which gave fairly low toughness values showed dimples associated with manganese silicate inclusions. This morphology is generally associated with fracture at relatively low loads with the inclusions providing ideal void initiation sites. On the other hand, for steel with low toughness values such as specimens H2M, H3C, H3A, S1C, S2C and S3C, shown in Plates 17, 23, 28, 33 and 38, fracture occurred by cleavage. This type of fracture is typical of brittle material with low toughness.

The fractographs showed that the crack extension process took place by the formation of very fine dimples (look like large stretch zones) at the crack tip, as shown in Plates 2, 4, 19, 26, 29, 35 and 39.

The fracture surface for specimen AM, AC, BM, Hydrie and some of Somdie steels, however indicated that fracture took place by cleavage associated with varying fracture toughness.

The change in fracture mode could well have been caused by the cooling rate for these blocks.

9.3 Load/Crack Mouth Opening Displacement Record for Measuring K_{ICSB}

Figs. 36-39 show load versus crack mouth opening displacement test records generated, employing the test procedure previously described.

From these curves one can quickly assess the order of magnitude loading ratio during the tests. For more brittle fracture, for example Figs. 37-8, 37-10, 37-13 38-1 and 38-13, the "linear load rise displacement" goes to failure whereas for more ductile failures, Figs. 36-2 and 36-3, the load rise displacement^{goes} to maximum load or instability. Two loading and unloading cycles have been done for evaluation^{of} plasticity (p), as shown in Fig. 36-2.

Measurement of the fracture toughness has been made in principle when the crack is anywhere within the central region of the specimen by measuring the crack advancing load and the crack length by applying appropriate specimen calibration factor for the crack length.

Particular fracture toughness has to be measured when the crack length is a_c , i.e. when its location is that at which the peak load occurs in an L.E.F.M. test. In addition, the peak load occurs also even in a non-LEFM when the crack length is close to a_c , such that the rate of change of load with crack length is small at $a = a_c$. In the case of crack jump material, as shown in Fig. 37-(1 - 5), load/crack mouth opening record, a crack jump rarely initiates exactly at (a_c) and the toughness

measurements have been made at the first crack jump and at the maximum load. In addition, the fast moving crack arrest at lower load level after propagating a short distance when the load is again increased, little further crack growth takes place until the next sudden jump. The load-crack mouth opening record of these tests are shown in Figs. 36-1 and 2, 36-8-11 and 37-6, 7, 9, 11, 12. Each time the crack begins a forward jump it can be assumed that the stress intensity factor is at its critical value, K_{ICSR} .

Tinting method has been used for measuring crack length in 'H1'Hydie steel and incorporated in Table 9.

Specimens H1 (O, C, A and B), the crack length after heat tinting is greater than the critical crack length.

Heat tinting crack length $\approx a_c$ in specimen H1M. Critical crack length in these specimens was calculated by using the following relationship.

$$\frac{a_c}{w-1.75} = 0.512 \quad (53)$$

w is the width of the specimen.

Fracture toughness of these steels was calculated as shown in Table 9.

In the case of Thermodie steel, tests recorded at load/crack mouth opening displacement, plasticity correction for these steels has been calculated as incorporated in data analysis section.

The test ⁽⁵³⁾ is considered invalid if $|p| > 0.2$, inasmuch as the theory assumed relatively small value of the plasticity.

It has been observed from the results that the fracture toughness varies with (p_c) . Barker ⁽⁵³⁾ observed experimentally that the factor $(1+p/1-p)^{\frac{1}{2}}$ can produce too large a value of K_{ICSR} when p becomes large.

The difference between $(1+p)$ and $(1+p/1-p)^{\frac{1}{2}}$ produces 2.4% difference in calculated K_{ICSR} if $p = 0.2$, 1.7% difference if $p < 0.2$ and 9.8% difference if $p > 0.2$.

9.4 Variation of Fracture Toughness Along Die Block

Fracture toughness test results are plotted against distance from top surface of die block, as shown in Plate 88 (1-5). Plate 88-2 shows that the toughness is indeed sharply peaked at the mid-radius of the die block,

Note the toughness of DM specimen ($208 \text{ MN/m}^{\frac{3}{2}}$).

In the case of Somdie steel (short bar), fracture toughness decreased from top surface towards the centre of the block.

Variation of microstructures along the die block give a good support for the effect of the cooling rate.

From the results of the three point bend, fracture toughness (K_{IC}) behaves absolutely different. However S2 specimens at mid-radius of the die block show indeed high fracture toughness (K_{IC}). This can be explained that fracture toughness along the crack front, or that region of lowest toughness control the fracture toughness of this specimen. This leads to the conclusion that the fracture was initiated by region of low toughness specimen S1, $57 \text{ MN/m}^{3/2}$, compared with short bar Somdie S20 and S3 with S2C Somdie short bar.

9.5 Notch bending test (K_{IC})

Test results are recorded by plotting autographically the applied force against the clip gauge displacement measured at the test piece surface across knife edge located on opposite sides of the notch, as shown in Fig. 35 and Plate 1. It was not necessary to construct the 5% secant line to determine the critical load (P_Q), because the load/crack opening displacement was sharply linear up to fracture.

As can be seen from test records 39-(1-6) and Table 12, very good correlation can be observed between fracture toughness calculated using short bar (K_{ICSB}) and fracture toughness calculated using three point bend specimen (K_{IC}). One can notice the results of two test methods by comparing specimen S1 ($K_{IC} = 57 \text{ MN/m}^{3/2}$) and Somdie steel short bar (S20, $K_{ICSB} = 148 \text{ MN/m}^{3/2}$). Both

tests have satisfied the conditions for the validity of the test, therefore the difference in results can be explained by different mechanical properties and different fracture toughness at various areas within the specimen.

British Standard (9, 61) and ASTM (10) have set minimum specimen size limits and recommendations for determining test validity. One condition is the linearity which states that the deviation of the test record from tip OA at load $0.8 p_Q$ is less than one fourth of the deviation from linearity of the test record at p_Q , as shown in Fig. 19, page 49

For all the specimens (Hydie and Somdie steels) examined, the linearity on the load/clip gauge mouth opening displacement was excellent, as shown in Fig. 39 (1-6). Sudden yielding did take place in these materials giving the appearance of LEFM behaviour.

The fracture surface showed that fracture had taken place by predominantly cleavage, as shown in Plates 16-39.

For valid K_{IC} results no specimen dimensions should be less than $2.5 \left(\frac{K_{IC}}{\sigma_{ys}} \right)^2$. These limits were based on results from tests on material Hydie and Somdie steels.

As a result of many tests carried out, the general observation can be made that if the ratio p_{max}/p_Q

exceeds 1:1 the apparent K_{IC} value will not be a good approximation to the plane strain fracture toughness of the material, K_{IC} . However, as stated above, each test must be considered separately and every variable should be taken into account.

9.6 Stress Assisted Martensitic Formation

The formation of martensite ahead of the crack tip and the crack path could be considered as a result of a depletion of carbon and alloy elements in the surrounding austenite and presumably causing a load elevation of M_s and M_d temperature of the alloys.

The observation of plate-like martensite in the area immediately adjacent to the fracture path and ahead of the crack tip, suggested that formation of martensite is stress-assisted, as described in section 1.2.1.

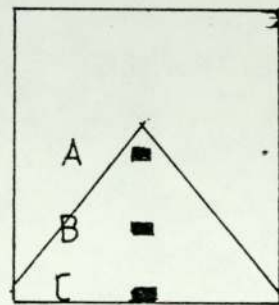
Tamura (47) in his recent work pointed out that the austenite is deformed at temperatures above M_s^σ (example T1 in Fig. 29, page 81), the austenite starts to deform plastically at σ_a and is strain hardened up to σ_b , and then martensitic transformation begins.

According to the above explanation, in Soudie steel, the banded structures are frequently induced by deformation near or above M_d .

The result of this layer of martensitic structure beside the high fracture toughness, under working conditions, is a good resistance against abrasive wear.

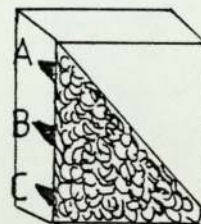
FRACTOGRAPHS AND MICROGRAPHS ARE
REPRESENTED BY A, B, C

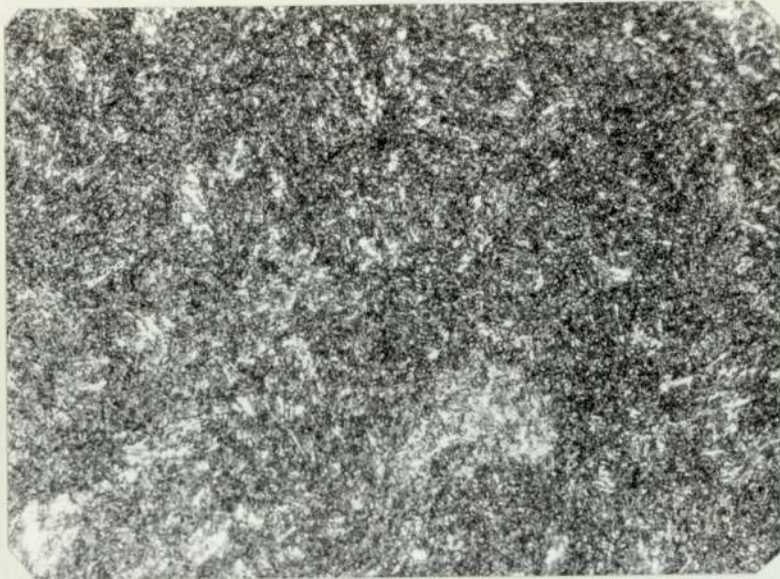
- A. Top of Fracture Surface
- B. Centre of Fracture Surface
- C. Edge of Fracture Surface



MICROSTRUCTURE

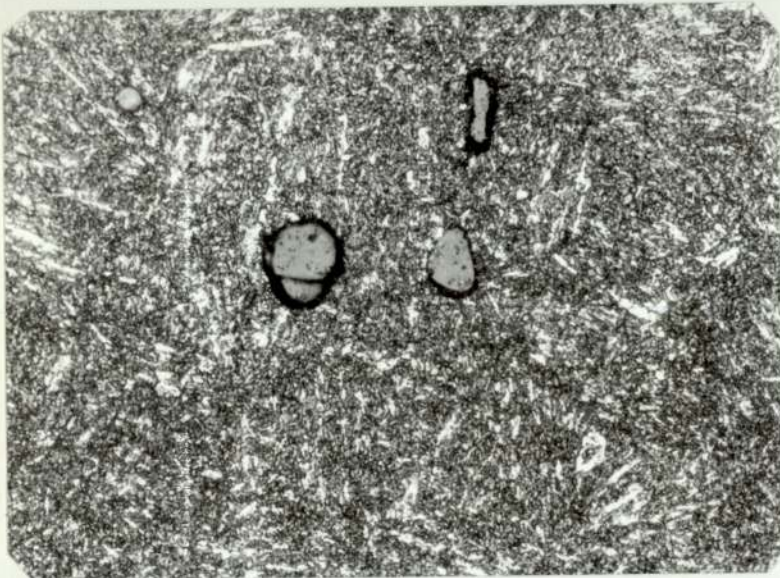
- A. Top Polished and Etched Fracture Surface.
- B. Center Polished and Etched Fracture Surface
- C. Edge Polished and Etched Fracture Surface





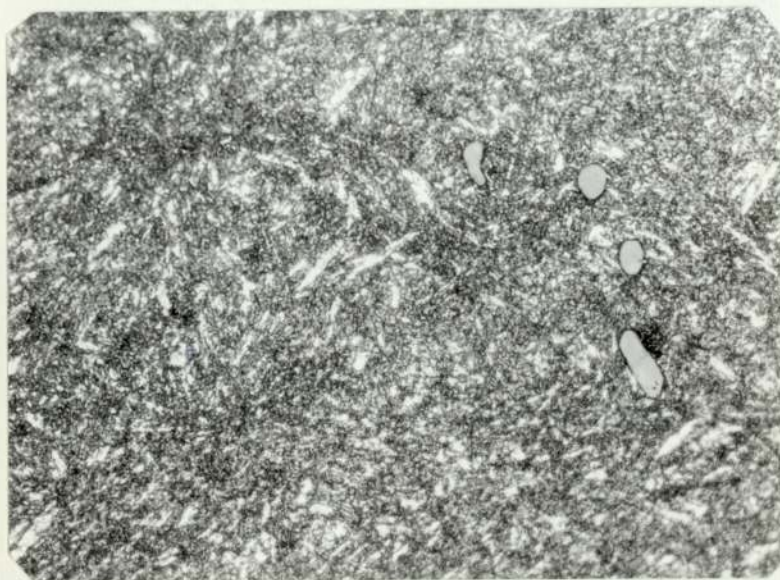
A. Top

Optical micrograph consisting mainly of tempered martensite (Ma . x844)



B. Centre

Optical micrograph showing tempered martensite, some free ferrite (white) and silicate inclusion with some MnS ppt within it (mag. x844)



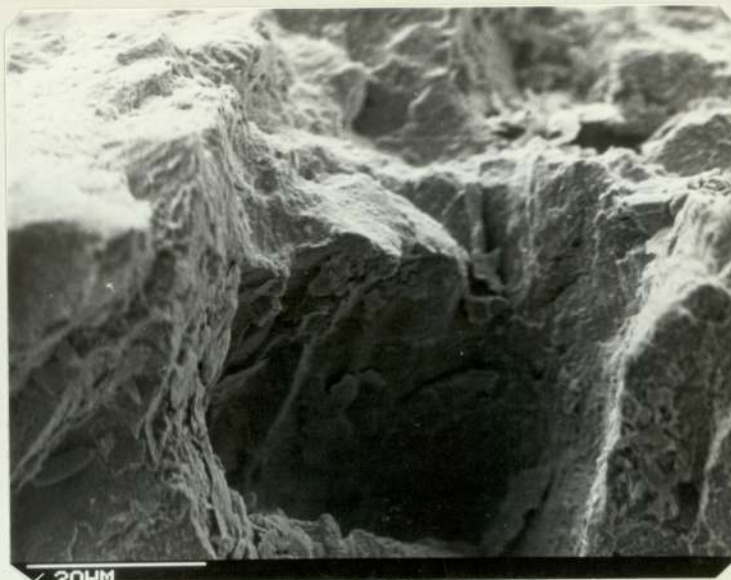
C. Edge

Optical micrograph showing tempered martensite, free ferrite and silicate inclusion (Mag. x844)

PLATE 2 Fracture surface of H.W. die steel
"Electem" AO

A. Top

Scanning electron fractograph showing a typical macrovoid. The top left shows the stretch zone with very fine dimples



B. Centre

Scanning electron fractograph showing the microvoids around deformed silicate inclusion



C. Edge

Scanning electron fractograph showing voids linked crack with elongated silicate inclusion and solidification at fluid silicates.

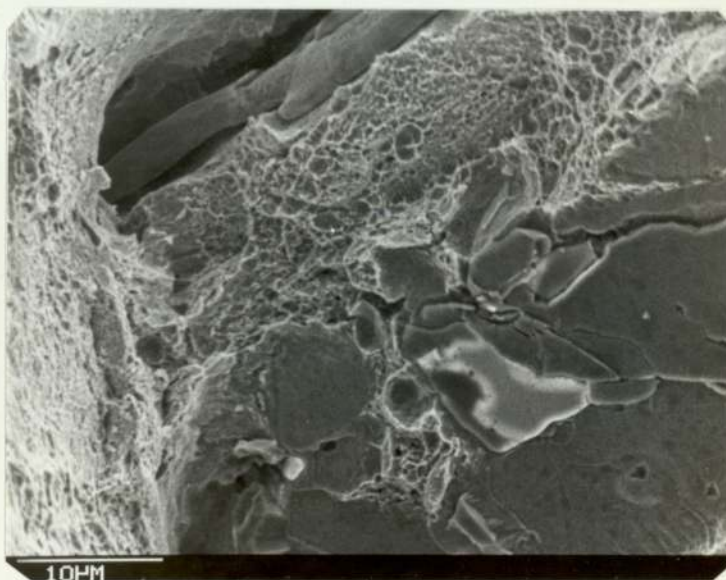
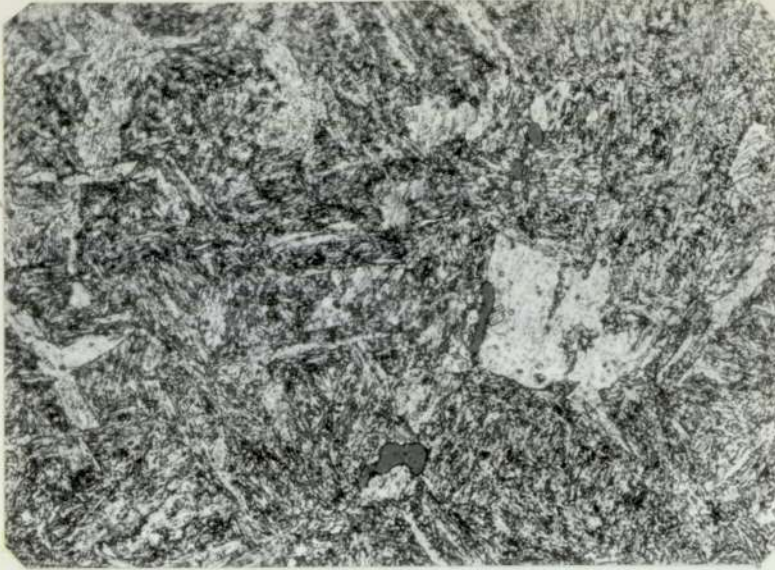
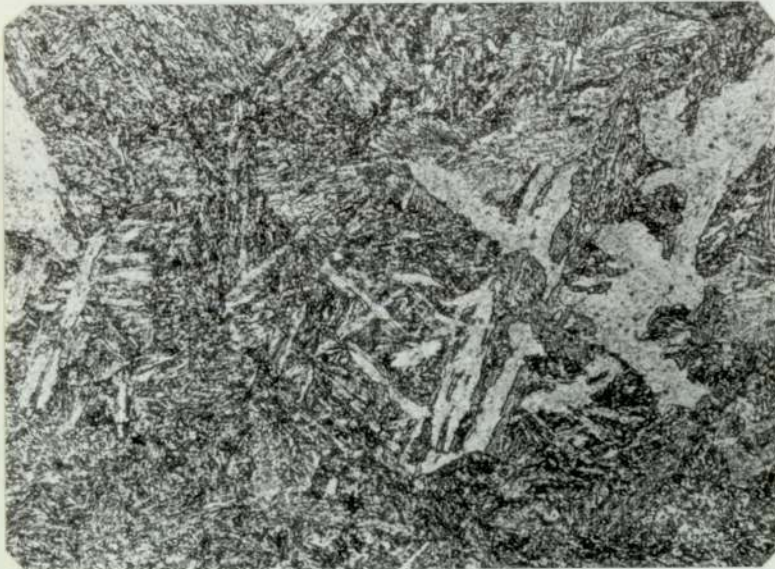


PLATE 41 Microstructure of H.W. die steel
"Electem" AM



A. Top

Optical micrograph showing silicate inclusion and tempered bainite (Mag. x844)



B. Centre

Optical micrograph showing structure of tempered bainite and some tempered martensite (Mag. x844)



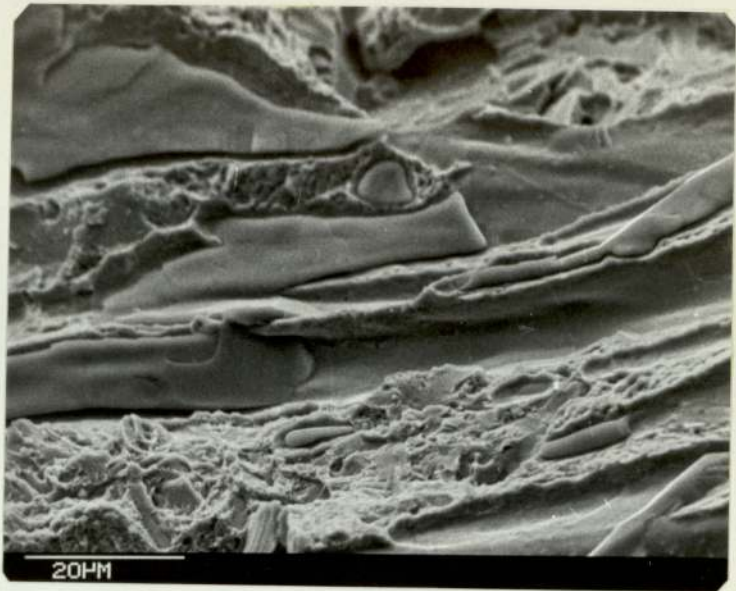
C. Edge

Optical micrograph showing carbide particles in a bainitic structure and manganese silicate inclusions (Mag. x844)

PLATE 3 Fracture surface of H.W. die steel
"Electem" AM

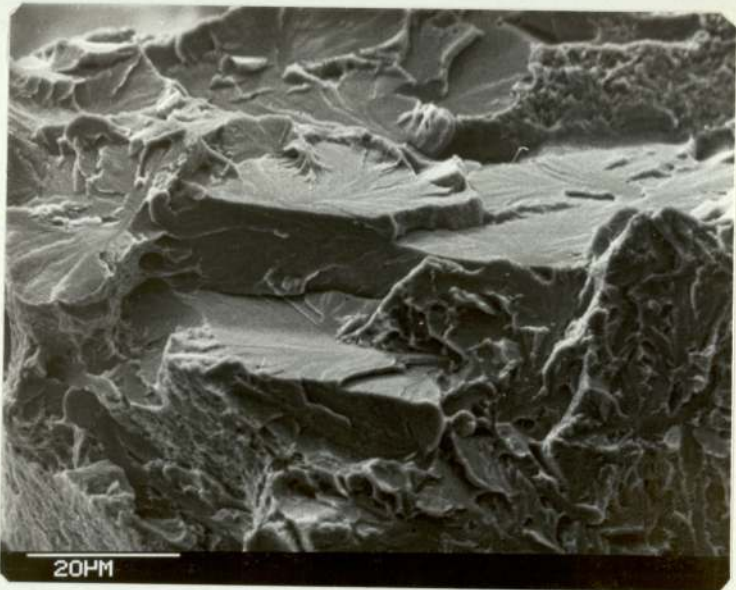
A. Top

Scanning electron fractograph showing ductile fracture surface with silicate inclusion surrounded by very fine dimples



B. Centre

Scanning electron fractograph showing brittle fracture surface isolated with ductile region



C. Edge

River pattern with isolated ductile region

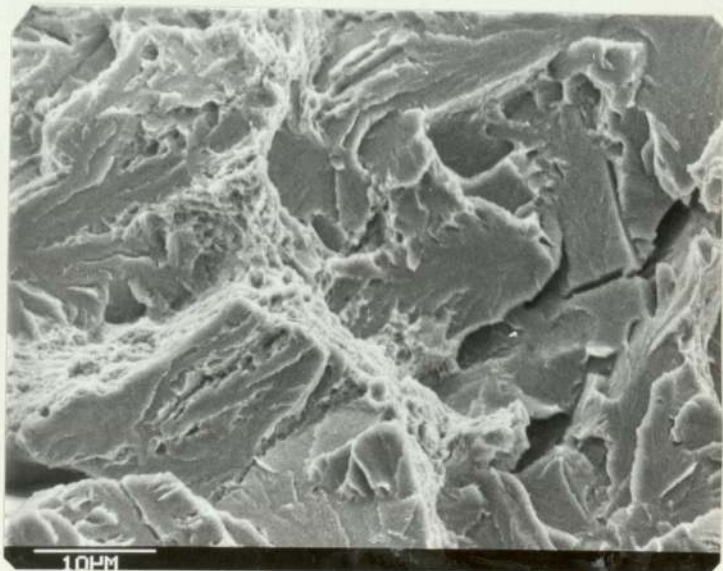
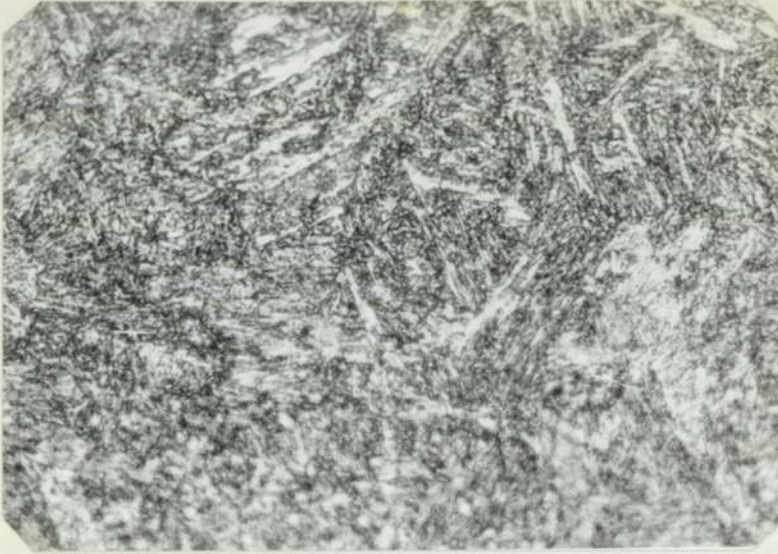
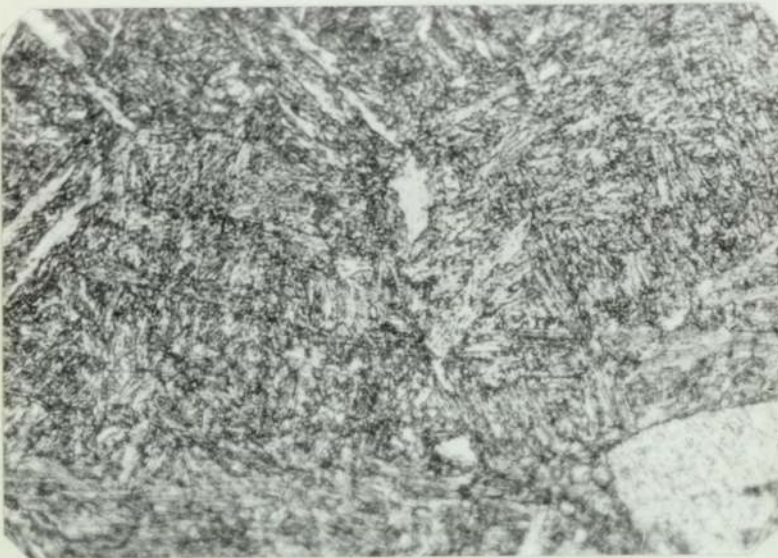


PLATE 43 Microstructure of H.W. die steel
"Electem" B0



A. Top

Optical micrograph
showing tempered
martensite (fine)
(Mag. x1688)



B. Centre

Optical micrograph
showing tempered
martensite (unhomo-
geneous microstructure)
(Mag. x1688)



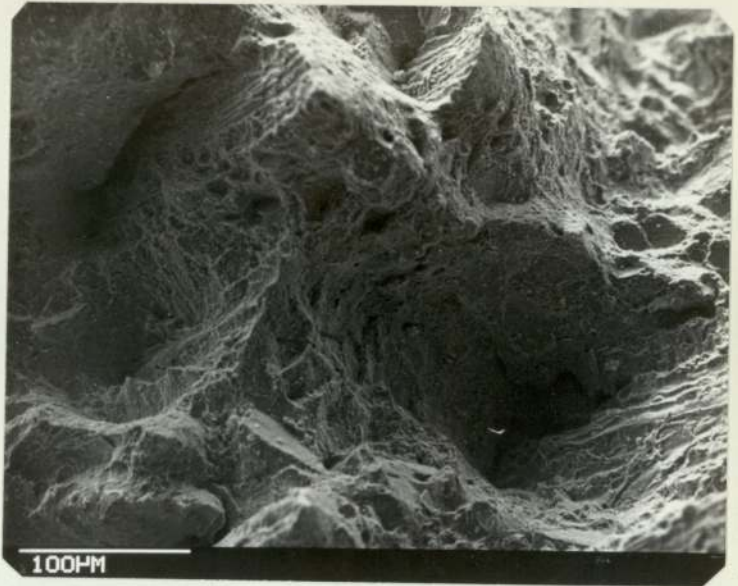
C. Edge

Optical micrograph
showing silicate
inclusion and
tempered martensite
(Mag. x1688)

PLATE 5 Fracture surface of H.W. die steel
"Electem" B0

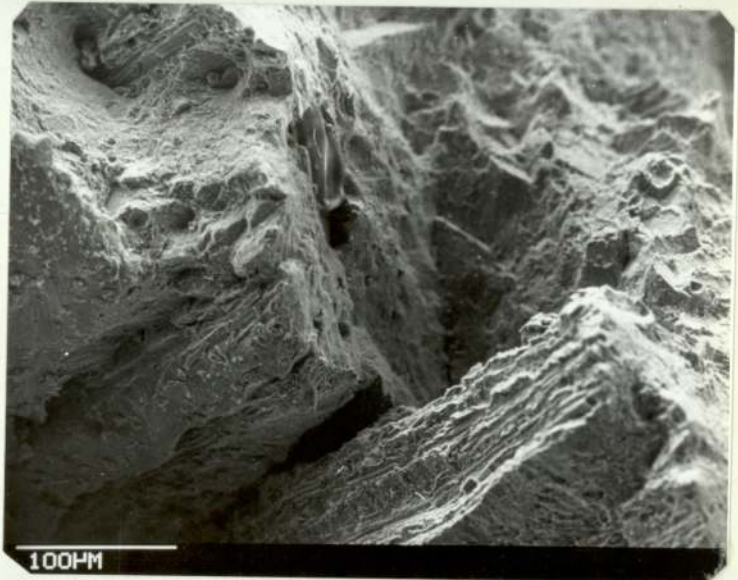
A. Top

Scanning electron
fractographs
showing micro and
macrovoids in
ductile fracture



B. Centre

Scanning electron
fractographs showing
fine voids with
elongated silicate
inclusions and some
MnS inclusions



C. Edge

Scanning electron
fractograph showing
coarse and fine
voids around the
silicate inclusion

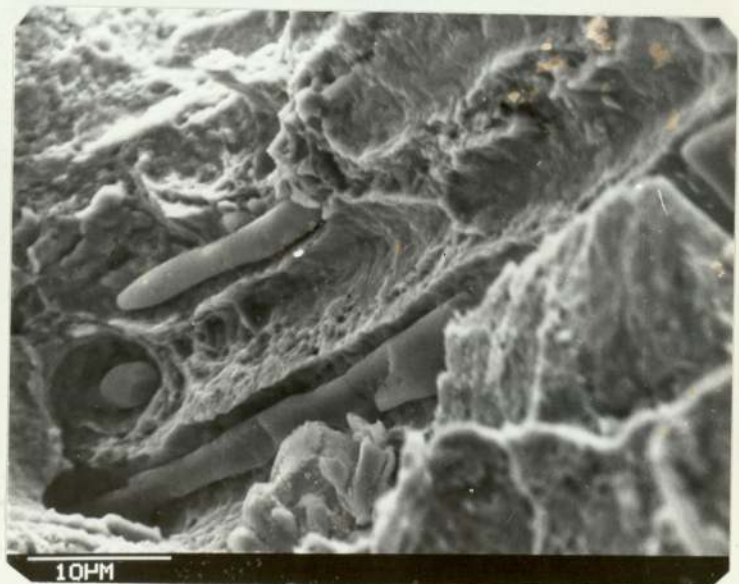
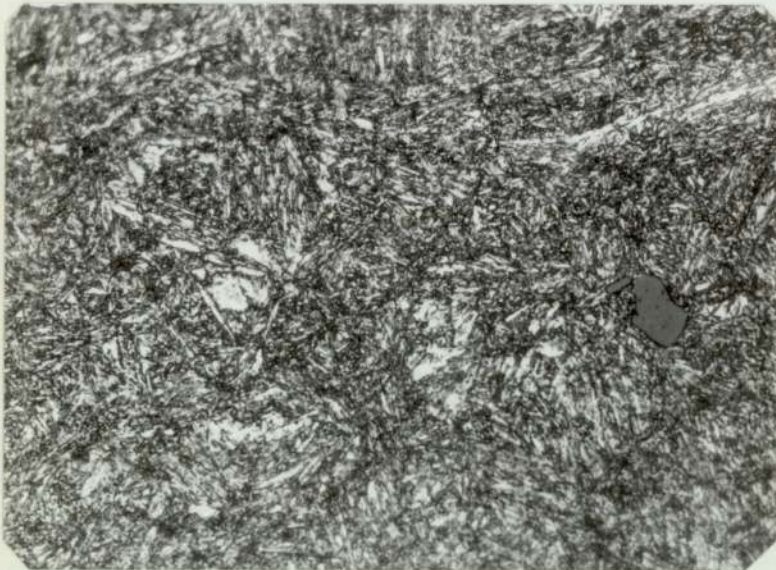


PLATE 44 Microstructure of H.W. die steel
"Electem" BM



A. Top

Optical micrograph showing deformed silicate inclusion (grey), tempered bainite and some ferrite (Mag. x844)



B. Centre

Optical micrograph showing tempered bainite inclusions, some tempered martensite and some free ferrite (Mag. x844)



C. Edge

Optical micrograph showing tempered bainite and some ferrite (Mag. x844)

PLATE 6 Fracture surface of H.W. die steel
"Electem" BM

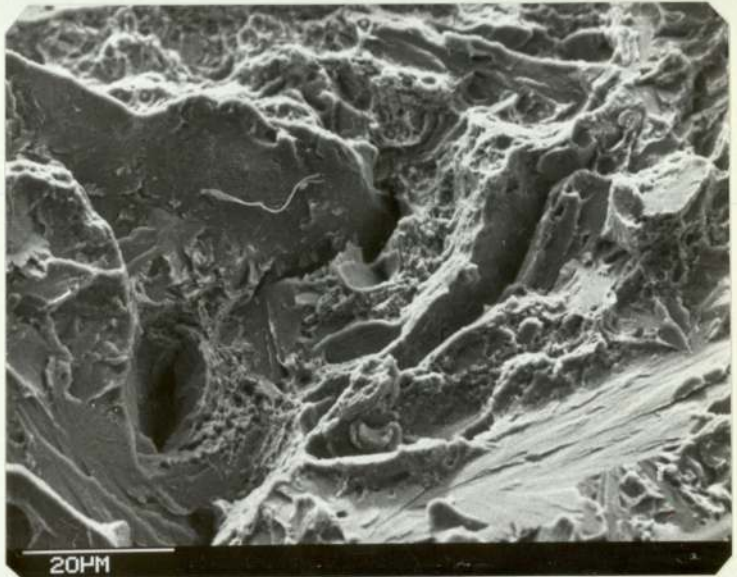
A. Top

Scanning electron
fractograph showing
brittle fracture
cleavage with crack
path across the
crystal



B. Centre

Unhomogeneous fracture
surface with discontinuous
crack



C. Edge

Scanning electron
fractograph showing
brittle fracture
cleavage

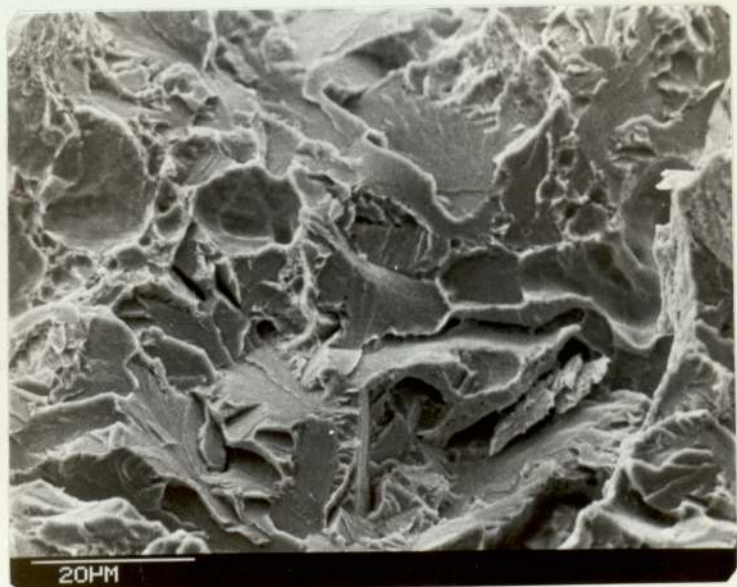
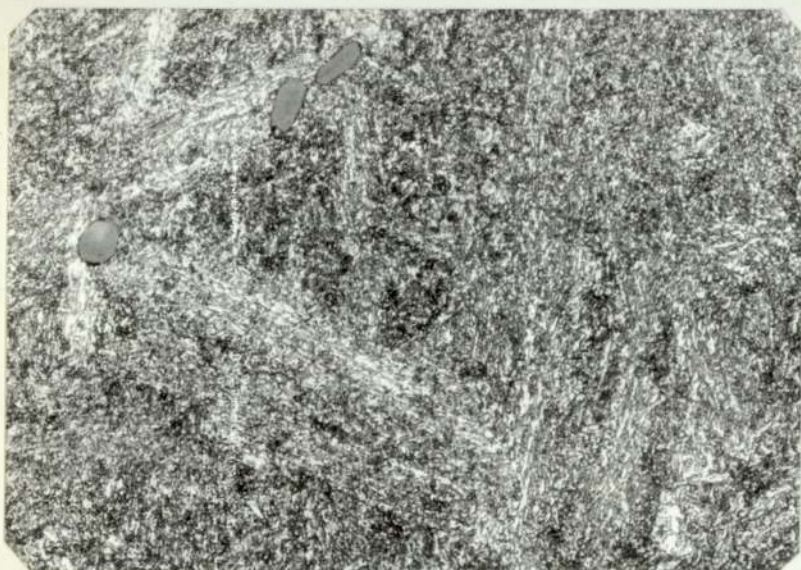


PLATE 45 Microstructure of H.W. die steel
"Electem" BC



A. Top

Optical micrograph showing deformed inclusions, tempered bainite and free ferrite (white areas) (Mag. x 844)



B. Centre

Optical micrograph showing mainly tempered bainite, some free ferrite (white areas) and silicate inclusions (Mag. x844)



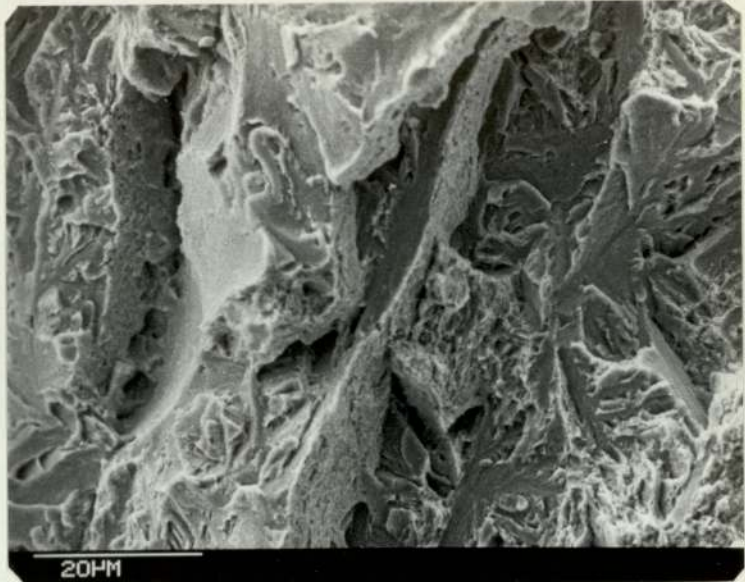
C. Edge

Optical micrograph showing mainly tempered bainite and some free ferrite (white areas) (Mag. x844)

PLATE 7 Fracture surface of H.W. die steel
"Electem" BC

A. Top

Scanning electron
fractograph showing
the microvoids
coalescence with
some cleavage



B. Centre

Scanning electron
fractograph showing
cleavage facet
surrounded with
microvoid ductile
area



C. Edge

Scanning electron
fractograph showing
the microvoid
surrounding the
inclusion with
some cleavage area

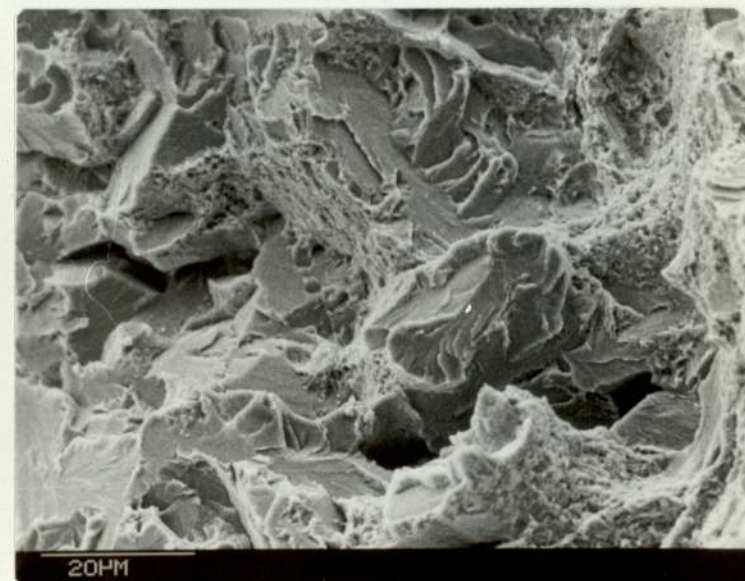
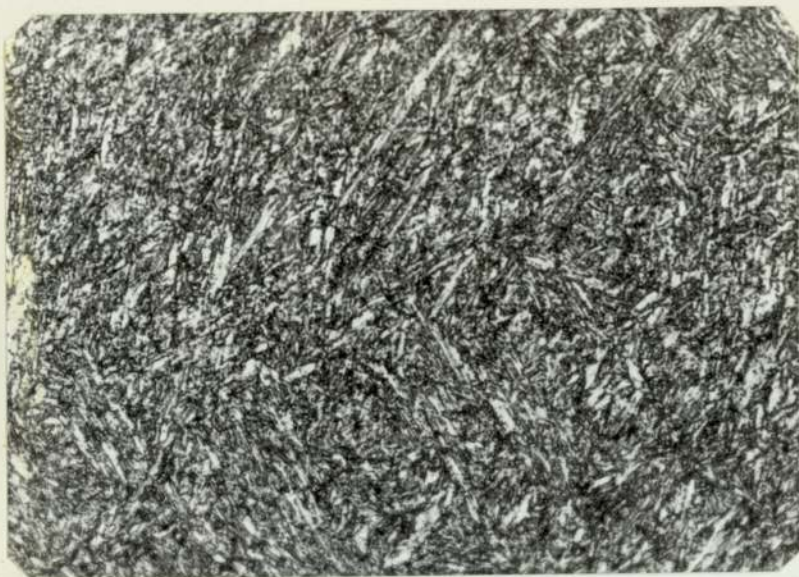
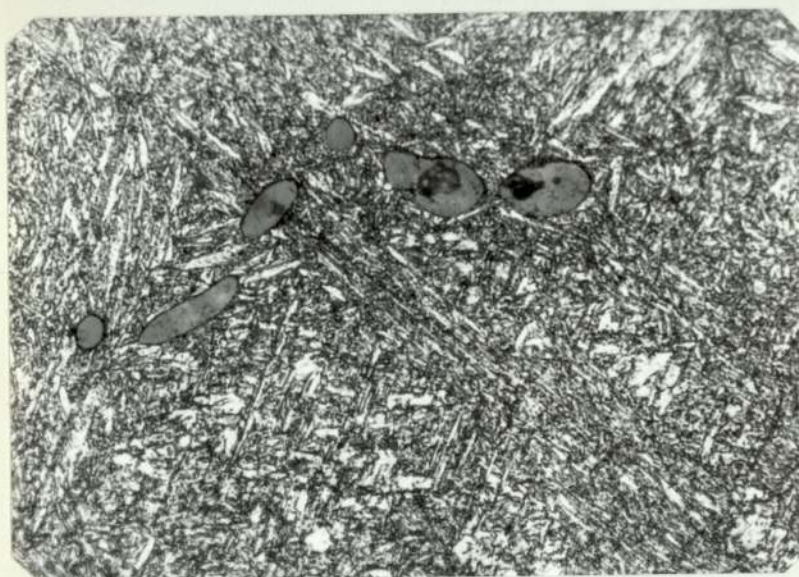


PLATE 46 Microstructure of H.W. die steel
PSomdie" CO



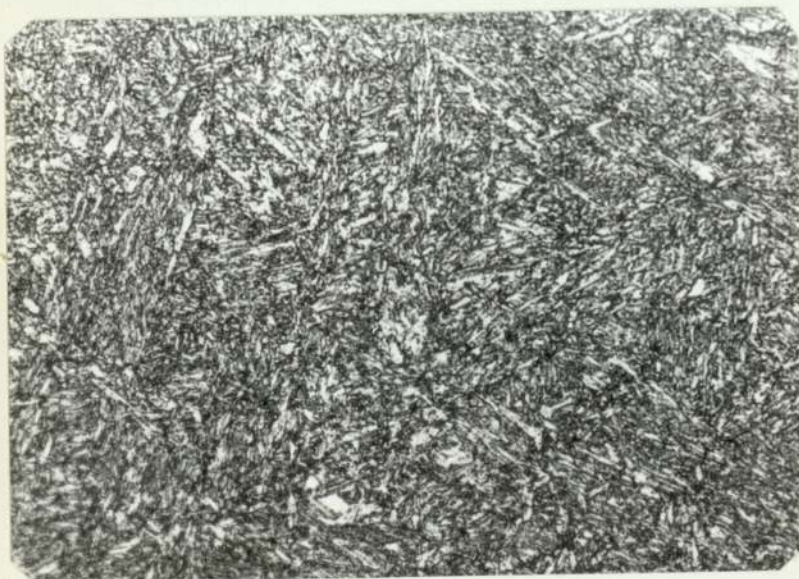
A. Top

Optical micrograph
showing tempered
martensite
(Mag. x844)



B. Centre

Optical micrograph
showing tempered
martensite with
silicate inclusions
and MnS ppt within
it
(Mag. x844)



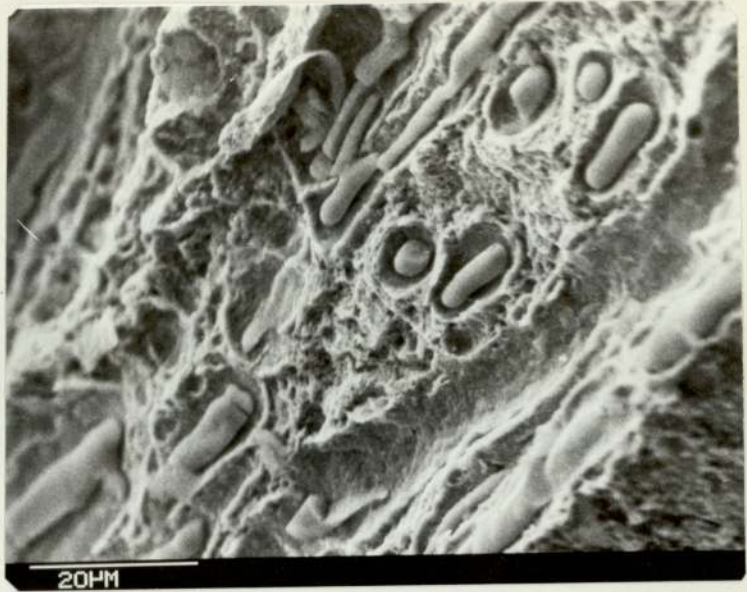
C. Edge

Optical micrograph
showing tempered
martensite
(Mag. x844)

PLATE 8 Fracture surface of H.W. die steel
"Somdie" CO

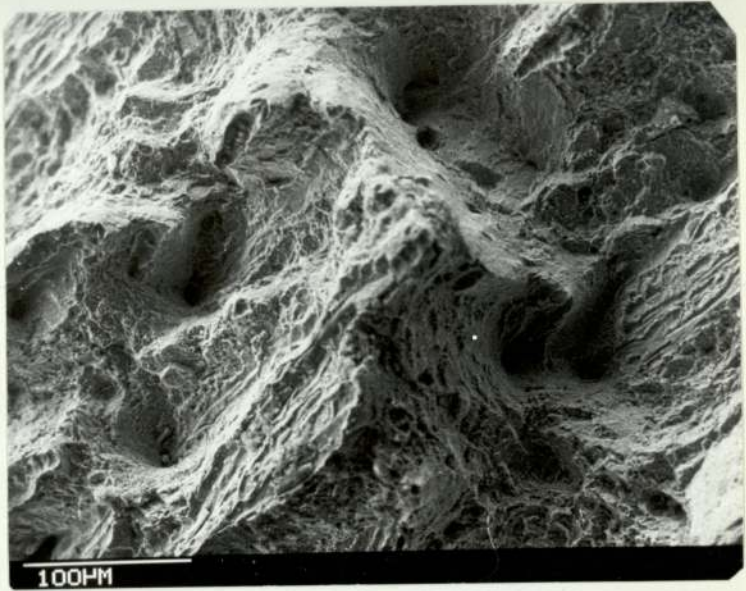
A. Top

Scanning electron
fractograph showing
silicate and MnS
inclusion
surrounded by
microvoid



B. Centre

Scanning electron
fractograph of
ductile fracture
surface showing
fine and coarse
voids



C. Edge

Scanning electron
fractograph showing
fine voids

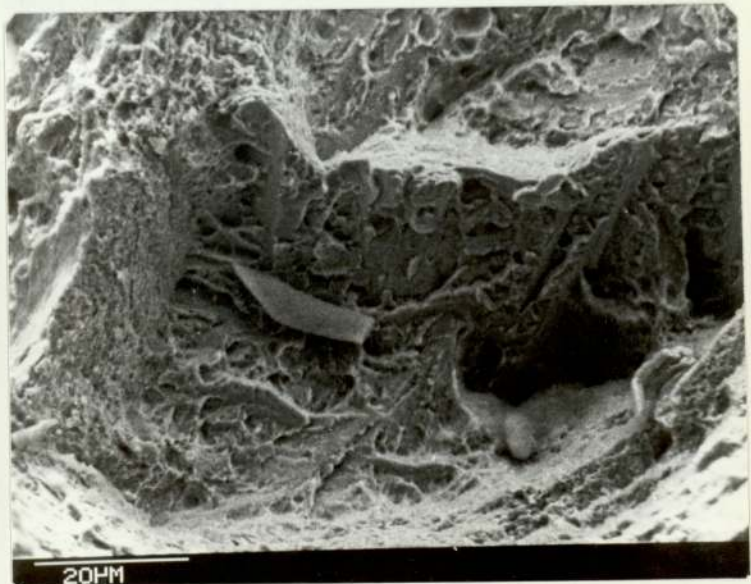
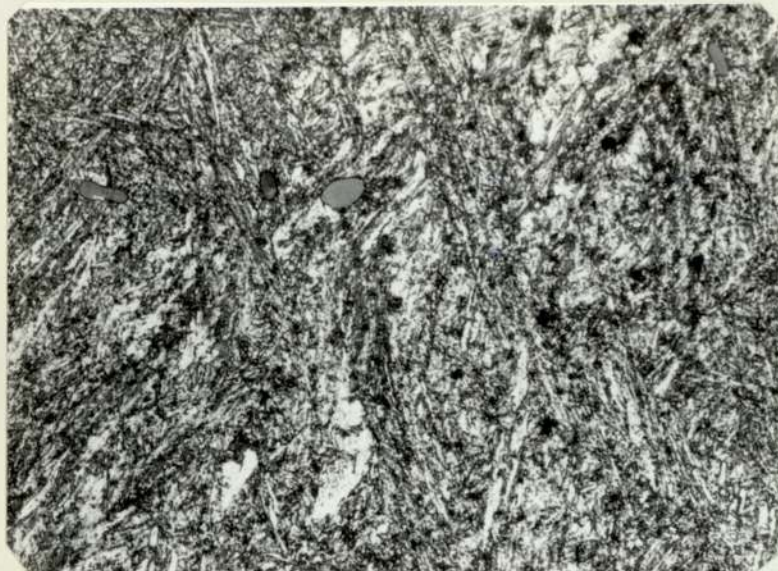


PLATE 47 Microstructure of H.W. die steel
"Somdie" CM



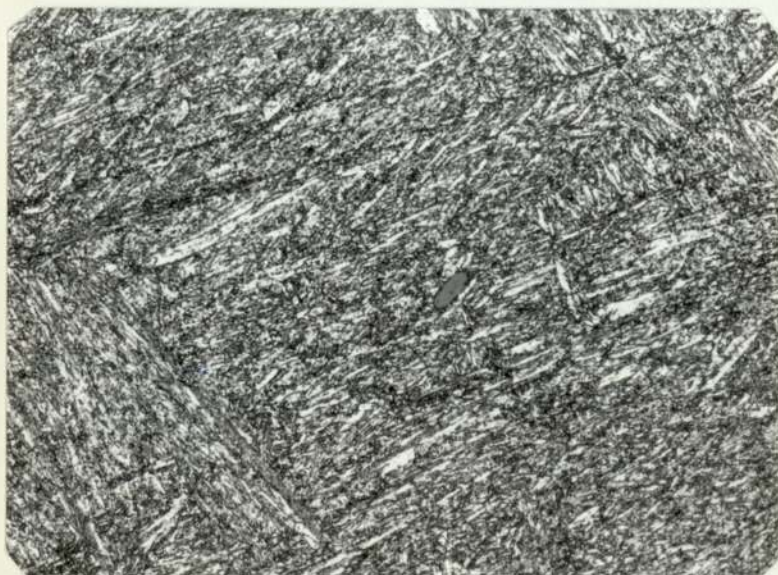
A. Top

Optical micrograph showing mainly tempered bainite and some tempered martensite (Mag. x844)



B. Centre

Optical micrograph showing mainly tempered bainite and some tempered martensite with some free ferrite (white areas) (Mag. x844)



C. Edge

Optical micrograph showing mainly tempered bainite with some tempered martensite (Mag. x844)

PLATE 9 Fracture surface of H.W. die steel
"Somdie" CM

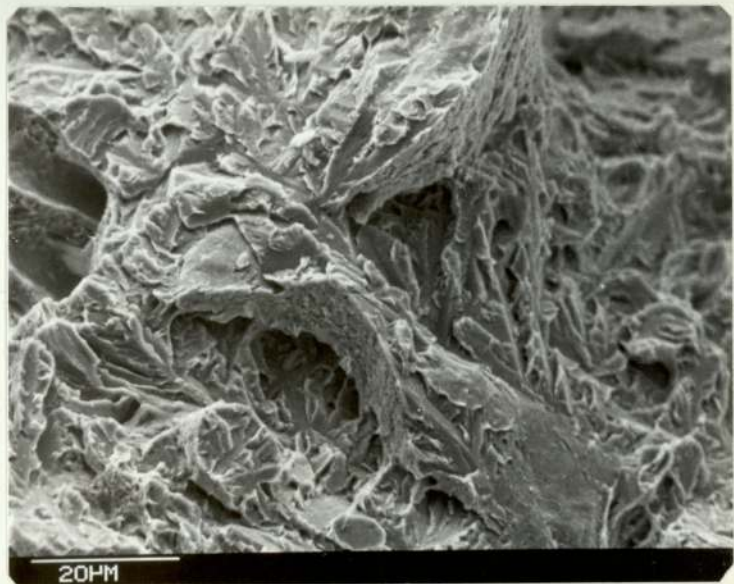
A. Top

Macro and microvoid
and a river pattern
on bottom half



B. Centre

Typical cleavage
brittle fracture

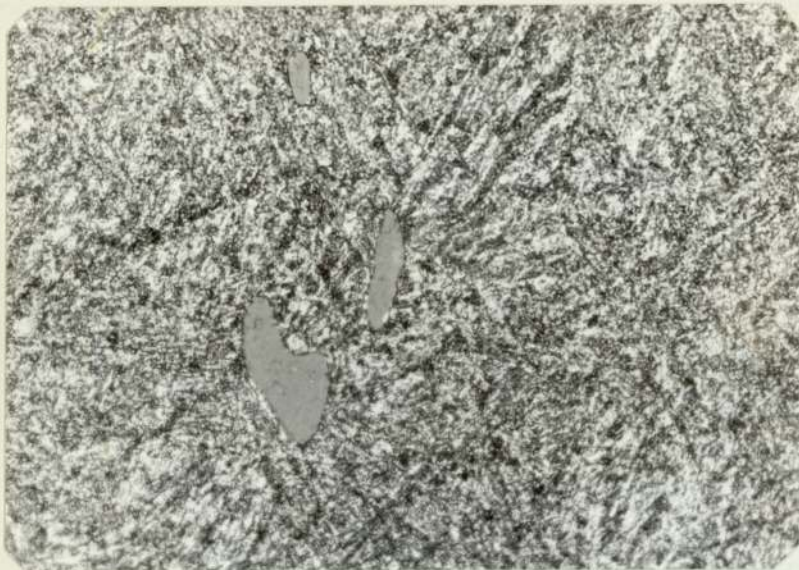


C. Edge

Cleavage brittle
fracture with
some sulphide
inclusions

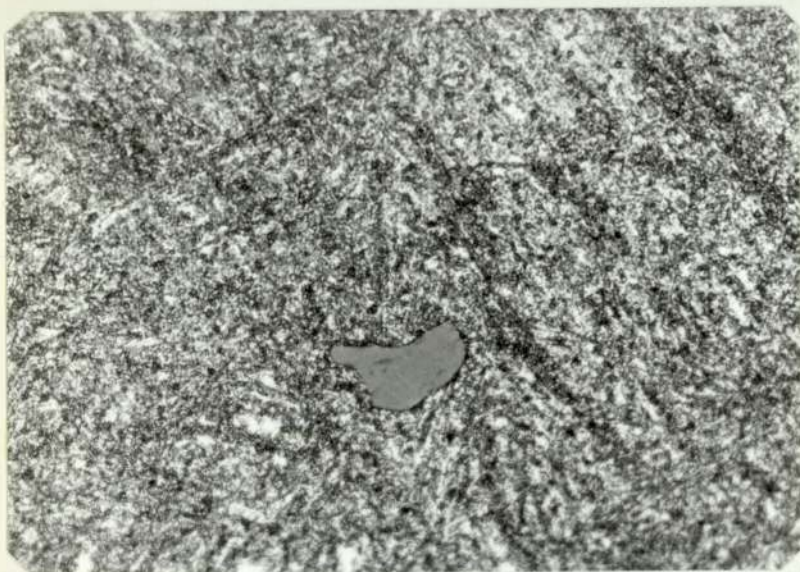


PLATE 48 Microstructure of H.W. die steel
"Somdie" CC



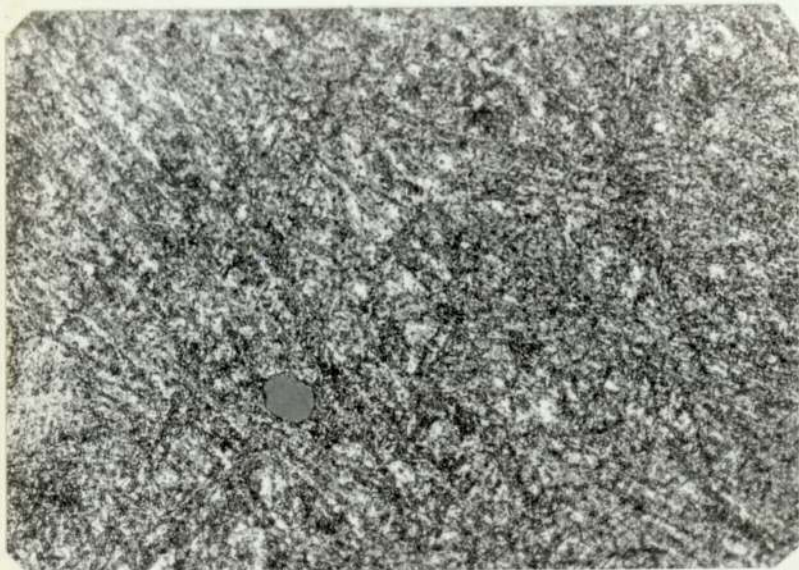
A. Top

Optical micrograph showing mainly tempered bainite with silicate inclusion (grey) (Mag. x844)



B. Centre

Optical micrograph showing mainly tempered bainite with silicate inclusion (Mag. x844)



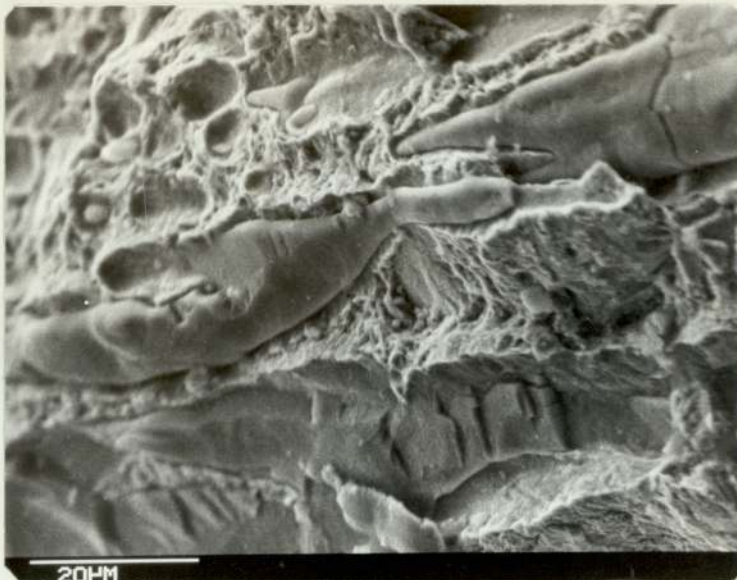
C. Edge

Optical micrograph showing mainly tempered bainite with silicate inclusion (Mag. x844)

PLATE 10 Fracture surface of H.W. die steel
"Somdie" CC

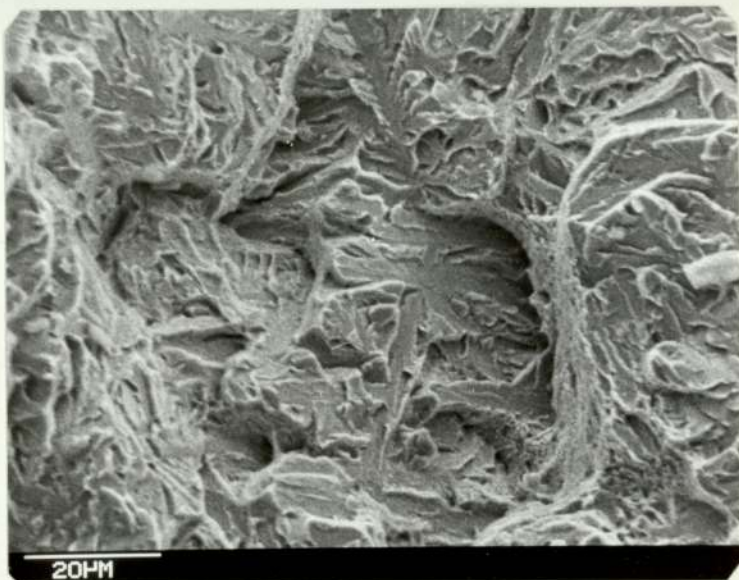
A. Top

Scanning electron fractograph showing large silicate inclusions surrounded by microvoids also some MnS sulphide



B. Centre

Scanning electron fractograph showing typical cleavage brittle fracture



C. Edge

Scanning electron fractograph showing the cleavage brittle fracture

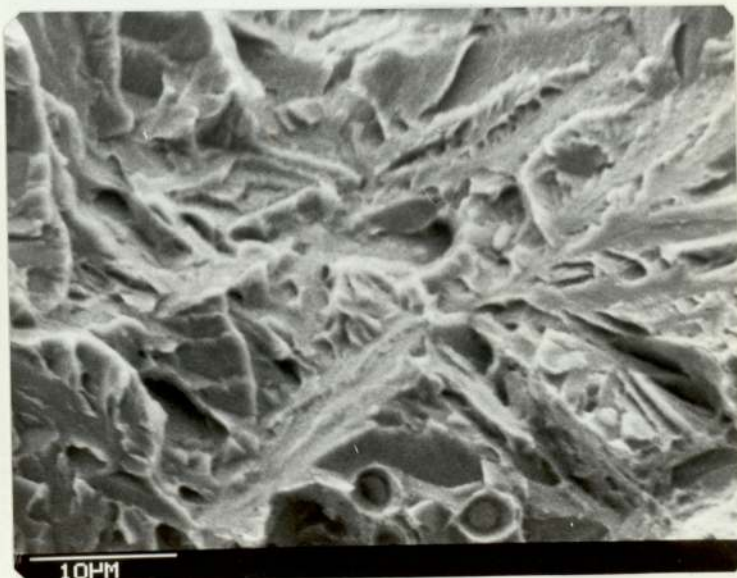
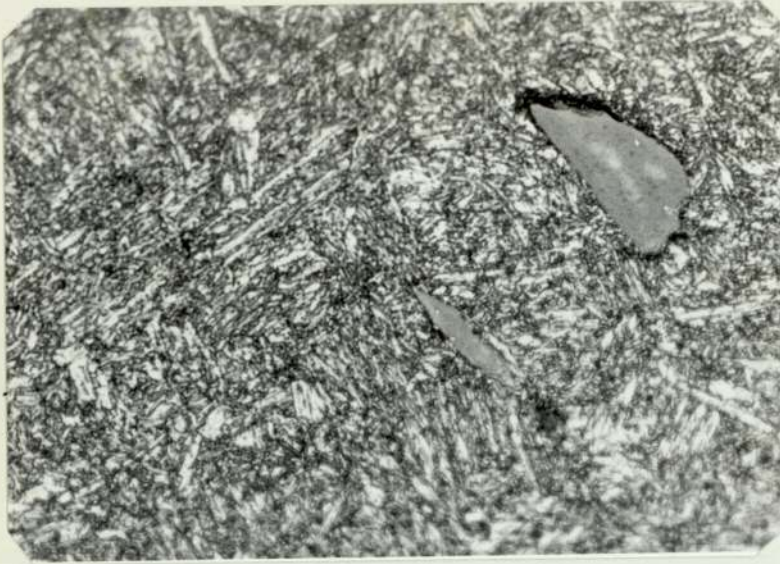
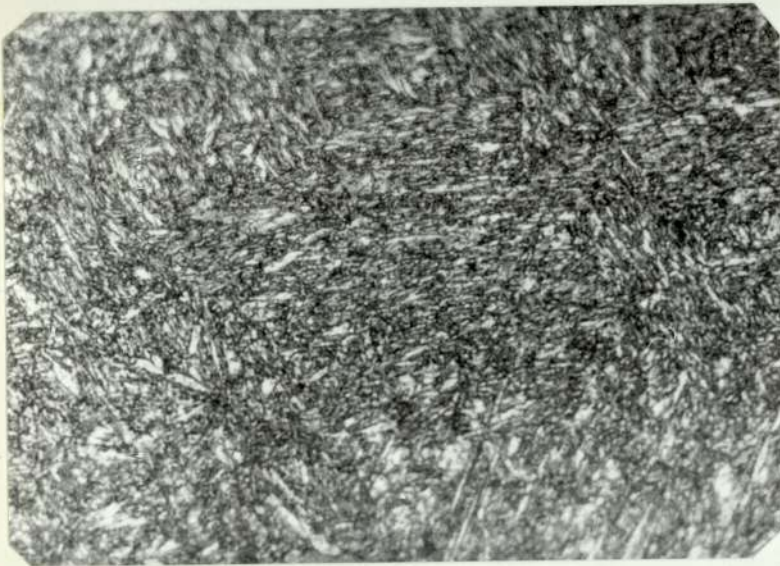


PLATE 49 Microstructure of H.W. die steel
"Somdie" DO



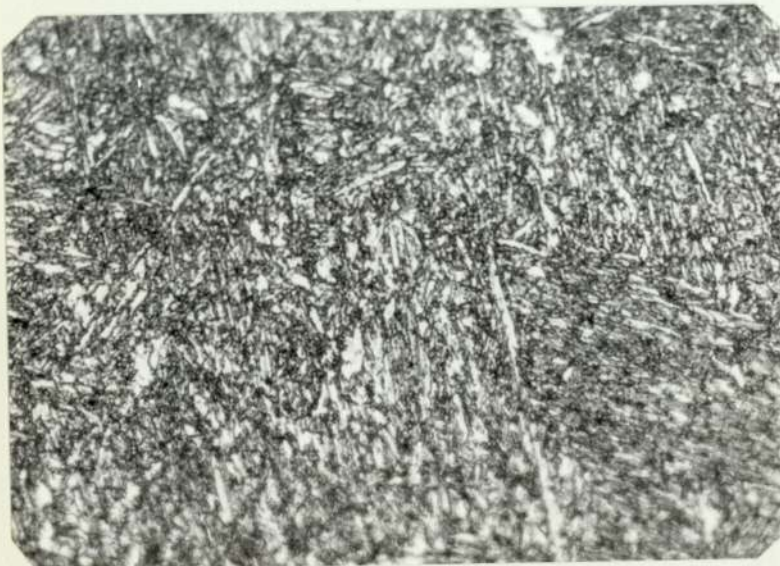
A. Top

Optical micrograph showing tempered martensite and silicate inclusion (grey)
(Mag. x1260)



B. Centre

Optical micrograph showing fine tempered martensite structure with aligned silicate inclusion
(Mag. x1260)



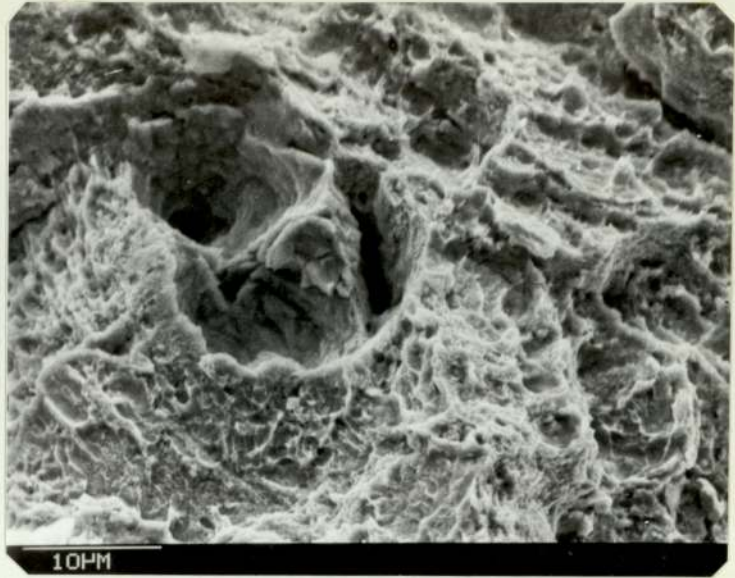
C. Edge

Optical micrograph showing tempered martensite
(Mag. x1260)

PLATE 11 Fracture surface of H.W. die steel
"Somdie" DO

A. Top

Scanning electron
fractograph showing
large voids
surrounded with
fine voids and some
micro-cracks



C. Edge

Scanning electron
fractograph showing
the coarse and fine
voids

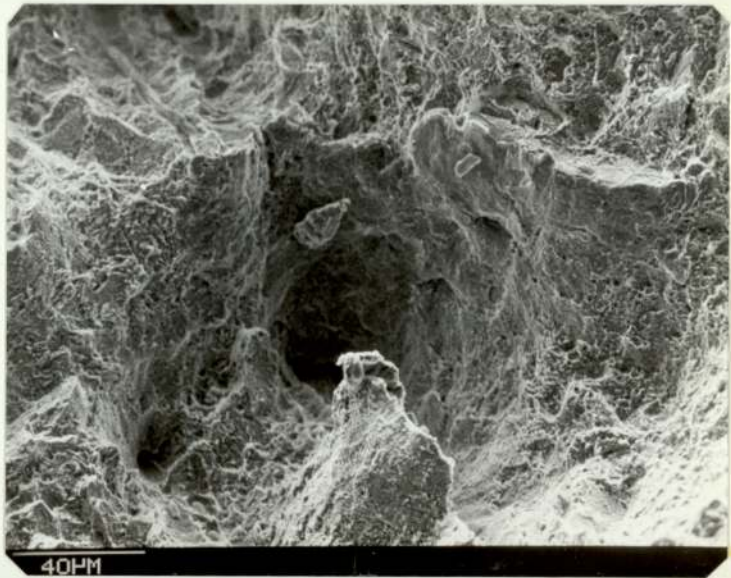


PLATE 50 Microstructure of H.W. Die steel
"Somdie" DM



A. Top

Optical micrograph showing very fine tempered martensite and some bainite (dark) and free ferrite (white areas) (Mag. x540)



B. Centre

Optical micrograph showing tempered martensite and bainite (Mag. x540)



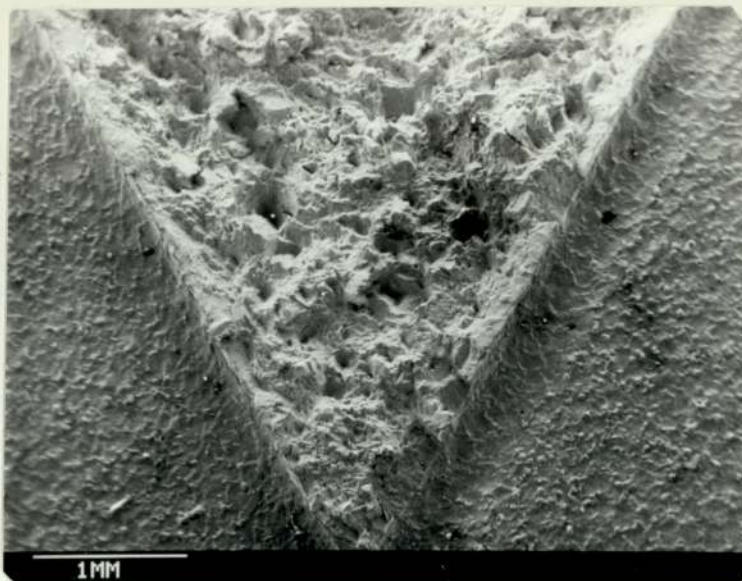
C. Edge

Optical micrograph showing tempered bainite, some tempered martensite and some free ferrite (white areas) (Mag. x540)

PLATE 12 Fracture surface of H.W. die steel
"Somdie" DM

A. Top

General appearance
of voids in
ductile fracture
surface



B. Centre

Ductile fracture
surface with
discontinuous
micro-cracks



PLATE 51 Microstructure of H.W. die steel
"Somdie" DC



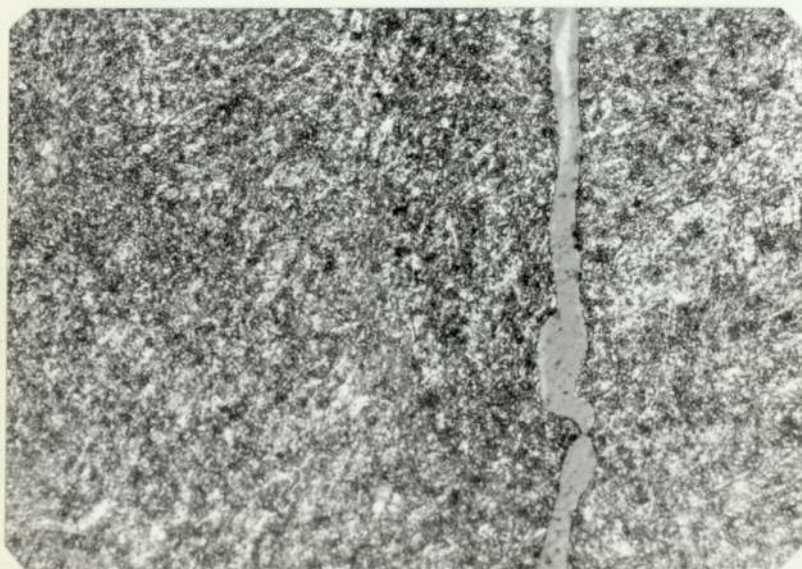
A. Top

Optical micrograph showing deformed silicate inclusion with MnS ppt within it, tempered bainite and some free ferrite (Mag. x844)



B. Centre

Optical micrograph showing silicate inclusion with tempered bainite in ferrite matrix (Mag. x844)



C. Edge

Optical micrograph showing vertical silicate inclusion with tempered bainite (Mag. x844)

PLATE 13 Fracture surface of H.W. die steel
"Somdie" DC

A. Top

Scanning electron fractograph showing typical cleavage brittle fracture



B. Centre

Macro and microvoids on the right side of the photograph, river pattern and the stretch zone on the top left



C. Edge

Scanning electron fractograph showing typical cleavage brittle fracture

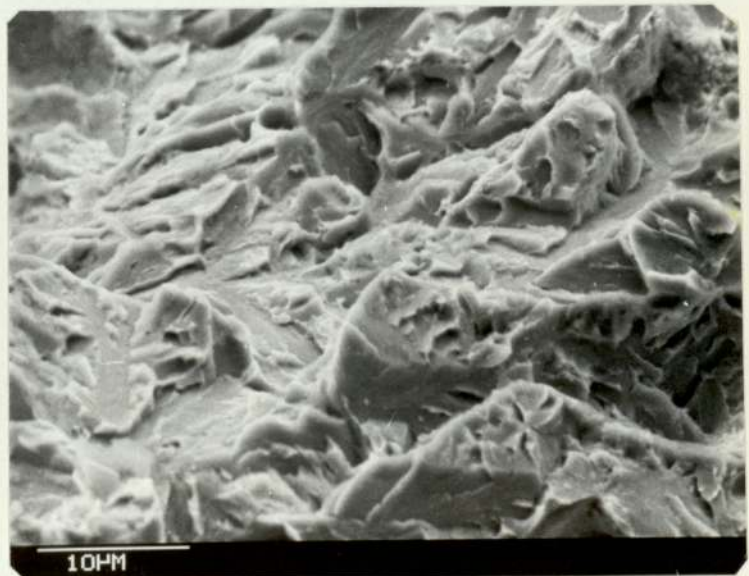
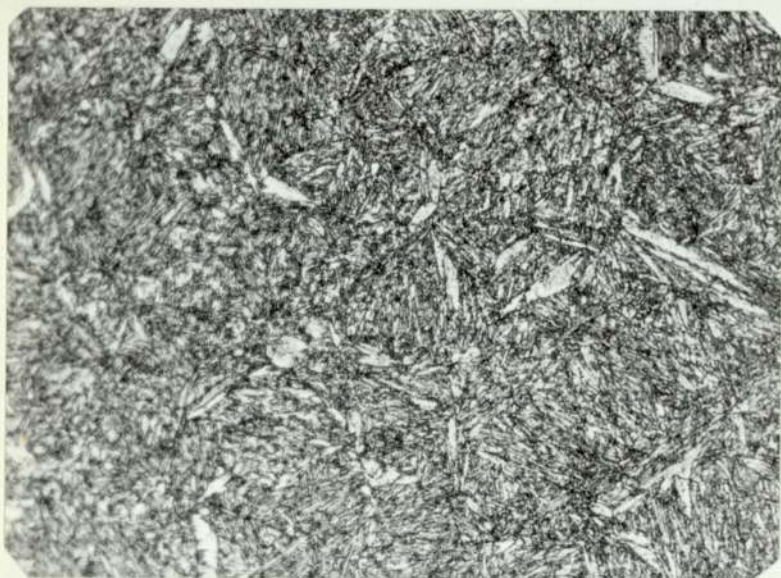


PLATE 52 Microstructure of H.W. die steel
"Thermodie" EO



A. Top

Optical micrograph
showing tempered
martensite
(Mag. x540)



B. Centre

Optical micrograph
showing tempered
bainite with
tempered martensite
(Mag. x844)



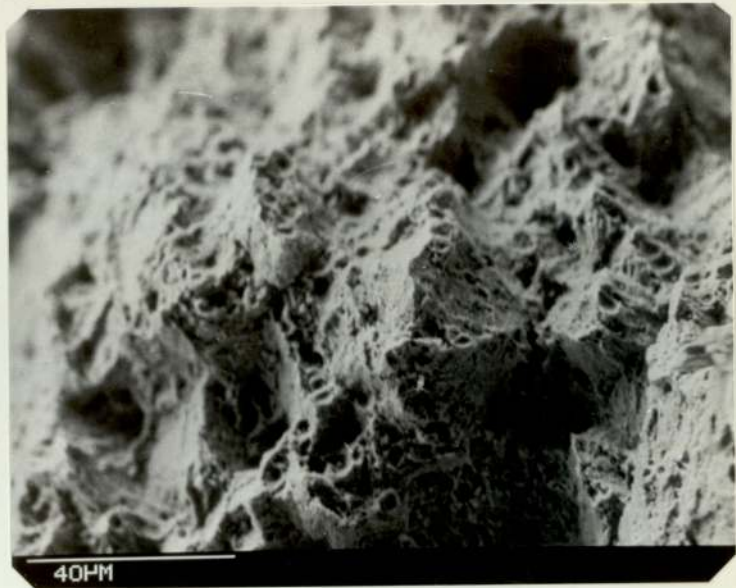
C. Edge

Optical micrograph
showing carbide
particle in a bainite
structure and silicate
inclusion
(Mag. x844)

PLATE 14 Fracture surface of H.W. die steel
"Thermodie" EO

A. Top

Scanning electron
fractograph showing
typical ductile
fracture surface
with dimples



B. Centre

Scanning electron
fractograph showing
macro and microvoids
with silicate
inclusion



C. Edge

Scanning electron
fractograph showing
microvoids with
elongated silicate
inclusion in the
worked direction



PLATE 53 Microstructure of H.W. die steel
"Thermodie" EC



A. Top

Optical micrograph showing tempered bainite (dark constituent) in a matrix of ferrite (white constituent) (Mag. x844)



B. Centre

Optical micrograph showing mainly tempered bainite and free ferrite (Mag. x844)



C. Edge

Optical micrograph showing mainly tempered bainite and some free ferrite (Mag. x844)

PLATE 15 Fracture surface of H.W. die steel
"Thermodie" EC

A. Top

Scanning electron fractograph showing quasi fracture surface with silicate inclusions



B. Centre

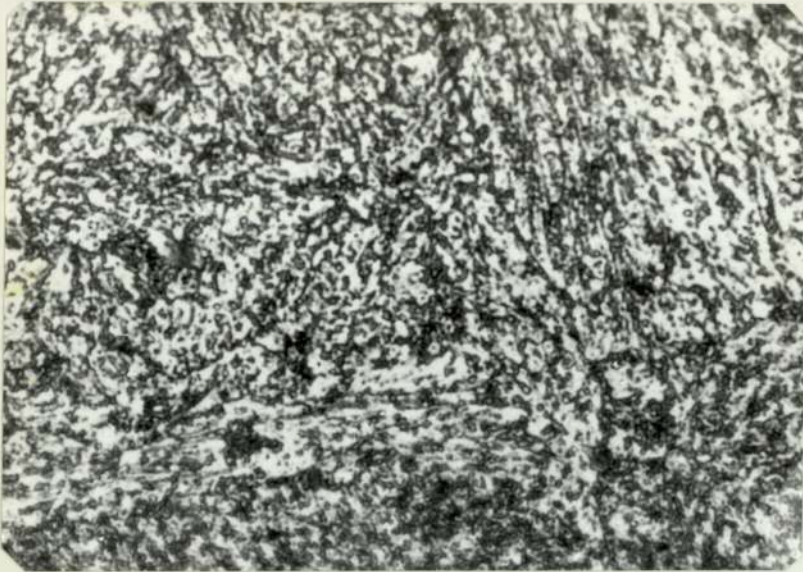
Scanning electron fractograph showing ductile fracture surface and cracks at the top right of the photograph



C. Edge

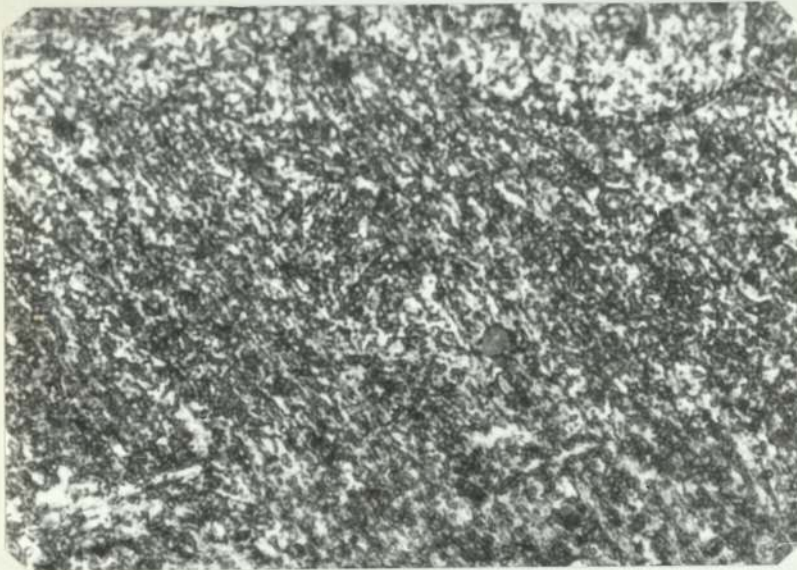
Scanning electron fractograph showing discontinuous cleavage surrounded by fine dimple structure





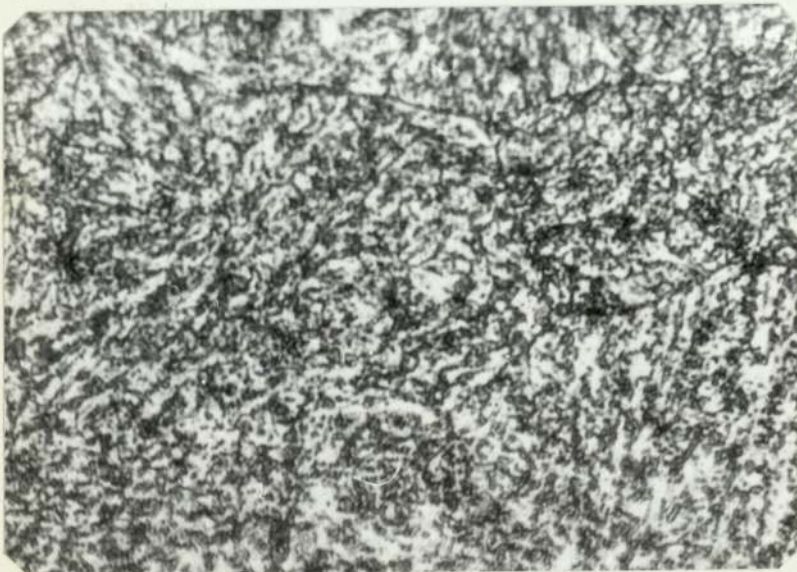
A. Top

Optical micrograph showing mainly carbide particles in a bainitic structure which is arranged in the different grain (Mag. x1688)



B. Centre

Optical micrograph showing carbide particles in a bainitic structure which is arranged in the different grain (Mag. x1688)



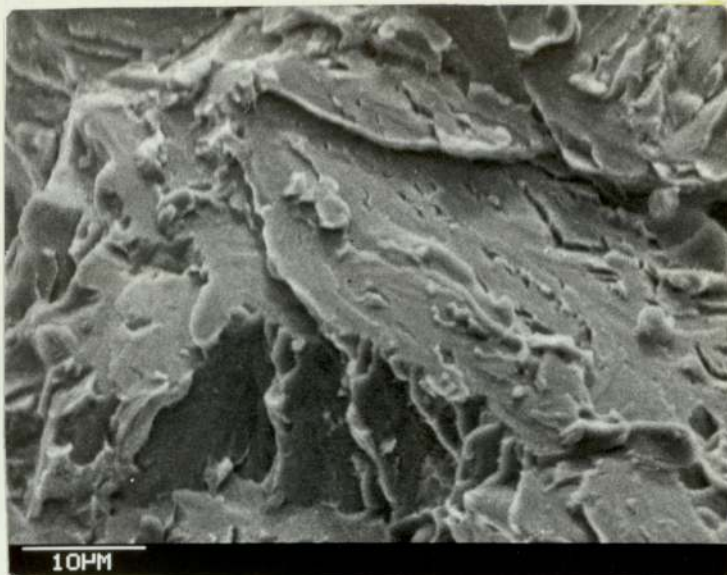
C. Edge

Same microstructure as A and B but small grain size (Mag. x1688)

PLATE 16 Fracture surface of "Hydie" steel H20

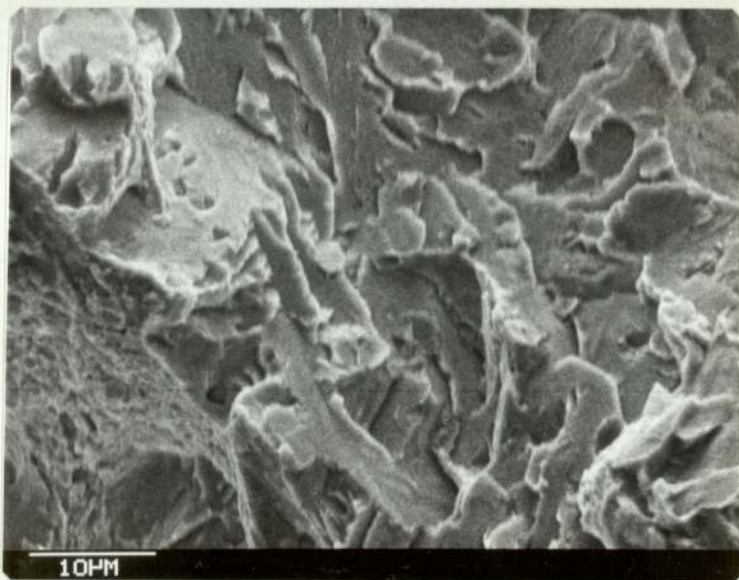
A. Top

Scanning electron
fractograph showing
cleavage facets
"fully brittle"



B. Centre

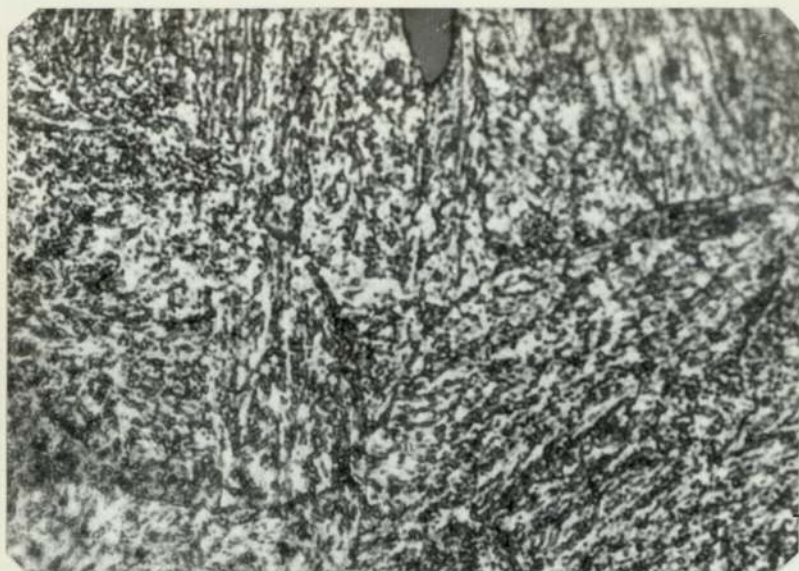
Scanning electron
fractograph showing
brittle fracture
surface



C. Edge

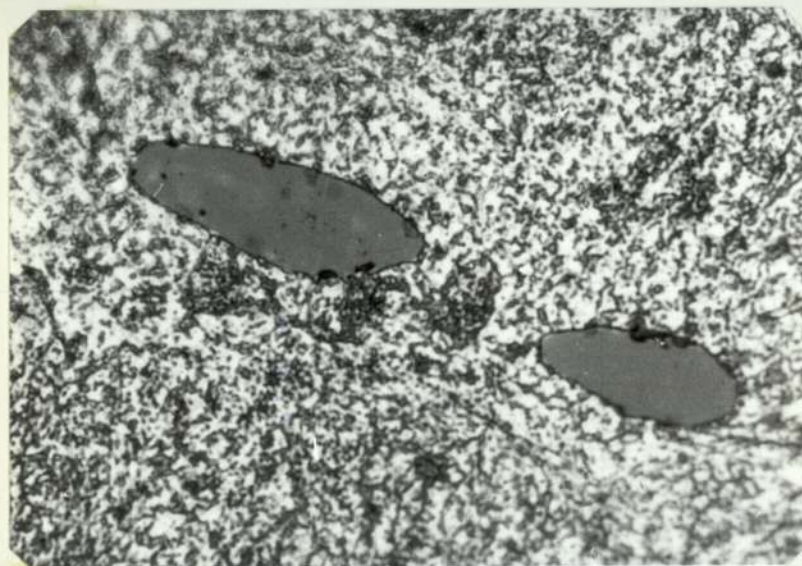
Scanning electron
fractograph showing
fully brittle
fracture surface





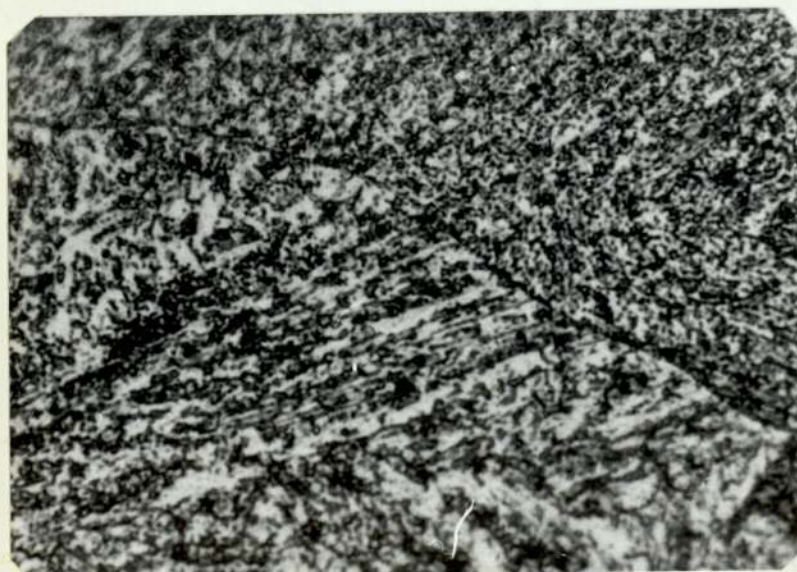
A. Top

Optical micrograph showing structure mainly consisting of carbide particles and silicate inclusions (dark grey) (Mag. x~~688~~)



B. Centre

Optical micrograph showing silicate inclusion with carbide particles in a bainitic structure (Mag. x~~1688~~)



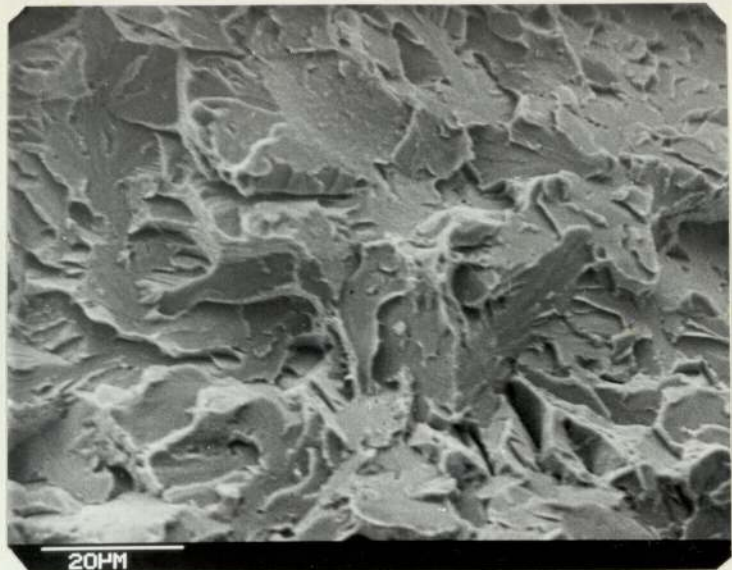
C. Edge

Optical electron micrograph showing carbide particles in a bainitic structure which is arranged in the different grain (Mag. x~~1688~~)

PLATE 17 Fracture surface of "Hydie" steel H2M

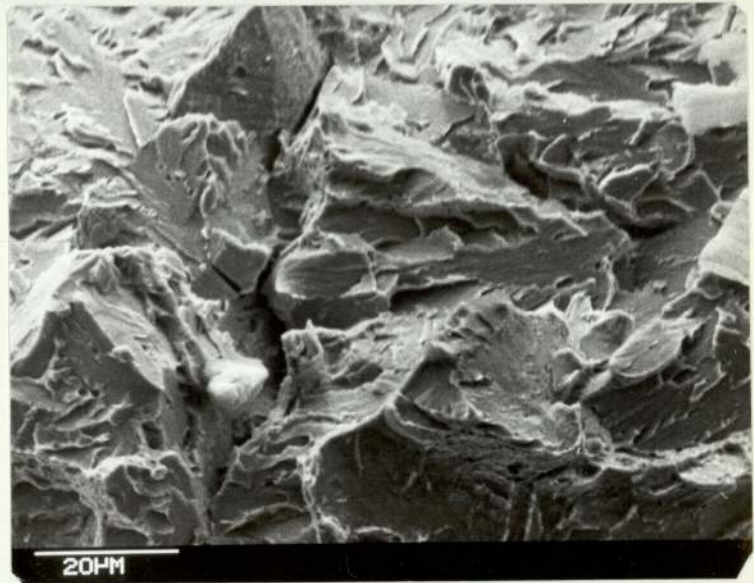
A. Top

Scanning electron fractograph showing the river pattern in a fully brittle fracture surface



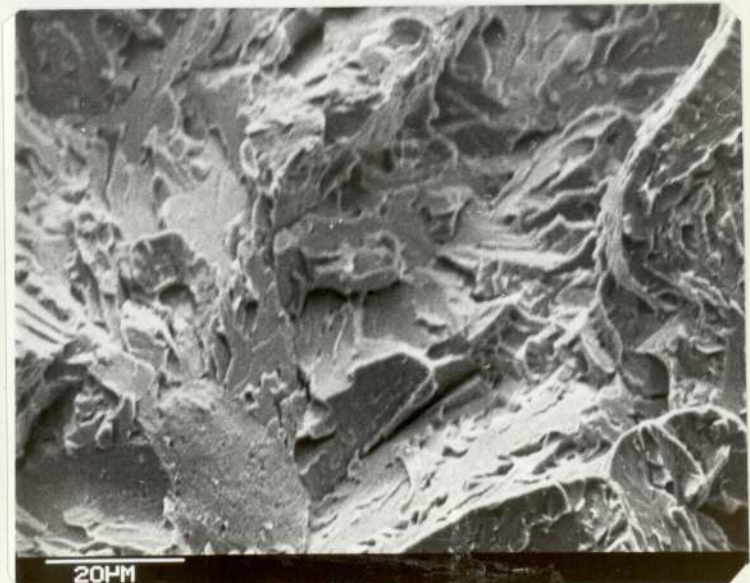
B. Centre

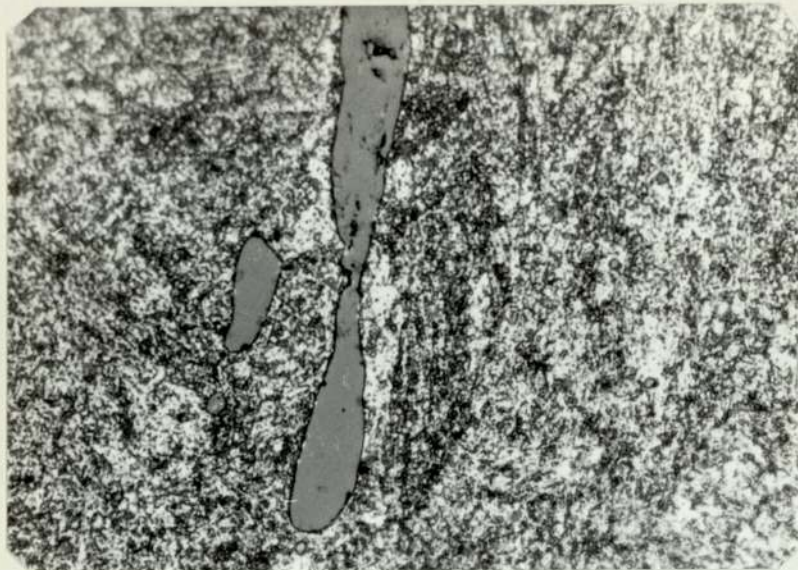
Scanning electron fractograph showing crack path within the crystal in cleavage brittle fracture surface



C. Edge

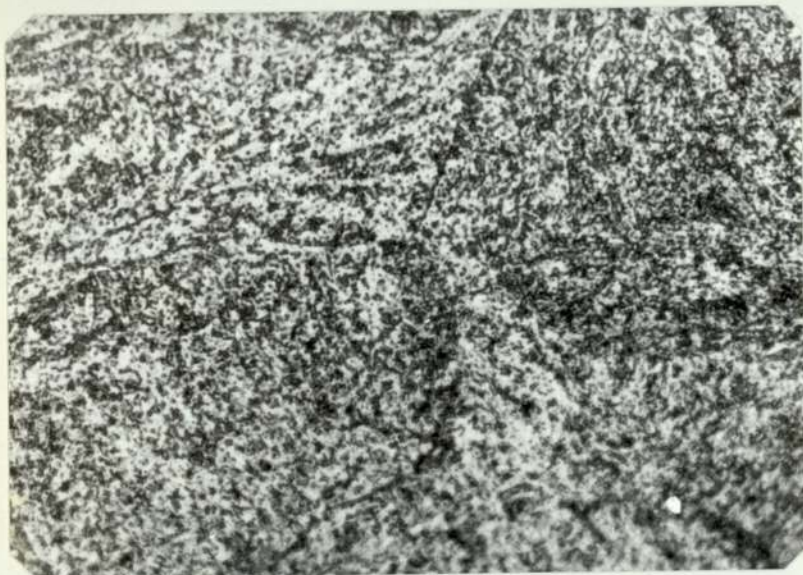
Scanning electron fractograph showing cleavage brittle fracture surface





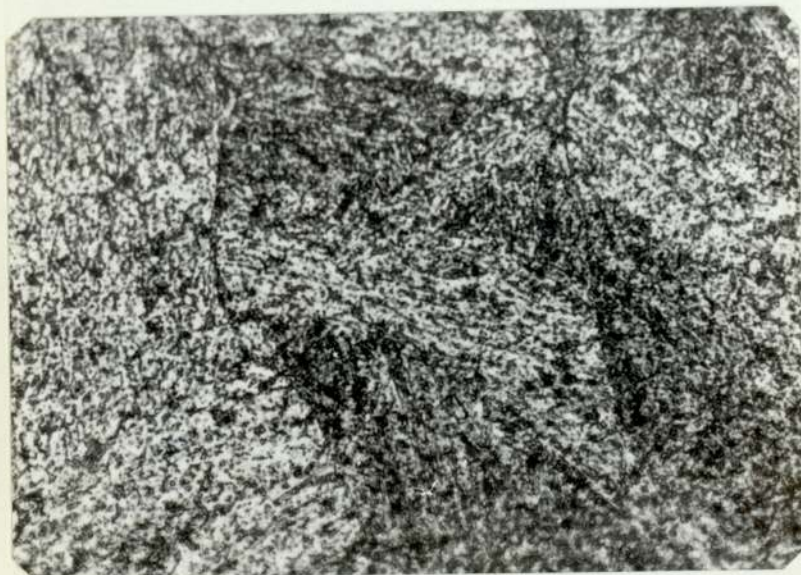
A. Top

Optical micrograph showing silicate inclusion with carbide particles in a bainitic structure (Mag. x1688)



B. Centre

Optical micrograph showing carbide particles in a bainitic structure which is arranged in the different grain (Mag. x1688)



C. Edge

Optical electron micrograph showing carbide particles in a bainitic structure which is arranged in the different grain, carbide particles are considerably coarser (Mag. X1688)

PLATE 18 Fracture surface of "Hydie" steel H2C

A. Top

Scanning electron fractograph showing typical brittle fracture cleavage, a large cleavage facet at the top of the photograph



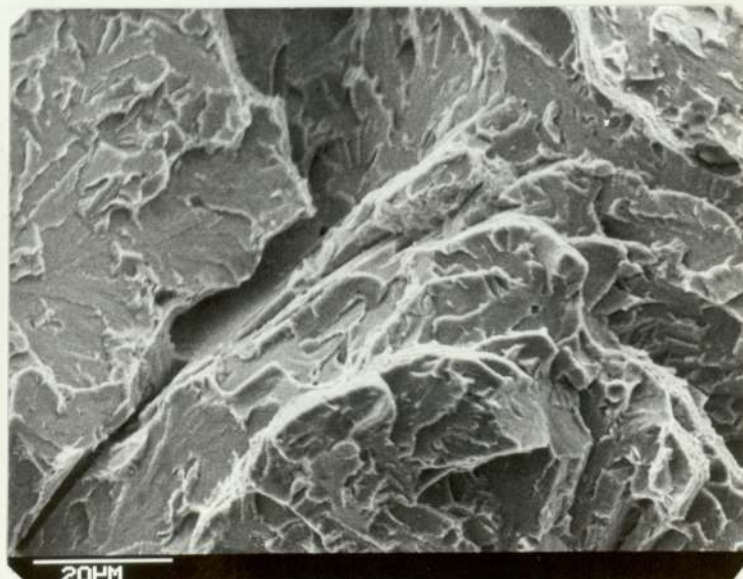
B. Centre

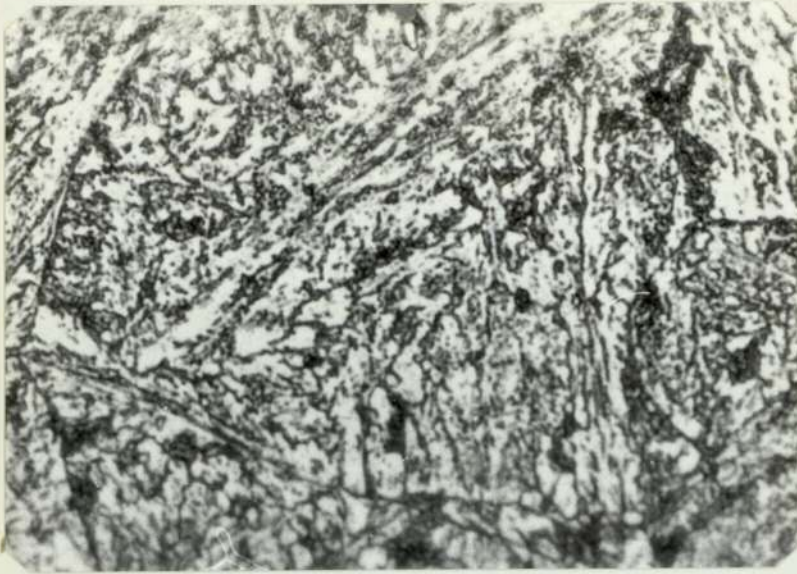
Brittle fracture surface area surrounded by fine dimples



C. Edge

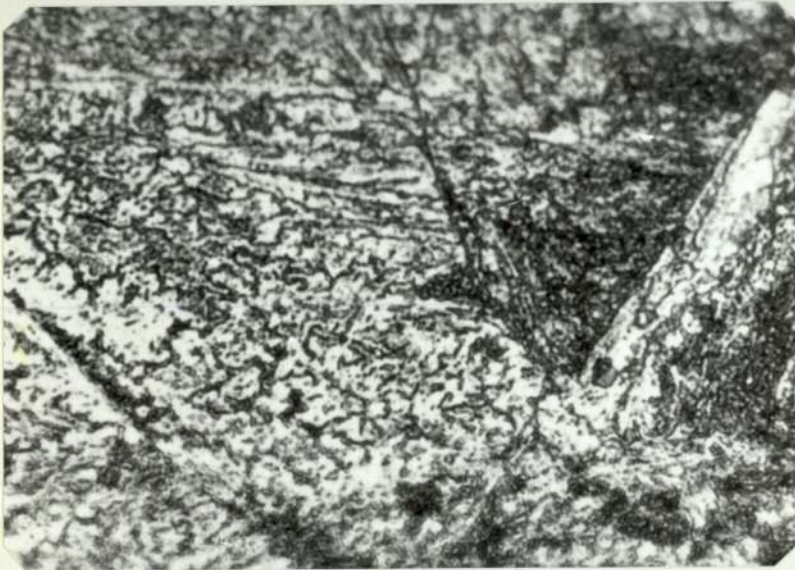
Scanning electron fractograph showing the crack path within crystal in brittle fracture cleavage





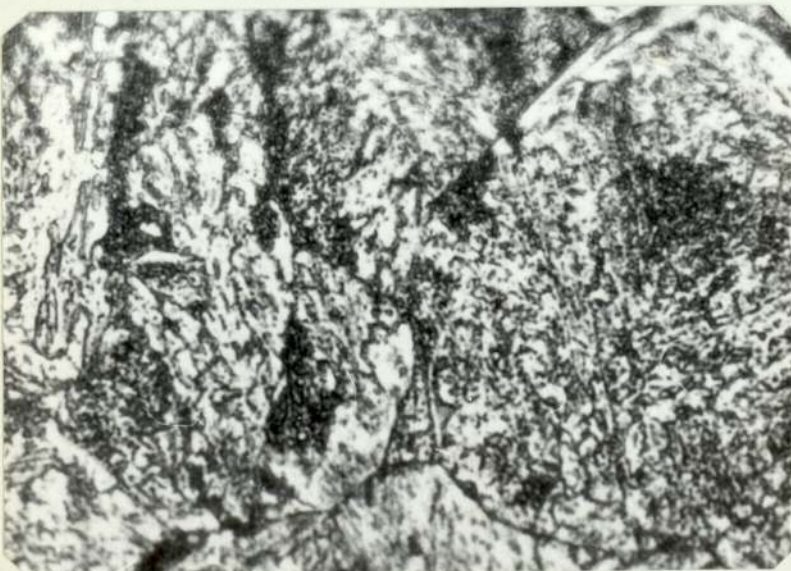
A. Top

Optical micrograph showing large carbide particles in a bainitic structure which is arranged in the different grain (Mag. x1688)



B. Centre

Optical micrograph showing a bainitic carbide particle (Mag. x1688)



C. Edge

Optical micrograph showing carbide particles in a bainitic structure which is arranged in the different grain (Mag. x1688)

PLATE 19 Fracture surface of "Hydie" steel H2A

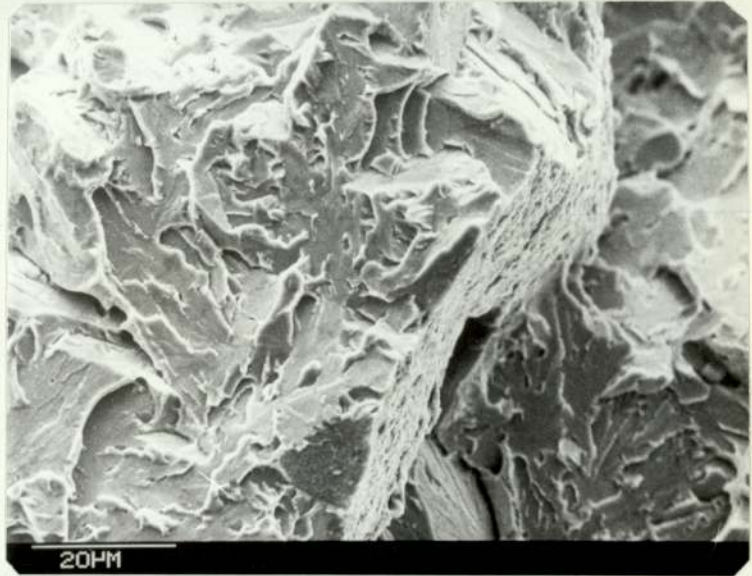
A. Top

Scanning electron fractograph showing large and small voids. Top left and right show river pattern



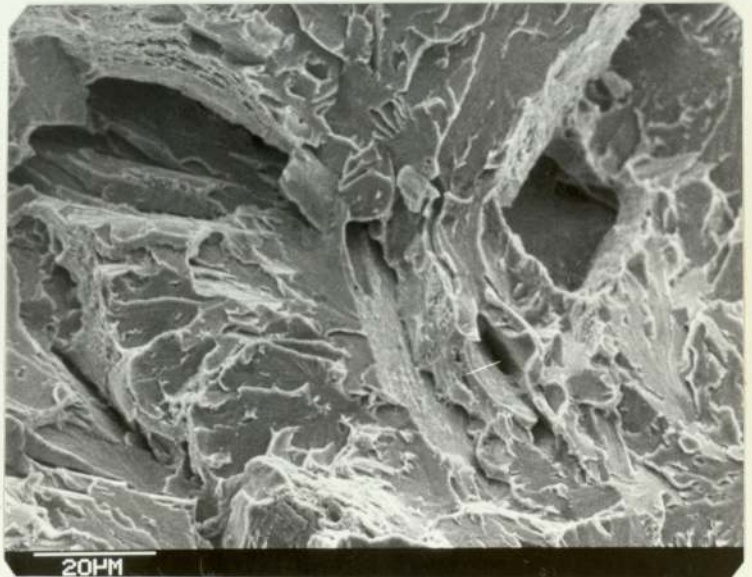
B. Centre

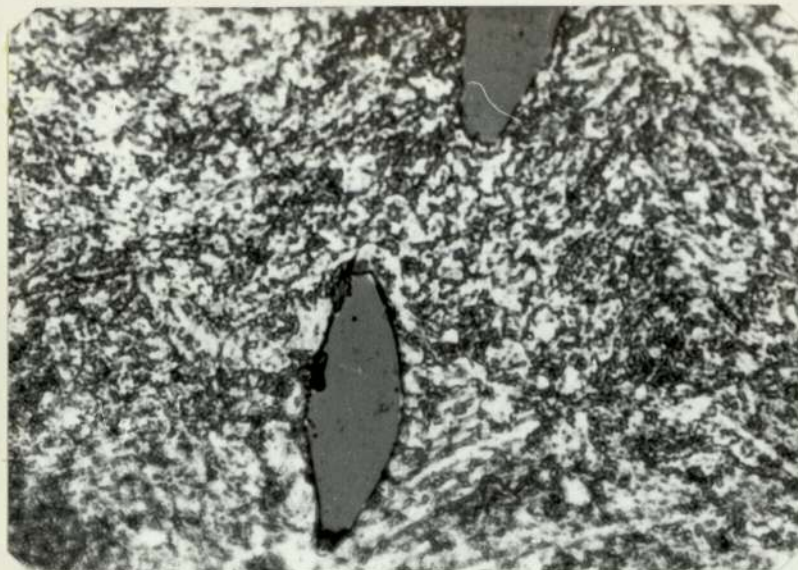
Scanning electron fractograph showing brittle fracture cleavage



C. Edge

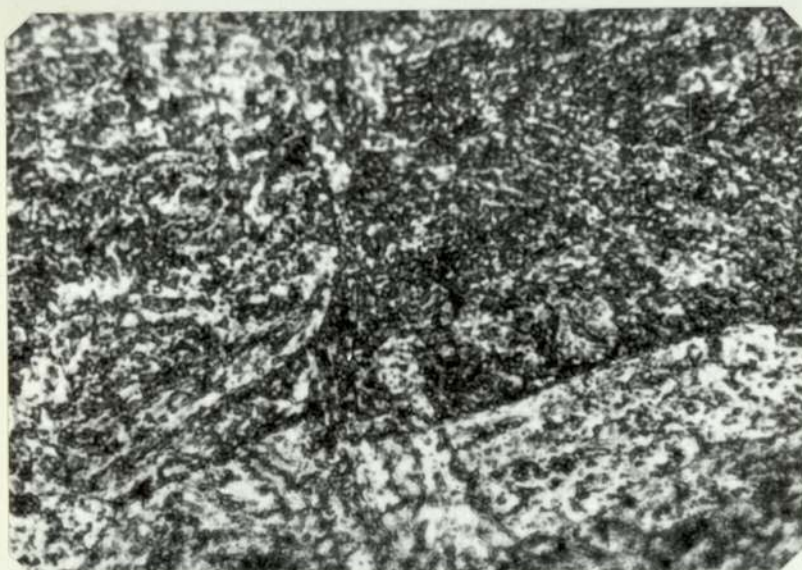
Scanning electron fractograph showing brittle fracture cleavage





A. Top

Optical micrograph showing silicate inclusion with carbide particles in a bainitic structure (Mag. x1688)



B. Centre

Optical micrograph showing carbide particles arranged in the different grain (Mag. x1688)



C. Edge

Same as B. (Mag. x1688)

PLATE 20 Fracture surface of "Hydie" steel H2B

A. Top

Scanning electron fractograph showing large void, steps and river pattern



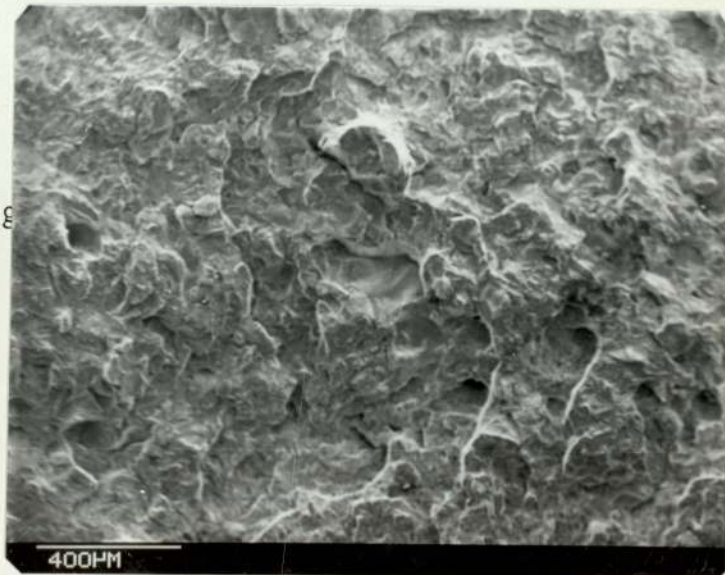
B. Centre

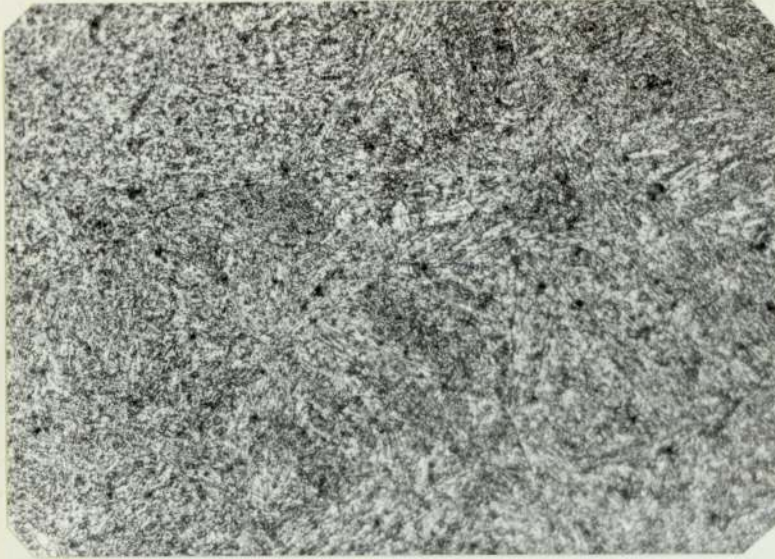
Brittle fracture cleavage



C. Edge

Scanning electron fractographs showing brittle fracture cleavage





A. Top

Optical micrograph showing carbide particles arranged in the different grain (Mag. x540)



B. Centre

Optical micrograph showing fine carbide particles at the top of the photograph, the bottom half consists of large size carbide particles (Mag. x 540)



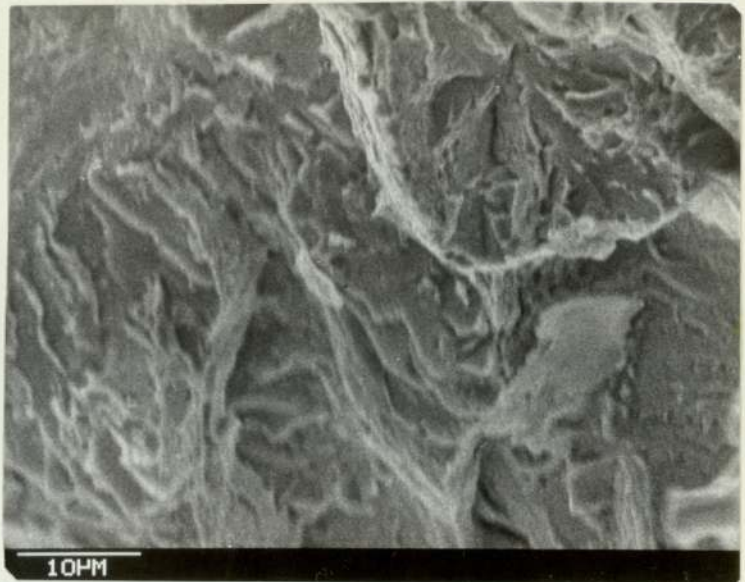
C. Edge

Optical micrograph showing carbide particles arranged in a bainitic structure. The direction is different with different grain (Mag. x540)

PLATE 21 Fracture surface of "Hydie" steel H30

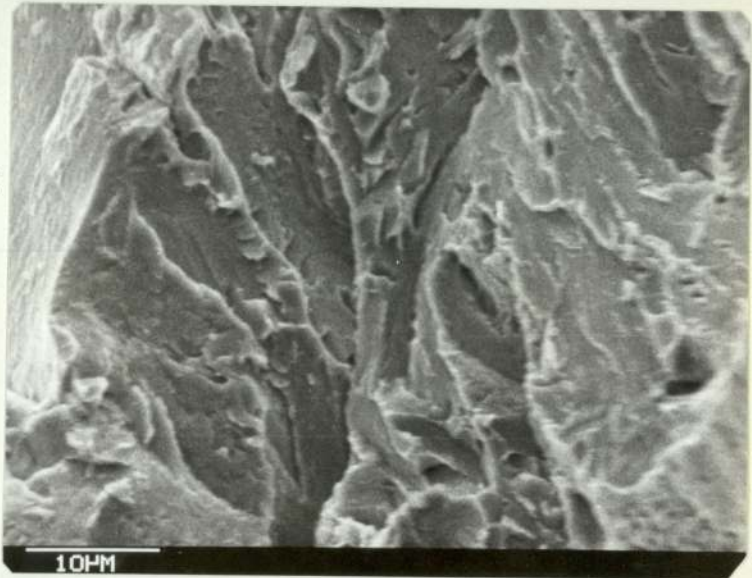
A. Top

Scanning electron fractograph showing cleavage fracture appearance at the point of chevron



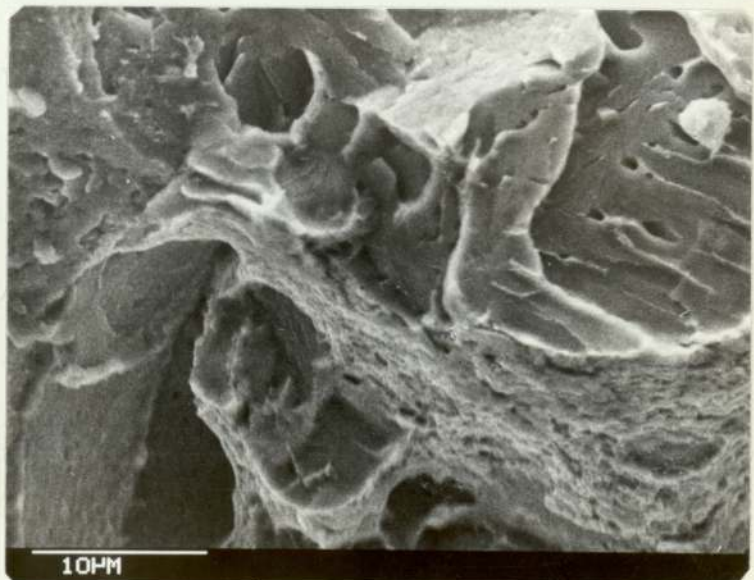
B. Centre

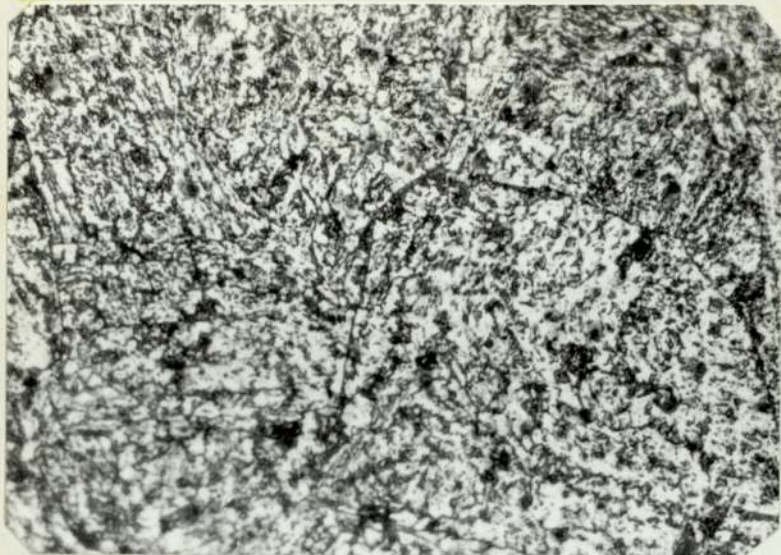
Scanning electron fractograph showing cleavage fracture facet



C. Edge

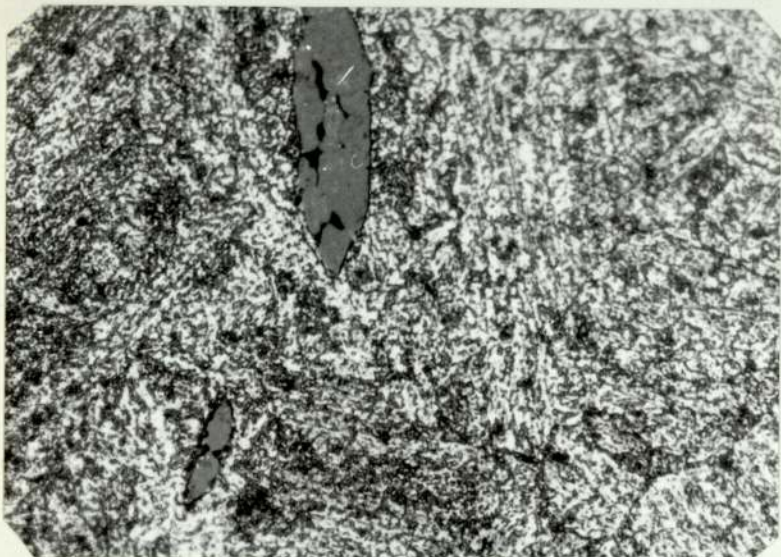
Cleavage fracture appearance with microvoids nucleated at the river pattern





A. Top

Optical micrograph showing coarse carbide particles arranged in a bainitic structure in the different grain
(Mag. x1688)



B. Centre

Optical micrograph showing carbide particles in a bainitic structure and silicate inclusions
(Mag. x1688)

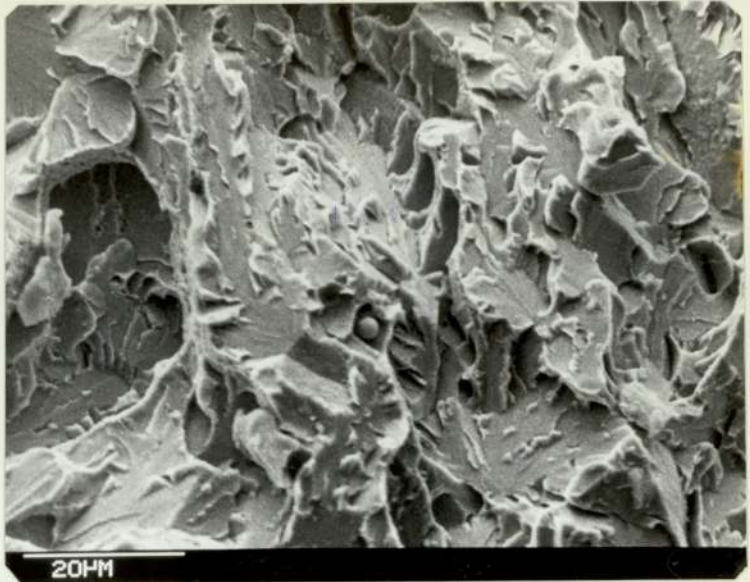


C. Edge

Optical micrograph showing carbide particle in ferrite matrix and silicate inclusions
(Mag. x1688)

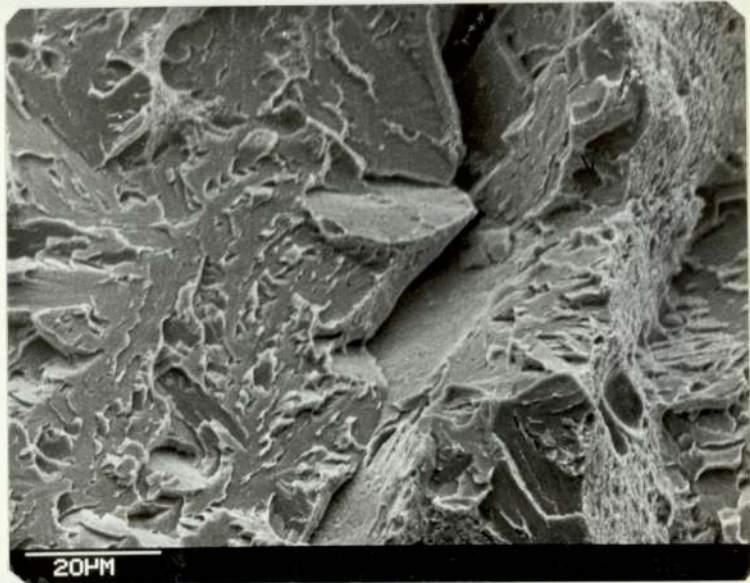
A. Top

Full brittle fracture cleavage with the river pattern and step formation



B. Centre

Scanning electron fractograph showing cleavage facet and the crack path within the crystal (continuous cleavage)

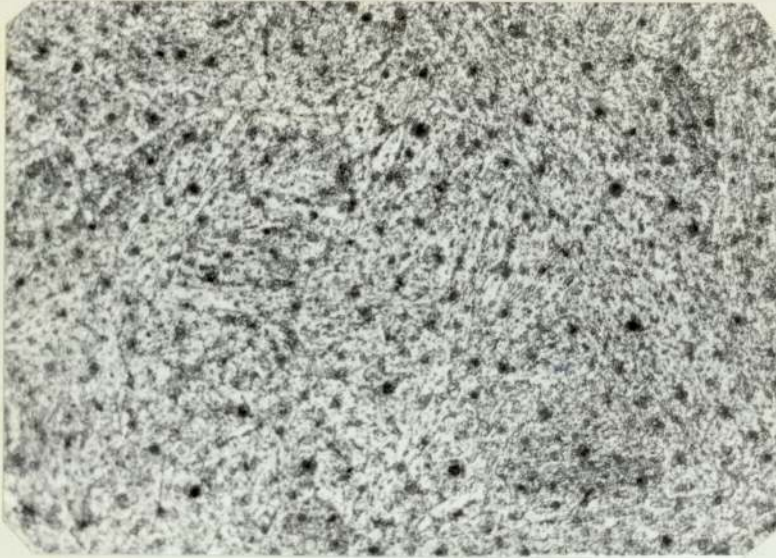


C. Edge

Brittle fracture cleavage with microvoid nucleation at the river pattern

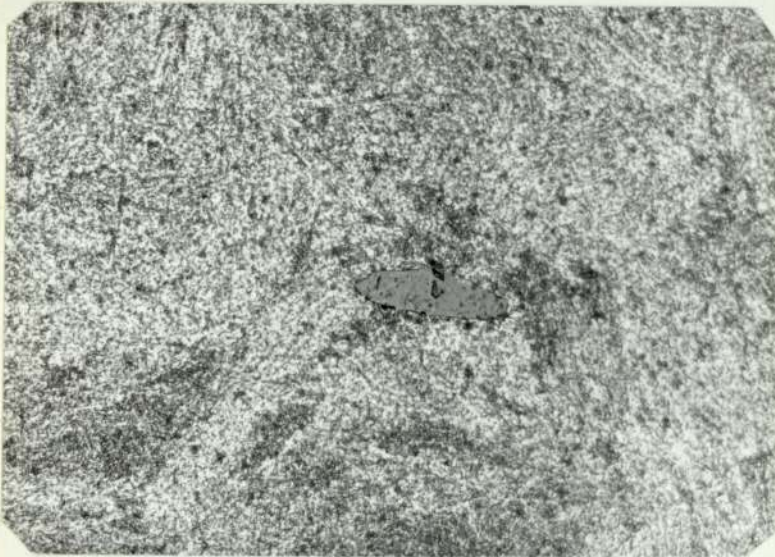


PLATE 61 Microstructure of surface of "Hydie"
steel H3C



A. Top

Optical micrograph
showing tempered
bainite
(Mag. x540)



B. Centre

Optical micrograph
showing silicate
inclusion with
carbide particle
in a bainitic
structure
(Mag. x540)



C. Edge

Optical micrograph
showing carbide
particle in a
matrix of ferrite
(Mag. x540)

PLATE 23 Fracture surface of "Hydie" steel H3C

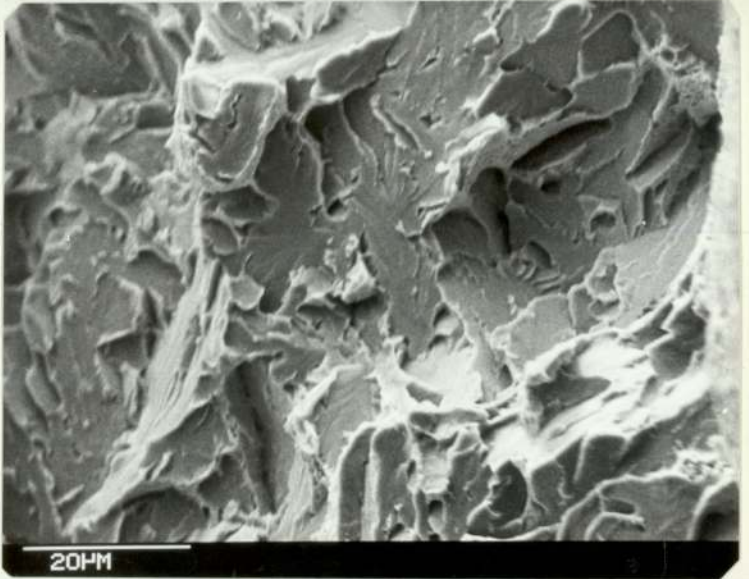
A. Top

Scanning electron
fractograph showing
brittle fracture
cleavage



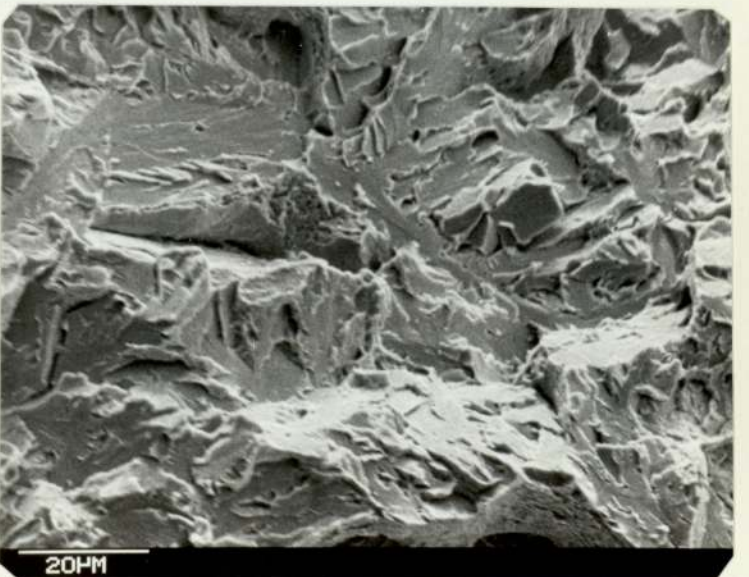
B. Centre

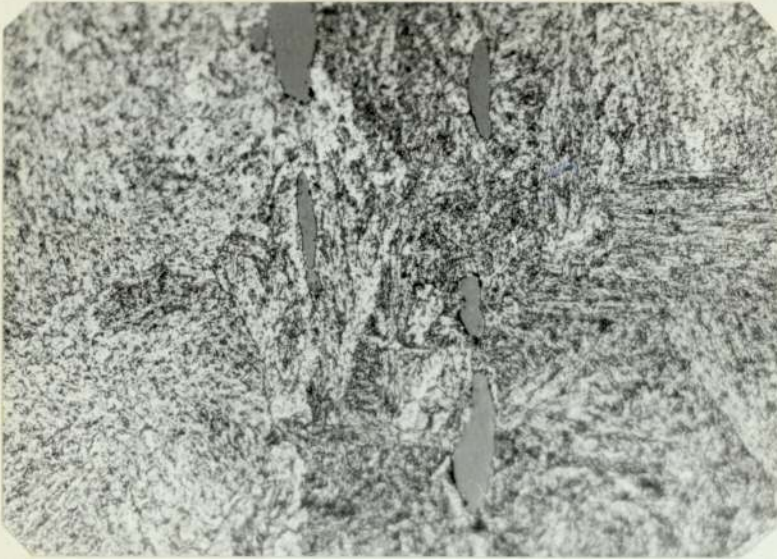
Scanning electron
fractograph showing
brittle fracture
cleavage



C. Edge

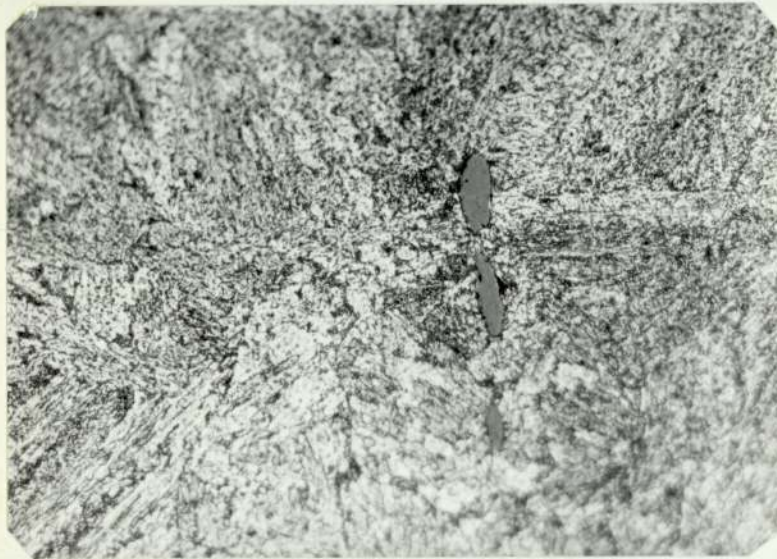
Scanning electron
fractograph showing
brittle fracture
cleavage





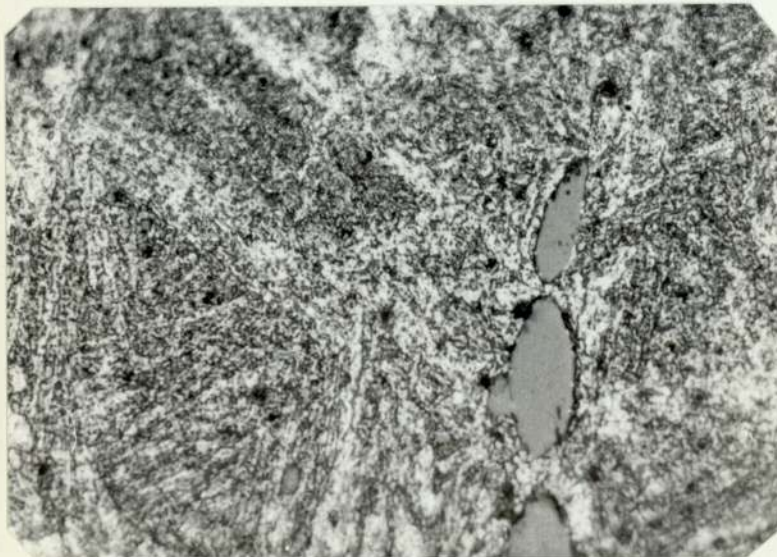
A. Top

Optical micrograph showing deformed silicate inclusions with concentrated fine carbide particles in a bainitic structure and the right half is coarse carbide particles (Mag. x540)



B. Centre

Optical micrograph showing silicate inclusions in the vertical direction with carbide particles in a bainitic structure arranged in the different direction (Mag. x540)



C. Edge

Optical micrograph showing inclusions in a vertical direction with carbide particles in a bainitic structure (Mag. x540)

PLATE 24 Fracture surface of "Hydie" steel H3A

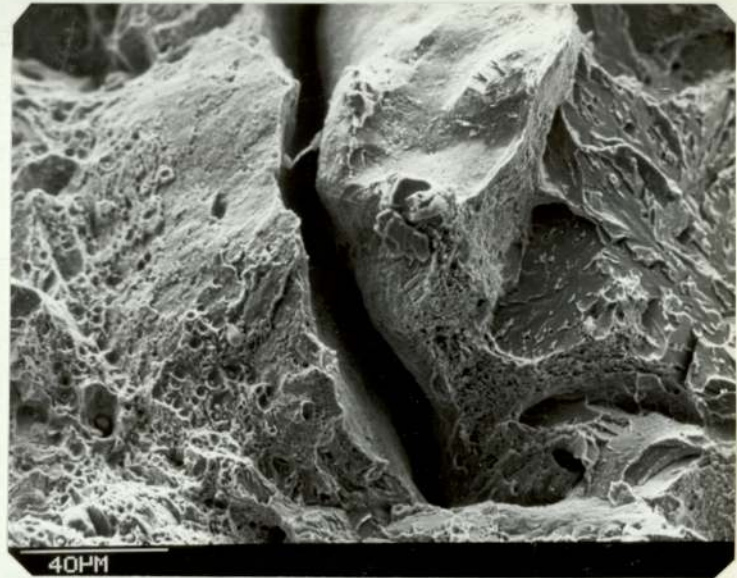
A. Top

Scanning electron fractograph showing brittle fracture cleavage.



B. Centre

Microvoids with globular inclusions surrounding the crack path within the crystal



C. Edge

Brittle fracture surface with microvoids linked together at river pattern of discontinuous cleavage

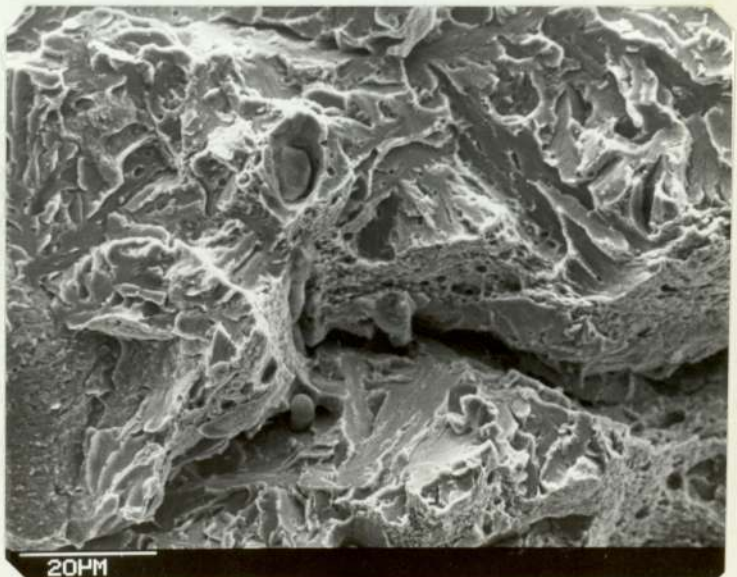
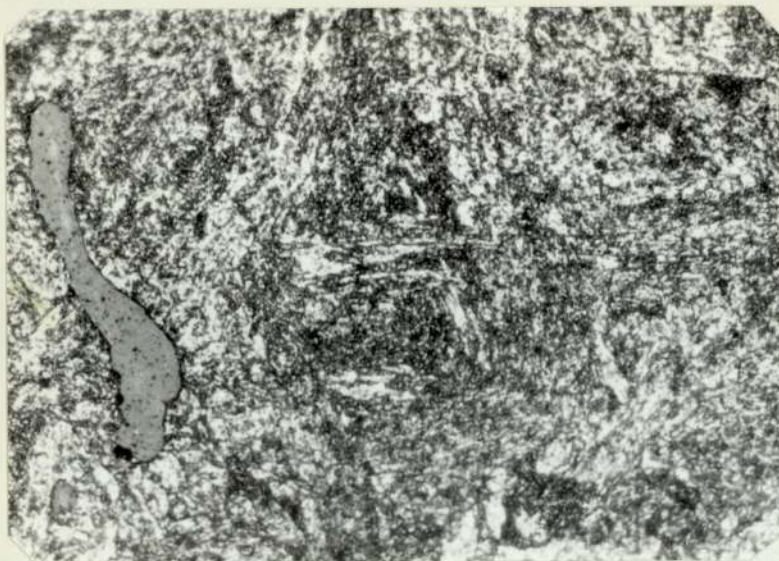


PLATE 63 Microstructure of "Hydie" steel H3B



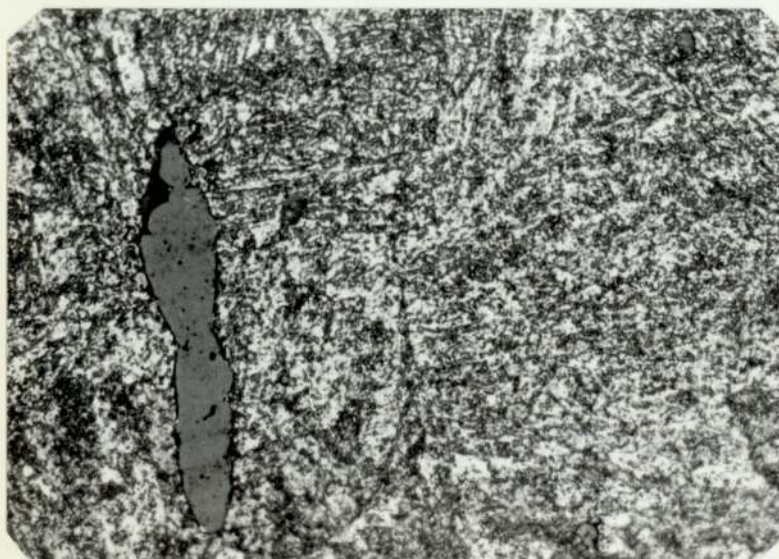
A. Top

Optical micrograph showing inclusions with carbide particles arranged in the different direction (Mag. x540)



B. Centre

Optical micrograph showing carbide particles in a bainitic structure (Mag. x540)



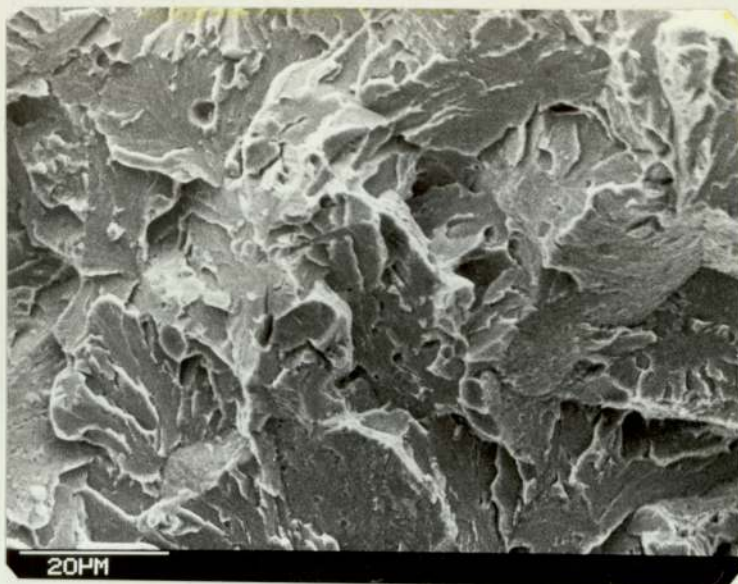
C. Edge

Optical micrograph showing carbide particles in a ferrite matrix and silicate inclusion with MnS ppt within it (Mag. x540)

PLATE 25 Fracture surface of "Hydie" steel H3B

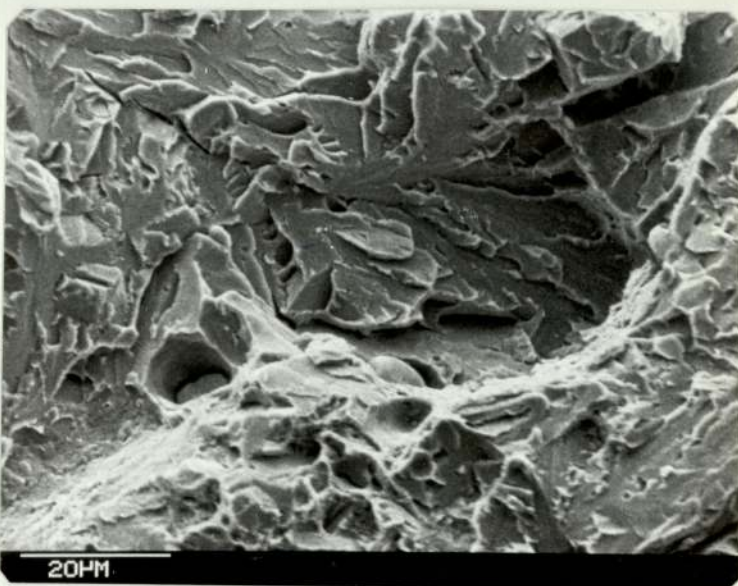
A. Top

Scanning electron fractograph showing brittle fracture cleavage with river pattern



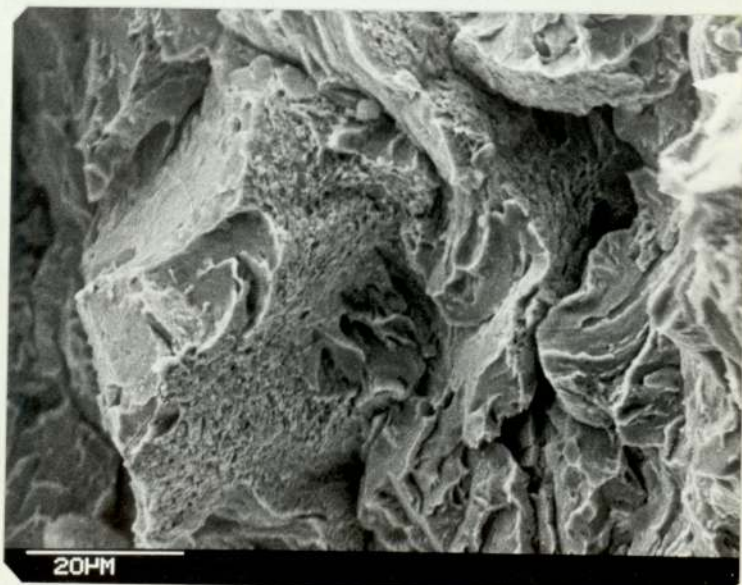
B. Centre

Scanning electron fractograph showing typical brittle fracture cleavage and discontinuous cleavage in some of the grains



C. Edge

Fine dimples and discontinuous cleavage





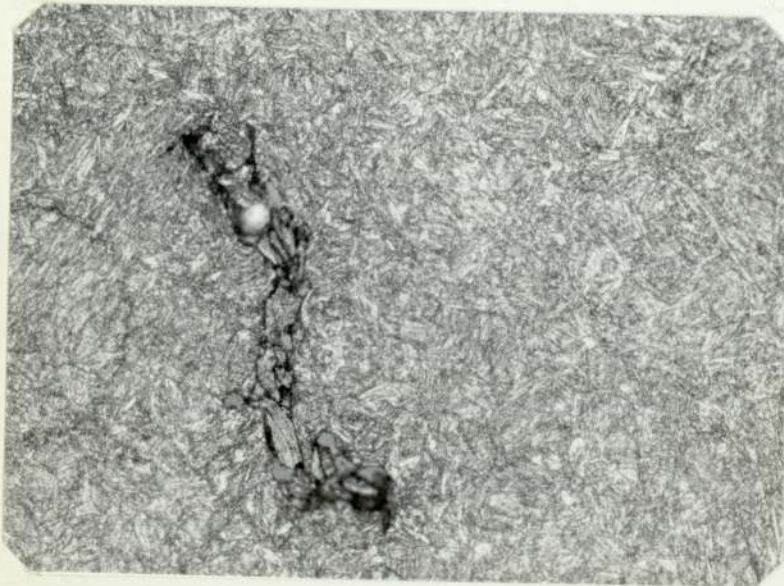
A - Top

Optical electron micrograph showing tempered bainite (dark) and upper bainite (grey)
Mag. x540



B - Centre

Optical micrograph showing tempered bainite and tempered martensite
Mag. x540

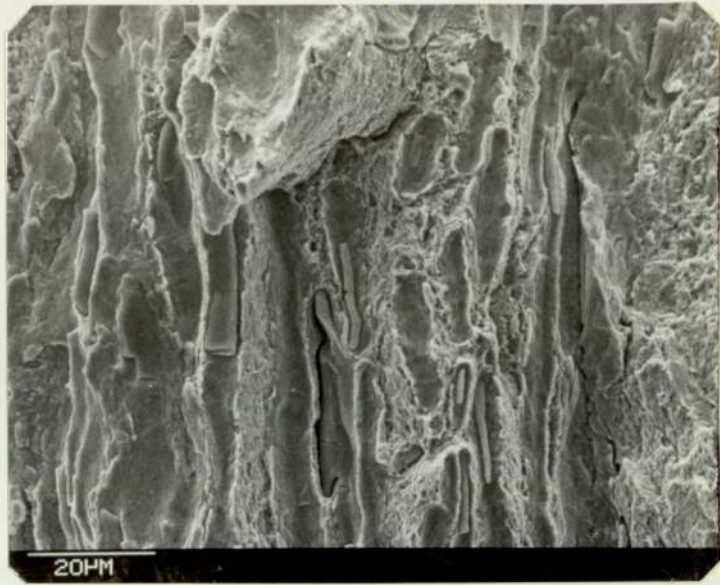


C - Edge

Optical micrograph showing tempered bainite and tempered martensite
Mag. x540

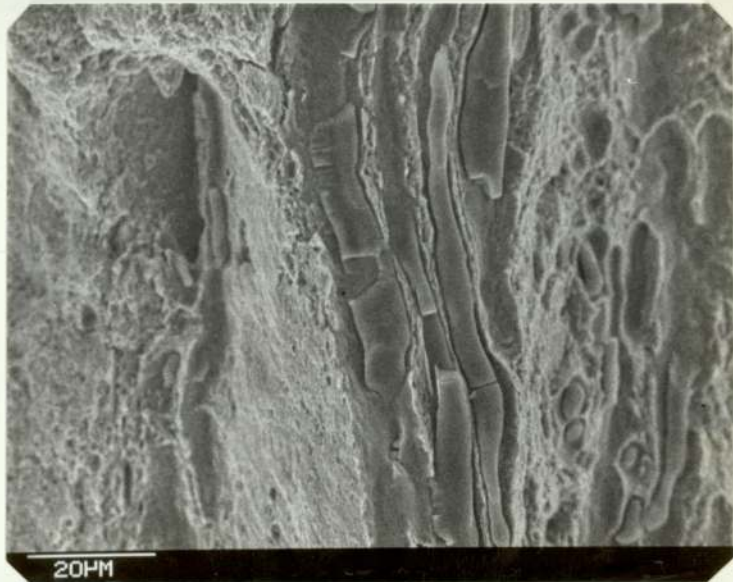
A - Top

Scanning electron
micrograph showing
deformed silicate
inclusion
surrounded by very
fine dimples
(ductile fracture
surface)



B - Centre

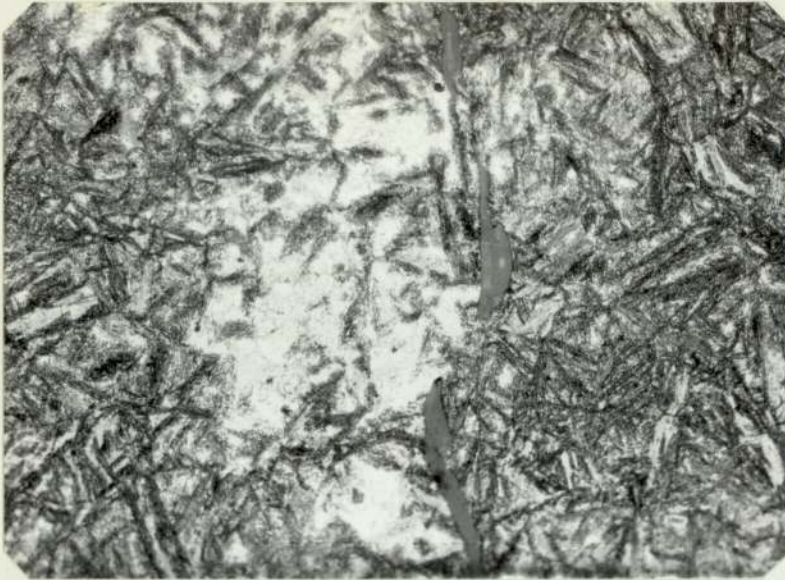
Scanning electron
micrograph showing
deformed inclusion
surrounded by very
fine dimples



C - Edge

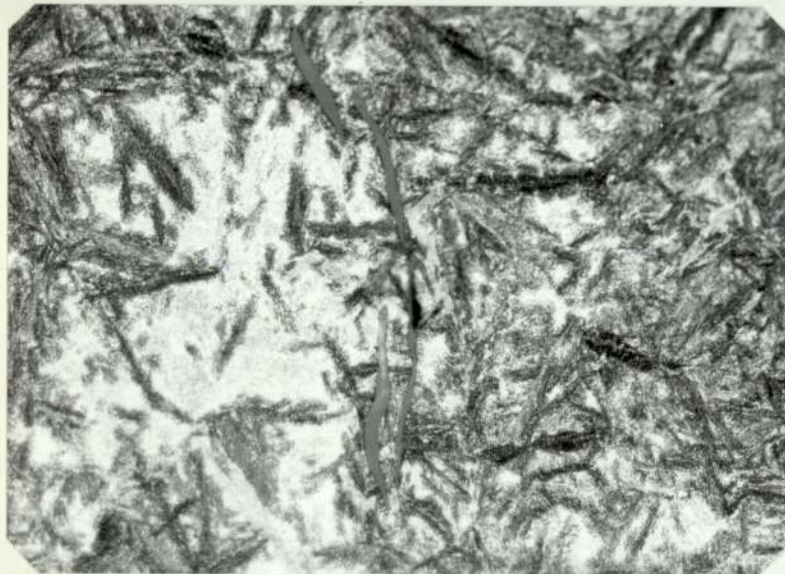
Scanning electron
micrograph showing
inclusion within
microvoid (ductile
fracture surface)





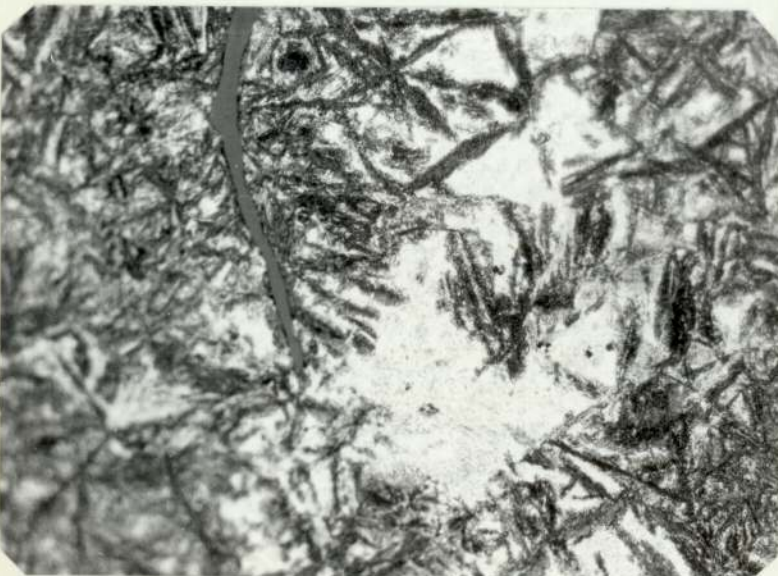
A - Top

Optical electron micrograph showing fine carbide within bainite plate (dark) banded along silicate inclusion
Mag. x540



B - Centre

Optical electron micrograph showing carbides within bainite plate and tempered martensite banded along silicate inclusion
Mag. x540



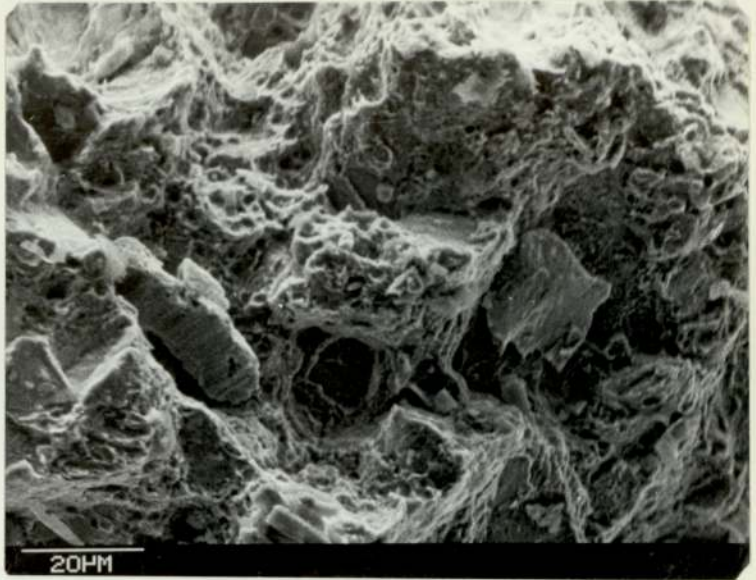
C - Edge

Optical electron micrograph showing fine carbide within bainite plate (dark area)
Mag. x540

PLATE 27 Fracture surface of H.W. die steel
Somdie S1M

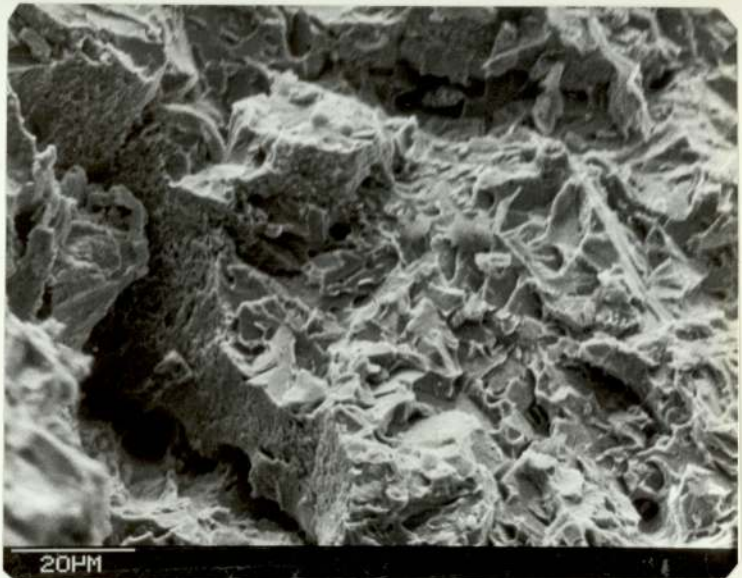
A - Top

Scanning electron
micrograph showing
ductile fracture
surface with macro
and microvoids



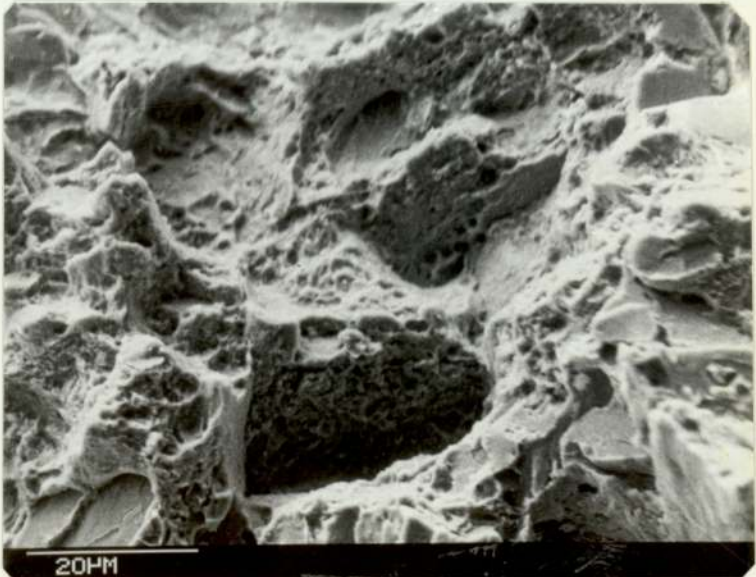
B - Centre

Scanning electron
micrograph showing
quasi fracture
surface crack path
at left photograph



C - Edge

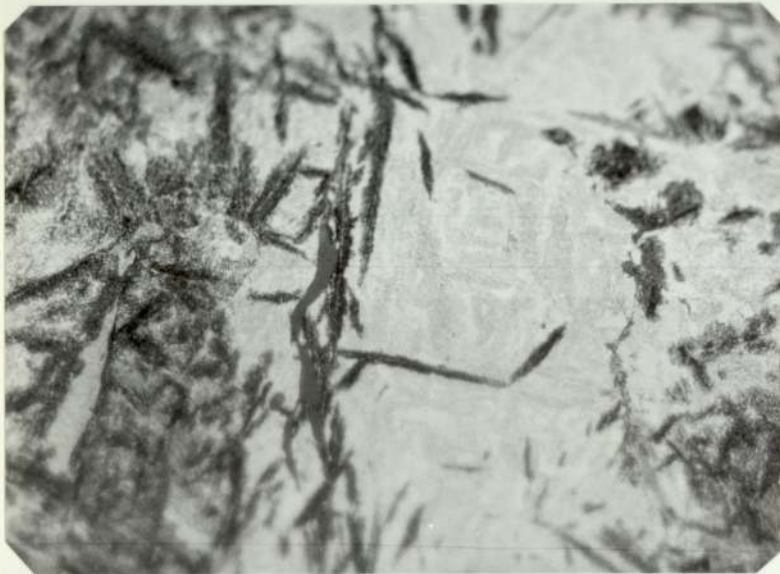
Scanning electron
micrograph showing
ductile fracture
surface with macro
and microvoids





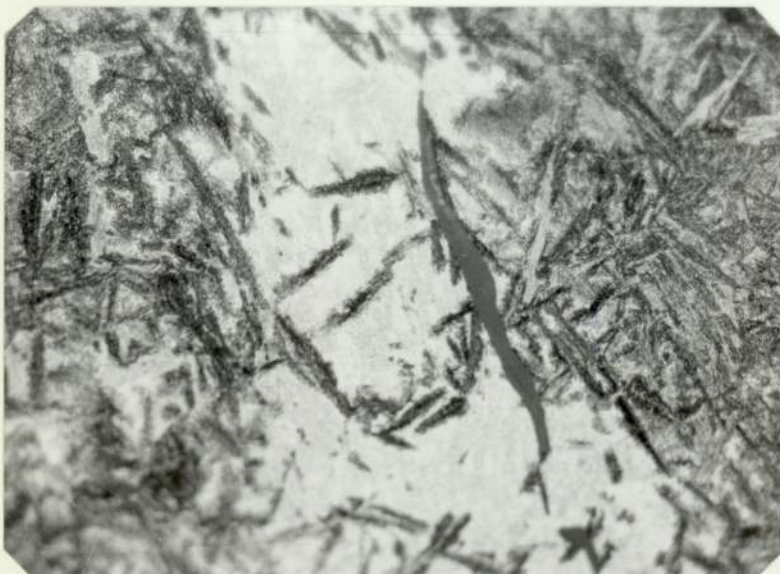
A - Top

Optical electron micrograph showing very fine carbide within bainite plate and tempered martensite
Mag. x540



B - Centre

Optical electron micrograph showing fine carbide within bainite plate (dark) banded along silicate inclusion upper bainite (grey)
Mag. x540



C - Edge

Optical electron micrograph showing carbide within bainite plates banded along inclusion
Mag. x540

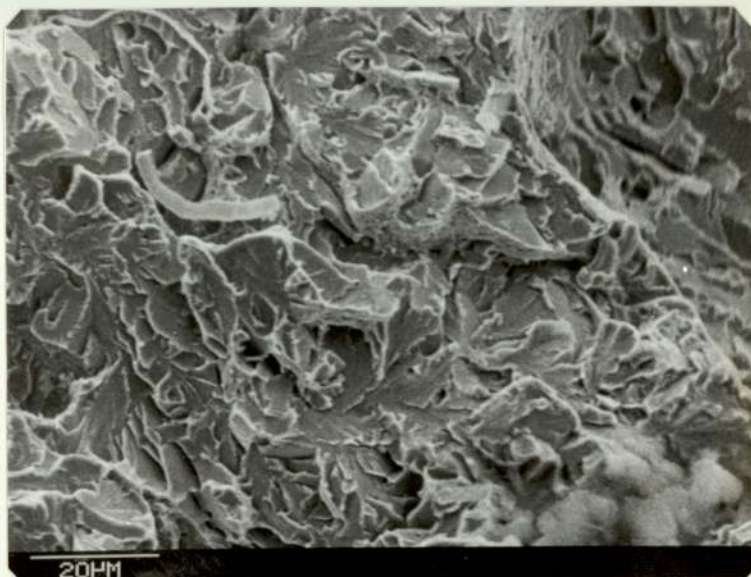
A - Top

Scanning electron micrograph showing cleavage facet with some very fine dimples



B - Centre

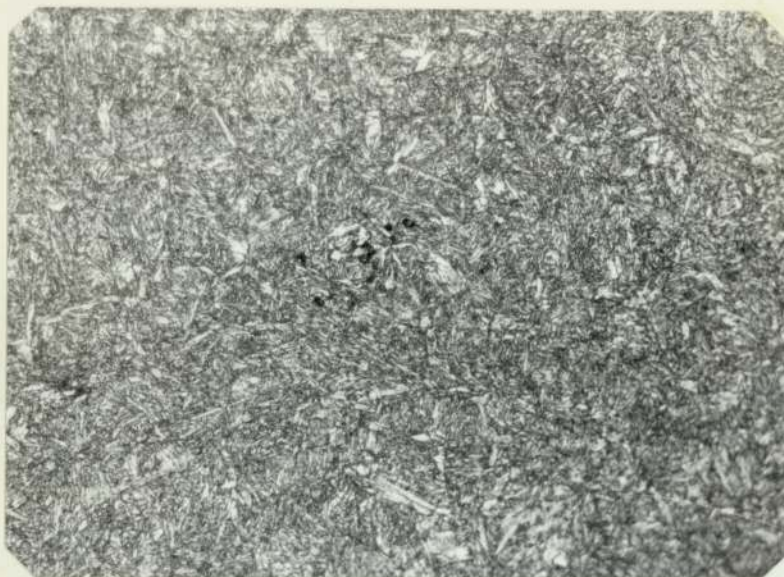
Scanning electron micrograph showing river pattern in cleavage brittle fracture



C - Edge

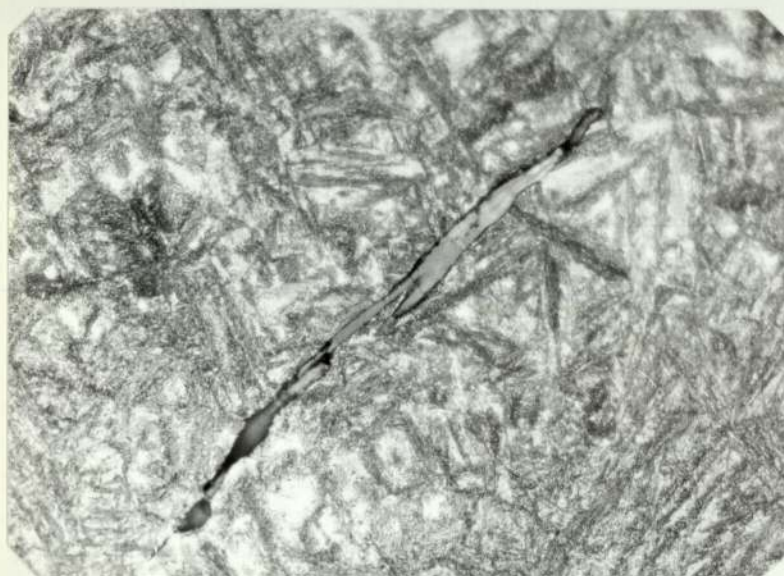
Scanning electron micrograph showing quasi fracture surface





A - Top

Optical electron micrograph showing tempered martensite and some tempered bainite
Mag. x540



B - Centre

Optical electron micrograph showing fine carbide particles within bainite plates and some of tempered martensite. (see inclusion cavity, bottom left)
Mag. x540



C - Edge

Optical electron micrograph showing fine carbide particles within bainite plates
Mag. x540

PLATE 29 Fracture surface of H.W. die steel
Somdie S1A

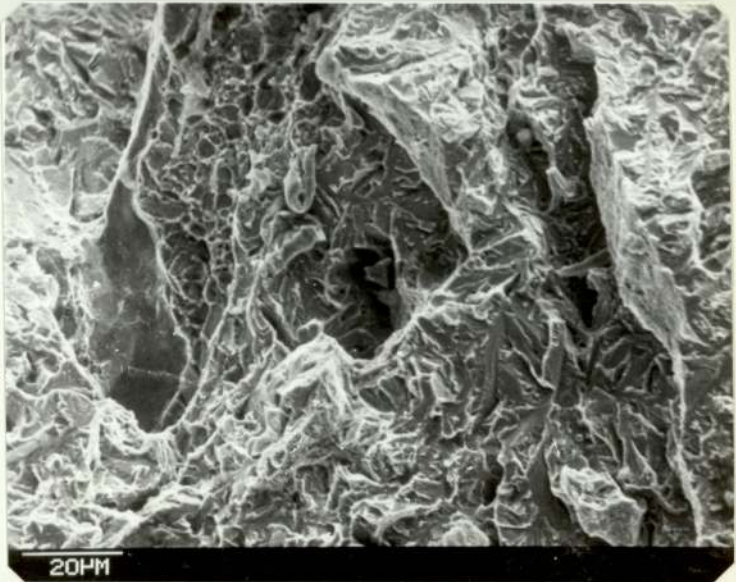
A - Top

Scanning electron micrograph showing macro and microvoid within ductile fracture surface



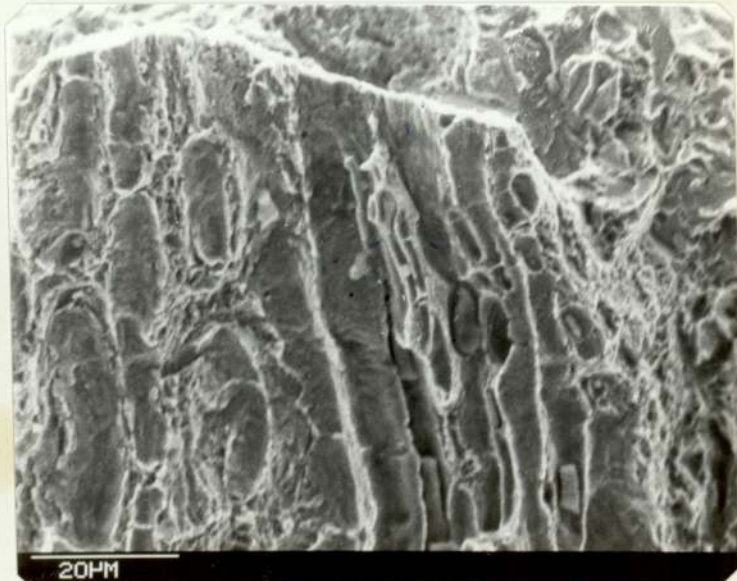
B - Centre

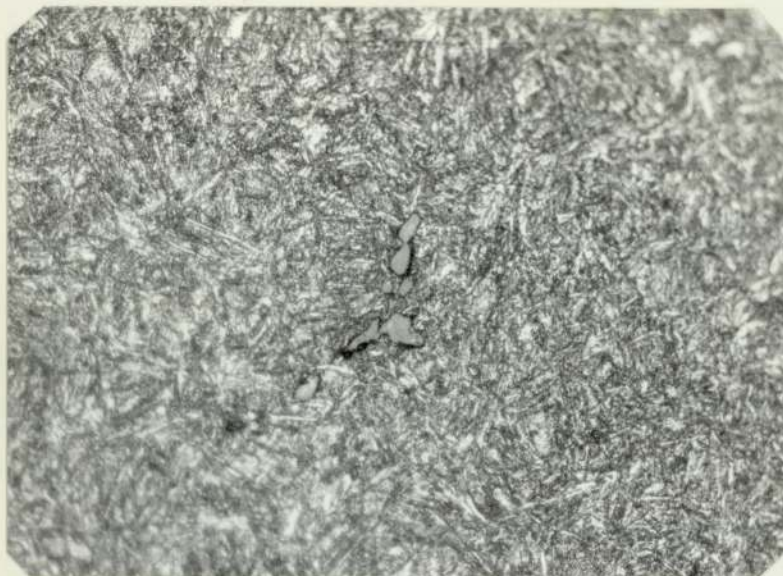
Scanning electron micrograph showing inclusion cavity (at left photograph) surrounded by brittle fracture surface



C - Edge

Scanning electron micrograph showing deformed inclusion parallel to fracture surface surrounded by dimple structure





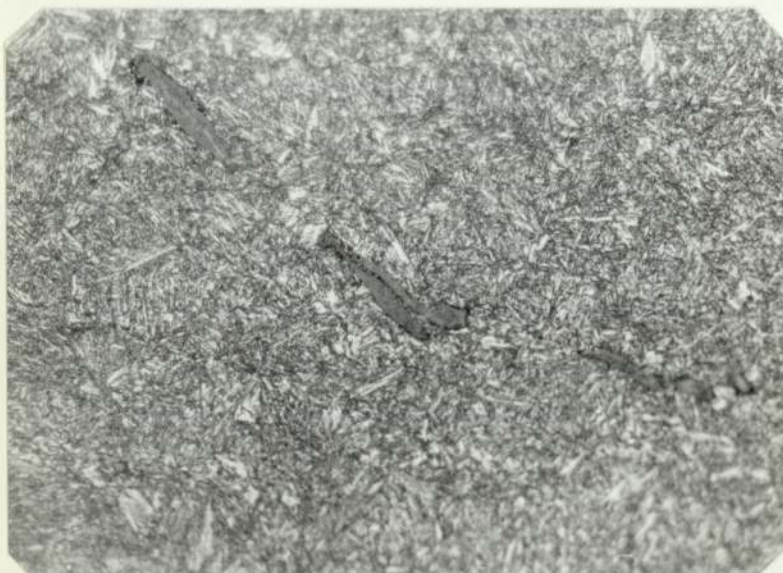
A - Top

Optical electron micrograph showing tempered martensite and some of tempered bainite
Mag. x540



B - Centre

Optical electron micrograph showing tempered martensite and elongated silicate inclusions
Mag. x540



C - Edge

Optical electron micrograph showing fine tempered martensite and silicate inclusions
Mag. x540

PLATE 30 Fracture surface of H.W. die steel
Somdie S1B

A - Top

Scanning electron micrograph showing microvoid and silicate inclusions at the chevron point



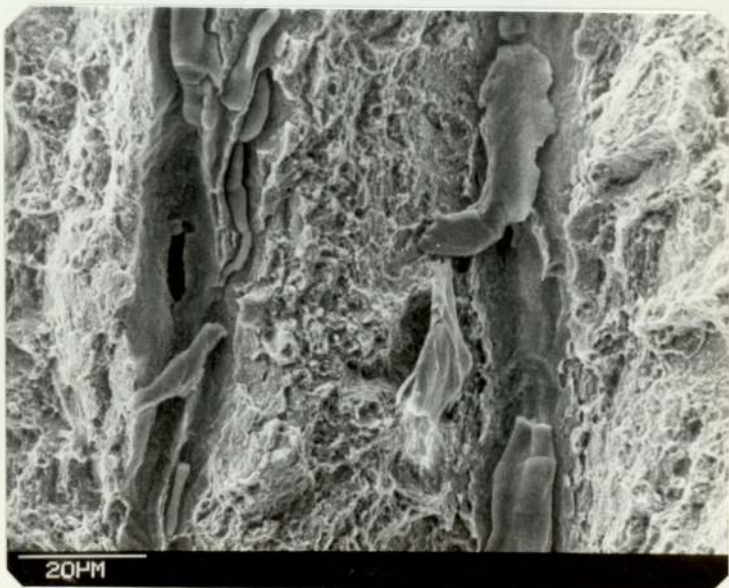
B - Centre

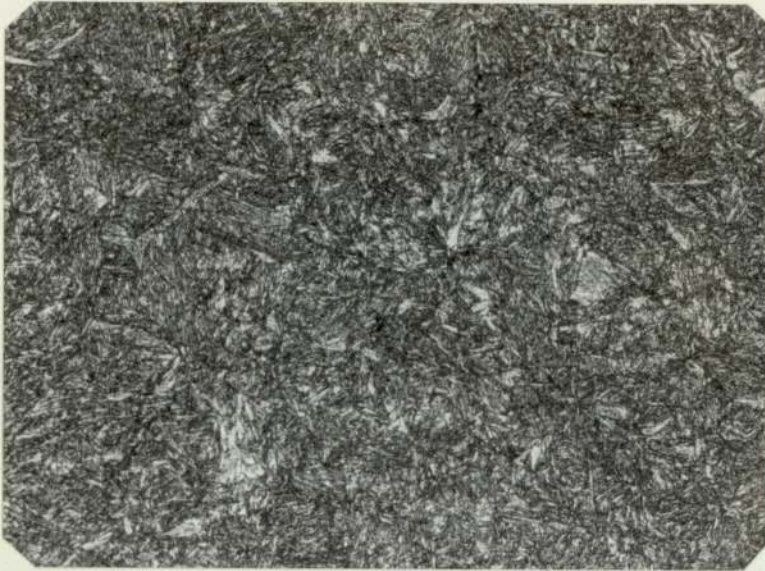
Scanning electron micrograph showing silicate inclusions surrounded by fine dimples



C - Edge

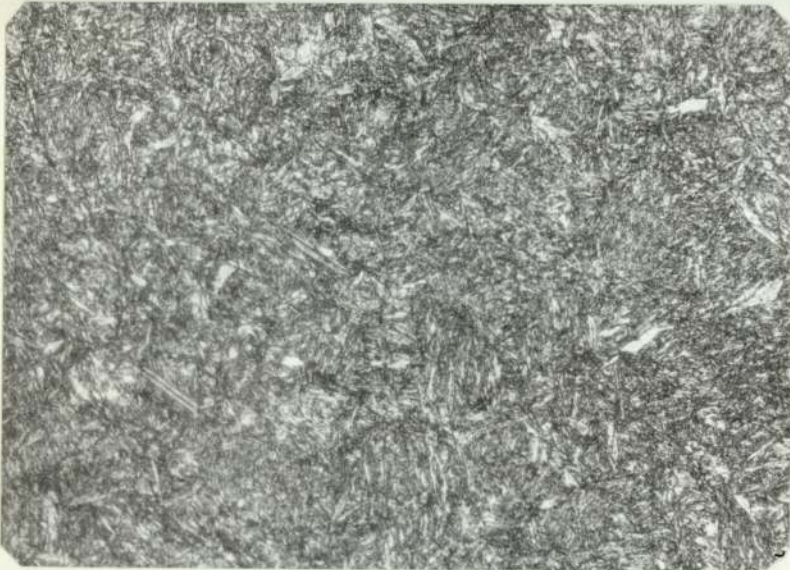
Scanning electron micrograph showing cracked silicate inclusions surrounded by dimples, left side photograph showing stretch area





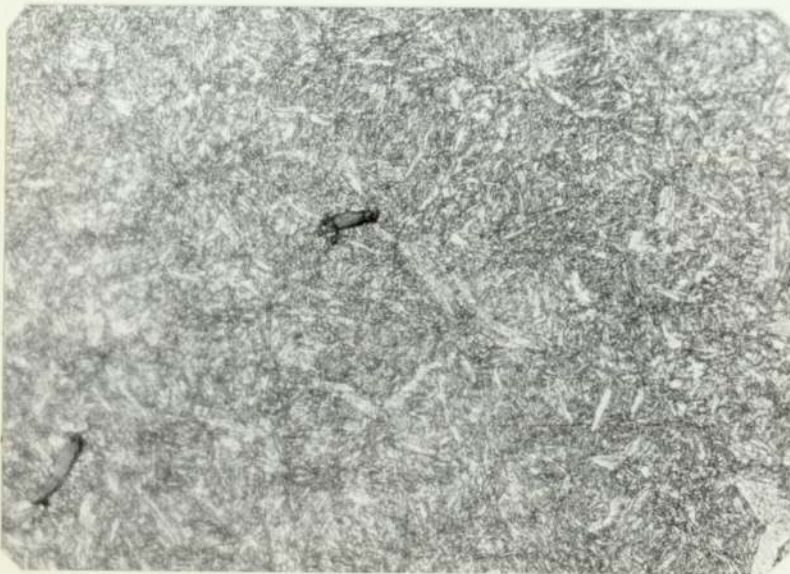
A - Top

Optical electron micrograph showing mainly tempered martensite and some bainite structure
Mag. x540



B - Centre

Optical electron micrograph showing mainly tempered martensite, tempered bainite and some free ferrite
Mag. X540

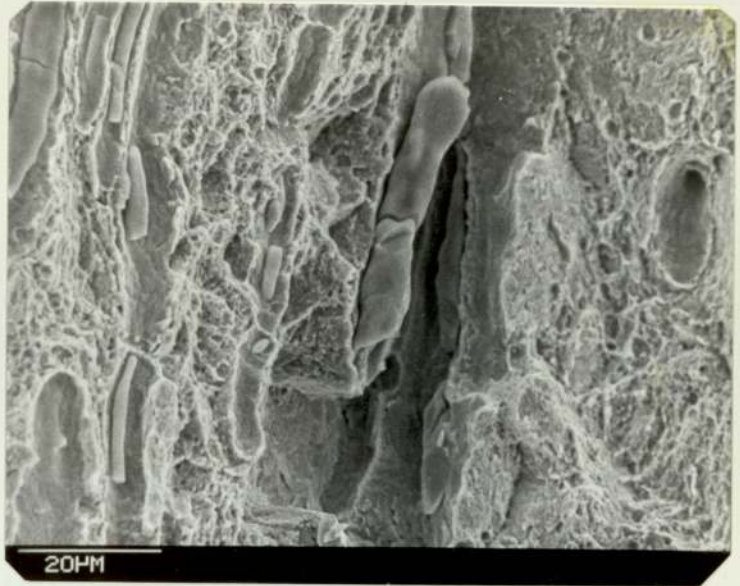


C - Edge

Optical electron micrograph showing tempered martensite and tempered bainite
Mag. x540

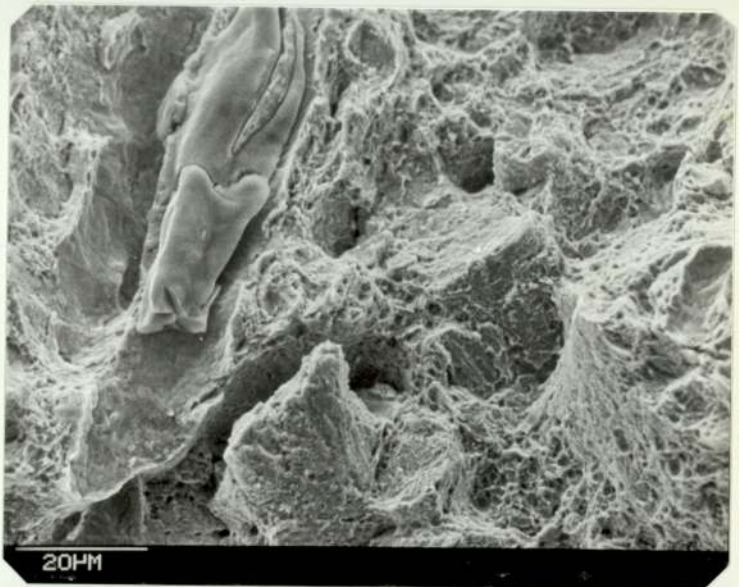
A - Top

Scanning electron micrograph showing cracked silicate inclusion surrounded by fine voids.



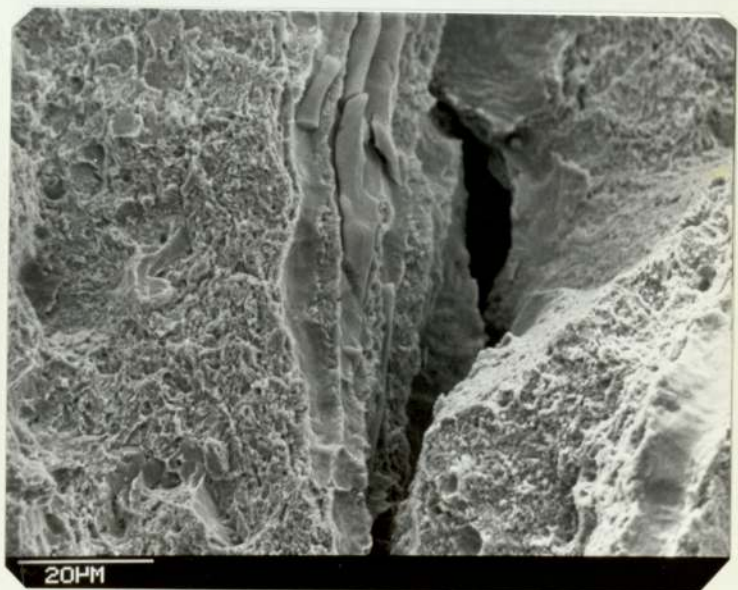
B- Centre

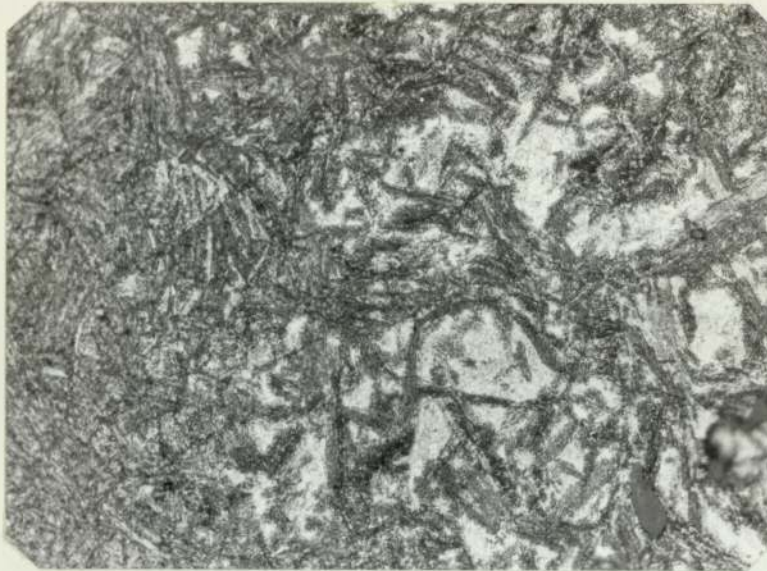
Scanning electron micrograph showing cracked silicate inclusion surrounded by macro and micro voids.



C - Edge

Scanning electron micrograph showing cracked inclusions surrounded by fine voids, crack path at the grain boundary.





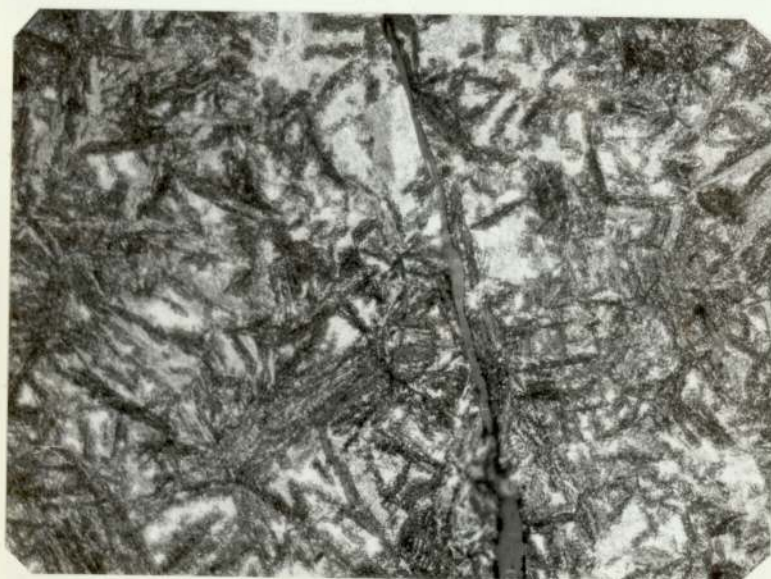
A - Top

Optical electron
micrograph showing
fine carbide
particle within
bainite plate
Mag. x540



B - Centre

Optical electron
micrograph showing
carbide particles
within bainite plate
Mag. x540

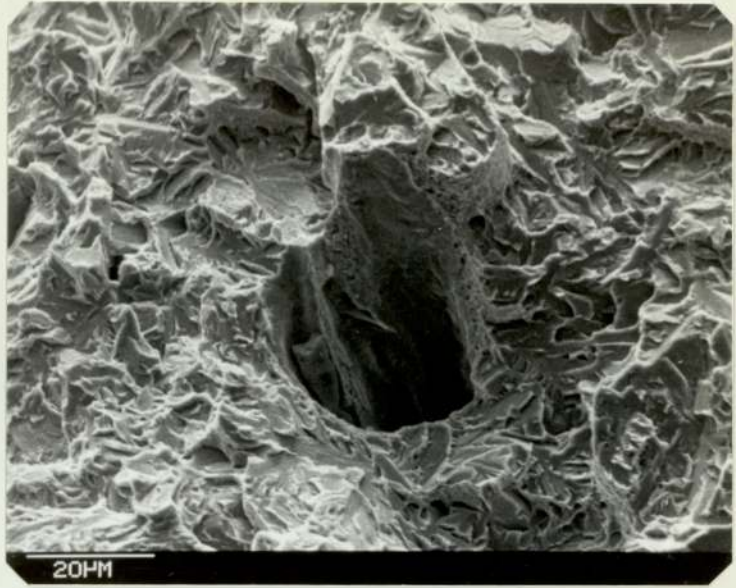


C - Edge

Optical electron
micrograph showing
fine carbide
particles within
bainite plate
Mag. x540

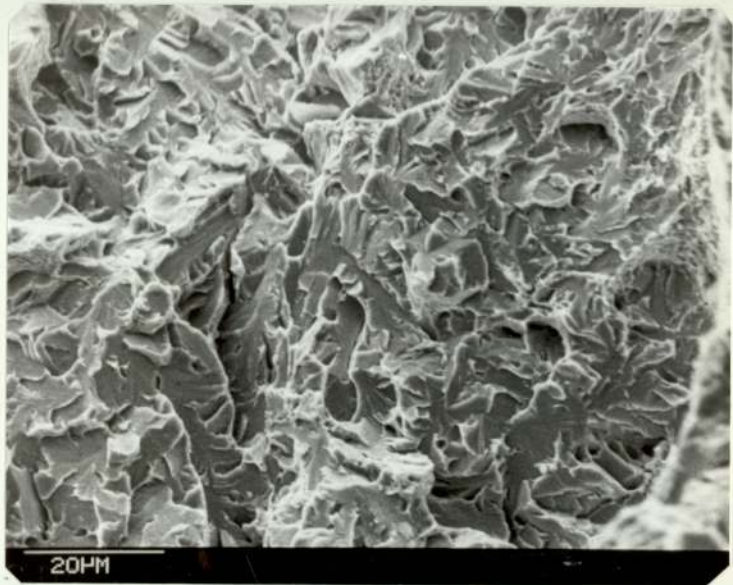
A - Top

Scanning electron micrograph showing large voids with cracked inclusions at the interior void surface surrounded by cleavage fracture surface



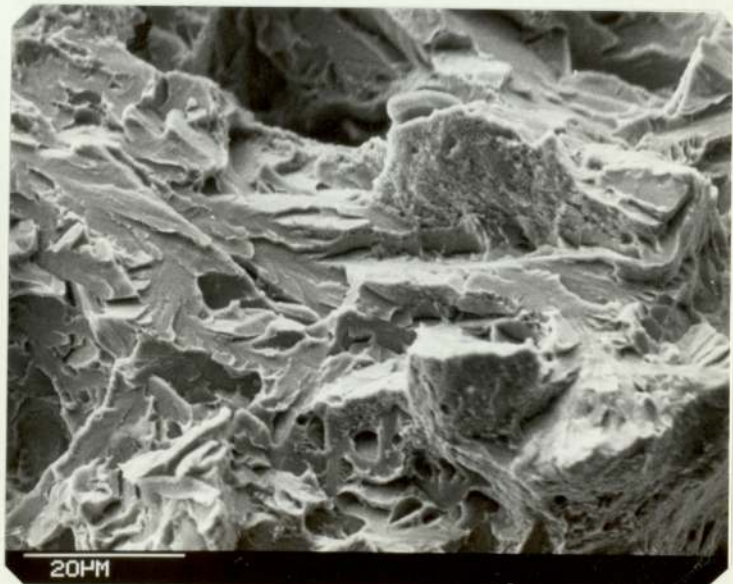
B - Centre

Scanning electron micrograph showing cleavage fracture surface



C - Edge

Scanning electron micrograph showing brittle fracture surface, with some fine dimples structures in same area



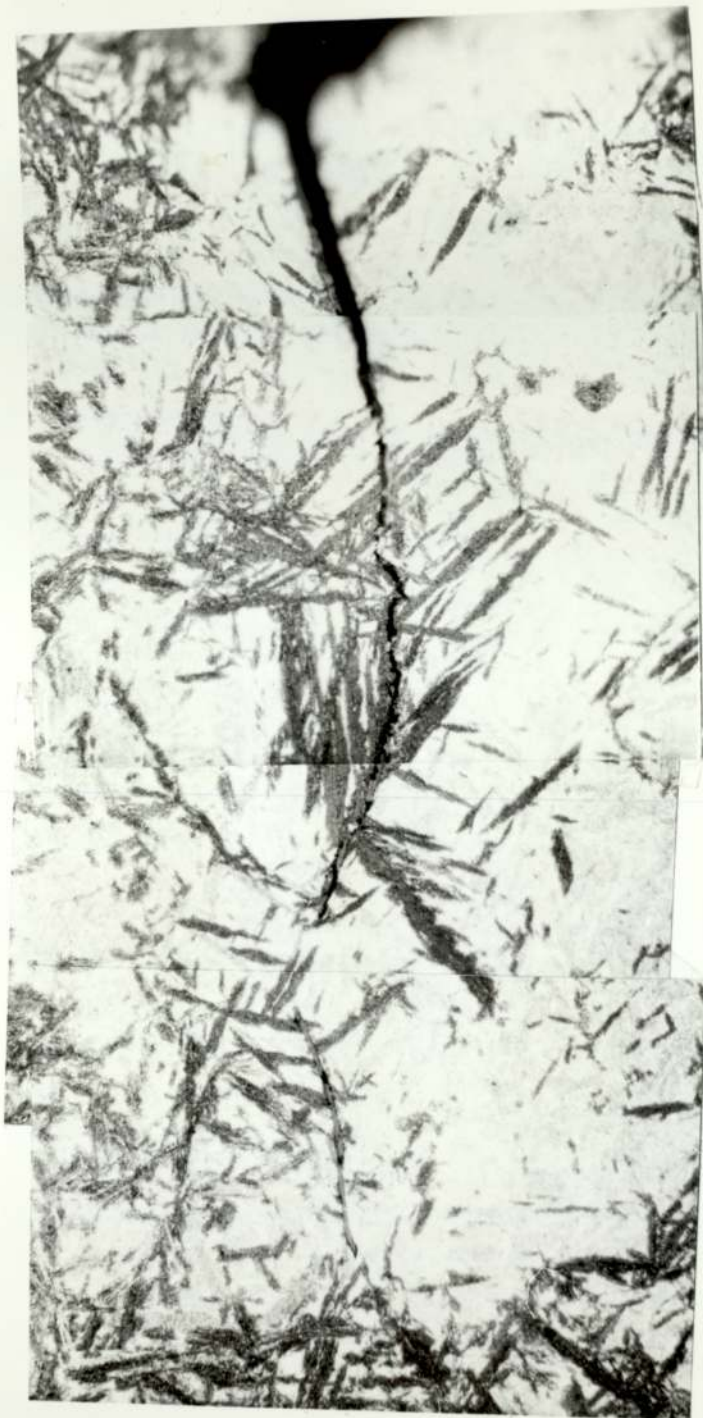
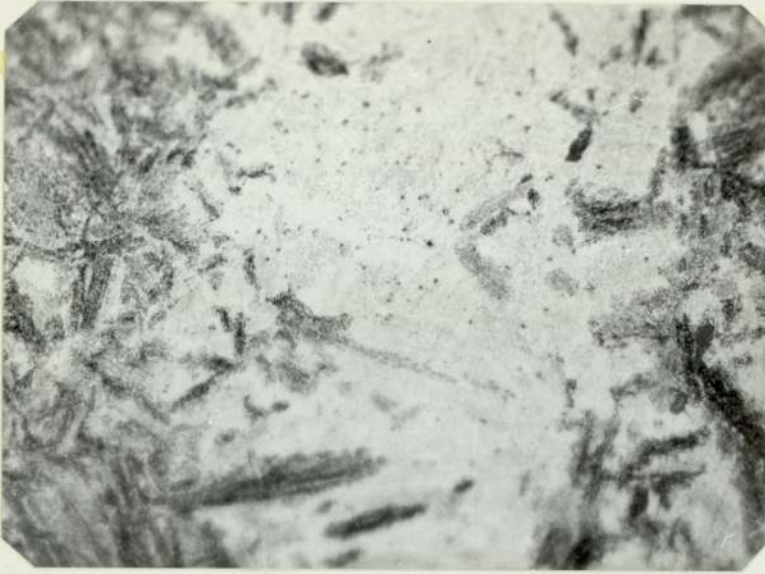


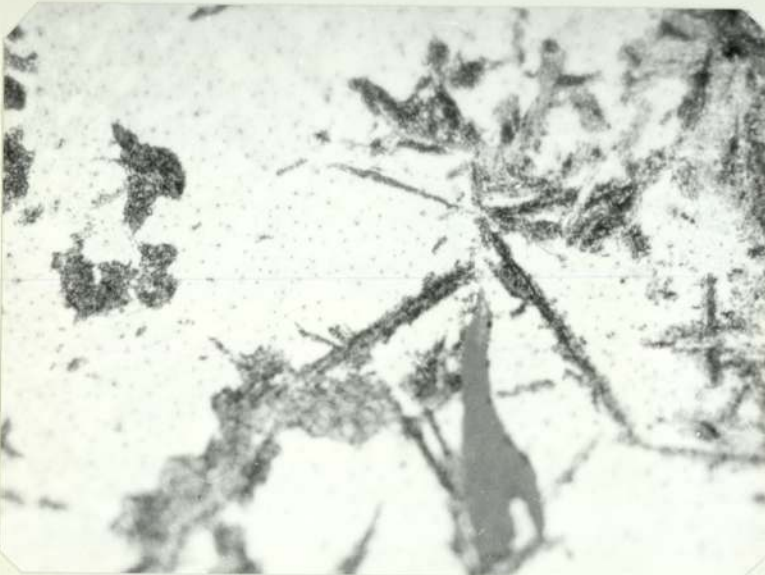
PLATE 70a Crack path in short bar specimen
S2M Soudie steel

PLATE 71 Microstructure of H.W. die steel, Somdie S2C



A - Top

Optical electron micrograph showing carbide particles within bainite plate
Mag. x540



B - Centre

Optical electron micrograph showing carbide particle within bainite plate and within upper bainite (light grey)
Mag. x540

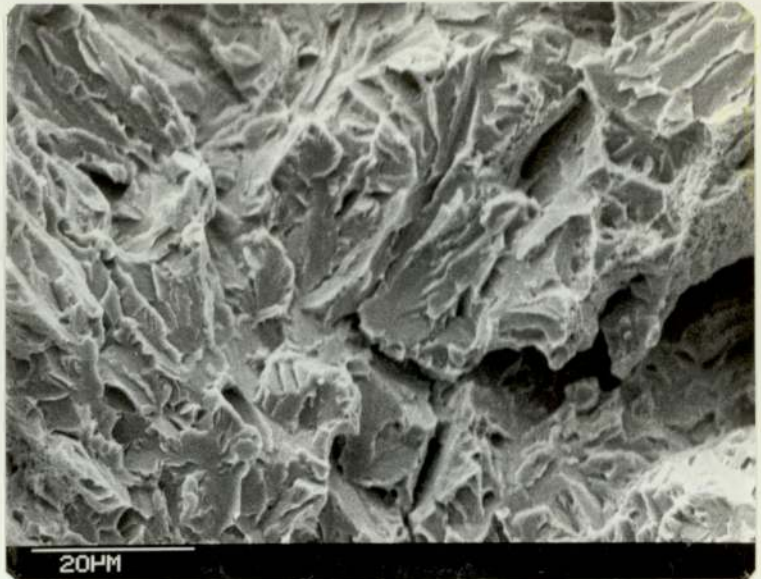


C - Edge

Optical electron micrograph showing fine carbide within bainite plate and fine carbide particle randomly distributed within upper bainite
Mag. x540

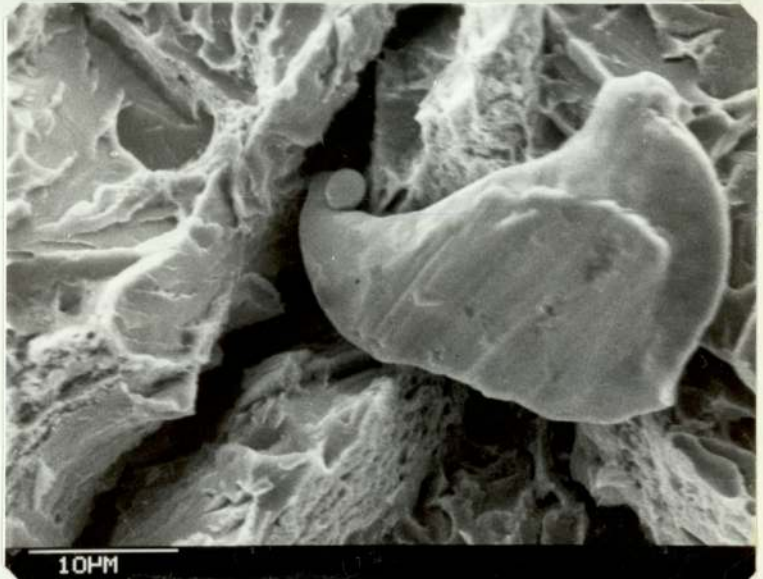
A - Top

Scanning electron micrograph showing cleavage area and fine dimple sides at the crack path.



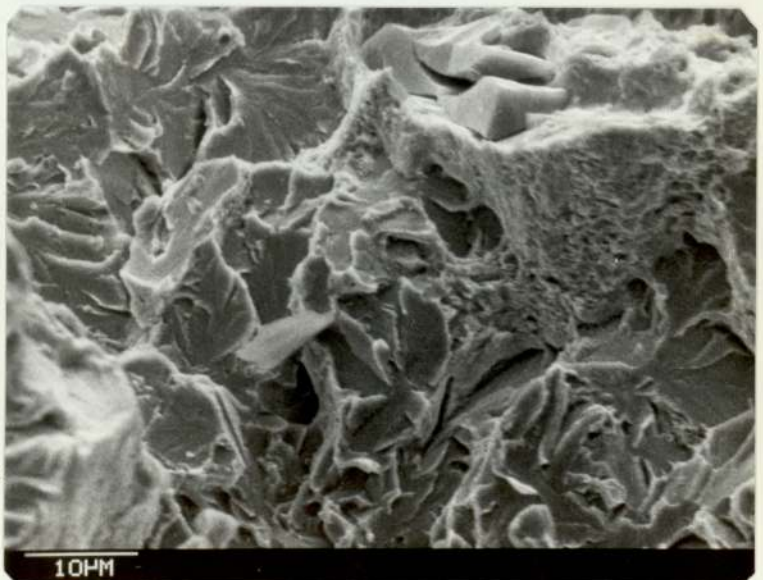
B - Centre

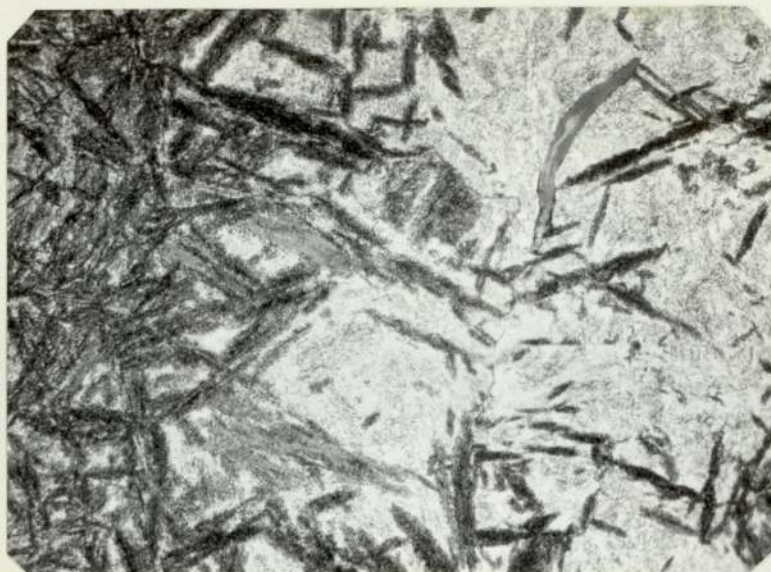
Scanning electron micrograph showing crack path surrounded by brittle fracture surface and fine dimples at the right edge of the crack.



C - Edge

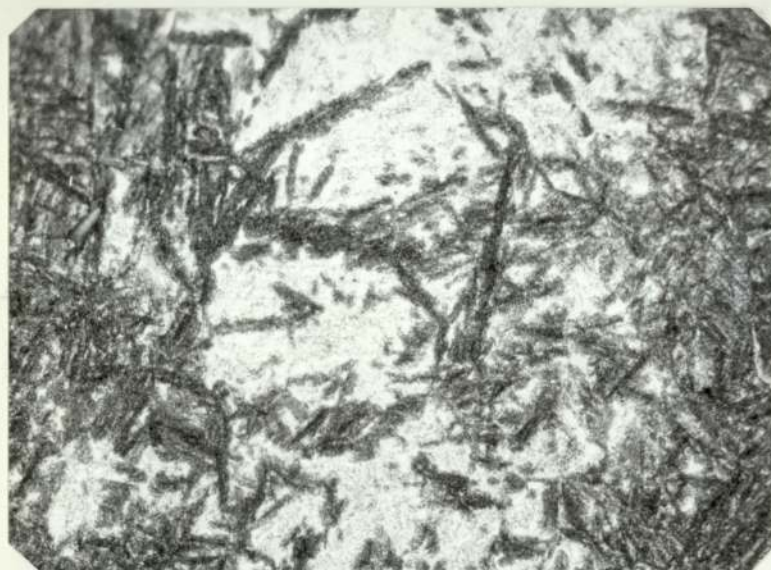
Scanning electron micrograph showing cleavage fracture surface at left side photograph and dimples structure at top right





A - Top

Optical electron micrograph showing fine carbide within bainite plate and upper bainite (light grey)
Mag. x540



B - Centre

Optical electron micrograph showing fine carbide particles within bainite plate
Mag. x540



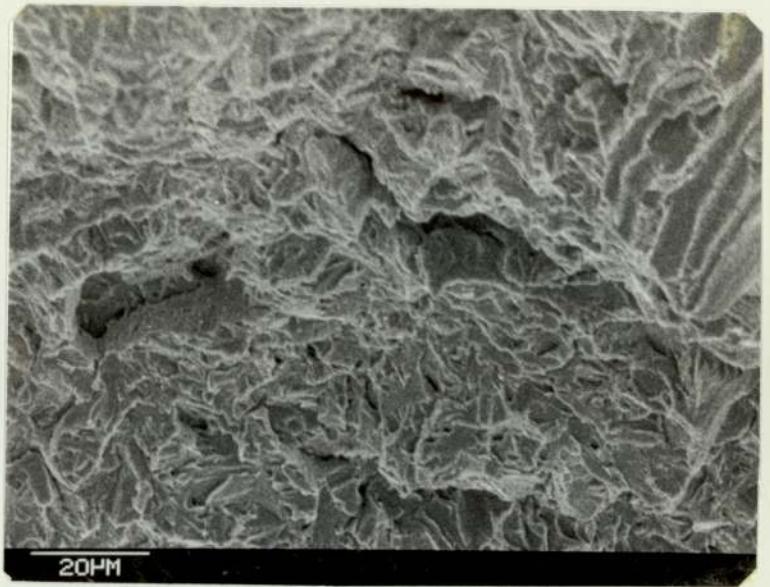
C - Edge

Optical electron micrograph showing tempered martensite and some of tempered bainite
Mag. x540

PLATE 34 Fracture surface of H.W. die steel
Somdie S2A

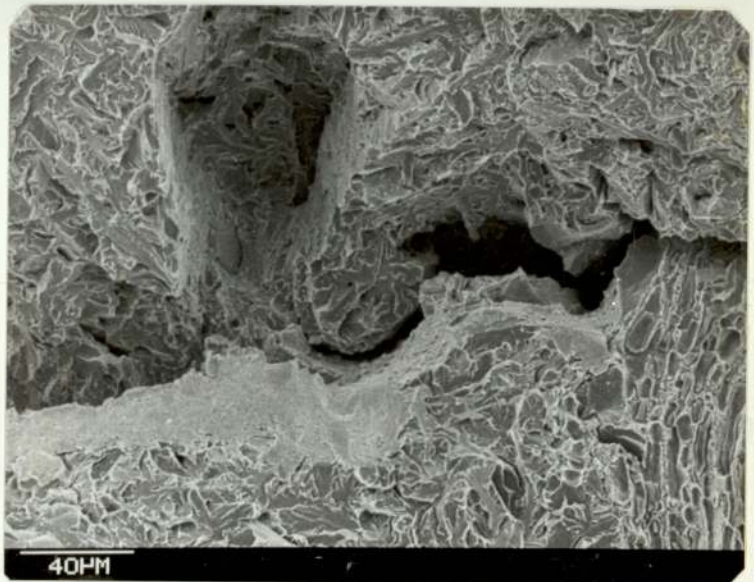
A - Top

Scanning electron micrograph showing brittle fracture surface with river pattern at top right photograph



B - Centre

Scanning electron micrograph showing brittle fracture surface and dimple structure at right side photograph



C - Edge

Scanning electron micrograph showing brittle fracture surface at left side photograph and deformed inclusion surrounded by dimples structure at right side photograph



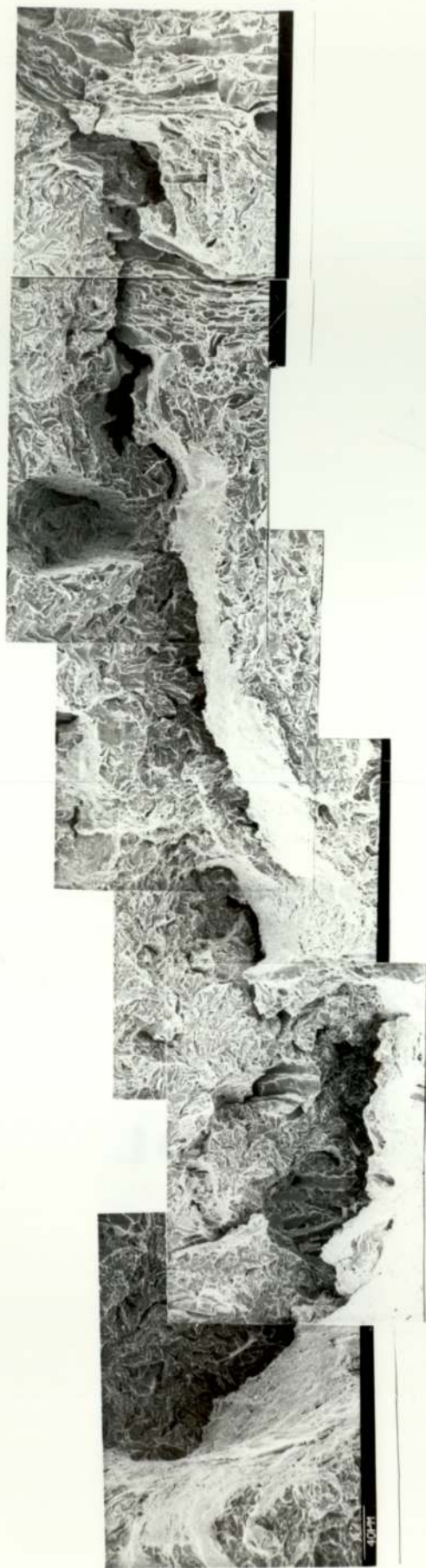


PLATE 34a

Crack path of short
bar specimen S2A
Somdie steel
(Notice the variety
in fracture surface)



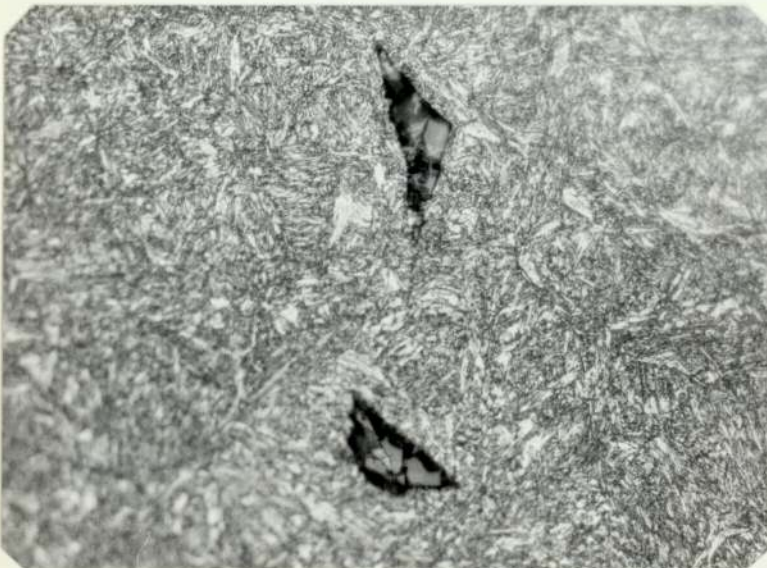
A - Top

Optical electron micrograph showing tempered martensite and manganese sulphide ppt. within silicate inclusion
Mag. x540



B - Centre

Optical electron micrograph showing tempered martensite and silicate inclusion lying at the tip of the fine crack (top left)
Mag. x540



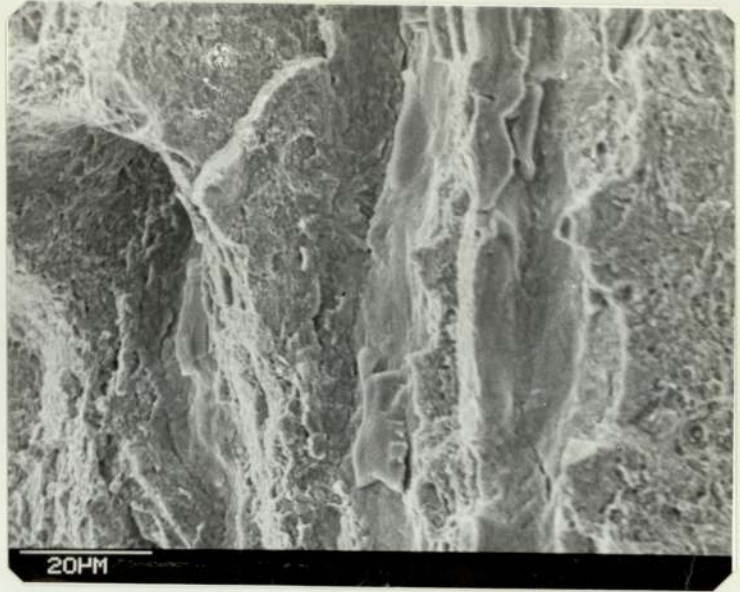
C - Edge

Optical electron micrograph showing silicate inclusion perpendicular to the fracture surface
Mag. x540

PLATE 35 Fracture surface of H.W. die steel
Somdie S2B

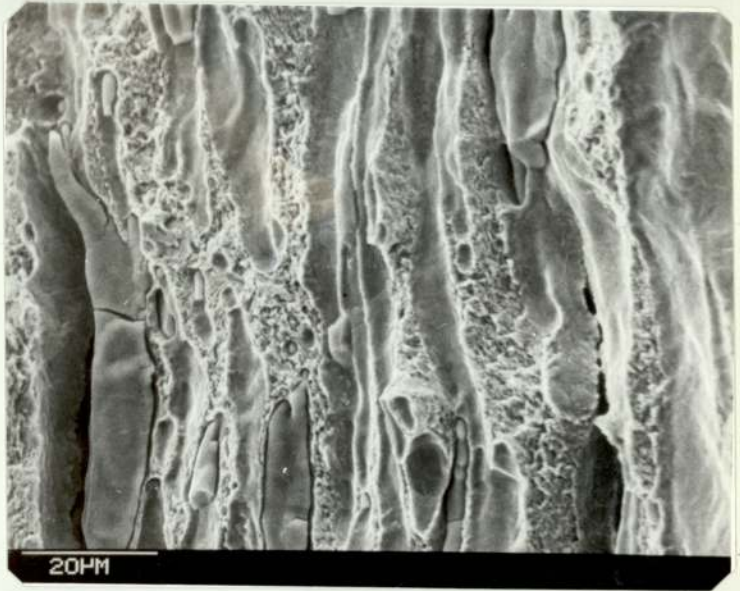
A - Top

Scanning electron
micrograph showing
typical ductile
dimple structures



B - Centre

Scanning electron
micrograph showing
stringer silicate
inclusions
surrounded by fine
voids with
inclusion inside



C - Edge

Scanning electron
micrograph showing
inclusion cavities
surrounded by very
fine voids stretch
area top left and
right side photograph





A - Top

Optical electron micrograph showing tempered martensite and tempered bainite. (see crack path linked with the inclusion cavity)
Mag. x540



B - Centre

Optical electron micrograph showing tempered martensite and tempered bainite (see inclusion cavity)
Mag. x540



C - Edge

Optical electron micrograph showing tempered martensite and tempered bainite
Mag. x540

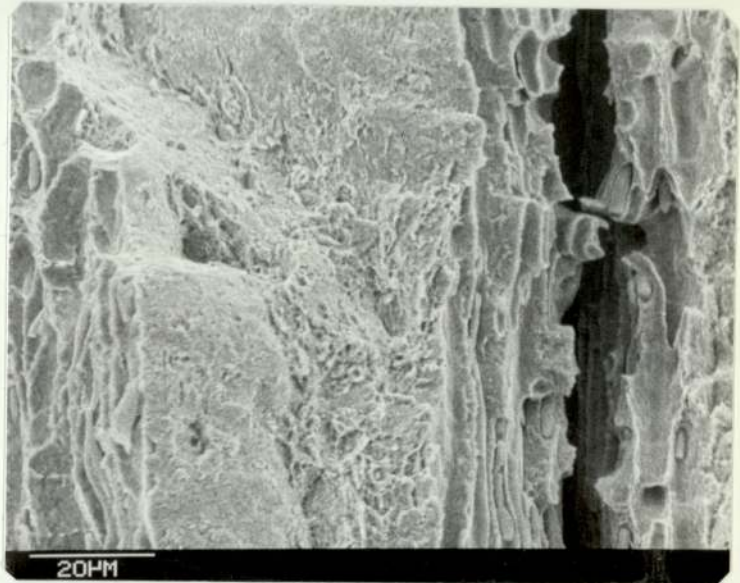
A - Top

Scanning electron micrograph showing deformed inclusion surrounded by dimples structure



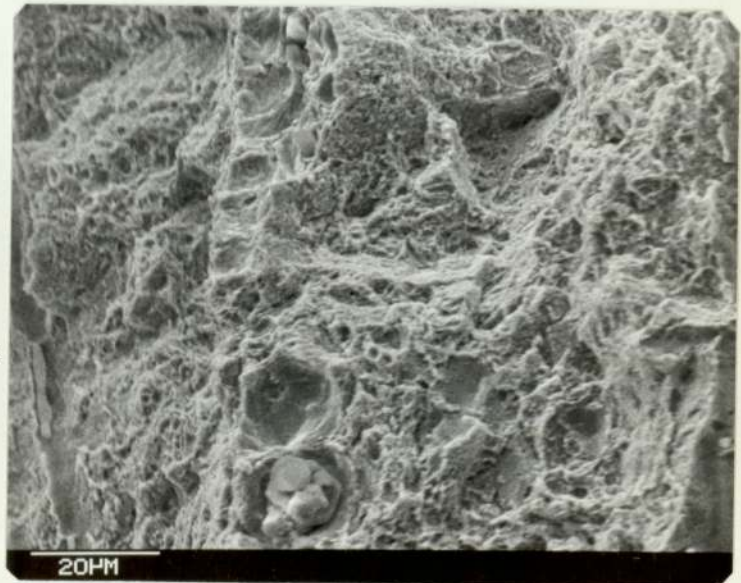
B - Centre

left
Scanning electron micrograph showing dimple structure at right side of photograph, deformed silicate inclusion surrounded by very fine dimples (right side photograph). (Notice the crack path)



C - Edge

Scanning electron micrograph showing macro and microvoids with inclusion inside void



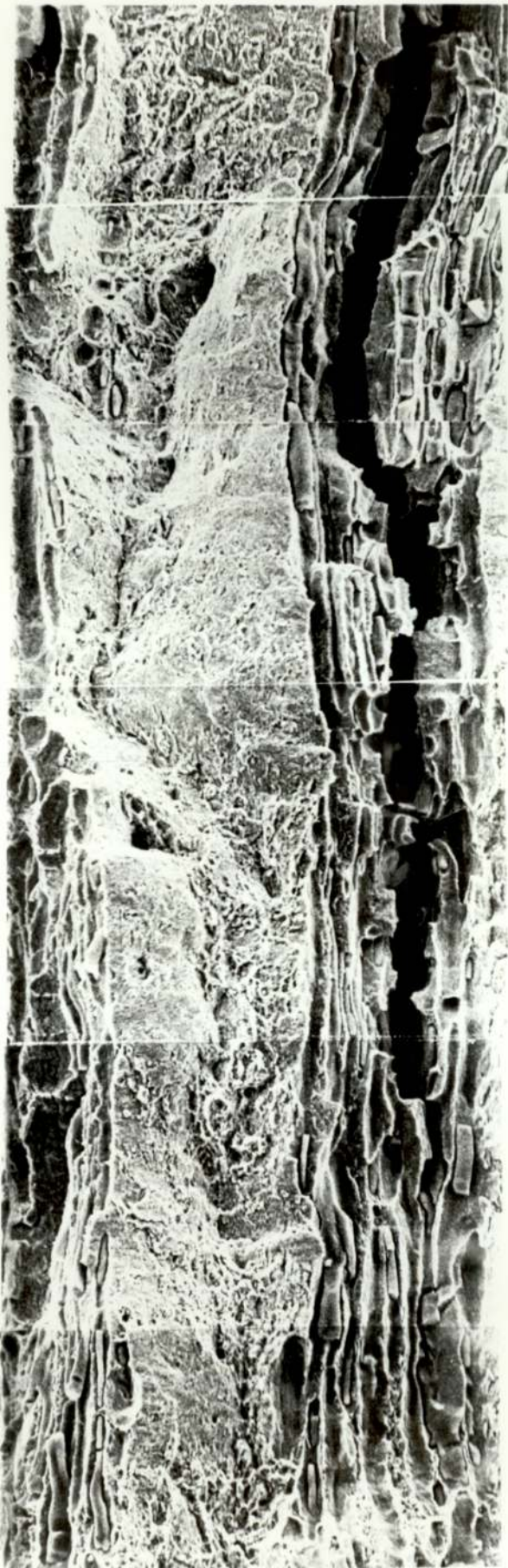
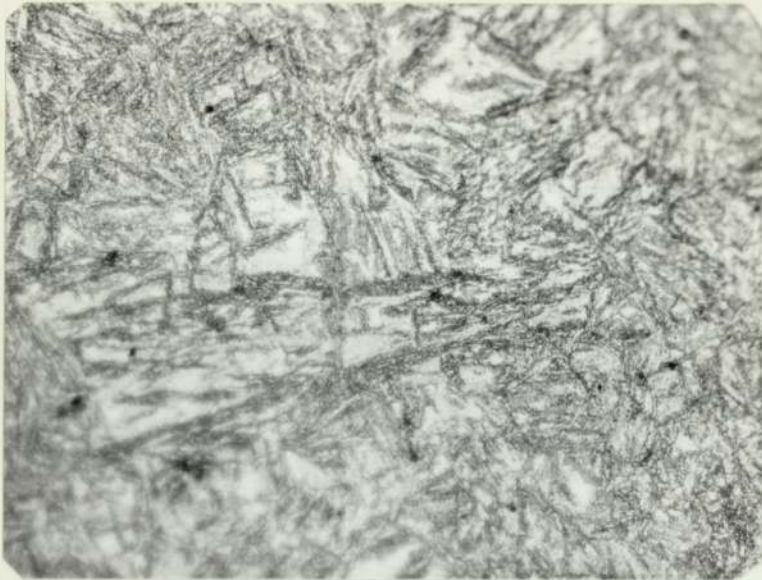


PLATE 36a

Crack path start at
chevron point down
to the centre of the
fracture surface.
Notice the coalescence
of cavities formed at
inclusion

S30 SPECIMEN.

PLATE 75 Microstructure of H.W. die steel, Somdie S3M



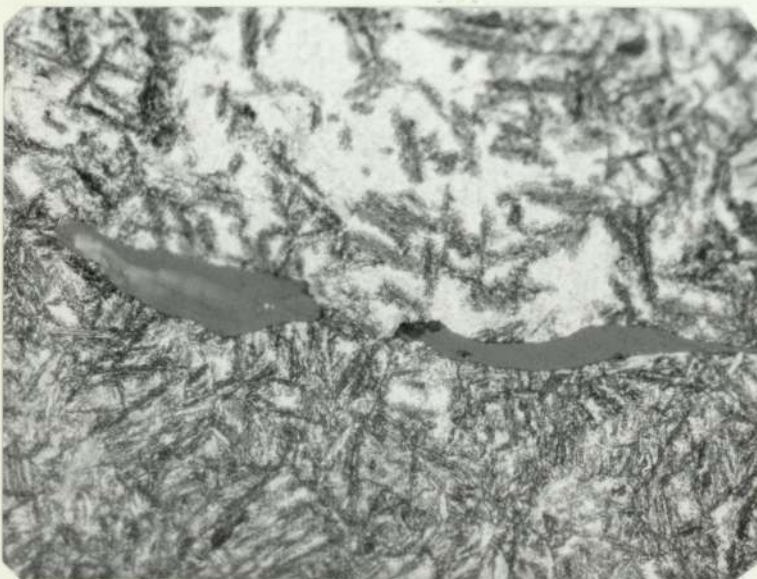
A - Top

Optical electron micrograph showing fine carbide particles within bainite plate
Mag. x540



B - Centre

Optical electron micrograph showing fine carbide particles within bainite plate
Mag. x540

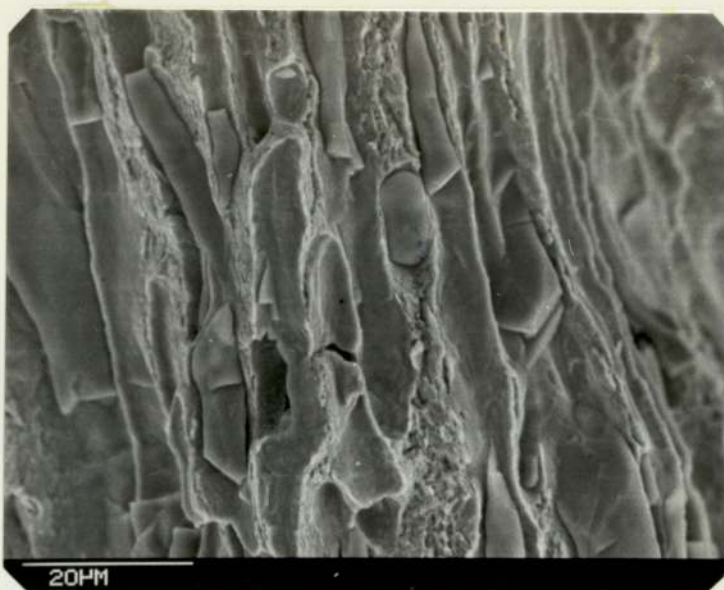


C - Edge

Optical electron micrograph showing fine carbide particles within bainite plate
Mag. x540

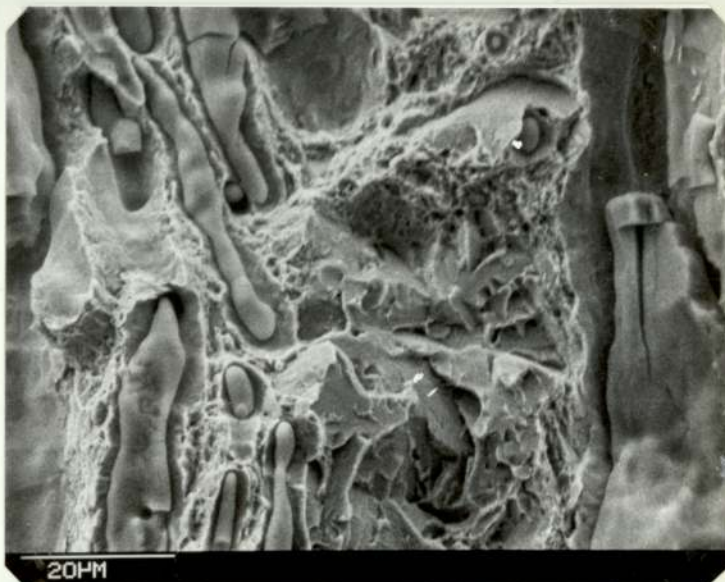
A - Top

Scanning electron micrograph showing high inclusion densities surrounded by fine dimples at chevron point



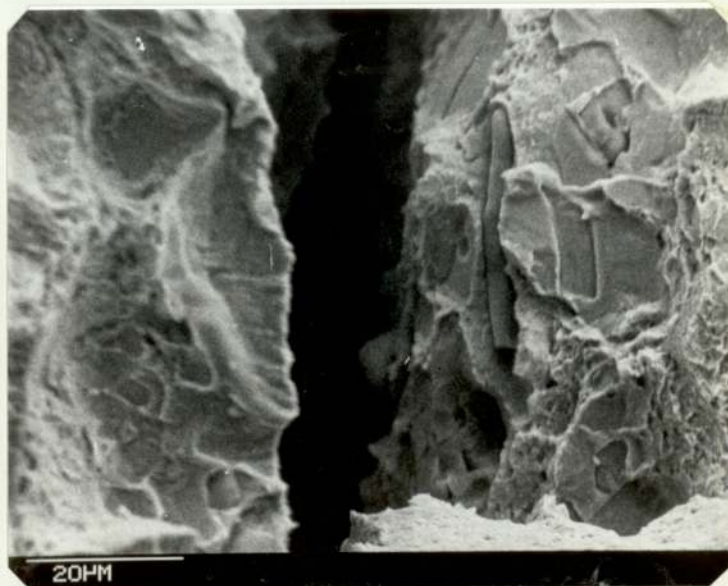
B - Centre

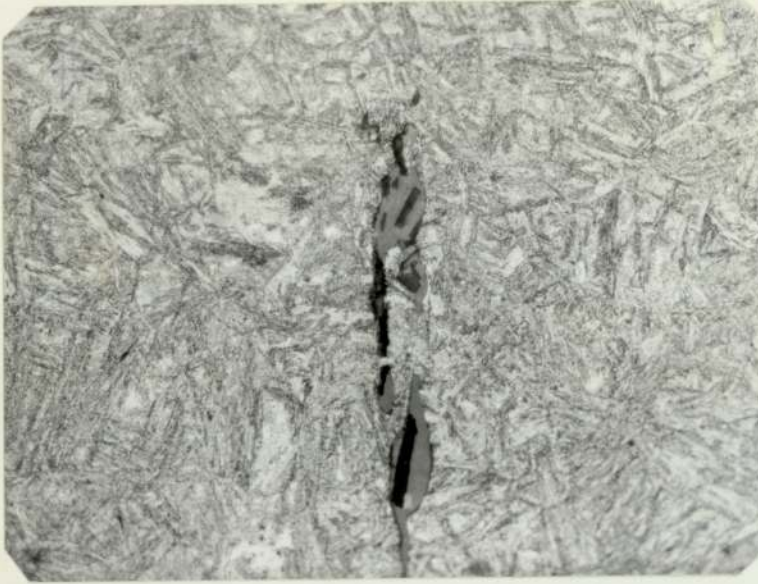
Scanning electron micrograph showing cracked silicate inclusion surrounded by dimples and brittle fracture surface (small area)



C - Edge

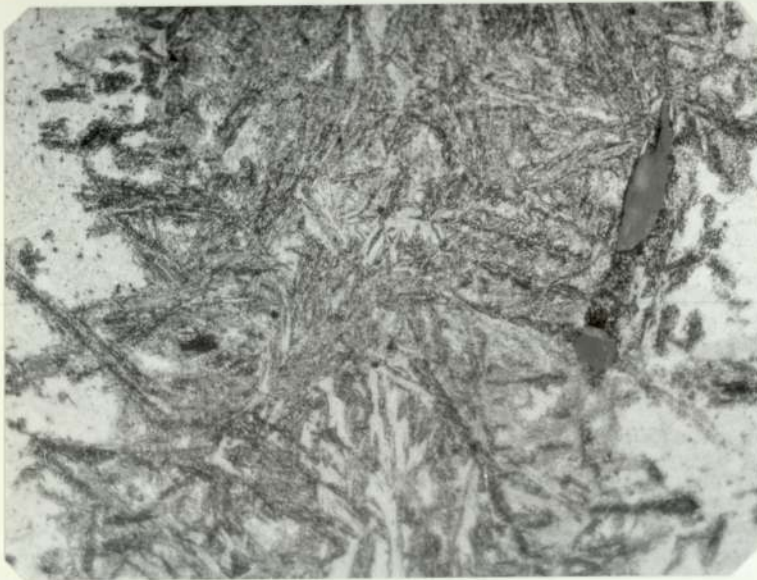
Scanning electron micrograph showing large inclusion cavity surrounded by inclusion within dimple structure





A - Top

Optical electron micrograph showing mainly fine carbide particles within bainite plate
Mag. x540



B - Centre

Optical electron micrograph showing fine carbide particles within bainite plate,
(see the bainite plate banded along inclusion)
Mag. x540



C - Edge

Optical electron micrograph showing fine carbide particles within bainite plate
Mag. x540

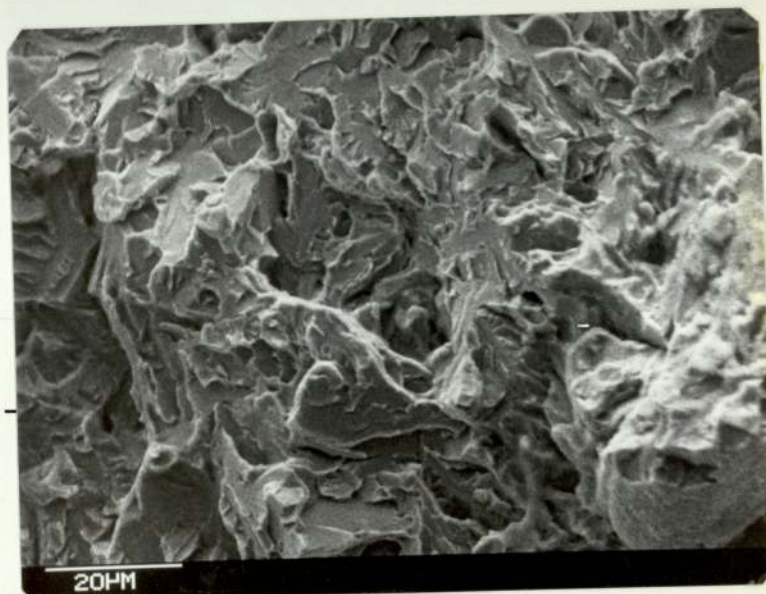
A - Top

Scanning electron
micrograph showing
cleavage fracture
surface



B - Centre

Scanning electron
micrograph showing
cleavage fracture
surface and
dimples structure
at right side photo-
graph



C - Edge

Scanning electron
micrograph showing
brittle fracture
surface, steps
and dimples at
right side
photograph

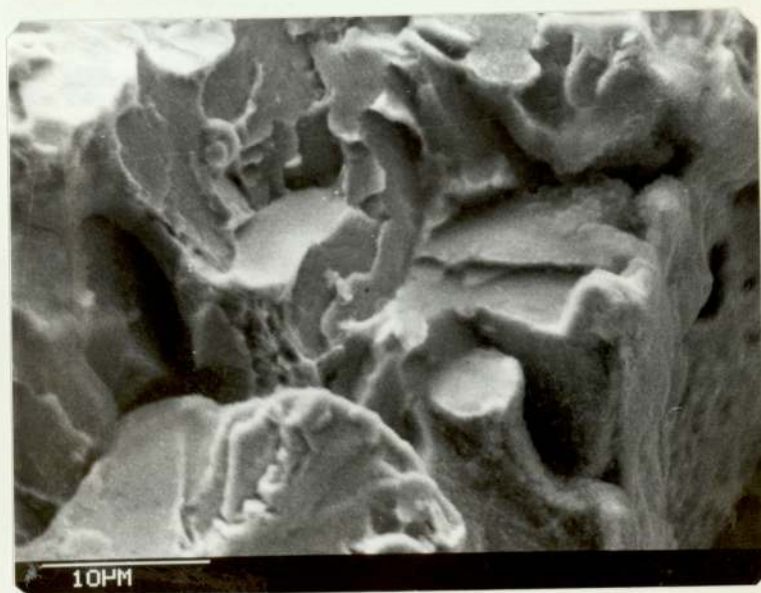
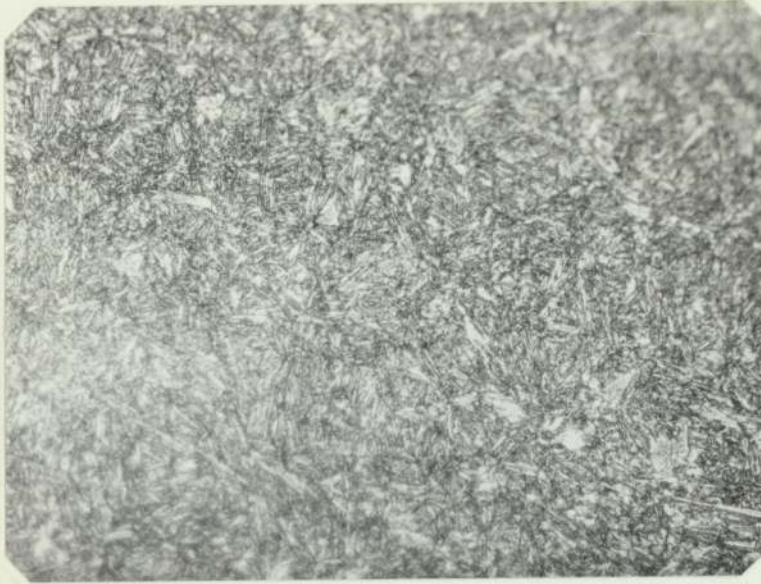


PLATE 77 Microstructure of H.W. die steel, Somdie S3B



A - Top

Optical electron micrograph showing tempered martensite and some of tempered bainite
Mag. x540



B - Centre

Optical electron micrograph showing tempered martensite and some of tempered bainite
Mag. x540

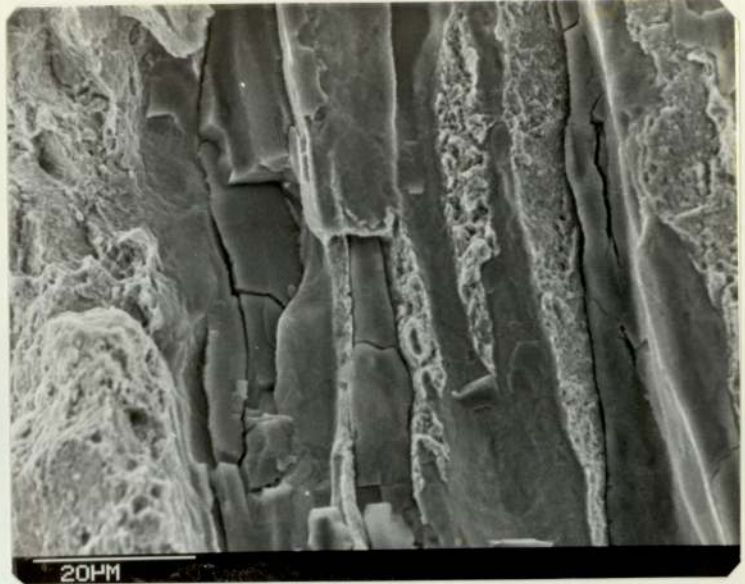


C - Edge

Optical electron micrograph showing tempered martensite and some of tempered bainite
Mag. x540

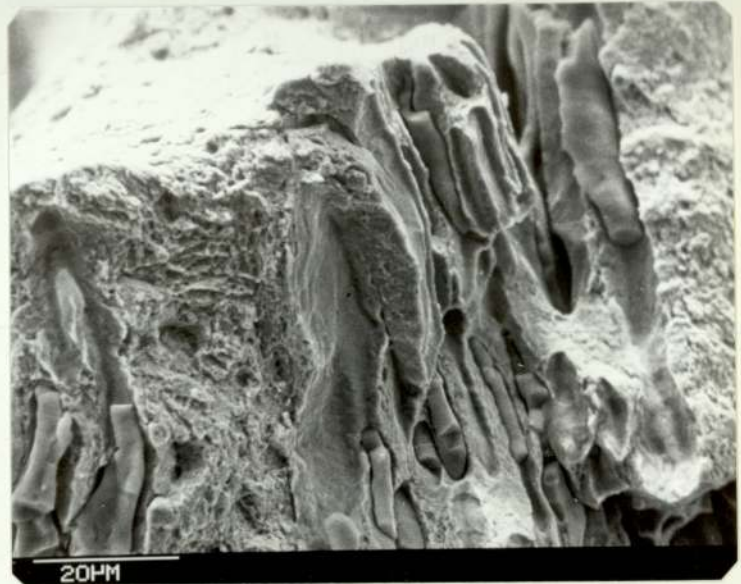
A - Top

Scanning electron
micrograph showing
cracked silicate
inclusion surrounded
by dimples
structure



B - Centre

Scanning electron
micrograph showing
silicate inclusion
surrounded by dimples
structure and very
fine dimples at top
left photograph
(stretch zone)



C - Edge

Scanning electron
micrograph showing
cracked silicate
inclusion
surrounded by dimples
structure



Plate 78

Scanning electron micrograph showing cleavage fracture surface near fatigue zone. (Three point bend specimen HO)

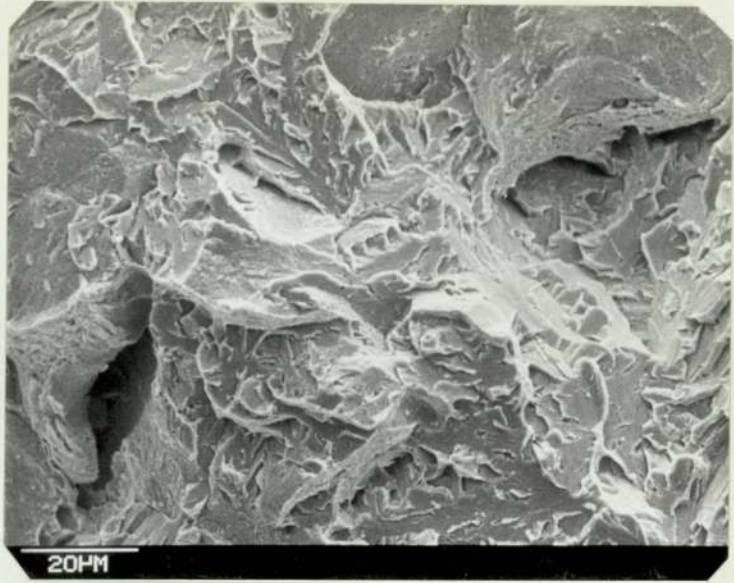


Plate 79

Scanning electron micrograph showing cleavage fracture surface near fatigue zone. (Three point bend specimen HM)

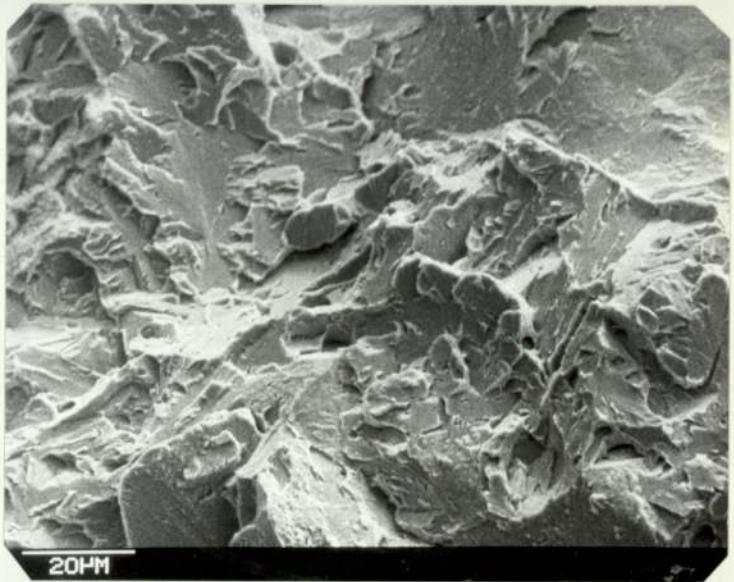


Plate 80

Scanning electron micrograph showing cleavage fracture surface near fatigue zone. (Three point bend specimen HC)

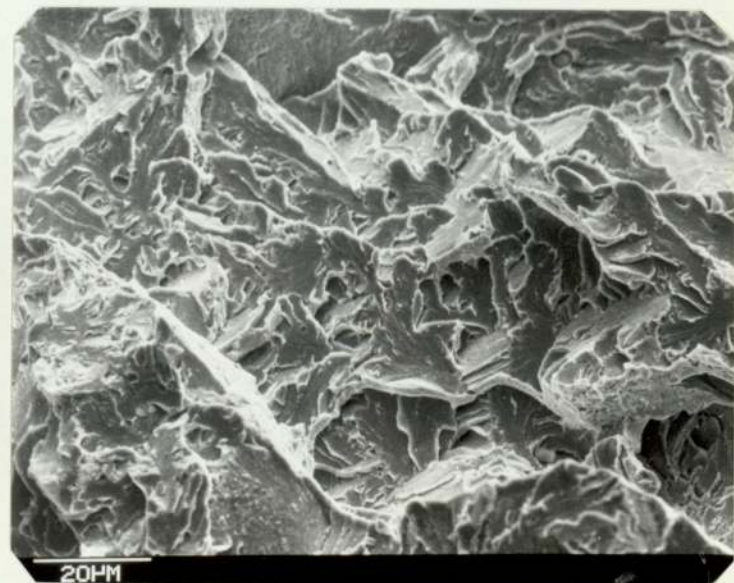


Plate 81

Scanning electron micrograph showing cleavage fracture surface near fatigue zone. (Three point bend specimen S1)

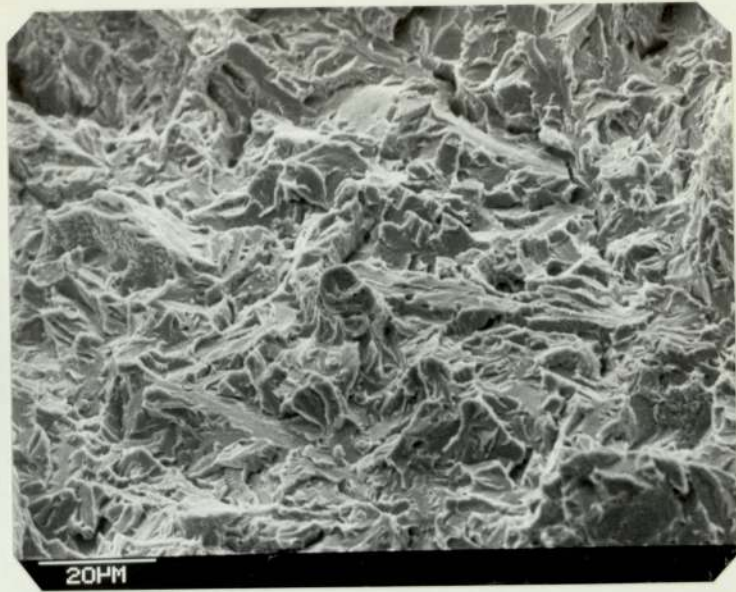


Plate 82

Scanning electron micrograph showing cleavage fracture surface near fatigue zone (Three point bend specimen S2)

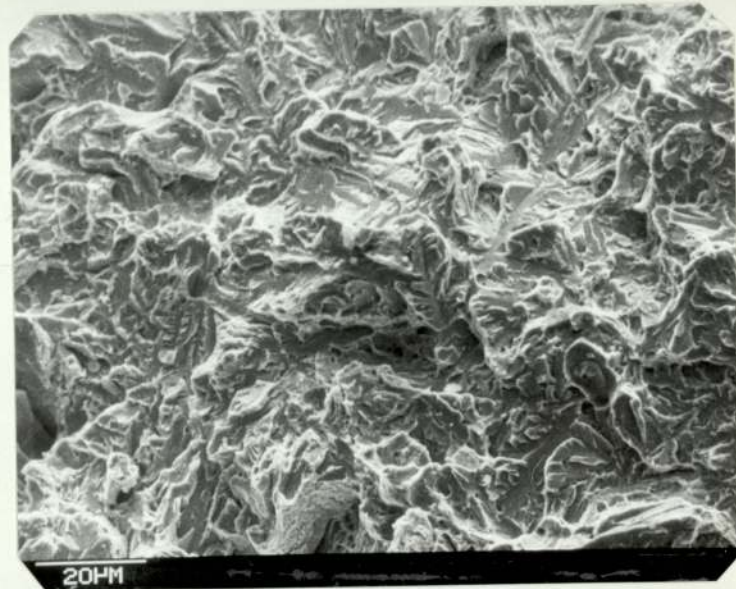


Plate 83

Scanning electron micrograph showing cleavage fracture surface near fatigue zone. (Three point bend specimen S3)



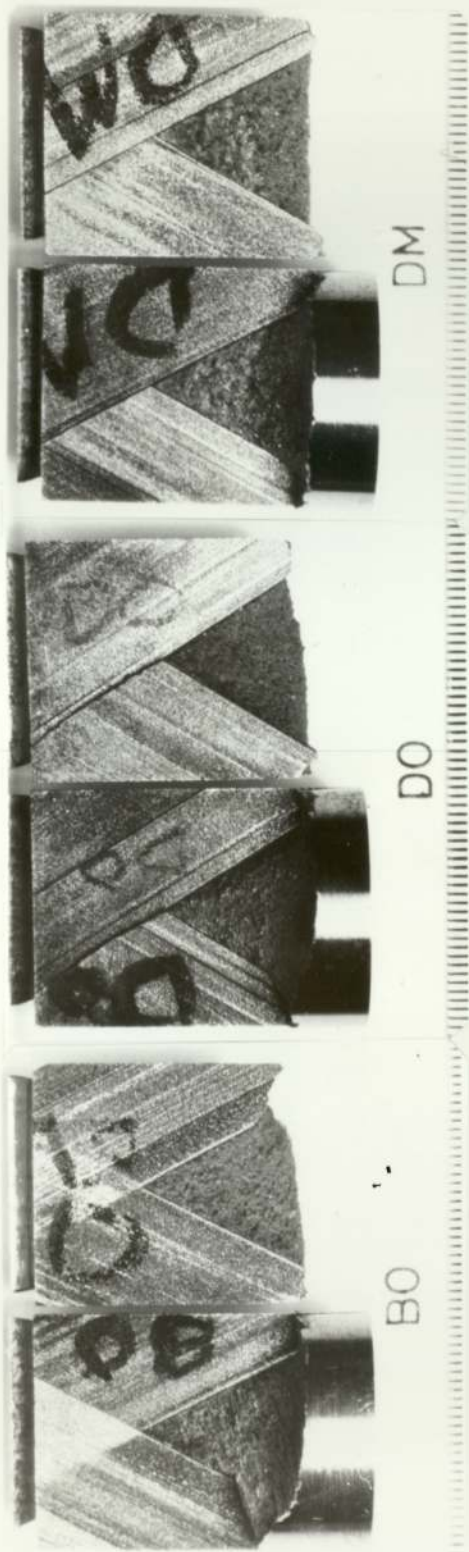


PLATE 84 General appearance of short rod fracture toughness test specimens, halves with imperfect crack guidance by the slots (mag. x4.5)



H3B



H3A



H3C



H3M



H3O

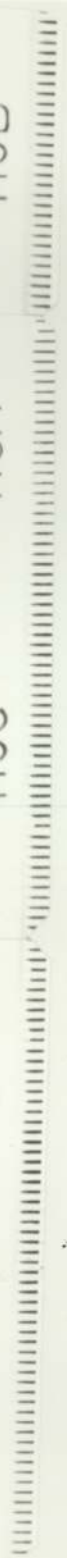


PLATE 85 General appearance of short bar fracture toughness test specimens (mag. x4.5)

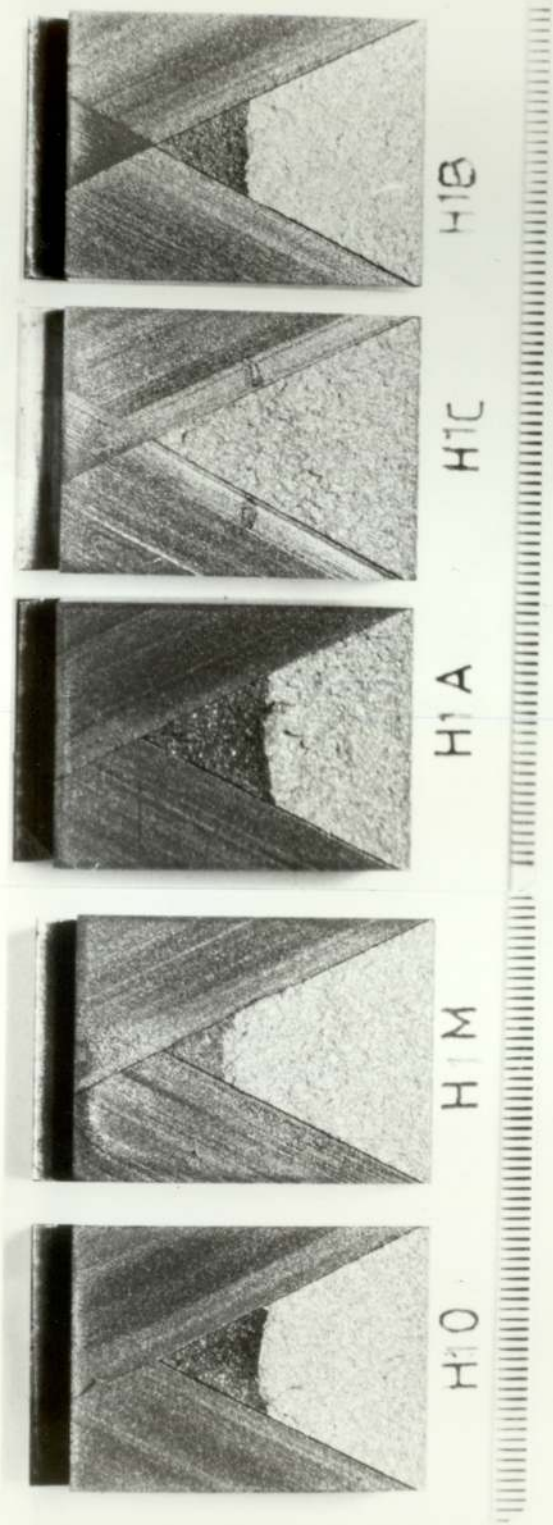
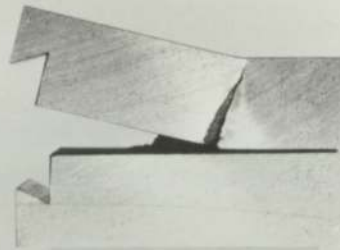


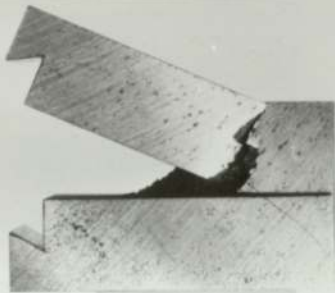
PLATE 86 General appearance of short bar fracture toughness test specimens after heat tinting process. The shaded area denotes the crack. (mag. x4.5)



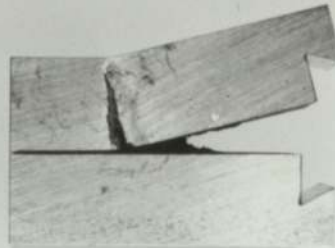
S10



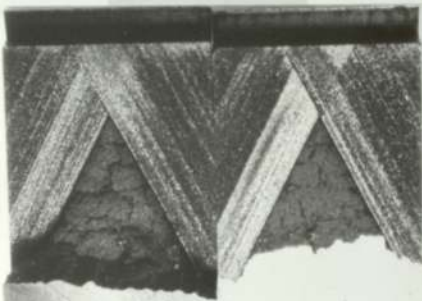
S30



S1B



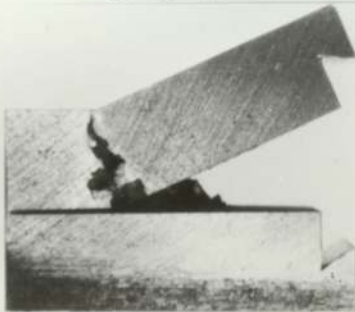
S3M



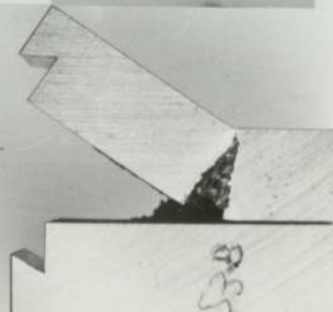
S2A



S3A



S2B



S3B

PLATE 87 General appearance of short bar fracture toughness test specimen Somdie

PLATE 88-1

Variation of fracture toughness of H.W.
die steel Electem with the distance
from the top surface of the block

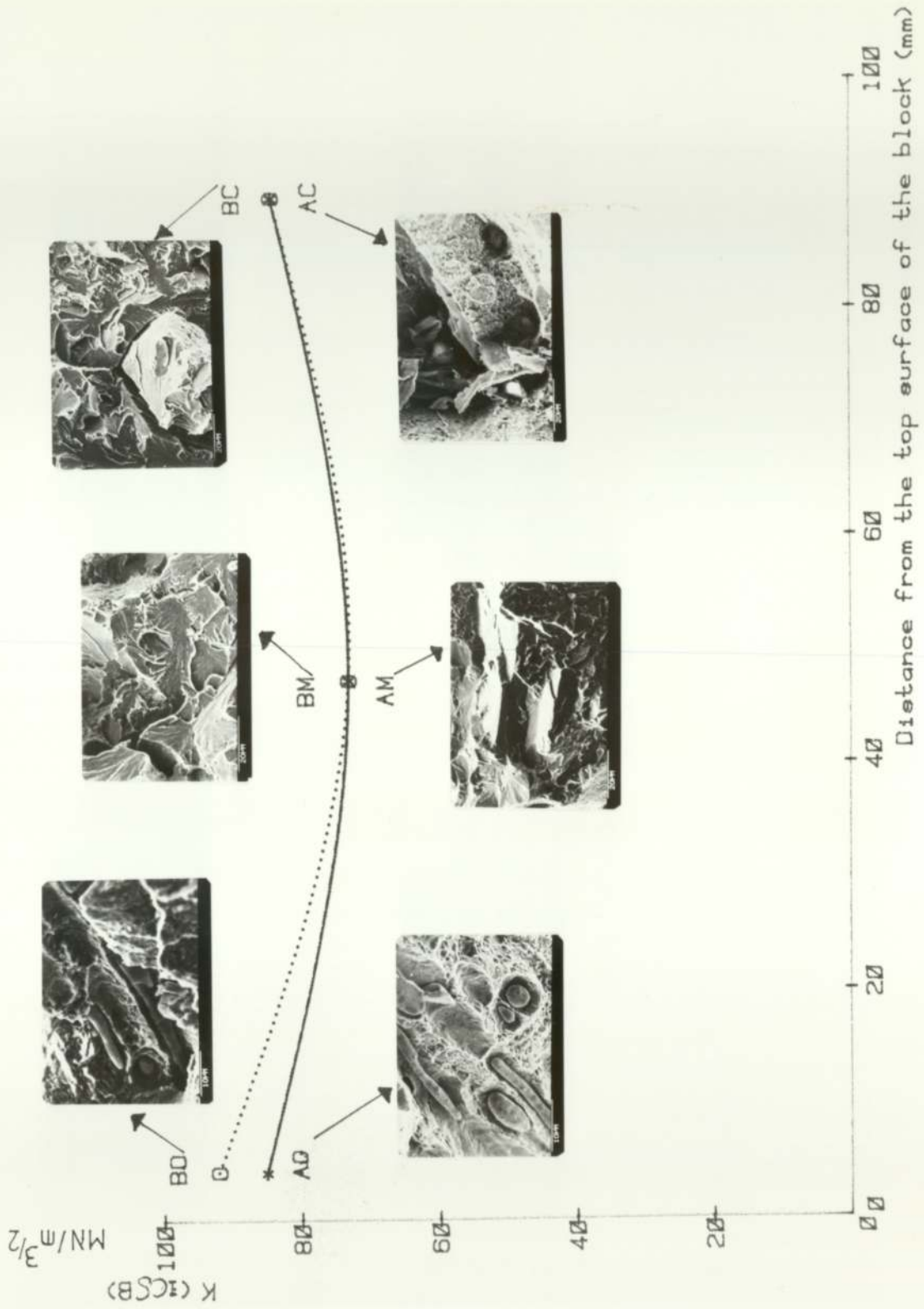


PLATE 88-2

Variation of fracture toughness of H.W.
die steel Somdie (short rod) with the
distance from the top surface of the block

MN/m^{3/2}

K (ICSB)

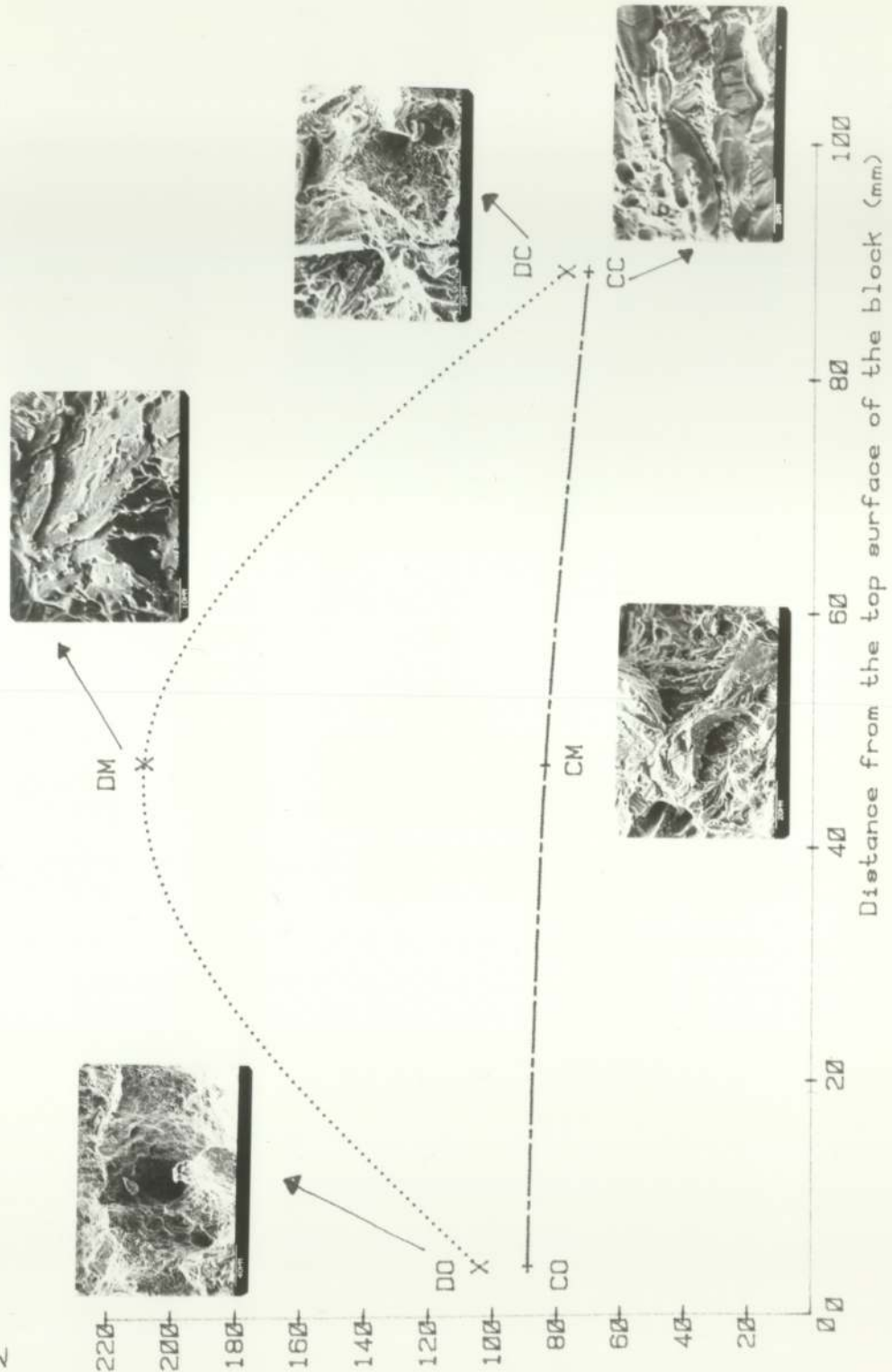


PLATE 88-3

Variation of fracture toughness of H.W.
die steel Thermodie with the distance
from the top surface of the block

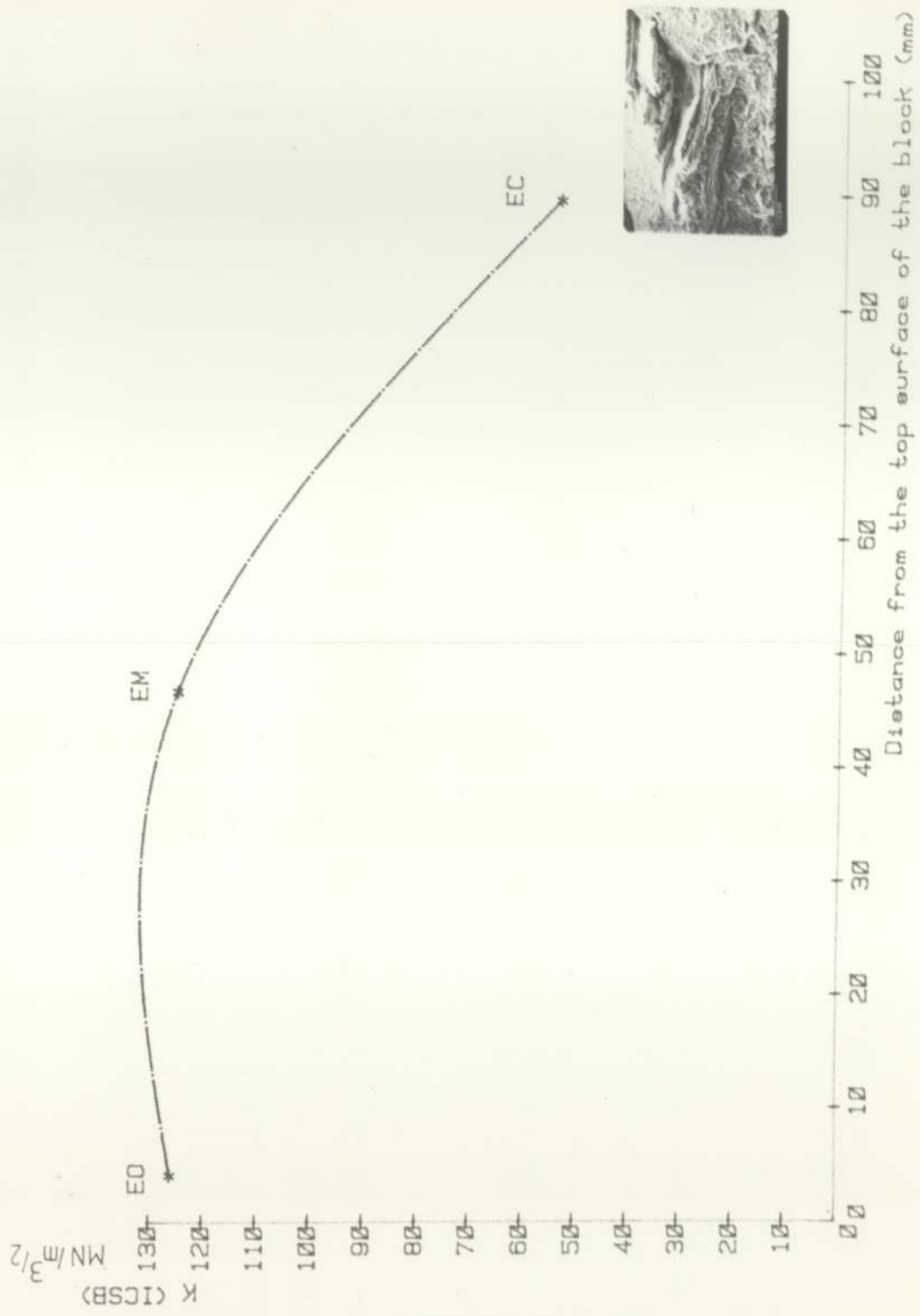


PLATE 88-4

Variation of fracture toughness of H.W.
die steel Hydie (short bar) with the
distance from the top surface of the block

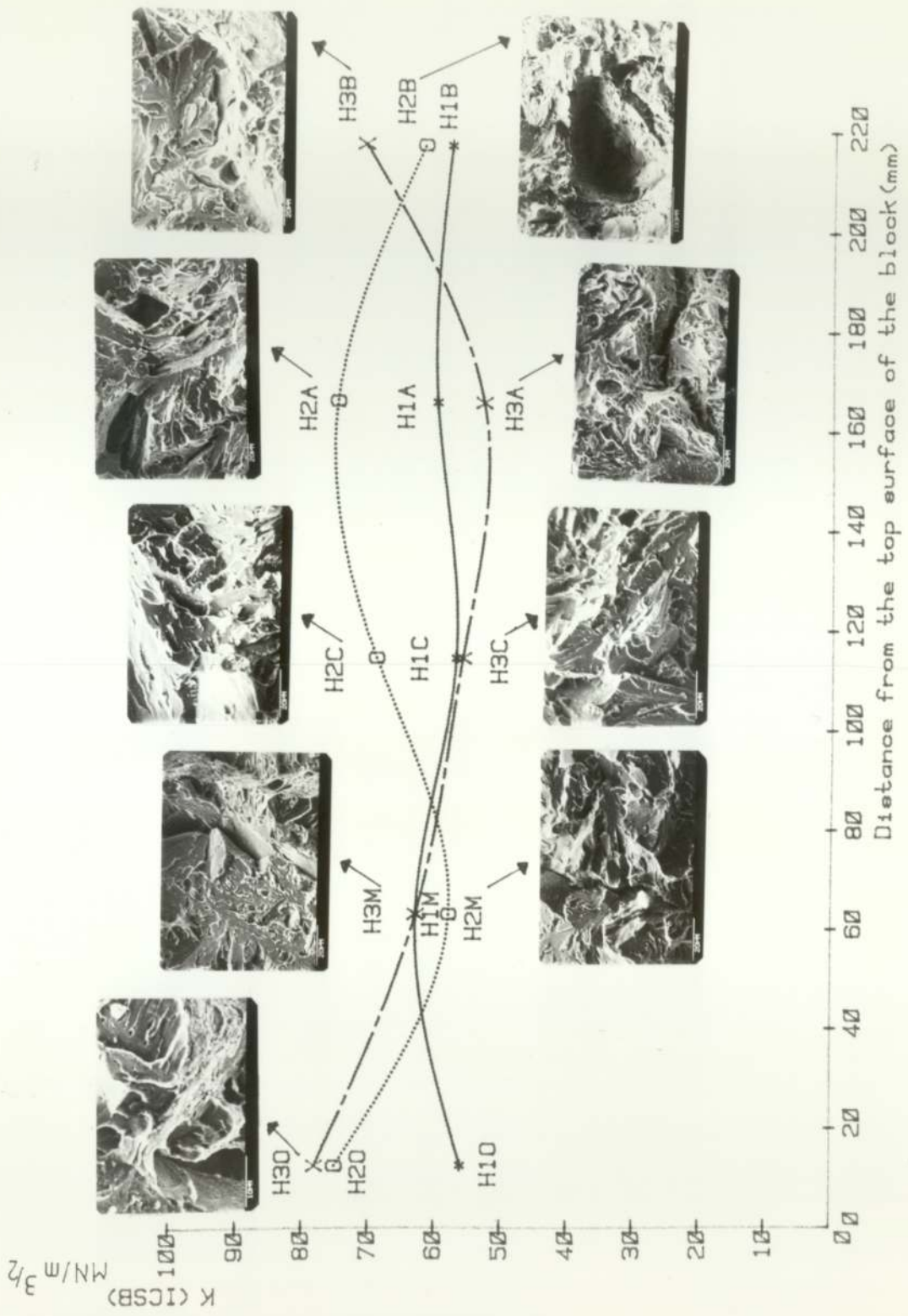
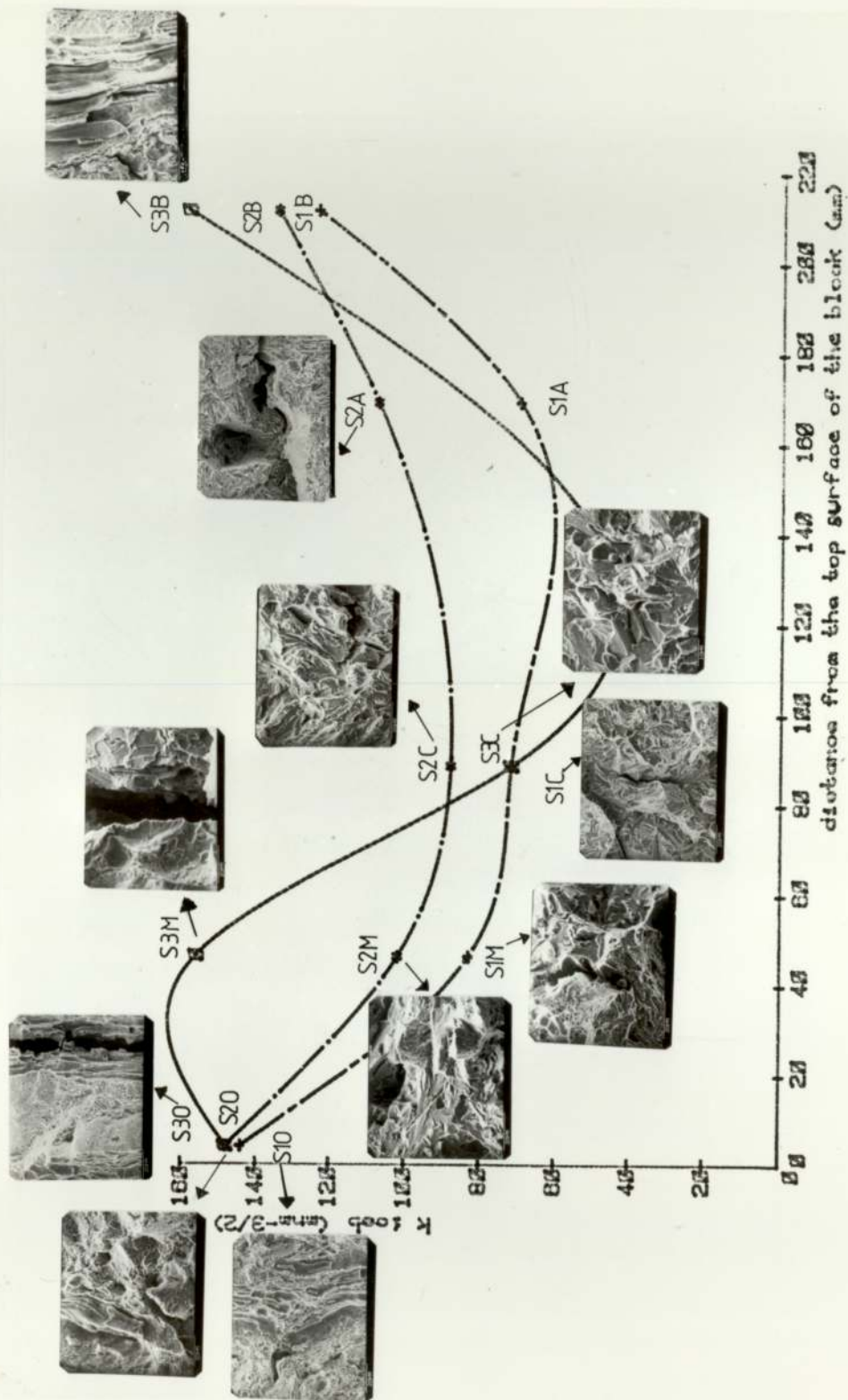


PLATE 88-5

Variation of fracture toughness of H.W.
die steel Somdie (short bar) with the
distance from the top surface of the block

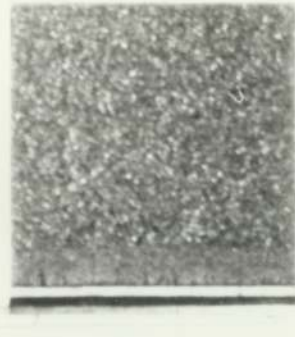




HO



HM



HC

A



S1



S2

B

Plate 89: General Appearance of Three Point Bend Specimens

A. Hydrie Steels

B. Somdie Steels

10. CONCLUSIONS

From the results the following conclusions have been drawn.

1. The fracture toughness was found to be influenced by the size^{and} distribution of the carbides and inclusions within the microstructure; with fracture toughness increasing with increase in particle distribution.
2. The die block specimens used showed peak toughness at different regions indicative of the variation in their microstructure. Suggestion is therefore made that each specimen be considered separately.
3. Excellent agreement was obtained between the short rod/bar fracture toughness test results (K_{ICSB}) and three point bend test result (K_{IC}). Therefore fracture toughness of H.W. die steel can be determined using short rod/bar specimen.
4. The analysis of notch bend tests with the evidence from fractographic examination near the fatigue zone reveal partial dimple ductile failure mechanism.
5. From the analysis it was found that the factor $\left(\frac{1+P}{1-P}\right)^{\frac{1}{2}}$ can produce too large a value for K_{ICSR} when plasticity (P) > 0.18 . However in the case of crack jump behaviour (P) is assumed equal to zero.

6. The load/crack opening displacement curves for the three point bend tests show distinct pop-in behaviour. Therefore it was not necessary to construct the 5% secant line to determine the critical load (P_Q).

REFERENCES

1. George E. Dieter, Mechanical Metallurgy, Sec.Ed., 1976, pp. 277-280.
2. L.M. Barker, TR 80-11, March 1980.
3. Herman D. Greenberge (Editor), 1966, pp. 1-32, (see E. Parke, "Theory and Background of Fracture Mechanics").
4. ASTM STP 559, part 1, 1973.
5. G.R. Irwin, J. App. Mech., Vol. 24, 1957, p. 361.
6. William F. Brown Jr., and John E. Srawley, A.S.T.M. Special Technical Publication No. 410.
7. A.A. Griffith, Phil. Trans. Soc., A.221, 1921, p. 163.
8. G.R. Irwin and J.A. Kies, Welding Research Supplement (9), 1954, pp. 193-198.
9. BS.5447, Method of Test for Plane Strain Fracture Toughness (K_{IC}) of Metallic Materials, 1977.
10. E.399-74, Annual ASTM Standard Part 10, 1975, pp. 561-580.
11. J.C. Ritter, Engineering Fracture Mechanics, (9), 1977, pp. 529-540.
12. Herman D. Greenberg, Editor, R.N. Katz and K.H. Abbott, 1966, p. 69.

13. Nelson, Schillin and Kaufman, Eng. Frac. Mech., Vol. 4, 1972, pp. 377-392.
14. J.F. Knott and D. Elliott, Worked Example in Fracture Mechanics, 1979, pp. 17-18.
15. A.S. Tetelman and A.J. McEvily Jr., 1966, pp. 61-83.
16. ASTM STP 381, 1964, pp. 1-22.
17. Karl-Hainzschw, Eng. Frac. Mech., 9, 1977, pp. 795-832.
18. J.H. Mulkerin and H. Rosenhed, Met. Trans. 22, 1971, p. 427.
19. A.J. Birkle, R.P. Wei and G.E. Pellissier, Trans. Am. Soc. Metals, 59, 1966, 981.
20. L.M. Barker, TR 80-37, May 1980.
21. L.M. Barker, TR 80-58, July 1980.
22. G.I. Taylor and A.A. Griffith, Proceedings Ins. Mech. Eng., 1917, pp. 733-809.
23. W.A. Spitzig, G.E. Pellissier, C.D. Beachem, A.J. Brother, M. Hill and W.R. Warke, (see A.S.T.M. STP 436, 1968, pp. 17-31.
24. C.D. Beachem and D.A. Moyn, ASTM STP 436, 1968, pp. 59-80 on Dept. Defence, Australia.
25. J.C. Lautridou and A. Pineau, Eng. Frac. Mech., Vol. 15, No. 1-2, 1981, pp. 55-71.

26. J.M. Krafft, Appl. Mater. Res., 3, 1964, 88.
27. L.M. Barker, Eng. Frac. Mech., Vol. 9, 1977, pp. 361-359.
28. L.M. Barker, International Journal Fracture, Vol. 15, No. 6, Dec. 1979.
29. L.M. Barker, TR 80-38, 1978, p.484.
30. BS.5762, Crack Opening Displacement, 1979.
31. A.A. Wells, Symposium College of Aeronautics and the Royal Aeronautics, Sept. 1961.
32. A.H. Cottrett, I.S.I., pp. 281-296.
33. F.M. Burrekin and D.E.W. Stone, Journ. of Strain Analysis, Vol. 1, No. 2, 1966, pp. 145-153.
34. D.S. Dugdale, Journ. Mech. Phys. Solids, Vol. 8, No. 2, 1960, pp. 100-104.
35. A.S.T.M. STP 410, 1967.
36. G.D. Fearnehough and B. Watkins, Int. Journ. Fract. Mech., 4, 3, 1968, pp. 233-243.
37. BS.18DD, Draft for Development, Method for COD Testing, 1972.
38. J.R. Rice, J. App. Mech., Vol. 35, 1968, p. 379.
39. A.S.T.M. Special Technical Publication No. 514, J.A. Beeley and J.D. Landes, pp. 1-20 and 24.39.

40. F.A. McClintock, Int. Frac., H. Leibowitz, ed., Vol. 3, 1971, pp. 47-225.
41. J.W. Hutchinson, J. Mech. and Phy. of Solids, Vol. 16, 1968, pp. 13-37.
42. P.G. Shewmon, Metal Science and Eng. Series, 1969, pp. 230-251.
43. P.W.K. Honeycombe and P. Hancock, ed., Metallurgy and Material Science Series, 1980.
44. R.A. Higgins, Eng. Met., Part 1, 1973.
45. Walter Somers Ltd., Die Steel Handbook.
46. I. Novikov, Translated from Russian by V. Afanasyer, 1978, p. 269.
47. Metal Science, Vol. 16, May 1982, pp. 245-253.
48. J.R. Patel and M. Cohen, Acta Metal., 1, 1953, 531.
49. H. Ondera, H. Gota and I. Tamura, Proceeding 1st Int. Symp. on "New Aspect of Martensitic Transformation", 327, 1976, Sendai, Japan, Japan Inst. Met.
50. G.F. Bollong and R.H. Richman, Phil. Mag., Vol. 19, 1969, p. 247.
51. L.M. Barker, TR 81-07, Feb. 1981.

52. BS.18, Tensile Testing of Metals "General"
Part 2, 1971.
53. L.M. Barker, TR 80-12, March 1980.
54. S.B. Biner and J.T. Barnby, The Measurement of
224 Al-alloy and Thermodie Fracture Toughness
by Using Non-Standard Short Rod/Bar Fracture
Test, Unpublished Work.
55. A.S. Steelman and A.J. McEvily Jr., Fracture of
Structural Materials, pp. 38-85.
56. D.S. Thompson and R.E. Zinckham, Eng. Frac. Mech.
Vol. 7, 1975, p. 389.
57. D.A. Curry and J.T. Knott, Metal Science, Jan.
1976, pp. 1-6.
58. C.J. McMahon and M. Cohen, Acta Met. 1965,
3, 591.
59. F.B. Pickering and S.W. Robinson, (see monograph
3, 1, Institution of Metallurgists, 1979).
60. F.B. Pickering, The Institution of Metallurgists,
Monograph No. 3, 1979 (see F.B. Pickering and
S.W. Robinson, pp. 127-143).
61. BS.3DD, Draft Method of Test for Plane Strain
Fracture Toughness, K_{IC} , 1971.
62. J.T. Barnby, J. NDT., Dec., 1971, pp. 385-390.
63. S.P. Lynch, Defence Science and Technology
Organisation, Dept. Defence, Australia